

Nanoparticle Liposome Interactions

THÈSE N° 8963 (2018)

PRÉSENTÉE LE 16 NOVEMBRE 2018

À LA FACULTÉ DES SCIENCES ET TECHNIQUES DE L'INGÉNIEUR
LABORATOIRE DES NANOMATÉRIAUX SUPRAMOLÉCULAIRES ET INTERFACES - CHAIRE CONSTELLUM
PROGRAMME DOCTORAL EN SCIENCE ET GÉNIE DES MATÉRIAUX

ÉCOLE POLYTECHNIQUE FÉDÉRALE DE LAUSANNE

POUR L'OBTENTION DU GRADE DE DOCTEUR ÈS SCIENCES

PAR

Zekiye Pelin GÜVEN

acceptée sur proposition du jury:

Prof. K. Scrivener, présidente du jury
Prof. F. Stellacci, directeur de thèse
Prof. L. Rodríguez Arriaga, rapporteuse
Prof. D. Fotiadis, rapporteur
Prof. R. Buonsanti, rapporteuse



ÉCOLE POLYTECHNIQUE
FÉDÉRALE DE LAUSANNE

Suisse
2018

Acknowledgments

Being a scientist was my childhood dream, so I successively followed the path which was described as the generic way to be a scientist for the last 11 years. From where I stand now, I am grateful seeing what I have achieved and the person I have become. Of course in this journey I was not alone and there are so many people I would like to thank;

First of all, my supervisor, Prof. Francesco Stellacci for giving me the opportunity of being a part of his group. I have evolved scientifically and emotionally immensely thanks to your openness to discussions, all kinds of questions, your new ideas and mentoring.

My thesis committee, Prof. Karen Scrivener, Prof. Dimitrios Fotiadis, Prof. Laura R. Arriaga, Prof. Raffaella Buonsanti, for kindly accepting to be in my thesis committee and evaluating my work. I specifically would like to thank Prof. Laura R. Arriaga for hosting me in her lab to finalize fusion experiments. Dr. Davide Demurtas, for introducing me to cryo-EM and patiently showing me the basics, pre and post processing of the beautiful images that I am now capable of taking. Ms. Chiara Donini for making my life easier with any administrative stuff.

During my PhD, I was part of one of the most awesome, friendly and smart group of people. I was lucky to be surrounded by them that have been basically friends more than colleagues. Marie, my cryo-sister, thanks a lot for being there whenever I need and showing every control experiments possible. Paulo, I appreciate every moment you spent on me for teaching. You both built up the basis of what I wrote in this thesis.

Elif and Ahmet, from the moment I stepped into lab I felt I was welcomed mostly thanks to you. Thanks for patiently answering all of my questions, your big smiles and delicious food. Evi and Nikos, you have always been the definition of loyal friends for me. Evi, you were an inspiration to me with your strength, determination, and manners. Nikos, I know that I can count on you whenever I need. Ula, thanks a lot for being other half of Pula, you have inspired

me a lot with your free-spirit and creativity. Zhi, thanks for your optimism in the lab, your help and for making me participate in cool projects.

Old Sunmil and new Sunmil, Sergio, Lydia, Ozgun, Jessica, Matteo, Anna, Maria, Huayan, Sam, Simone, you made every moment in the lab valuable for me. I would like to thank all the post-docs in the Sunmil, Kellen for kindling my curiosity about nanoparticles, Sam and Rosie for being awesome officemates and answering my endless questions, Matej for all the coffee-breaks and non-bike related discussions, Marta for all your huge help and criticism to my experiments, and Quy for your help with everything.

The collaborators, Dr. Mukarram A. Tahir, thanks a lot for showing me the non-european part of the scientific world. I enjoyed going through all the up and downs in the project with you as a peer and a friend. All the NCCR-MSE family, Alex, Angelo, Viktoria, Rafael It was so much fun being with you every year.

My dearest friends, Naz, Berfin, Gamze, Poyzan, Deniz, Baris, Aydin, Ayca for supporting me, being there for me whenever I need. I appreciate every non-scientific silly discussions we had, you kept me going.

My family, annem ve babam, ananem ve dedem I am privileged to be your daughter and granddaughter. All my life, regardless of what I do, I have always felt your endless support and love. Sizi cok seviyorum ve her sey icin tesekkur ediyorum. My little but actually not that little sister, Selin, It is good that I was determined to have a sibling. Thanks to you, I know I won't be alone no matter what. My family in France, Marc, Christine, Gerard, Bernadette, Isabelle and Antonio, I can't thank enough for making me feel like a part of the family from the beginning.

Last but not least, Christophe, my love, I can't thank you enough for the last 4 years. You were always there for me, to comfort me, to cheer me up, to support me. Thanks a lot for insisting having Aslan. His furry cuddles calmed me down whenever I need. This PhD would not be possible without you both. I am looking forward spending rest of my life with you learning and discovering new things. I love you to the moon and back.

Abstract

Protein-mimetic materials are of great interest for biotechnology to grant protein-like properties to artificial systems. Additionally, these materials can be used to shed light on the fundamental properties of proteins in many environments. Nanoparticles, in particular, offer a wide choice of parameters like size, core material, and surface chemistry that can be modified to better mimic proteins. Recently, it was shown that amphiphilic gold nanoparticles are able to fuse with and penetrate cell membranes in an energy independent manner. This behavior is similar to that of cell penetrating peptides.

The objective of this thesis was to investigate the key parameters that allow amphiphilic nanoparticles to fuse with lipid bilayers and to generate nanoparticles capable of performing other protein-like functions.

The thesis start with a systematic study on the interaction between amphiphilic gold nanoparticles and liposomes. All particles studied had a gold core, whose size varied from 1.7 to 6 nm. Amphiphilic ligand shells were achieved by using mixtures of a hydrophobic and hydrophilic ligand, with the hydrophobic one limited at 30% of the mixture because of solubility limitations. The liposomes studied had a size range of 60 to 300 nm. We found many different interactions. Sulfonated particles interacted with small vesicles (smaller than 60 nm) mediating clustering of vesicles, similar to adhesive proteins. The same particles, once combined with larger liposomes, behaved like curvature inducing proteins, that is they generated flat areas terminating in high curvature joints.

Particles at the highest degree of amphiphilicity (*i.e.* a loading of the hydrophobic molecules at the limit of solubility), however, showed an even larger variety in interactions. The largest particles (~5 nm) fused with lipid membranes (independent on the liposome size) like cell penetrating peptides. Particles of intermediate size (~3 nm) fused with the membranes and brought liposomes in close proximity (like the less amphiphilic ones). These particles had an additional important property, they were able to mediate a fusion event upon Ca^{2+} addition

between the adjacent liposomes. Hence these particles behaved as SNARE proteins and can be considered as the first synthetic material to be fusogenic. The smallest particles in this category fused with the lipid bilayer (as all others in this family), were fusogenic (as the middle sized ones) and spontaneously generated ring patterns on the liposomes. These rings were found to delimit flat vesicle regions. This latter phenomenon does not seem to have a biological analog.

Overall, we find that amphiphilic nanoparticle can be considered as protein analogs, especially proteins that interact with membranes. In particular when the degree of amphiphilicity is high we achieved a series of particles that behave as membrane proteins, and depending on their size show different functions. These findings offer insight to decode the key factors in the interaction between nanoparticles and lipid bilayers and provide the first hints on how to use nanoparticles model systems to gain a better understanding on some key features of protein and protein functions.

Keywords: gold nanoparticles, amphiphilic, liposomes, protein-mimetic, fusogens

Résumé

Les matériaux protéines-mimétiques présentent un grand intérêt pour la biotechnologie en conférant des propriétés protéiques à des systèmes artificiels. En outre, ces matériaux peuvent être utilisés pour faire la lumière sur les propriétés fondamentales des protéines dans de nombreux environnements. Les nanoparticules, en particulier, offrent un large choix de paramètres tels que la taille, le matériau du noyau et la chimie de surface pouvant être modifiés pour mieux imiter les protéines. Récemment, il a été montré que les nanoparticules d'or amphiphiles sont capables de fusionner et de pénétrer les membranes cellulaires d'une manière indépendante de l'énergie. Ce comportement est similaire à celui des peptides pénétrant dans les cellules.

Les objectifs de cette thèse étaient d'étudier les paramètres clés qui permettent aux nanoparticules amphiphiles de fusionner avec les bicouches lipidiques et de générer des nanoparticules capables d'exécuter d'autres fonctions protéiques.

Cette thèse a débuté par une étude systématique de l'interaction entre les nanoparticules d'or amphiphiles et les liposomes. Toutes les particules étudiées avaient un noyau d'or dont la taille variait de 1,7 à 6 nm. Les enveloppes de ligands amphiphiles ont été obtenues en utilisant des mélanges d'un ligand hydrophobe et hydrophile, le composé hydrophobe étant limité à 30% du mélange en raison des limitations de solubilité. Les liposomes étudiés avaient une taille comprise entre 60 et 300 nm. Nous avons trouvé de nombreuses interactions différentes. Les particules sulfonées interagissaient avec de petites vésicules (inférieures à 60 nm) assurant le regroupement des vésicules, de manière similaire aux protéines adhésives. Ces mêmes particules, une fois combinées avec de plus grands liposomes, se sont comportées comme des protéines induisant une courbure, c'est-à-dire qu'elles ont généré des zones plates se terminant par des joints à forte courbure.

Les particules ayant le plus haut degré de pouvoir amphiphile (c'est-à-dire une charge des molécules hydrophobes à la limite de la solubilité) présentaient cependant une plus grande

variété d'interactions. Les plus grosses particules (~5 nm) ont fusionné avec des membranes lipidiques (indépendamment de la taille des liposomes) à la manière de peptides pénétrant des cellules. Des particules de taille intermédiaire (~3 nm) ont fusionné avec les membranes et rapproché les liposomes (tout comme les particules moins amphiphiles). Ces particules avaient une propriété importante supplémentaire, elles étaient capables de provoquer un événement de fusion lors de l'addition de Ca^{2+} entre les liposomes adjacents. Ces particules se sont donc comportées comme des protéines SNARE et peuvent être considérées comme le premier matériau synthétique à être fusogène. Les plus petites particules de cette catégorie fusionnaient avec la bicouche lipidique (comme toutes les autres de cette famille), étaient fusogènes (comme celles de taille moyenne) et généraient spontanément des motifs annulaires sur les liposomes. Il a été trouvé que ces anneaux délimitaient des régions de vésicules plates. Ce dernier phénomène ne semble pas avoir de pendant biologique.

Dans l'ensemble, nous constatons que les nanoparticules amphiphiles peuvent être considérées comme des analogues protéiques, notamment des protéines qui interagissent avec les membranes. En particulier lorsque le degré d'amphiphilicité est élevé, nous avons obtenu une série de particules qui se comportent comme des protéines membranaires et qui ont, selon leur taille, montré des fonctions différentes. Ces découvertes permettent de décoder les facteurs clés de l'interaction entre les nanoparticules et les bicouches lipidiques et fournissent les premières indications sur la façon d'utiliser les modèles de nanoparticules pour mieux comprendre certaines caractéristiques clés des protéines et des fonctions protéiques.

Mots-clés : nanoparticules d'or, amphiphiles, liposomes, protéines-mimétiques, fusogènes

Table of Contents

Abstract.....	iii
Résumé.....	vii
Table of Contents.....	ix
List of Figures	xi
List of Tables.....	xv
List of Abbreviations	xvii
Introduction and Structure of the Thesis	1
1 Membranes.....	5
1.1 Cellular Membranes	5
1.2 Membrane Lipids.....	6
1.3 Membrane Proteins.....	8
1.3.1 Curvature inducing proteins	9
1.3.2 Cell adhesion proteins	10
1.3.3 Fusion proteins	11
1.3.4 Cell-penetrating peptides	14
1.4 Lipid Bilayers	16
1.4.1 Lipids.....	16
1.4.2 Liposomes	20
1.5 Attempts for Synthetic Cell Membrane Proteins	23
2 Nanoparticles and Membranes	25
2.1 Nanoparticles	25
2.1.1 Binary SAM nanoparticles.....	29
2.2 Overview of the Applications of Mixed Ligand Nanoparticles.....	30
2.3 Nanoparticles and Cells	32
2.3.1 Cellular uptake of nanoparticles	33
2.3.2 Cellular uptake of MUS:OT gold nanoparticles.....	37
2.3.3 Toxicity of nanoparticles.....	40
2.4 Nanoparticles and Lipid Bilayers	41
2.4.1 MUS:OT nanoparticles and lipid bilayers.....	42
2.5 Synthesis and Characterization of MUS:OT Particles	54
3 Design Parameters on Nanoparticle-Liposome Interactions.....	57
3.1 Introduction	57
3.2 Materials and Methods	58
3.3 Results.....	60
3.3.1 Individual attachment.....	63

3.3.2	Vesicle aggregation.....	65
3.3.3	Close packed arrangements	66
3.3.4	Bilayer insertion.....	71
3.3.5	Ring formation	73
3.4	Discussion	73
3.5	Conclusions	77
4	<i>Nanoparticle Mediated Vesicle Fusion.....</i>	79
4.1	Introduction	79
4.2	Materials and Methods	81
4.3	Results and Discussion.....	83
4.3.1	Simulations	83
4.3.2	Cryo-EM studies.....	87
4.3.3	Content mixing assay	90
4.4	Conclusions	95
5	<i>Ring Formations.....</i>	97
5.1	Introduction	97
5.2	Materials and Methods	99
5.3	Results and Discussion.....	100
5.3.1	Cryo-EM	100
5.3.2	Leakage assay	104
5.4	Conclusion.....	107
6	<i>Conclusions and Outlook</i>	109
6.1	Conclusions	109
6.2	Outlook	112
6.2.1	Characterization of other protein-mimetic features	112
6.2.2	Artificial cells.....	113
	<i>Appendix A</i>	117
	Protocol for the synthesis and characterization of MUS:OT gold nanoparticles	117
	<i>Appendix B</i>	131
	Additional images of nanoparticle-liposome systems.....	131
	<i>Appendix C</i>	139
	Cryo electron microscopy.....	139
	<i>References.....</i>	143
	<i>Curriculum Vitae.....</i>	169

List of Figures

Figure 1-1 The fluid mosaic membrane of Singer and Nicholson.	6
Figure 1-2 Lipid raft domains are formed by saturated phospholipids, sphingolipids, cholesterol.....	7
Figure 1-3 Schematic illustration of functions that cellular membrane proteins undertake on the cell membrane.	8
Figure 1-4 Schematic representation of membrane curvature induced by membrane proteins.	9
Figure 1-5 Schematic illustrations of different types of cell junctions.	11
Figure 1-6 Schematic illustrations of membrane-fusion events that take place in the cell. ..	12
Figure 1-7 Schematic representation of the fusion model suggested for SNARE proteins. ...	13
Figure 1-8 Schematic representation of the different classes of CPPs and how they interact with bilayers.	15
Figure 1-9 Different types of lipid molecules.	17
Figure 1-10 Characteristics of lipid molecules used to calculate the packing factor.....	19
Figure 1-11 Schematic representation of lipid aggregates formed in water.....	20
Figure 1-12 Scheme of a unilamellar liposome and different ways to modify it.....	22
Figure 2-1 Schematic representation of nanoparticles with various materials, shape, and surface coverage.	26
Figure 2-2 Schematic illustration of the nucleation theory.	28
Figure 2-3 Domain formation on the surface of nanoparticles with different ligand couples at thermodynamic equilibrium.....	29
Figure 2-4 Schematic representation of MUS:OT nanoparticles.	31
Figure 2-5 Different endocytic pathways to enter into the cell.	34
Figure 2-6 Illustrations of three possible nanoparticle non-specific interaction with cell membrane.	35
Figure 2-7 Cell uptake of amphiphilic nanoparticles.	39
Figure 2-8 Schematic illustration of various approaches for design of nanoparticle liposome hybrid systems.....	41

Figure 2-9 CLSM images of MUS:OT nanoparticles incubated with GUVs made of various lipids.	44
Figure 2-10 AFM topography images of DOPC supported bilayers incubated with MUS:OT 34%OT nanoparticles in PBS.....	45
Figure 2-11 Schematic illustration of capacitance measuring set-up based on nanoparticle adsorption	46
Figure 2-12 Schematic representation of the interaction between MUS:OT nanoparticles and lipid bilayer.	47
Figure 2-13 a) Representation of the ligands on the gold nanoparticles in simulations. b) Suggested surface morphology on the nanoparticles. c) Free energy diagram of nanoparticles as a function of size, ligand ratio, and surface morphology	50
Figure 2-14 Representation of the All-MUS particles through the transition states of membrane embedding.	51
Figure 2-15 Simulation snapshots representing the behavior of MUS:OT 50:50 particles in the bilayer.....	52
Figure 2-16 Snapshots of simulations showing the process of nanoparticles forming chain like structures and how cholesterol is depleted from the vicinity of nanoparticles.....	53
Figure 3-1 DOPC liposomes incubated with nanoparticles coated with different ligand molecules.	62
Figure 3-2 Stereopair images of MUP particles incubated with DOPC liposomes.....	63
Figure 3-3 Individual attachments of nanoparticles on the liposomes.	64
Figure 3-4 Frames from constructed tomograms liposomes with MUS:OT 20%OT (2.8 ± 1.4 nm) particles showing individual attachments of nanoparticles on the bilayer.	64
Figure 3-5 All MUS (2.7 ± 1.3 nm) particles forming vesicle aggregates with multiple vesicles.	65
Figure 3-6 MUS:OT 20%OT, (2 ± 0.9 nm) nanoparticles bridging two vesicles.....	66
Figure 3-7 MUS:OT 10%OT (5.1 ± 1.5 nm) nanoparticles forming vesicle aggregates.	66
Figure 3-8 a) Fractionated MUS:OT 10%OT (3.1 ± 0.5 nm) nanoparticles incubated with large liposomes > 100 nm.	67
Figure 3-9 Fractionated MUS:OT 10%OT (1.7 ± 0.5 nm) nanoparticles incubated with liposomes > 100 nm..	68

Figure 3-10 Non fractionated MUS:OT 10%OT (2.8 ± 1.4 nm) nanoparticles incubated with large liposomes larger than 100 nm.	69
Figure 3-11 All-MUS (2.3 ± 0.7 nm) nanoparticles incubated with large liposomes > 100 nm.	70
Figure 3-12 a) MES (1.8 ± 0.6 nm) particles, b) MPSA (1.8 ± 0.5 nm) particles, c) MUS:OT 10%OT (1.7 ± 0.5 nm) particles with DOPC liposomes	70
Figure 3-13 A frame from constructed tomogram showing nanoparticle, MUS:OT 30%OT (2.4 ± 1.9 nm), in the bilayer.	71
Figure 3-14 A frame from aligned file of tomogram acquisition and the 3D construction of the tomogram with Chimera.	72
Figure 3-15 MUS:OT 30%OT (2.1 ± 1 nm) particles forming ring patterns with small liposomes.	73
Figure 4-1 The representation of the nanoparticles in the coarse-grained molecular dynamics.	83
Figure 4-2 Snapshots from the simulations of planar bilayers.	84
Figure 4-3 Snapshots from the simulations of the fusion process that was mediated by MUS:OT 50%OT nanoparticles.	85
Figure 4-4 Snapshots from simulations pointing the transition states during stalk and pore formation.....	86
Figure 4-5 Snapshots from the simulations illustrating different initial states of fusion process.	86
Figure 4-6 Cryo-EM images representing different stages of nanoparticles mediated fusion process	88
Figure 4-7 The frames from the tomograms of liposomes incubated with MUS:OT 30%OT nanoparticles upon addition of Ca^{2+}	89
Figure 4-8 Schematic illustration of how content mixing assay measures the fusion event..	90
Figure 4-9 Fluorescence measurement during the fusion process.	91
Figure 4-10 Fluorescence measurement of fusion process.....	92
Figure 4-11 Fluorescence measurements of nanoparticle mediated fusion process with different types of nanoparticles.	93
Figure 4-12 Fluorescence measurements of fusion events with MUS:OT 30%OT nanoparticles.	93

Figure 4-13 Demonstration of nanoparticle mediated fusion at the microscale.	94
Figure 5-1 Stereopair images of MUS:OT 30%OT-1 (2.1 ± 1 nm) ring formations on liposomes, recorded by cryo-EM.	100
Figure 5-2 Stereopair images of MUS:OT 30%OT-1 (2.1 ± 1 nm) ring formations on liposomes, recorded by cryo-EM, a) after 1 hour incubation, b) after overnight incubation.....	101
Figure 5-3 Overnight incubation of MUS:OT 30%OT-1 (2.1 ± 1 nm) particles with DOPC liposomes with higher nanoparticle and liposome concentration.	101
Figure 5-4 Stereopair images of MUS:HDT 20%HDT (2.6 ± 1.3 nm) ring formations on liposomes, recorded by cryo-EM.....	102
Figure 5-5 Stereopair images of MUS:OT 30%OT-2 (2.4 ± 1.9 nm) (batch B) ring formations on liposomes, recorded by cryo-EM.....	102
Figure 5-6 Fluorescence spectra of SRB-loaded liposomes (SUV) after overnight incubation with nanoparticles.....	104
Figure 5-7 Fluorescence spectra of 5 μ M SRB ligand only incubated with nanoparticles, demonstrating the quenching effect of the nanoparticles.....	105
Figure 5-8 Fluorescence spectra of SRB loaded liposomes after 1 hour incubation with nanoparticles in an external solution with 50mM NaCl.	105
Figure 6-1 Graphical summary of nanoparticle-liposome systems and fusogenic behaviors as a function of size and hydrophobic content.....	111
Figure 6-2 MUS:OT 10%OT particles incubated with larger liposomes.....	113
Figure 6-3 Examples to compartmentalization with nanoparticles and liposomes.....	115

List of Tables

Table 1-1 Vesicle types regarding size and number of lipid layers.....	21
Table 3-1 Chemical structures of thiolated ligands coating the surfaces of the nanoparticles.	59
Table 3-2 List of nanoparticles that were used in the experiments and their representative core diameters in nm.. ..	61
Table 5-1 Amount of liposomes (all sizes) and aggregates imaged by cryo-EM and ring patterns observed.....	103

List of Abbreviations

2D	Two dimensional
3D	Three dimensional
3T3	Mouse fibroblast cell
a	Optimum head group area
a.u.	Arbitrary Unit
AFM	Atomic force microscopy
All-MUS	Coated with only MUS ligands
AuNP	Gold nanoparticles
B16-F0	Melanoma cells
BAR	Bin, Amphiphysin, Rvs
BODIPY	Boron-dipyrromethene
br-OT	Branched-octanethiol (3,7 dimethyloctane 1-thiol)
CPPs	Cell penetrating peptides
cryo-EM	Cryogenic electron microscopy
CLSM	Confocal Laser Scanning Microscopy
DC2.4	Dendritic mouse clonal cells
DLS	Dynamic light scattering
DLVO theory	Derjaguin, Landau, Verwey, Overbee theory
DNA	Deoxyribonucleic acid
DOPC	1,2-dioleoyl- <i>sn</i> -glycero-3-phosphocholine
DOPG	1,2-dioleoyl- <i>sn</i> -glycero-3-phosphoglycerol
DPA	Dipicolinic acid
DPPC	1,2-dipalmitoyl- <i>sn</i> -glycero-3-phosphocholine
EM	Electron microscopy
ER	Endoplasmic reticulum
FRET	Förster resonance energy transfer
GUV	Giant unilamellar vesicle

HDT	1-Hexadecanethiol
HeLa	Cervical cancer cells
l_c	Critical chain length
MALDI-TOF	Matrix assisted laser desorption ionization-time of flight
MD	Molecular dynamics simulations
MES	2-Mercaptoethanesulfonic acid
MPS	mononuclear phagocyte system
MPSA	3-Mercapto-1-propanesulfonic acid
MPSA:OT	Coated with MPSA and OT together
MUP	11-mercaptoundecane-1-phosphonic acid
MUS	11-mercaptoundecane-1-sulfonic acid
MUS:br-OT	Coated with MUS and br-OT together
MUS:OT	Coated with MUS and OT together
NaCl	Sodium Chloride
naCPPs	Non-amphiphilic cell penetrating peptides
NBD-PE	1,2-dioleoyl-sn-glycero-3-phosphoethanolamine-N-(7-nitro-2-1,3-benzoxadiazol-4-yl)
NMR	Nuclear magnetic resonance
OT	1-octanethiol
P	Dimensionless packing value
PA	Phosphatidic acid
paCPPs	Primary amphiphilic cell penetrating peptides
PBS	Phosphate buffered saline
PC	Phosphatidylcholine
PE	Phosphatidylethanolamine
PEG	Polyethylene glycol
PG	Phosphatidylglycerol
PI	Phosphatidylinositol
PS	Phosphatidylserine
saCPPs	Secondary amphiphilic cell penetrating peptides
SAM	Self-assembled monolayers

sar1	Secretion-associated, Ras-related
SAXS	Small angle x-ray scattering
SNARE	Soluble N-ethylmaleimide-sensitive factor attachment protein receptor
SPION	Superparamagnetic iron nanoparticles
SRB	Sulphorhodamine B
STM	Scanning tunneling microscopy
SUV	Small unilamellar vesicle
TAP	Trimethylammonium-propane
TEM	Transmission electron microscopy
TGA	Thermogravimetric analysis
TMA	N,N,N-Trimethyl-10-undecenylammonium chloride
UV-vis	Ultra violet-visible spectroscopy
v	Volume
VAMp	Vesicle-associated membrane protein
ZW	Zwitterionic (3-[(11-mercapto-undecyl)-N,N-dimethyl-amino]-propane-1-sulfonate)

Introduction and Structure of the Thesis

The study of human biology, ranging from traditional medicine to experimental gene therapy, is based on and guided by a fundamental need to understand the minute interactions occurring between the building block of the human body, the cell, and its environment. Due to the complex nature of a cell, however, the direct study of cell-matter interaction is a multiparametric problem, where a cause and effect relationship is often difficult to establish, study and modulate. It is therefore necessary to develop artificial, simplified yet accurate model systems, that will allow the study of cells' interaction with matter.

Liposomes have been proposed and studied as model systems for cell membranes, in addition to various applications ranging from therapeutics to medical imaging. Since, liposomes are consisted of two main compartments; the aqueous interior and hydrophobic bilayer, they can be used and modified variously. For instance, drugs can be loaded in the liposomes to reduce the side-effects¹, or liposomes facilitate the targeted delivery directed by chemical modifications on the surface². Meanwhile, they serve as model systems to study matter insertion to the cell membrane or they serve as mini reactors for chemical reaction to take place³.

Nanoparticles have also been used widely in biological and medical applications. Most of these applications benefit from physicochemical properties of nanoparticles which vary drastically depending on the characteristics of nanoparticles consisting of size, shape, composition, etc.⁴ Recently, nanoparticle-liposome systems have gained significant interest, as the nanoparticles' broad range of composition, functionality, and stability can be employed to improve and expand the functionality and applications range of liposomes⁵. A nanoparticle's ability to induce a strong response to externally-applied fields such as ionizing radiation, magnetic field, and light supposedly contributes to advantages of these liposome systems in the fields of therapeutics and diagnostics. The nanoparticle-liposome systems have

been utilized as a platform in which the liposomes serve as a model membrane to investigate the biomimicry behavior of nanoparticles³.

Based on these observations, the objective of this thesis is to mediate biological functions using protein-mimetic amphiphilic nanoparticles. In other words, we aim to design nanoparticle-liposome hybrid systems to achieve specific functions typically displayed in biological systems.

Recently, amphiphilic MUS:OT gold nanoparticles coated with a binary ligand monolayer have been shown by Verma⁶ and Van Lehn^{7,8}, experimentally and computationally, respectively, to penetrate into lipid membranes following non-endocytic pathways. Additionally, the same nanoparticles can accommodate a third type of molecule in their monolayer, while employing the same pathway to pass the cell membranes⁹. On the contrary, when liposomes made of neutral phospholipids instead of biologic cells are used, these nanoparticles prefer to stay in the membrane or stick to its surface. These characteristics have made the MUS:OT nanoparticles perfect candidates for cell membrane protein-mimetics for any biological function which can take place when liposomes are used.

Taken together, this study depicts the interaction of MUS:OT nanoparticles with DOPC liposomes as a model membrane system. To be able to understand the key factors governing this interaction between MUS:OT nanoparticles and liposomes, it is screened as a function of nanoparticle size, surface chemistry of nanoparticles, and the size of the liposomes. In the end, this study provides answers on whether the interactions between nanoparticles and liposomes resemble the function of membrane proteins, and how these proteins are placed in the membranes. Finally, based on the design parameters of the nanoparticle-liposome systems, the fusogenic behavior of nanoparticles is investigated.

This thesis is divided into 6 chapters.

Chapter 1 begins with an overview of the cell membranes and how cell membrane proteins contribute to the functionality of the membrane. In particular, curvature inducing proteins, adhesive proteins, fusion proteins, and cell penetrating peptides are described in detail.

Moreover, a comprehensive review of lipid molecules and how they self-assemble into the liposomes is provided. Finally, an overview on how synthetic materials are used as cell membrane mimics closes this chapter.

Chapter 2 focuses on gold nanoparticles, and in particular their physicochemical properties that can be advantageous in biological applications. Then a comprehensive review of how nanoparticles (mostly gold nanoparticles) interact with cells is provided followed by a review of the literature on mixed ligand nanoparticles. Furthermore, the interaction between lipid bilayers and nanoparticles is shown. Finally, experimental and computational works on amphiphilic MUS:OT nanoparticles with lipid bilayers are detailed here.

In Chapter 3, the experimental work carried out by the candidate and aimed to characterize the interaction between nanoparticle and liposome as a function of size and surface chemistry of nanoparticles, and the liposome size is presented and discussed. Cryo-electron microscopy was used to characterize these systems mostly with stereopair images and to acquire further details cryo-electron tomography was acquired.

The main driving force for the interaction between nanoparticles and liposomes was found to be the negatively charged sulfonated head groups of the ligands that were on the surface of gold nanoparticles. Different from sulfonated nanoparticles, cationic nanoparticles (TMA) have been observed to disrupt vesicles, while neutral (PEG) and zwitterionic (ZW) nanoparticles were classified as non-interacting. Another type of amphiphilic nanoparticles, MUP particles, did not demonstrate significant interaction either.

Within MUS:OT particles-liposome systems, 5 distinctive types of formations were observed; individual attachment on the surface, vesicle aggregation, bilayer insertion, ring formation, and close packed arrangement. Furthermore, the resemblance between these formations and membrane proteins is discussed. All the synthesis and characterization procedures for the particles are described in Appendix A. Additional cryo-EM images taken under the conditions discussed are presented in Appendix B. A mechanistic description of the technique of cryo-EM is described in Appendix C.

Chapter 4 details the experimental work carried out to demonstrate nanoparticle mediated fusion of vesicles upon introduction of Calcium ions (Ca^{2+}) to the systems. MUS:OT nanoparticles with 30%OT on the surface showed the best fusogenic behavior compared to All-MUS nanoparticles. Furthermore, the effect of the Ca^{2+} concentration on the fusion event was investigated, as well as the time scale of the fusion process. In addition to fluorometric assays of vesicle fusion, cryo-EM was also used to quantify the liposome diameters in order to form a histogram of the liposome size following different conditions. Additionally, cryo-EM tomograms pointed the membrane insertion of the particles following the fusion event. The results from Chapter 4 were recently submitted as a paper in a peer reviewed journal.

Chapter 5 presents the detailed characterization of ring formations on the liposomes. Cryo-EM images allowed the observation of the formation of rings with different particles. Fluorescence assays indicated that the structure of liposomes after the ring formation remained closed and not disrupted.

Chapter 6 finally summarizes the outcomes of this thesis and how they can be used in future studies. For future projects, characterization of mechanical properties of liposomes upon interacting with MUS:OT particles and possible use of vesicle aggregates as compartments to contribute the complexity of artificial cell projects are proposed.

The appendices provide the synthesis and characterization protocols for MUS:OT nanoparticles including the synthesis of MUS ligand (Appendix A), more images of the nanoparticle-liposome systems mentioned (Appendix B), and the review the technique of cryo-EM (Appendix C).

1 Membranes

This chapter has the following outline. First, it presents an overview on the cell membranes and how cell membrane proteins contribute to the functionality of the cell membrane. Curvature inducing proteins, adhesion proteins, and fusion proteins, are described in detail. The descriptions of membrane proteins are necessary for the discussion about resemblance between nanoparticles and proteins in Chapter 3. Second, even though cell penetrating peptides are not a permanent cell membrane protein, they will be reviewed as well due to their similarities to our subject nanoparticles. Third, a comprehensive overview of the lipid molecules, how they self-assemble into the liposomes is provided. Finally, an overview about how synthetic materials including nanoparticles are used as cell membrane mimics closes the chapter.

1.1 Cellular Membranes

Cellular membranes are the structures surrounding the cell (plasma membrane) and certain subcellular organelles (internal membranes). Cellular membranes are mainly responsible for cell protection and organization. A membrane contains various types of lipid molecules as building blocks, and accommodates 50 or more different proteins. Therefore, it displays a heterogeneous lateral distribution of its components. In 1972 Singer and Nicholson proposed the Fluid Mosaic Membrane model to describe the cell membrane as a dynamic entity (Figure 1-1). In this dynamic structure lipids and proteins are able to move in the lateral direction¹⁰. Thanks to their complexity, cell membranes have a semi-permeable nature, deciding which substances and in what quantities can enter a cell or organelle. Moreover, cellular membranes perform vital functions such as transport, signal transduction, food entrapment, recognition, biosynthesis, etc.¹¹ The main building blocks of a cellular membrane are phospholipids and glycolipids with various head groups, chain lengths, and degrees of unsaturation¹². Additionally, steroids and solely hydrocarbon moieties contribute to the formation of the membrane¹³.

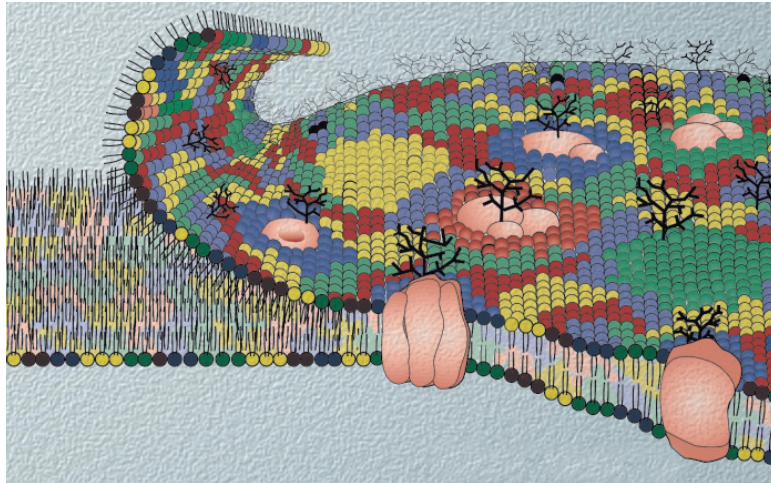


Figure 1-1 The fluid mosaic membrane of Singer and Nicholson. Different colors represent various types of lipids. Adapted with permission from reference ¹⁴.

1.2 Membrane Lipids

Lipids in the cell membrane differ in two ways: (i) the chemical structure of individual lipid molecules *i.e.* having multiple double bonds, and (ii) compositional differences, which is the proportional amount of different lipids in certain domains¹⁵ (Figure 1-2). The chemical structure of the lipid molecules dictates their individual properties, whereas compositional variation determines their collective behavior in a membrane. Combination of these two factors regulates the function of lipids in a membrane.

Chemically, lipids in a membrane are mostly double chained phospholipids and glycolipids, having 16 or 18 carbons per chain, in which one of the chains is not saturated¹³. In particular, the most abundant lipids in nature are glycerol-phospholipids¹⁶. The phospho- and glycolipids are combined in a functional membrane with steroids (*i.e.* cholesterol) and sphingolipids. One of the main advantages of having mostly unsaturated lipids and branches in the membrane is the retention of the membrane's fluidity at physiological temperatures, even though saturated lipids with chain melting temperature above the physiological temperatures exist in the membrane. This fluidity enables the bending of the membrane in the limit of packing constraints. Moreover, the fluidity of the bilayer allows the lateral diffusion of proteins in the membrane and makes it permeable by small molecules.

The lipid composition of the membrane is different in different types of cells and organelles. It is even possible to find differences in the compartments at the suborganellar scale. This diversity of the lipids and lipid domains (different phases) affects the metabolism and selective transport mechanism in every organelle. In other words, the variety of the lipids facilitates phenomena like cell division, energy storage, signal transduction, and fusion¹².

In a cell membrane it is possible for certain types of lipids, mostly cholesterol and relatively saturated glycolipid or sphingolipid molecules, to assemble for a short time, forming lipid domains called lipid rafts. The lipid rafts can have varying sizes, spanning from nanodomains to platforms, and are in general more ordered than the surrounding bilayer, due to hydrogen bonding between the cholesterol and sphingolipids¹⁷. Lipid rafts concentrate raftophilic proteins¹¹. Moreover, rafts can alter the conformation of a protein and consequently, the function. For example, the high packing density of the lipids in the rafts can block certain raftophilic membrane proteins and reduce protein-mediated signaling¹¹.

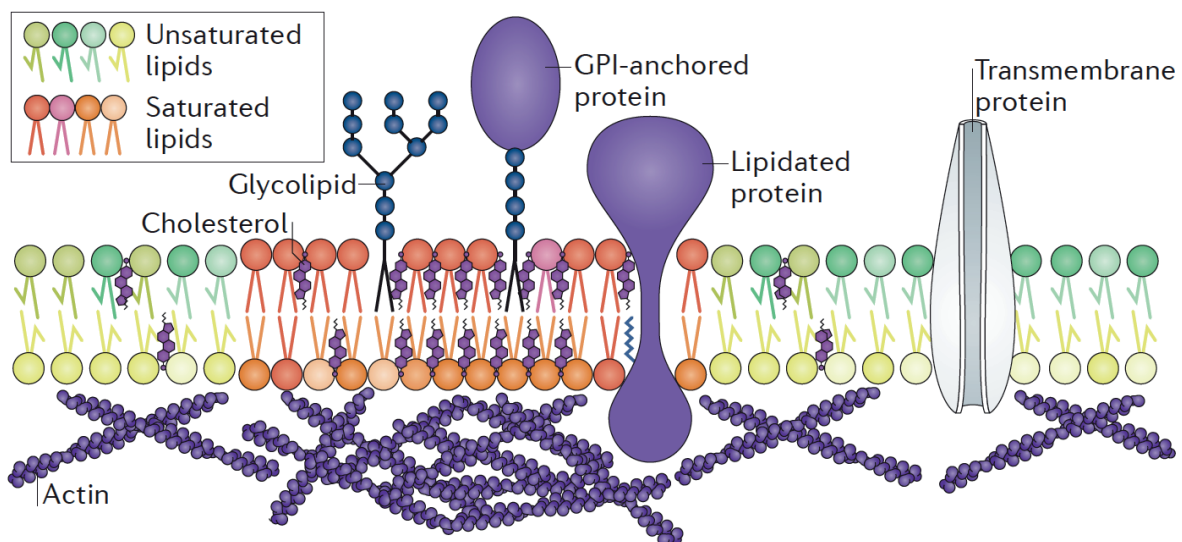


Figure 1-2 Lipid raft domains are formed by saturated phospholipids, sphingolipids, cholesterol. Membrane proteins also can be located in lipid rafts. Due to this crowded assembly, lipid rafts are high in order with decreased fluidity. Adapted with permission from reference ¹¹.

Having lipids associating with many cell functions, certain mutations, defects and disorders on the lipids, as well as on the enzymatic pathway of lipid metabolism are directly correlated with diseases¹⁵. Certain changes in the chemical structure of lipid molecules can result in

many genetic diseases like hereditary sensory and autonomic neuropathy leading a loss in pain sensation¹⁸. Additionally, any domination or decrease on certain types of lipids stems certain types of disorders. For example, ceramide accumulation on the bilayer is correlated to depression¹⁹ and reduction on docosahexaenoic acid which is a fatty acid leads to infertility effecting the membrane shaping during the sperm formation²⁰. Since many changes in lipidome causes diseases like type 2 diabetes²¹, cancer²², Alzheimer disease, and dementia²³, some components are good biomarkers as well for the diagnostics.

1.3 Membrane Proteins

In addition to keeping the intracellular parts intact, the cell membrane is the host of many membrane proteins. Cell membrane proteins are mostly amphiphilic and can fold into multiple configurations. Cell membrane proteins associate with the lipid bilayer in different ways, and in this way dictate various properties of the cell membrane including signal transduction, transport, and cell-cell recognition (Figure 1-3).

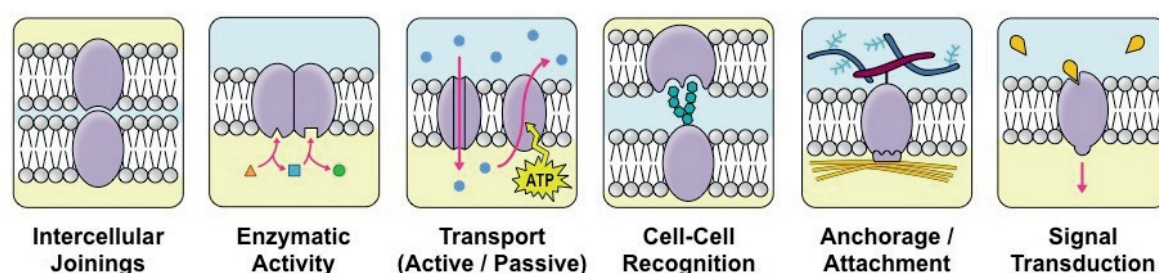


Figure 1-3 Schematic illustration of functions that cellular membrane proteins undertake on the cell membrane. These functions include intercellular attachments, enzymatic activity, transport, cell-cell recognition, attachment, and signal transduction. The image is taken from <http://ib.bioninja.com.au/>.

Membrane proteins can permanently integrate into the membrane or temporarily associate with the membrane. They are divided into 2 groups based on their locations on the membrane; integral and peripheral proteins. As a result of their amphiphilic nature, integral membrane proteins have some parts that are either inserted in or completely span the membrane (*i.e.* transmembrane proteins). On the other hand, peripheral membrane proteins do not incorporate into the hydrophobic parts of the membrane but attach to a binding site provided by integrated membrane proteins²⁴. If this peripheral membrane protein is a lipidated protein, then the anchor points are also provided by lipids¹¹. Due to the fluid nature

of the cell membrane, integral membrane proteins can diffuse laterally in the membrane and, for instance, some transmembrane proteins can aggregate in the membrane after diffusing towards each other. It should be noted, that aggregation of proteins in the membrane is also correlated to the packing constraints of the lipid bilayer¹³. Although there are various types of proteins on or in a cell membrane, in the scope of this thesis, curvature inducing, adhesive, and fusogenic membrane proteins will be reviewed further. Additionally, cell penetrating proteins will be explained even though they do not remain on the membrane, but, rather, traverse it.

1.3.1 Curvature inducing proteins

Membrane curvature is required for certain cellular functions, *i.e.* endocytosis, cell division. These proteins function by inducing curvature in the membrane. There are two main mechanisms for membrane proteins to be able to curve the membrane; (i) scaffold mechanism and (ii) the local spontaneous curvature mechanism²⁵ (Figure 1-4). In the scaffold mechanism, individual proteins or protein aggregates are required to maintain a shape, which the membrane bends towards. Moreover, such proteins should have a sufficient rigidity, so that the membrane cannot relax back to its original shape. Lastly, there should be an affinity between such proteins and lipid head groups, for the lipid bilayer to adjust itself into the shape of the proteins²⁶. For instance, BAR (Bin, Amphiphysin, Rvs) domain-containing proteins have an arc-like shape allowing them to surround the membrane and provide scaffolds for the curvature formation^{27,28}. Additionally, positively charged moieties on the surface of this protein provide the required affinity towards the lipid head groups and subsequent strong interactions²⁹.

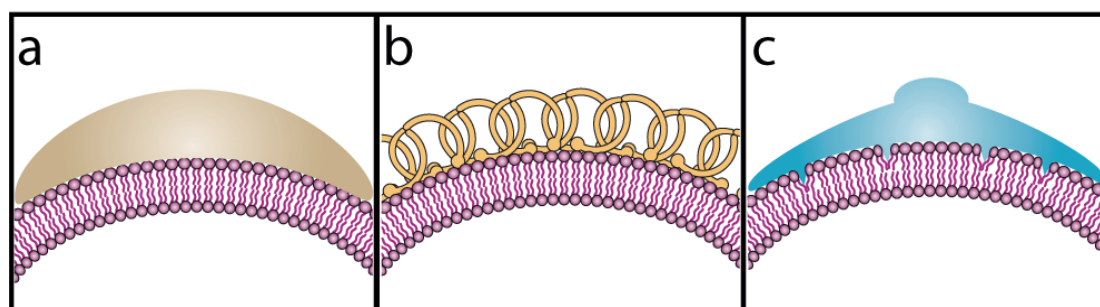


Figure 1-4 Schematic representation of membrane curvature induced by membrane proteins. a,b) Scaffold mechanism, c) Local spontaneous curvature mechanism. Adapted with permission from reference ²⁵.

The local spontaneous curvature mechanism depends on the local deformation on the lipid packing of the membrane, which emerges as a result of the insertion of amphiphilic domains of proteins into the lipid bilayer. Proteins that have amphipathic helical structures (*i.e.* Epsin, Sar1) are considered as candidates to follow this pathway to induce curvature^{30,31}. It should be noted that proteins can combine both of the previously described methods in order to curve a membrane. For instance, Clathrin with its adaptor protein, an endocytic protein, forms a coat-protein scaffold on the bilayer that promotes the bud formation³², without necessitating the presence of an integrated membrane protein to enable curvature formation³³.

1.3.2 Cell adhesion proteins

Cell adhesion plays a key role in the formation of three-dimensional tissues by individual cells. In addition to retaining the structural integrity of tissues, cell adhesion may also mediate signal transmittance between adjacent cells through junction points³⁴. Different structures can facilitate cell adhesion following various types of junctions; tight junctions, adherent junctions, gap junctions, and desmosomes³⁵ (Figure 1-5). Proteins occluding in adjacent cell membranes interlock to form tight junctions in which the two plasma membranes are sealed together, forming a continuous junction³⁶. These junctions limit the passage of small ions and water molecules. Adherens junctions are mediated by cell membrane glycoproteins belonging in the Cadherins family³⁷. Cadherins in adjacent cell membranes interact with each other in a zip-like formation. These junctions have more space compared to tight junctions and are supported from the interior of the cell through actin filaments. Gap junctions are formed by the interaction of proteins called connexons. Connexons from adjacent cell membranes interact and establish a continuous tunnel between cells. This tunnel allows molecules smaller than 1000 Da to pass through³⁸. Desmosomes are structured by desmosomal Cadherin proteins in the adjacent cell membranes³⁹. This type of joints anchor intermediate filaments to the cell membrane towards the cytoplasm⁴⁰. That is why desmosomes are found mostly in epithelial cells in which they help retain the structural integrity of cells against abrasion.

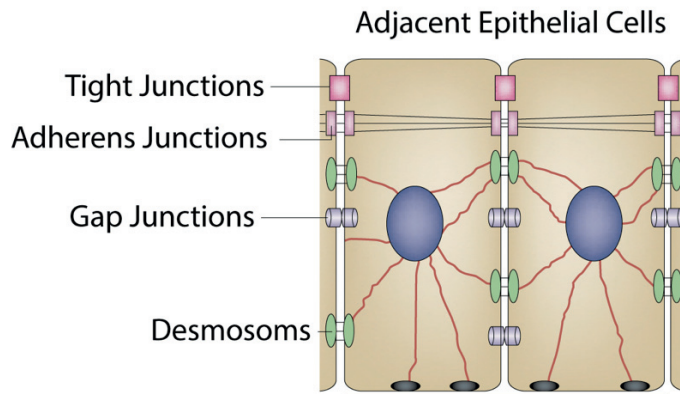


Figure 1-5 Schematic illustrations of different types of cell junctions. Adapted from reference ⁴⁰ with permission.

1.3.3 Fusion proteins

Cell membrane fusion is essential for biological functions like reproduction, morphogenesis, and cargo transport⁴¹. Based on the type of the cellular functions membrane fusion can take place in heterotypic (between different compartments, *e.g.* between the cell membrane and subcellular organelles, between the cell and extracellular compartments) or homotypic fashion (between similar entities, *e.g.* between cells, between subcellular organelles). Moreover, certain fusion events require a stimulus to proceed, just like Ca^{2+} ions or a pH change. All these variabilities further underline the diversity of fusion mechanisms in various biological functions. For example, cell-cell fusion is essential for fertilization, whereas fusion between cells and extracellular vesicles is important for delivery of neurotransmitters. However, in each type of fusion, various energy barriers and intermediate stages should be overcome for the process to occur. To reduce the energy barriers of the intermediate stages, different components (*e.g.* tethering proteins) or mechanisms (*e.g.* inducing high curvature on the counter membrane) participate in the fusion process. Figure 1-6 illustrates various types of fusion events that take place in different cellular areas.

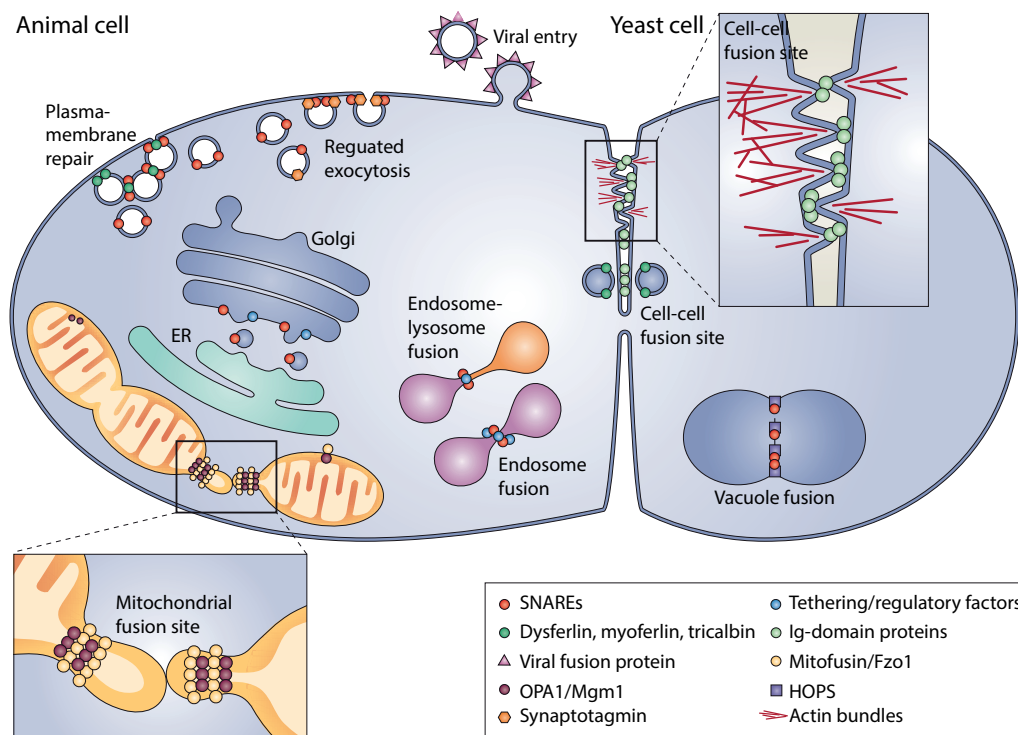


Figure 1-6 Schematic illustrations of membrane-fusion events that take place in the cell. Modified with permission from reference ⁴².

In a generic fusion event, first the membranes should come closer (a few nanometers) in order to mediate the fusion and be destabilized by their proximity to each other. However, electrostatic repulsion due to lipid head groups and hydration forces between two membranes sets a high energy barrier⁴³. Lipid molecules can protrude out of the membrane to initiate a contact with the adjacent membrane, as to minimize the free energy of the system. During the next step of membrane fusion, a stalk formation between the adjacent membranes is observed, in which the outer layers of the membranes develop a wider with each other and eventually merge. Certain fluorescence assays using FRET (Förster resonance energy transfer) couples can distinguish stalk formation during formation of hemifusion⁴⁴. In the event of hemifusion, although the outer layers of the membranes (proximal leaflet) are mixed together, the inner layer of the bilayers (distal leaflet) still stands as a barrier between two different compartments. Therefore, at the hemifusion stage, the contents of the two compartments still do not mix. As a final step, the fusion pore starts to open and get larger, finalizing the fusion process and leading to a relaxation of the membrane.

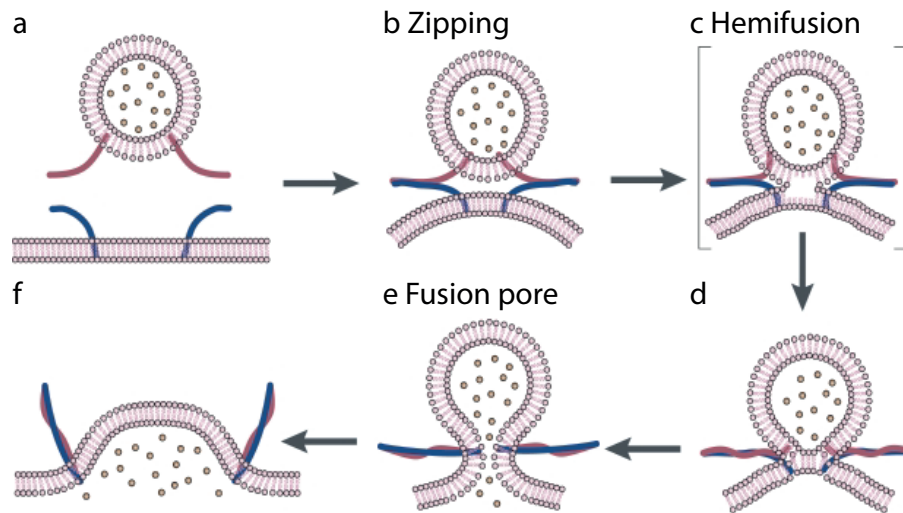


Figure 1-7 Schematic representation of the fusion model suggested for SNARE proteins. a) The extracellular compartment approaches the bilayer with the cargo molecules, b) The SNARE complexes zip and bring the two bilayers closer. c) A lipid protrusion then commenced the hemifusion process in which only the proximal leaflets mix, followed by d) limited mixing between distal leaflets. e) Fused lipids form the bilayers vertical to SNARE complexes and a fusion pore starts to form, followed by f) complete fusion, after which all the cargo molecules are delivered. Adapted with permission from reference ⁴⁵.

SNARE (soluble N-ethylmaleimide-sensitive factor attachment protein receptor) proteins are the most prominent protein family that facilitates the fusion events in the cellular functions⁴⁵. The first discovered SNARE proteins are the synaptic proteins syntaxin⁴⁶, SNAP-25 (25 kDa synaptosome-associated protein)⁴⁷ and VAMP (vesicle-associated membrane protein), also known as synaptobrevin⁴⁸. SNARE proteins are multidomain proteins consisting of transmembrane domains and two helical bundles. These helical bundles are called SNARE motifs. Prior to fusion, SNARE motifs do not have any alignment⁴⁹. When SNARE proteins from opposing membranes form a zip-like structure (called a SNARE complex), these 4 helical bundles align⁵⁰. This alignment brings the opposing membranes within a distance of 2-3 nm⁵¹ and, thus, fulfills the first requirement of the fusion. Then, the fusion event proceeds slowly by following the aforementioned pathway^{45,49,52} (Figure 1-7). However, fusion in the synaptic cleft should happen really fast to release neurotransmitters and, thus, a Ca^{2+} dependent fusion process takes place in the neurons⁵³. In this fusion type the SNARE complex consist of 4 helical bundle forms in which syntaxin-1 and SNAP-25 are placed on the plasma membrane and synaptobrevin on synaptic vesicles⁵³. Upon addition of the action potential (Ca^{2+}), Ca^{2+} ions bind to two domains of synaptotagmin, which is a synaptic protein that binds to Ca^{2+} and

the calcium sensor in neuronal exocytosis⁵⁴. These bindings cause synaptotagmin to interact with the phospholipid membrane and displace complexin, a synaptotagmin competing protein, in the SNARE complex⁵⁵. The fusion occurs in about 200 ms and neurotransmitters are released⁵⁶. SNARE proteins also facilitate the fusion process between synthetic liposomes.

1.3.4 Cell-penetrating peptides

Cell-penetrating peptides (CPPs) are the vehicles to deliver cargo towards the cell membrane. Not only CPPs deliver biological molecules such as proteins (*e.g.* insulin) and oligonucleotides, they also play a role in the delivery of various non-biological cargo just like liposomes, nanoparticles, and polymers⁵⁷. In general CPPs are short peptides made of fewer than 40 amino acids. Therefore, CPPs are low in toxicity, taken up by several types of cells, and they can traverse the cell membrane with a cargo regardless of its size or type⁵⁸.

CPPs can form complexes with cargo both through a covalent bond and noncovalently. For example, CPPs can conjugate covalently with neutral cargo, such as small drug molecules via a disulfide or amine bonds, or specific linkers⁵⁹. Noncovalently, CPPs can couple with nucleic acids through electrostatic and/or hydrophobic interactions⁶⁰. CPPs can penetrate into the cell with or without the cargo. Prior to their uptake by cell membranes, CPPs interact with the cell membranes. To be able to investigate this behavior further, a specific classification of CPPs has been used to differentiate between their affinities to lipids, membrane insertion capacities, and structural transitions upon binding⁶¹. These classes are primary amphiphilic CPPs (paCPPs), secondary amphiphilic CPPs (saCPPs), and non-amphiphilic CPPs (naCPPs).

PaCPPs contain sequentially hydrophobic and cationic domains as a part of their primary structure. The amount of amino acid residues (~20) in the structure is long enough for them to span the bilayer⁶². PaCPPs have a strong affinity towards both neutral and anionic lipid membranes. Moreover, they decrease the surface tension through binding to the membrane⁶³. Taken together, hydrophobic interactions dominate paCPPs' membrane interactions⁶⁴.

SaCPPs are shorter than paCPPs and exhibit amphiphilic behavior upon a change in the secondary structure, triggered by interactions with membranes^{65,66}. SaCPPs have higher affinity to anionic lipid bilayers, proportional to the number of anionic lipids in the membrane. Once bound to the membrane, their secondary structure evolves in a helical or β -sheet type in which the charged and uncharged parts of the peptides segregate. Thus, after membrane insertion, saCPPs exhibit amphiphilicity.

NaCPPs are the shortest peptides among the three types and consist of almost always cationic amino acids. NaCPPs only bind to the membranes having a high ratio of monovalent anionic lipids, unless they are modified to have some amphiphilicity, *e.g.* acylation. In fact, once the naCPPs display amphiphilicity intrinsically or through modification, naCPPs perturb the membrane through pore formation^{67,68}.

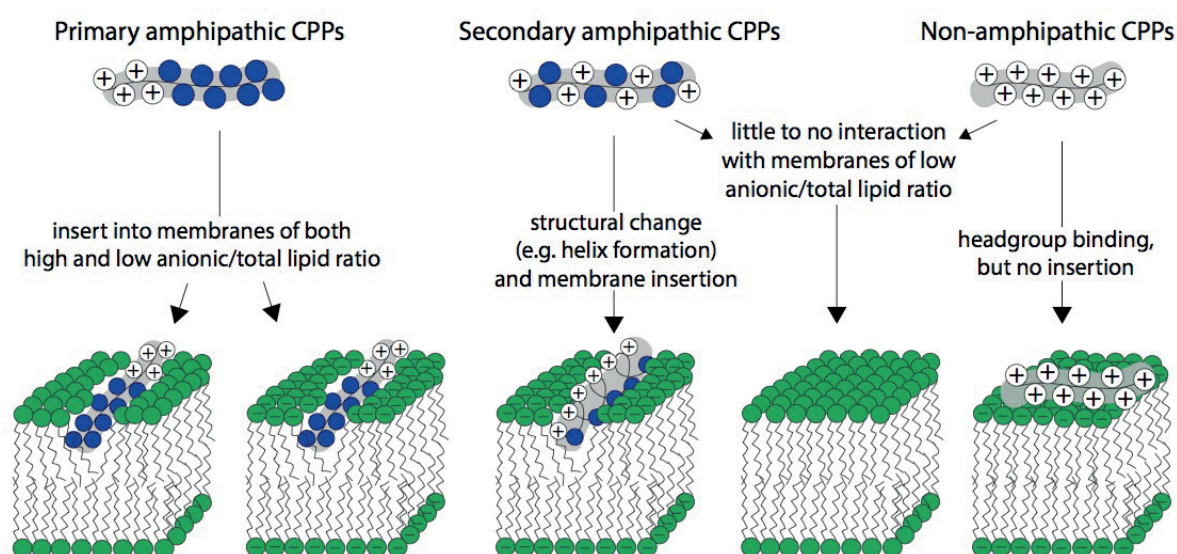


Figure 1-8 Schematic representation of the different classes of CPPs and how they interact with bilayers. The figure is adapted with permission from reference ⁶⁹.

Most of the CPPs and CPPs-cargo conjugates enter the cell membrane through an energy-dependent path, *e.g.* endocytosis⁷⁰. Direct translocation across the membrane is still possible for certain cases such as high peptide concentration⁷¹. Once the CPPs are internalized via endocytosis, they need to escape from the endosomes. To do so, CPPs can interact with the membrane of the endosomes through hydrophobic and electrostatic interactions, which lead to the disruption of the endosomes' membrane. Also, according to the proton sponge theory,

the endosomes are disrupted due to osmotic pressure⁷². Following release from endosomes, the cargo needs to be dissociated from the peptides in order to reach the target point. That is why one of the components of the CPP-cargo complex should have a high binding affinity to a cytosol element⁷³. This competitive binding facilitates dissociation of the cargo in the cytosol. Moreover, based on the target not only CPPs can be modified, but CPP-cargo complexes can be formed synthetically.

1.4 Lipid Bilayers

Lipid bilayers are the systems formed by the assembly of mainly lipid molecules. In addition to lipid molecules, they can contain cholesterol, fatty acids, and sphingomyelins, just like a cell membrane. Therefore, these systems are considered as models of cell membranes and are used to study the behavior of cell membrane proteins. In this part of the introduction, we will investigate lipid molecules and how they assemble into different systems. Moreover, we will go through how properties of lipid molecules including shape and charge affect the formation of different aggregates including micelles, bilayers and vesicles. Finally, we will go through the use of liposomes as model systems in the literature.

1.4.1 Lipids

Lipids are amphiphilic molecules that contain both hydrophobic and hydrophilic parts. The polar head group of the amphiphiles is hydrophilic, whereas the hydrocarbon chain tail is the hydrophobic part. The hydrophobic part of the lipid molecules consists of one or two alkyl chains. These alkyl chains may differ in the total length of carbons and the number of double bonds in them. Lipid molecules are classified as unsaturated or saturated, having double bonds or not in the acyl chains, respectively. Based on the types of the head groups, lipid molecules can naturally occur either as zwitterionic (ZW) (*i.e.* phosphatidylcholine (PC), phosphatidylethanolamine (PE)) or anionic (*i.e.* phosphatidylglycerol (PG), phosphatidylserine (PS)) (Figure 1-9). Cationic head groups can be found only synthetically (*i.e.* trimethylammonium-propane (TAP)) since they do not exist naturally.¹⁶

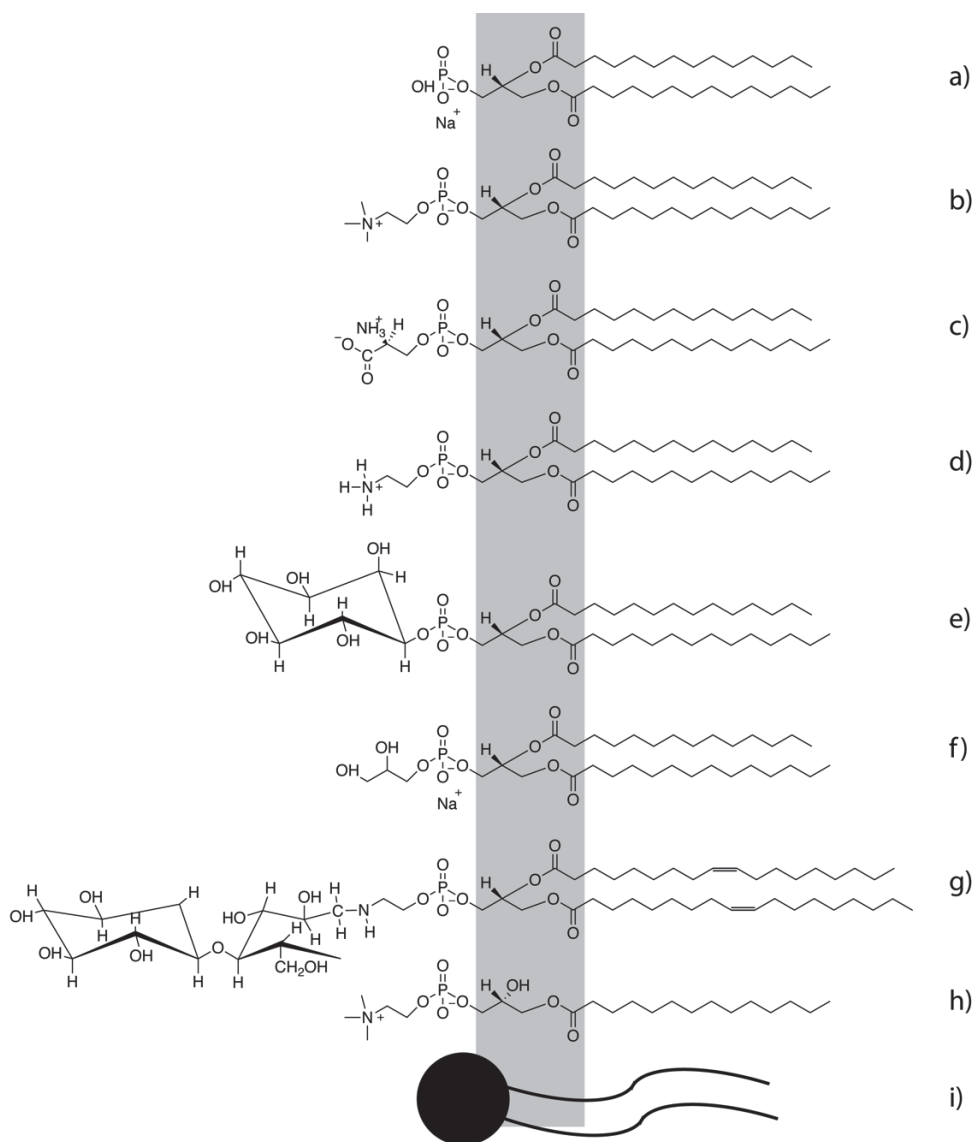


Figure 1-9 Different types of lipid molecules. The left side of the grey panel represents the head group, whereas the right side shows the hydrophobic chains. a) Di-myristoyl phosphatidic acid (PA), b) Di-myristoyl phosphatidylcholine (PC), c) Di-myristoyl phosphatidylserine (PS), d) Di-myristoyl phosphatidylethanolamine (PE), e) Di-myristoyl phosphatidylinositol (PI), f) Di-myristoyl phosphatidylglycerol (PG), g) Glycolipid, h) Lysolipid with a palmitoyl chain, i) schematic of a lipid molecule with hydrophilic head group and hydrophobic ligands. The figure is adapted with permission from reference ⁷⁴.

Amphiphilic lipid molecules can spontaneously self-assemble and pack into different types of aggregates in aqueous solutions depending on the shape, charge, and length of the lipid molecules. Direct formation of aggregates means that the overall free energy (conversely, the chemical potential) of the system of aggregates is lower than the free energy of dispersed lipid molecules in the medium¹³. Considering only the lipid molecules, their self-organization

into aggregates decreases the entropy of the system due to a decrease in the number of microstates for the lipid molecules to disperse in the final state. However, once the aqueous solution is also considered together with lipid molecules, the system changes. When the lipid molecules are dispersed in aqueous solutions, the hydrophobic parts of individual lipid molecules hinder hydrogen bonding between water molecules. By doing so, water molecules become more ordered and subsequently the entropy decreases. Due to this entropically unfavorable state, lipid molecules form aggregates, in which their hydrophobic parts are not in contact with water molecules. The entropic driving force due to an intermediate free energy increase in the aqueous part of the system is defined as 'The Hydrophobic Effect'. In addition to the entropic driving force, there are intermolecular interactions, including repulsion between head groups and attractive hydrophobic interfacial forces in aggregates¹³.

For the formation of the aggregates, a critical number of the lipid molecules in the solution is required. This requirement is due to the low chemical potential of the system at very low concentrations of the lipid molecules; the chemical potential is lower than the energy required to transfer one lipid molecule from a dispersed system to an aggregate. Upon increase of the concentration of lipid molecules the chemical potential of the system remains constant. This concentration is defined as Critical Micelle Concentration, in which aggregates and individual lipid molecules coexist at equilibrium. Once the nucleation of the aggregates occurs, Ostwald ripening makes the lipid aggregates grow by transfer of lipid molecules from small aggregates to bigger ones.

Having all the interaction mechanisms during aggregate formation explained, next, the effect of the shape of the lipid molecule in aggregate formations should be explored. The relative size of the head group and hydrophobic tail determines the bilayer curvature. To distinguish between the shape of the lipid molecules, a dimensionless packing value, P , is defined:

$$P = \frac{v}{al_c} \quad (1.1)$$

where v is the volume of the chain, a is the optimum headgroup area, and l_c is the critical chain length (Figure 1-10).

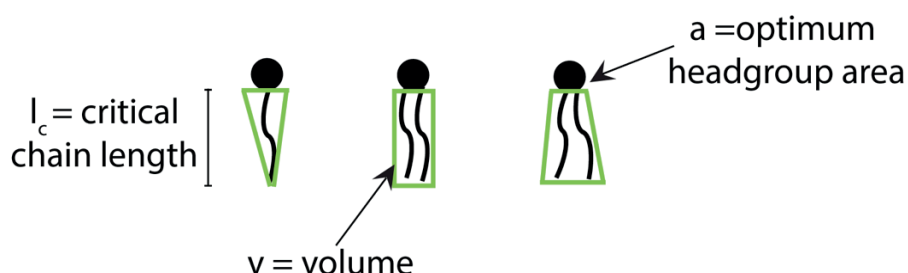


Figure 1-10 Characteristics of lipid molecules used to calculate the packing factor. l_c : chain length, v : volume, and a : headgroup area.

If P is equal to 1, these lipids form a lamellar bilayer. $P > 1$ points to the formation of inverted micelles. The values of $P < 1$ should be considered in three different parts. $\frac{1}{2} < P < 1$ leads to the formation of vesicles, $\frac{1}{3} < P < \frac{1}{2}$ leads to the formation of cylinders and $P < \frac{1}{3}$ directs the lipid molecules into spherical micelles (Figure 1-11). There are multiple ways to alter the effective shape of lipid molecules. The factors affecting the headgroup area are the intrinsic size of the headgroup, the degree of hydration of the headgroup, changes in ionic strength, pH and temperature. Additionally, the critical chain length is determined by branched, unsaturated chains, double-chains, temperature or addition of a co-surfactant. Moreover, a cylindrical lipid molecule can transform into a conical one by an increase in temperature or through enzymatic reactions that may lead to a loss of a fatty acid chain or reduction of the headgroup⁷⁵.

The overall components of the lipid molecules define their phase transition temperature. This specific temperature separates the solid-ordered from the liquid-disordered phase. In the solid-ordered phase the lipid molecules align perfectly and a thicker membrane is obtained compared to the liquid-disordered phase, in which lipids are disordered and not aligned.

Amphiphilic structures are softer and more fluid-like and consequently, in the aggregates they diffuse, twist, turn and flip out of the membrane, led by thermal motion¹³. Therefore, amphiphilic structures exhibit a broad distribution of size and no definite size or shapes.

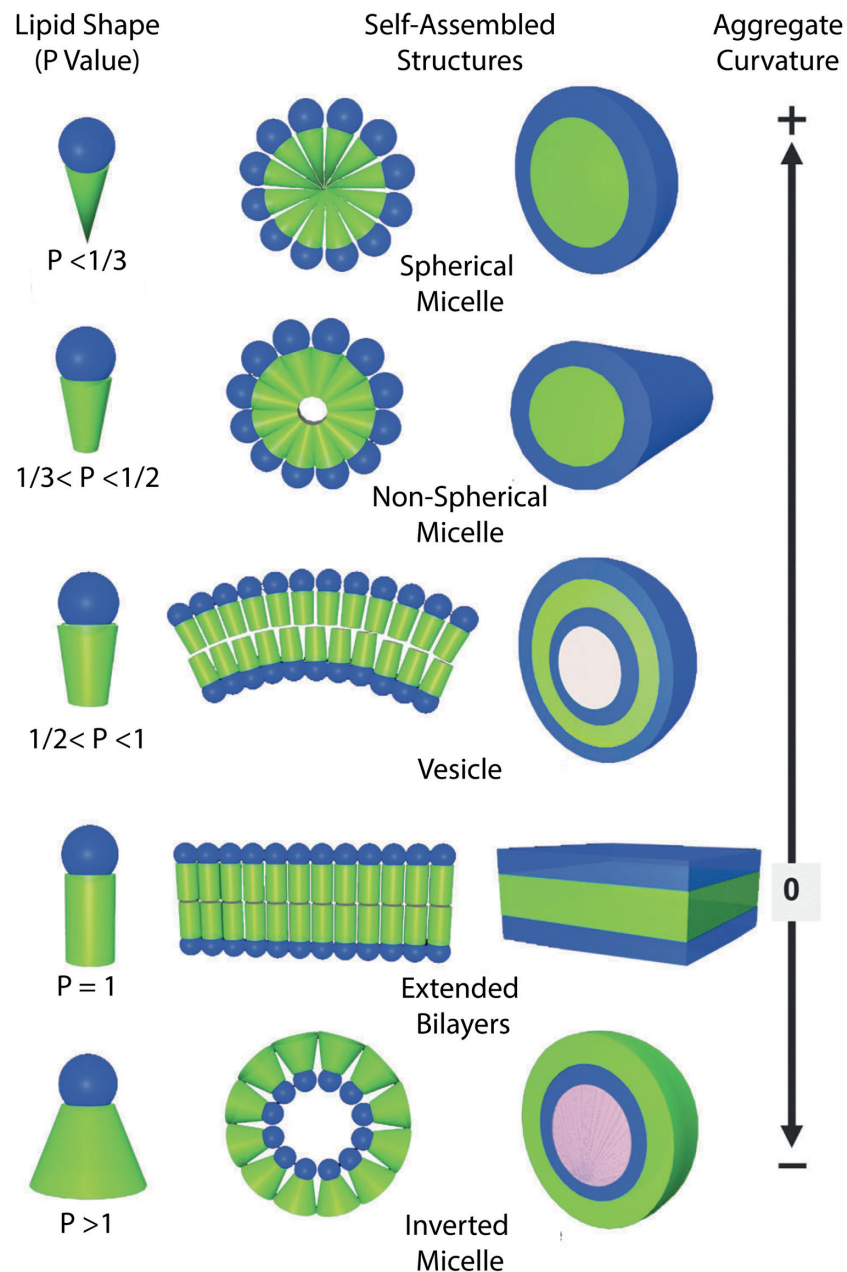


Figure 1-11 Schematic representation of lipid aggregates formed in water. A P value of the lipid molecules sets limits on the formation of different aggregates and curvatures. Adapted with permission from reference ⁷⁶.

1.4.2 Liposomes

Liposomes are compartments that are generated by the encapsulation of a fluid by amphiphilic lipid molecules. Natural formation of vesicles from lipid bilayers is observed in order to maintain cellular functions including fusion, cell division, secretion, transportation, and phagocytic or endocytic uptake⁷⁷. Liposomes can be generated artificially using lipid

molecules, leading to a wide size of application areas ranging from drug delivery to diagnostics^{2,78,79}. Additionally, liposomes are crucial model systems for biological processes, used for investigation of several cellular functions like fusion and exocytosis^{43,80–83}.

Research using artificial liposomes made of natural or synthetic lipids has gained interest since they were first generated by Alec D. Bangham in 1961⁸⁴. In artificial liposome generation, layers of lipids (~5 nm) self-assemble to form a spherical, osmotically balanced structure with a hydrophobic bilayer interior surrounded by a hydrophilic exterior. Lipid vesicles are classified in terms of their size, lipid composition, charge and lamellarity (Table 1-1).

Table 1-1 Vesicle types regarding size and number of lipid layers.

Vesicle Type	Diameter Size	Number of Lipid Bilayer
Unilamellar Vesicle	All Size Range	One
Small Unilamellar Vesicle	20-100 nm	One
Large Unilamellar Vesicle	> 100 nm	One
Giant Unilamellar Vesicle	> 1 μ m	One
Oligolamellar Vesicle	0.1-1 μ m	Approximately 5
Multilamellar Vesicle	All Size Range	5-25
Multi Vesicular Vesicle	> 1 μ m	Multi Compartmental Structure

The building block lipid molecules define physicochemical properties of the liposomes, including net surface charge, hydrophobicity, size, fluidity, and packing of the lipid bilayers. Additionally to lipids, some moieties such as cholesterol or sphingomyelin can also participate in vesicle formation, causing changes of properties such as water permeability, stability, and fluidity. The biocompatible nature of vesicles makes them attractive candidates for biological transportation and drug delivery with active and passive targeting^{3,78,85,86}. Moreover, their structure grants them a high loading capacity (a high therapeutic index for drugs) while minimizing side effects and toxicity of encapsulated drugs. The loaded substance can be entrapped in the hydrophobic part of the bilayer, in the hydrophilic exterior, or the aqueous core of the liposome (Figure 1-12).

Taken together, liposomes can be modified variously to serve as model cell/membrane systems with less complexity than cell membranes⁸⁷. For example, GUVs - spherical structures of 50 μ m diameter- has been used to study the domain formation in the cell membranes.

Also, GUVs form the base for artificial cell studies like cell division, compartmentalization, protein expression^{88–90}. Recently, microfluidic techniques have been used to production of contolled monodisperse GUV populations to be studied further as biological systems⁹¹.

Smaller liposomes mostly used to study single molecules in a biomimetic environments as model systems^{92,93}. However, they have many applications like nanoreactors in which many synthesis can take place⁹⁴. Furthermore, surface of small and large liposomes can be modified for increasing the blood circulation time *e.g.* introduction of PEG. Such liposomes are referred as ‘stealth’. These liposomes benefit from PEG-induced steric hindrance with a decrease in the attachment of plasma proteins, and cell-surface proteins to the liposome surface. Doing so, liposomes are uptaken by mononuclear phagocyte system (MPS) less, and consequently have a longer blood circulation time. For intstance, Doxorubicin is a toxic drug and liposomal systems are used to minimize its side-effects in clinical usage⁹⁵. A commercial drug for metastatic breast cancer treatment, ‘Myocet®’, utilizes a non-stealth liposome to encapsulate Doxorubicin, whilst ‘DOXIL®’, used to treat Kaposi’s Sarcoma, has a stealth liposome formulation⁹⁶.

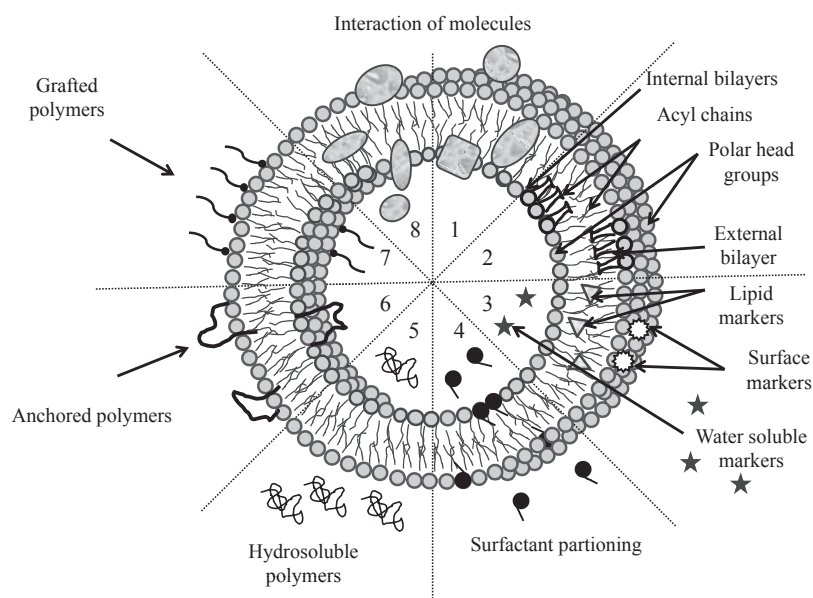


Figure 1-12 Scheme of a unilamellar liposome and different ways to modify it. Reproduced with permission from reference ⁹⁷.

1.5 Attempts for Synthetic Cell Membrane Proteins

Since a lot is known about proteins starting from their chemical structures, sequence analysis to their folding behavior, all this knowledge is applicable to modifying already existing proteins, as well as generating synthetic equivalents. These attempts under the roof of synthetic biology are based on several research goals: (i) to be able to generate artificial proteins to carry on unorthodox functions, which do not naturally occur in biological systems. To do so, these artificial proteins can be integrated into biological systems, and therefore, cells and even organisms may adopt new properties⁹⁸. (ii) To be able to generate an artificial cell in which every function can be conducted by non-biological entities. The protein analogues can add complexity to these artificial cells⁹⁹. (iii) To re-engineer the natural proteins in order to extend or improve their functions by using synthetic protein analogues or combining them with synthetic molecules^{100,101}.

For instance, in recent works inorganic nanoparticles have been generated or modified to be able to maintain enzymatic cellular functions¹⁰². One can say that inorganic nanoparticles, produced as a batch of different sizes and shapes are not comparable to proteins, which have a precisely determined size and chemical structure. There are, however, various similarities between nanoparticles and proteins, which make inorganic nanoparticles good candidates as protein mimics^{103,104}. Both nanoparticles and proteins react in similar ways to changes in the environment, such as pH and ionic strength. For example, their binding behaviors to cell membranes may be altered due to changes in their surface charge, directly affected by pH and ionic strength¹⁰⁵. Also, the surface properties of nanoparticles can be tailored to accommodate larger object, just like protein complexes¹⁰⁶. Moreover, nanoparticles have advantages over proteins such as low price, ease of preparation, tunability of their catalytic activity and high stability against denaturation¹⁰⁷. Therefore, inorganic nanoparticles can be conveniently used for biological functions^{108,109}. For instance, the core of the gold nanoparticles is shown to mimic glucose oxidase¹¹⁰, peroxidases¹¹¹, catalase¹¹², whereas the surface monolayer of gold nanoparticles mediates nuclease¹¹³, esterase¹¹⁴, and silicatein¹¹⁵ like functions.

Although inorganic nanoparticles can mimic certain cellular functions, their transmembrane protein-like properties have been poorly studied so far. One of the closest example consists of palladium nanoparticles used in combination with monoamine oxidase to design a biometallic catalyst for deracemization of racemic amines¹¹⁶. These particles were internalized by the cell membrane and then assumed to remain close (maybe attached) to the inner membrane surface. Also other nanoparticles have been shown traversing the cell membrane with a cargo, these nanoparticles, however, do not facilitate the transportation of cargo by integrating in the membrane, like membrane proteins^{9,117}. There are, however, other attempts to form transmembrane proteins synthetically. For instance, Gurezka *et al.* artificially synthesized transmembrane segments based on leucine and alanine residues¹¹⁸. Mihara *et al.* designed an artificial membrane protein consisting of flavin and porphyrin moieties to mediate electron transfer across the membrane¹¹⁹. Moreover, Palivan *et al.* combined stimuli responsive peptides with genetically modified channel porins to create pH responsive valves in a membrane¹²⁰. A similar trend is observed in fusogenic proteins. Despite the existence of studies on synthetic fusogenic peptides, no inorganic metal nanoparticles has been proven to mediate membrane fusion as of yet¹²¹.

2 Nanoparticles and Membranes

This chapter focuses on the literature about amphiphilic MUS:OT nanoparticles, their interactions with cells and bilayers, and consequent application areas. To do that, this chapter starts with an explanation on the nanoparticles, their physicochemical properties and how hosting binary mixtures of ligands affects these properties. Then, an overview of applications of mixed ligand, mostly MUS:OT nanoparticles is provided. After this, cellular uptake of nanoparticles is presented, followed by a detailed review of studies on MUS:OT nanoparticles' interactions with cells. Moreover, the interaction of particles with lipid bilayer is provided with a focused investigation on the interaction of MUS:OT particles. Finally, the synthesis and characterization procedures of MUS:OT nanoparticles followed in this work are described, followed by the motivation for this thesis.

2.1 Nanoparticles

Nanoparticles are the intermediate states between individual atoms/molecules and large bulk materials. The size of the nanoparticles can range from 1 to 100 nm. Having nano-range size grants them many interesting physical properties, attributed to the quantum phenomenon¹²². These physical properties are dictated by their shape, size, composition, structure, and surface properties¹²³ (Figure 2-1). All these design parameters have made nanoparticles excellent candidates in an immense amount of application areas, such as catalysis, imaging, sensing, energy storage and food science^{102,124–126}. Although the chemical nature of nanoparticles can be extremely diverse, comprising of materials such as polymers, silicates, and carbon, to name a few¹²⁷, within the scope of this thesis mostly noble metal nanoparticles will be reviewed, with a focus on gold nanoparticles.

Noble metal nanoparticles have gained significant traction in recent years. Their electrical, thermal, chemical, optical and surface properties, to name a few, can be easily and accurately tuned by careful selection of nanoparticle size and shape, providing a very attractive platform both for basic science research and applications¹²⁸.

One of the most interesting characteristics of noble metal nanoparticles is the fact that they display a different absorbance peak from their bulk counterparts, which results from coherent oscillations of the electrons in the conduction band due to resonant excitation by incident photons¹²⁹. This phenomenon is called surface plasmon resonance and it is sensitive to size, shape, surface ligand, core charge, solvent, and the temperature of the nanoparticles^{123,124,130}. That is why nanoparticles have different colors from their bulk counterparts. Surface plasmon resonance does not only depend on properties of individual nanoparticles but also nanoparticle assemblies. The existence of nearby nanoparticles results in a shift in the absorbance peak towards higher wavelengths due to interparticle plasmon coupling¹³¹. Surface plasmon resonance is of particular importance because of its sensitivity towards the environment which contributes majorly to a subsequent sensor application.

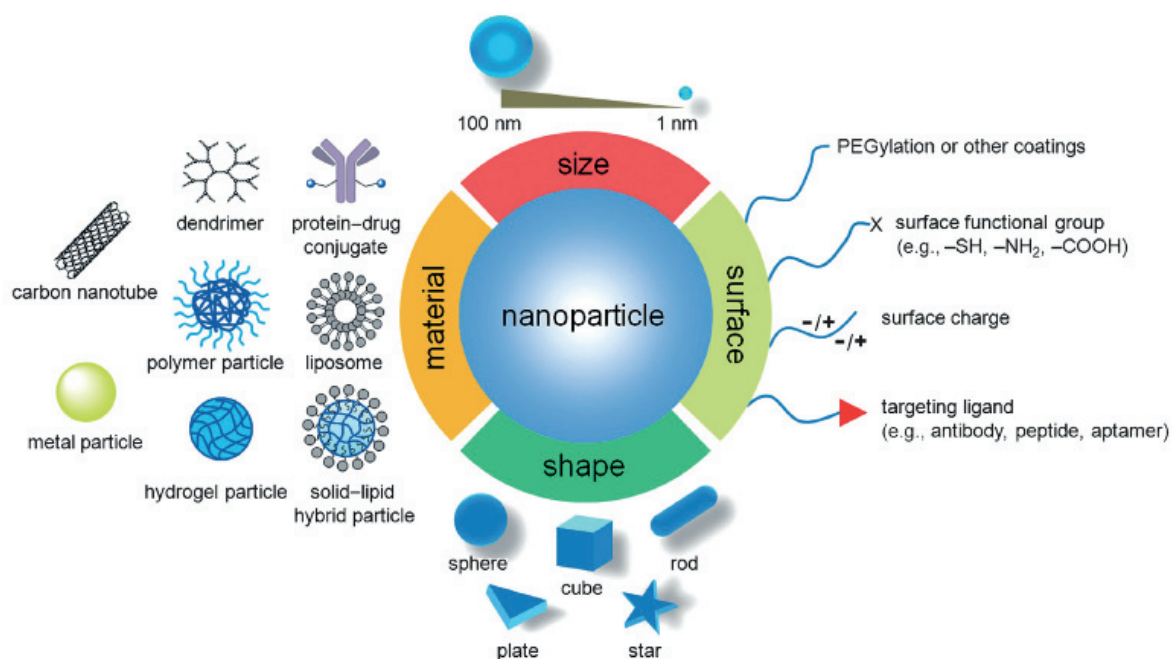


Figure 2-1 Schematic representation of nanoparticles with various materials, shape, and surface coverage. The figure is adapted with permission from reference ¹³².

Moreover, nanoparticles have a large surface area, in which surface atoms experience a different environment than their bulk counterparts. Surface atoms in nanoparticles differ in terms of reactivity, electronic state, free energy, etc. from bulk atoms. Thus, these atoms tend to decrease their free energy through adsorption of ligand molecules. This chemical way to modify the surface of nanoparticles is the key to granting them biocompatibility and low toxicity for certain applications¹³³.

Metal nanoparticles can be synthesized through a top-down process in which a bulk material is divided into smaller particles or a bottom-up approach in which the chemical synthesis of nanoparticles from their constituent metal atoms takes place¹³⁴. Small nanoparticles are mostly synthesized following a bottom-up approach. First, in 1857 Faraday obtained gold colloids by reduction of chloroaurate solution with white phosphorus¹³⁵. Later, in the 1950s, Turkevich produced gold nanoparticles through reduction of chloroauric acid with trisodium citrate in aqueous solution¹³⁶. Since then, studies on the bottom-up approach to synthesize gold nanoparticles have accelerated. In general, metal nanoparticles are prepared by the reduction of a metal precursor, mostly metal salts dissolved in the reaction media, by reducing agents such as sodium borohydride, trisodium citrate, etc. This process also involves organic ligands, which act as stabilizers via their adsorption on the particle surface.

The growth mechanism of nanoparticles' formation has been the subject of many research projects. Starting from the 1950s, LaMer's explanation for nucleation and growth has been used¹³⁷. This theory considers a critical concentration in which the reaction solution is supersaturated with the monomers (metal salts). At that concentration, the energy barrier for the nucleation can be compensated by a rapid nucleation of the monomers. In other words, the Gibbs free energy of the system reaches a local maximum prior to nucleation due to the high surface area of monomers, and, starting at nucleation, decreases. The nuclei formed should be bigger than a critical size to proceed to this stage¹³⁷. Once the nucleation starts, the concentration of the monomers decreases below the critical concentration and the nucleation stops. The amount of nuclei in this step defines the number of particles formed at the end of the reaction. The remaining monomers or nuclei smaller than the critical size in the system diffuse towards the particles' surfaces, coalescing, and the particle grows until the system reaches an equilibrium between monomers and particles (Figure 2-2). Lately, a different explanation of the growth mechanism of nanoparticles has been proposed, which considers the colloidal stability of the system, in contrast to LaMer's thermodynamic stability-based theory¹³⁸. According to this theory, the nuclei grow through aggregation and coalescence with other nuclei until the final size is colloidally stable. These colloidally stable nanoparticles stop growing because they cannot overcome an energy barrier to aggregate further. Although the latter model has been used to explain nanoparticle growth lately, no consensus has been reached.

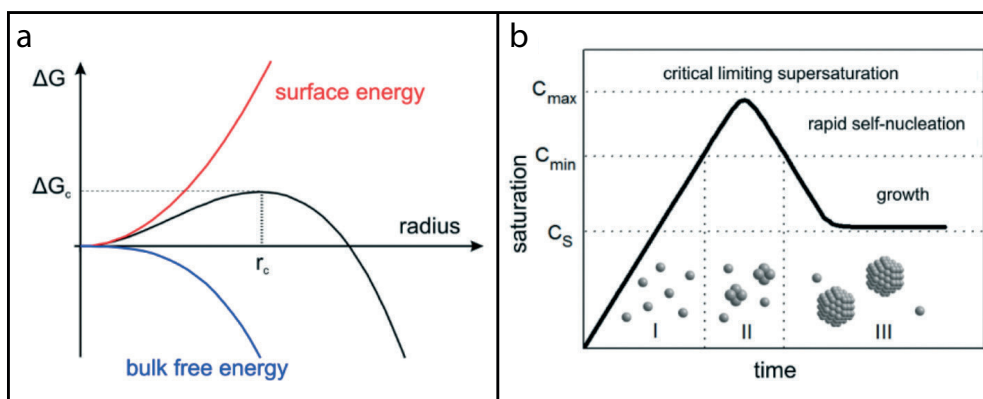


Figure 2-2 Schematic illustration of the nucleation theory. The figure is reproduced and modified with permission from reference ¹³⁸.

Surface coverage of the nanoparticles is analogous to having a second identity because the end groups of the constituent molecules on the surface of the nanoparticles determine the interfacial properties of the nanoparticles¹³⁹. These end moieties of the ligands can be alcohols, esters, sulfonates, phosphates, etc. and certain end groups that enable further chemical modifications of the ligands¹²⁷. End groups of the ligands in direct contact with a solvent serve as a barrier for nanoparticles and also determine their colloidal stability. In the case of stability, in a suitable solvent charged end groups grant an additional kinetic stabilization to the nanoparticles by introducing coulombic repulsion. This repulsion overcomes the short-range van der Waals attraction forces and sets an interparticle distance based on valency, charge, and concentration of the particles. This phenomenon is described by the DLVO theory¹³.

The formation and behavior of the surface coatings of the nanoparticles can be explained by the principles of self-assembled monolayers (SAMs). SAMs are molecularly thin films spontaneously formed by the self-organization of molecules, called ligands, on a particular substrate¹⁴⁰. The properties of SAMs are largely determined by the composition and structure of the ligands. For instance, alkanethiols with carbon chains containing 8 - 13 carbon atoms can assemble with an $\sim 30^\circ$ tilt relative to the normal of a gold surface. Shorter ligands tend to have a configuration more perpendicular towards the substrate. Ligand density is also an important characteristic of SAMs. In low-density monolayers, ligands tend to be more disordered, aligned parallel to surface, whereas in higher-density monolayers the ligands adopt a standing-up, more ordered phase¹⁴¹. One of the most studied substrate-SAM couples

is the Au (111)-S system. Similar to thiol SAMs on Au (111) surface, thiolated ligands bind to the gold core of nanoparticles semi-covalently through chemisorption¹⁴¹. At equilibrium, these bonds are dynamic, desorbing and re-adsorbing to the surface in a timescale of hours, allowing reorganization of the ligands on the surface¹⁴².

2.1.1 Binary SAM nanoparticles

Combination of multiple ligands in SAMs allows the fine-tuning of SAMs' properties¹⁴³. This phenomenon can be explained not only through the combination of multiple chemical functionalities in a single, binary, SAM, but also through the organization of the different ligands in a SAM. Organization of ligands in SAMs takes place in such a way as to allow the system to minimize its Gibbs free energy, G . Ligand mixing maximizes the entropic component of G , whereas phase separation minimizes its enthalpic component¹⁴⁴. This interplay between enthalpy and entropy leads to ligand mixing or phase separation and determines the geometry of the formed ligand domains on the surface. Furthermore, the curvature of the nanoparticle surface introduces additional geometric constraints to the pattern formation¹⁴⁵.

Having in mind that SAM formation aims to a decrease of the overall free energy, a mismatch between length and bulkiness of alkane chains can increase the conformational entropy of the ligands, where the shorter and less bulky ligands surround the longer, bulkier ones. This interface-based entropic gain dictates the formation of alternating ligand domains on the surface, called stripe-like domains^{146–148}. Not only the length mismatch, but also the relative ratio of the ligands in a SAM can affect the domain formation on the surface of nanoparticles (Figure 2-3).

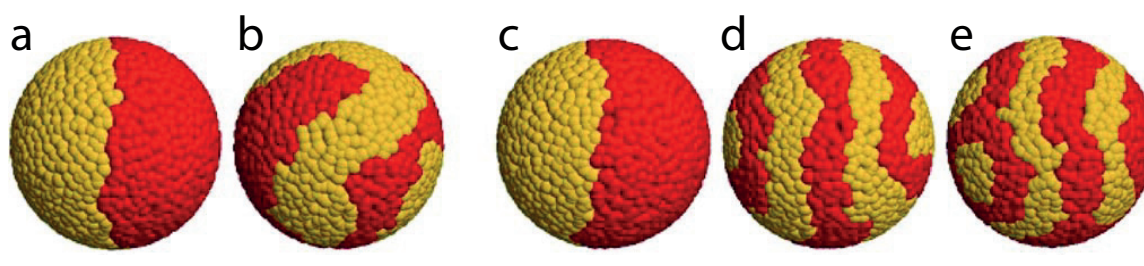


Figure 2-3 Domain formation on the surface of nanoparticles with different ligand couples at thermodynamic equilibrium. a) Length ratio 4:4, equal bulkiness, b) Length ratio 6:6, yellow surfactants have bulkier

headgroups, c) Length ratio 4:6, equal bulkiness, d) Length ratio 4:7, equal bulkiness, e) Length ratio 4:13, equal bulkiness. The figure is adapted with permission from reference ¹⁴⁶.

Furthermore, MD simulations have shown that the thickness of these stripe-like domains can be correlated to various factors, such as the length of individual surface ligands, mismatch in the ligand lengths, and the repulsion between surface ligands¹⁴⁸. Experimentally, domain formation in binary SAMs on gold nanoparticles has been characterized qualitatively by STM and MALDI-TOF. Recently, SAXS was used to further characterize domain formation quantitatively^{149–151}.

Our group has demonstrated that certain ligand combinations including alkane-alcohol and alkane-carboxyl couples lead to the formation of ribbon-like patterns on the surface of gold nanoparticles. These hydrophilic and hydrophobic domains formed on the gold surface were very thin, ~ 5 Å, and resembled the domains formed on the surface of folded proteins^{143,152}. That was why water-soluble, amphiphilic nanoparticles were designed by combining alkane-sulfonic acid terminated alkanes on a surface which could eventually act as proteins. The role of mixed ligand surface structure for the behavior of nanoparticles in biological systems will be discussed further.

2.2 Overview of the Applications of Mixed Ligand Nanoparticles

Of all the noble metal nanoparticles, gold nanoparticles are perhaps the most thoroughly studied and widely applied. One of the keys to the wide applications of gold nanoparticles in biomedical research is that their surface properties can be easily engineered for various purposes^{153,154}. Such versatility allows the control of the intermolecular interactions between the nanoparticles and biomolecules¹⁵⁵. Hydrophobicity and charge have a decisive role, among many other surface parameters, on the biological relevance of the nanoparticles^{156–158}. In order to fine-tune such surface properties, a mixture of ligand molecules with hydrophobic and hydrophilic (*e.g.* charged) functional groups is often used, to generate amphiphilic nanoparticles^{103,159}. These group of nanoparticles having a binary ligand combination on the surface will be referred as ‘mixed ligand nanoparticles’ hereafter.

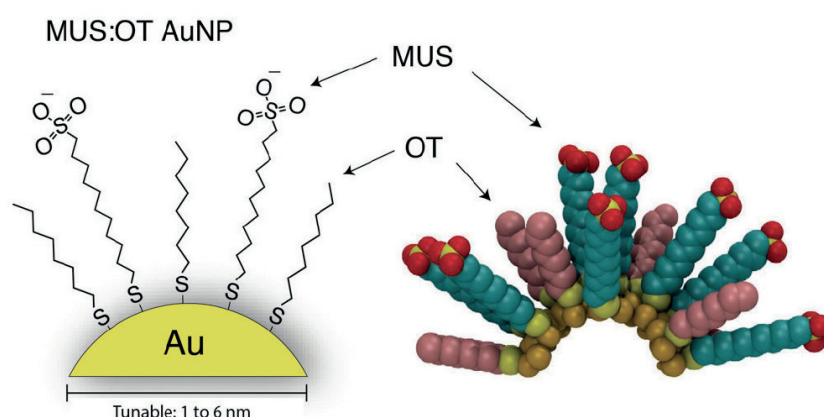


Figure 2-4 Schematic representation of MUS:OT nanoparticles. Ligands 1-octanethiol (OT) and 11-mercaptoundecane-1-sulfonic acid (MUS) coat the surface of gold core with different relative ratios. This figure is adapted further with permission from ¹⁶⁰.

One prominent example of such type of nanoparticles are gold nanoparticles co-protected by 1-octanethiol and 11-mercaptoundecane-1-sulfonic acid (from now on stated as MUS:OT nanoparticles), that have been shown to exhibit many interesting functions^{6,7,161}. First, thanks to the MUS:OT 34%OT ligand combination, the colloidal stability of this nanoparticle type in water is very high (up to 33% in weight). Equally high is the colloidal stability of these nanoparticles in phosphate buffer saline, which forms the basis for most the biological applications. Moreover, these particles do not precipitate in relatively low pH, *e.g.* pH 2.3 and high salt concentrations, *e.g.* 1 M NaCl¹⁶². The amphiphilic nature of the ligand shell allows MUS:OT nanoparticles to fuse with lipid bilayers spontaneously, in order to reduce their hydrophobic solvent accessible surface area¹⁶⁰. Compared to All-MUS nanoparticles (nanoparticles having only MUS ligands on their shell), the higher hydrophobic ligand content on nanoparticles, *i.e.* MUS:OT 34%OT, increases the span of their core diameters, which still allow fusion into lipid bilayers¹⁶⁰. Similarly, MUS:OT 34%OT nanoparticles can be internalized in cells through an energy-independent penetration mechanism in less than a minute and can also carry oligonucleotides as cargo into tumor cells^{9,163,164}. Moreover, MUS:OT 50%OT nanoparticles can be integrated into liposomes and be precisely delivered to tumor sites, in order to enhance radiotherapeutic killing of cancer cells¹⁶⁵. The interaction of MUS:OT particles with the cell membrane and lipid bilayers will be discussed further in detail.

Furthermore, the interactions between the MUS:OT nanoparticles and proteins have been studied. Different self-assembled organizations of the ligand shell correlate to distinctive binding modes of MUS:OT 34%OT nanoparticles with various proteins compared to All-MUS particles¹⁶⁶. Recently, it has been reported that MUS:OT 34%OT nanoparticles can be utilized as a broad-spectrum antiviral agent that irreversibly destroys viruses due to multivalent electrostatic bindings of MUS ligands and non-local couplings of OT ligands to capsid proteins¹⁶¹. In all these cases, it has been found that the hydrophobic content, as well as the core size of the nanoparticles, is very important for bio-nano interactions. These diverse, excellent properties of MUS:OT nanoparticles have prompted many theoretical and computational studies, with the main aim to shed light on the nature of the interactions between MUS:OT 50%OT nanoparticles and various biological materials^{167–175}.

MUS:OT particles are the most studied mixed ligand nanoparticles, with an abundance of studies focusing on improvement of their properties, such as solubility and self-assembly^{176,177}. Moreover, using mixed ligand nanoparticles facilitates higher efficiency in biological applications consisting mostly of drug delivery^{178,179}. To increase the efficiency of drug delivery and blood circulation time, such particles were modified either with PEG^{180–182} or a zwitterionic ligand combination, *e.g.* sulfonate and tertiary amine¹⁸³. Also, mixed ligand nanoparticles have been used in non-biological applications such as colorimetric metal ion detection and catalysis¹⁸⁴. For instance, 3-mercapto-1-propanesulfonic acid (MPSA):OT nanoparticles have shown higher catalytic activity than All-MPSA homoligand nanoparticles in acetylation reaction¹⁸⁵.

2.3 Nanoparticles and Cells

Nanoparticles can be synthesized with many different shapes, sizes, and surface chemistry. Moreover, they can self-assemble, ultimately displaying different properties than individual particles¹⁸⁶. Surface coatings of nanoparticles make them capable of targeting various biological objects^{153,187}. These characteristics combined make nanoparticles an attractive solution for several biological and medicinal applications like imaging, therapeutics, and drug delivery^{127,128}. In all these applications however, to mediate the function that they are devised

for, the nanoparticles should reach the target efficiently and precisely. In fact, delivery and targeting at the subcellular level is really important not only to understand the complex events occurring during these processes, but also to design therapies that can modulate them. For instance, nanoparticles carrying oligonucleotides should reach the nuclei to efficiently facilitate the delivery⁴. Yet, prior to any subcellular function, nanoparticles first need to traverse the cell membrane.

2.3.1 Cellular uptake of nanoparticles

Controlling the route of nanoparticle uptake is important for mediating their intracellular fate and biological response. Prior to cellular uptake, nanoparticles can interact with the cell membrane directly or indirectly, interacting with membrane embedded receptors or associating with lipid bilayers, respectively. Cellular uptake of nanoparticles can then follow one of two routes; passive (energy independent) or active (energy dependent) transport. Particularly in passive uptake, nanoparticles can diffuse through the membrane without perturbing the lipids during traversing or a protein channel in the membrane aids the diffusion of nanoparticles¹⁸⁸.

Active transport can have many forms. One of the most common is endocytosis, a process during which, nanoparticles to be transported into the cell are internalized through their enclosure in vesicles are formed directly from the cell membrane. To be able to explain the internalization of nanoparticles by endocytosis, four subcategories of endocytosis can be discerned; phagocytosis, macropinocytosis, caveolae-dependent or clathrin-mediated endocytosis, and non-receptor mediated endocytosis in which caveolae and clathrin are receptor molecules^{189,190} (Figure 2-5). Phagocytosis occurs in certain mammalian cells which have phagocytic receptors in the membranes, *e.g.* macrophages. These phagocytic receptors initiate the engulfing of nanoparticles by the cell membrane, eventually forming an internal phagosome.

The second subcategory of endocytosis, pinocytosis, takes place in almost all cell types and is governed by hydrophobic and electrostatic interactions. During pinocytosis the cell

membrane invaginates and traps the local extracellular fluid and any object found in the vicinity. Therefore, pinocytosis is a non-specific mechanism for uptake¹⁹¹.

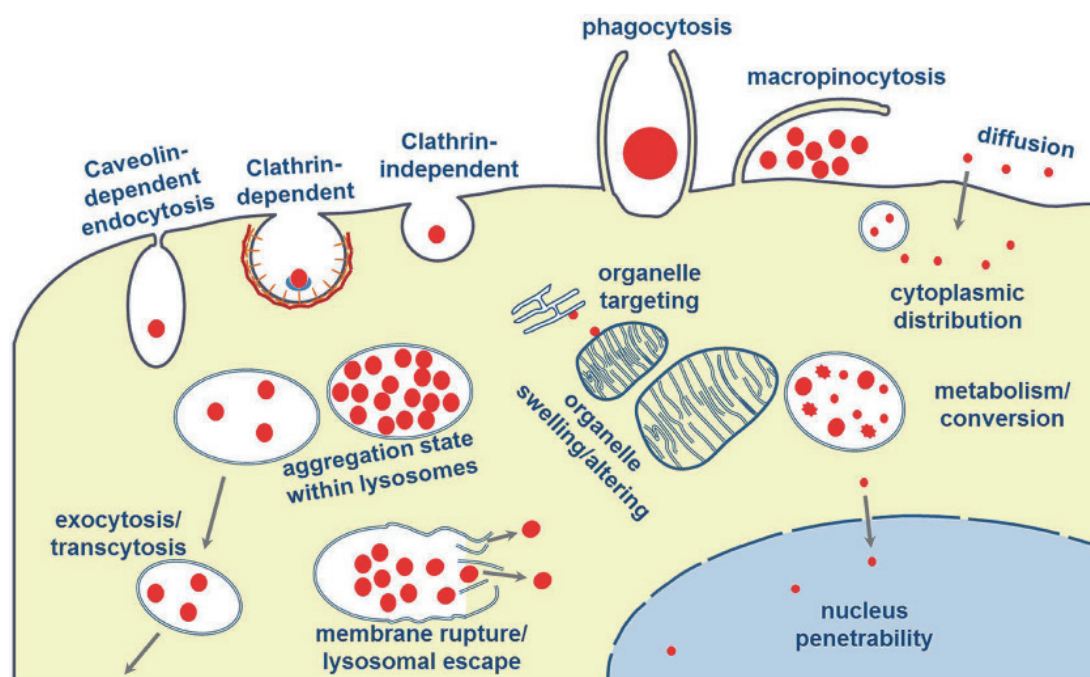


Figure 2-5 Different endocytic pathways to enter into the cell. The figure is adapted from reference ¹⁹² with permission.

Clathrin mediated endocytosis is governed by ligand binding to clathrin receptors, followed by polymerization of clathrins and pit formation. Once the pit is invaginated, enzymes (*e.g.* dynamin) form a tube around the neck of the pit and then lead to fission of the vesicle via constriction around the neck^{32,33}. Dynamin also plays a role in caveolae mediated endocytosis, in which caveolae is a subdomain of glycolipid rafts of the cell membrane^{193,194}.

During non-receptor mediated endocytosis, the last endocytosis mechanism discussed here, nanoparticles come across the membrane and their uptake is mediated by physicochemical forces alone¹⁹⁵. There are three parameters playing a role in this phenomenon; adhesion energy between nanoparticles and membrane, membrane bending modulus, and membrane surface tension¹⁹⁶. If the adhesion energy of nanoparticle to the membrane is not sufficient, nanoparticles collide randomly with membranes and do not attach on their surface. If the adhesion energy is high enough, nanoparticles remain on the membrane and can be partially wrapped by the membrane. The ease with which the membrane can wrap nanoparticles is dependent on the membrane bending modulus; smaller nanoparticles require a higher

degree of bending than their larger counterparts. Once the adhesion energy overcomes the energy barrier associated with the membrane curving, nanoparticles are completely wrapped by the membrane and internalized ¹⁹⁷(Figure 2-6). This interplay of adhesion energy and membrane modulus define a critical radius for nanoparticles above which they can be internalized by the membrane¹⁹⁸.

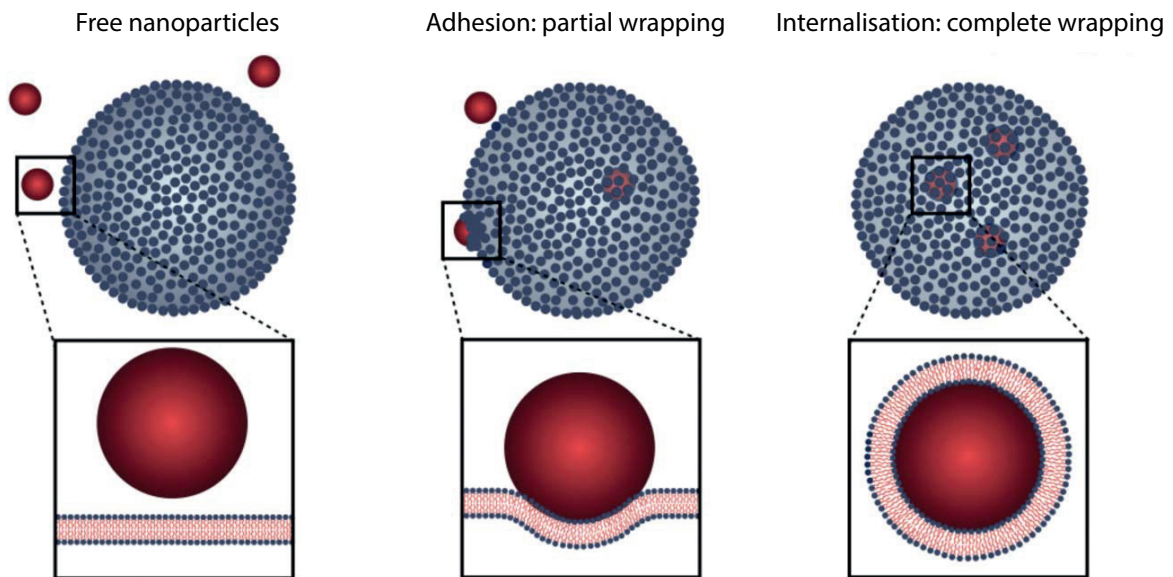


Figure 2-6 Illustrations of three possible nanoparticle non-specific interaction with cell membrane. Figure is adapted from reference ¹⁹⁹ with permission.

The interaction of nanoparticles with cells, for example the selection of uptake mechanism, the efficiency of internalization, and their localization in the cell, is strongly affected by the intrinsic properties of nanoparticles. Mechanistically speaking, small nanoparticles were more likely to be internalized through passive uptake than larger nanoparticles. For example, 2 nm small gold nanoparticles displayed a higher percentage of internalization through the passive uptake mechanism than 6 and 15 nm nanoparticles²⁰⁰. The uptake of larger nanoparticles was mediated mostly by active transport mechanisms. Although the sizes of nanoparticles differed regarding the different mechanisms, as well as different cell lines and cell types, it was generally considered that nanoparticles having a core of 30-50 nm are uptaken at maximum efficiency¹⁸⁸. Nanoparticles smaller than 200 nm were typically internalized through clathrin mediated endocytosis. Further increase of the nanoparticles' size shifted the endocytosis mechanism from clathrin to caveolae mediated endocytosis, the most common intake mechanism of nanoparticles with a size around 500 nm.

The effect of gold nanoparticles' characteristics other than size on their uptake remains less well-studied. For example, there have been contradicting results regarding the effect of nanoparticle shape. In a study by Chan *et al.*, it was observed that spherical gold nanoparticles are uptaken more easily than rod shaped gold nanoparticles with a size of 14-74 nm²⁰¹. Peiris *et al.* studied the internalization of rod shaped particles compared to a sphere, cylinders, and cubes, and determined that rod shape were uptaken more²⁰². Taken together, it is concluded that a definite correlation between nanoparticle shape and internalization is difficult to be observed.

Ligand type and surface charge also played a role in the uptake of nanoparticles, since they determined the secondary identity of nanoparticles. In general, neutral nanoparticles having a coating of either non-charged ligands or zwitterionic ligands displayed lower internalization by cells than charged ones¹²⁰. Among charged groups, cationic particles showed an improved uptake rate when compared to anionic particles, due to their favorable interaction with the generally negatively charged cell membrane²⁰³. Moreover, higher charge density displayed the higher amount of internalization. Chemically speaking, the cationic functional groups of the surface ligands, *e.g.* amines (-NH₂) induced higher cellular uptake than negatively charged ones, *e.g.* carboxyl groups (-COOH), or neutral ones, *e.g.* hydroxyl groups (-OH)^{181,204}. Another aspect that determine the cellular uptake was the hydrophilic and lipophilic nature of the surface ligands of the nanoparticles. The cellular internalization of the nanoparticles diminished with an increase in the hydrophilicity of the surface. This effect was exploited, amongst other things, for increasing nanoparticles' circulation time in the bloodstream, by modifying their surface with a hydrophilic polyethylene glycol (PEG) coating²⁰⁵.

Cellular uptake of nanoparticles can be further improved by combining multiple ligands on the nanoparticles' surface, tailoring their properties and interactions with cells^{174,198}. For example, Lund *et al.* experimentally demonstrated that by combining multiple ligands on a nanoparticle surface and creating different organization states of said ligands, cellular uptake was altered significantly²⁰⁷. The importance of bulky hydrophobic groups interspersed in a mixed ligand nanoparticle coating was studied by Gao *et al.*, who studied the interaction of anionic nanoparticles with the cell membrane²⁰⁶. Similarly, a study by Xia *et al.* demonstrated

that mixed ligand Janus nanoparticles were internalized by cells more efficiently than single-ligand nanoparticles²⁰⁸.

The interaction of nanoparticles with their local environment also has a significant effect on any subsequent nanoparticle-cell interaction. The formation of a protein corona on nanoparticles, originating from proteins and biological molecules present in serum, modifies drastically their overall chemical properties¹⁵⁷. This effect was well demonstrated in a study by Giljohann *et al.*, where binding of serum proteins on the surface of intrinsically anionic nanoparticles maximized their previously moderate cellular uptake²⁰⁹.

Once nanoparticles have entered the cells through endocytosis, their intracellular location directly affects their functions. Nanoparticles can either remain in the cell, endocytically transported to organelles like lysosomes, the Golgi complex, and mitochondria, or they may be directly exocytosed out of the cell. Endocytic transfer takes place through the encapsulation of nanoparticles in vesicles and their transport to the desired location. Although certain nanoparticles (*i.e.* those targeting the Golgi apparatus (not sure about the correct term here)) can favor endocytic transfer, other types of nanoparticles are unstable in the acidic ($\text{pH} < 4$) chemical environment of the endocytic vesicles and may be degraded before reaching their target¹⁸⁹. To overcome this problem, nanoparticles are designed to directly enter the cells, overpassing the endocytosis by force or by helping other moieties such as CPP chaperones^{210,211}.

2.3.2 Cellular uptake of MUS:OT gold nanoparticles

As previously described, to fulfill the biological function that nanoparticles are designed for, they should almost always be uptaken by cells through passive transport pathways. In that way, damage to cells is minimized and, at the same time, nanoparticles can predictably reach their subcellular targets. Recently, it was demonstrated by our group that MUS:OT 34%OT amphiphilic nanoparticles interact with cells in the most efficient way, thus creating a valuable tool for nanoparticle-cell studies. MUS:OT 34%OT nanoparticles were observed to demonstrate low protein binding, thus avoiding the formation of a protein corona, and did not aggregate in physiological conditions. This behavior was attributed to their high degree

of ligand ordering on the surface and high water solubility. The cellular uptake of MUS:OT 34%OT nanoparticles was verified by conducting multiple studies in which these nanoparticles were incubated with dendritic mouse clonal cells (DC2.4) in parallel with All-MUS, and MUS:br-OT 34%br-OT. To compare the surface structure of the MUS:OT particles, nanoparticles were synthesized with branched octanethiol (br-OT) which inhibits the formation of ribbon like structures on the surface instead of octanethiol. These groups of nanoparticles also enabled the comparison of the effect of heterogeneous ligand combinations and also the surface structures of mixed ligand nanoparticles. Confocal laser scanning microscopy (CLSM) and transmission electron microscopy were used to evaluate the behavior of the nanoparticles. Prior to imaging in CLSM, nanoparticles were labeled with a thiolated BODIPY dye. Their cellular internalization and consequent distribution in living cells was studied²¹². To avoid any quenching from nanoparticles, BODIPY with $\lambda_{\text{excitation}}$ 630 nm / $\lambda_{\text{emission}}$ 650 nm was chosen for labeling. Following incubation at 37 °C, MUS:OT 34%OT nanoparticles showed eightfold more fluorescence than All-MUS and MUS:br-OT 34%br-OT particles, indicating higher cell entry⁶. This high amount of cell entry, however, consisted of both passive and active uptake. To distinguish between active and passive uptake, cells were incubated with nanoparticles at 4 °C or treated with sodium azide and 2-deoxyglucose, in order to inhibit the endocytic uptake. Cell uptake of All-MUS and MUS:br-OT 34%br-OT particles decreased drastically in comparison to MUS:OT 34%OT. This observation indicated that the mechanism of cell internalization of MUS:OT 34%OT nanoparticles was diffusion based passive uptake mediated, whereas other nanoparticles were uptaken through energy-dependent active transport pathways (Figure 2-7). To investigate if nanoparticles lead to pore formation in cell membrane during internalization, calcein was included in the system during incubation of nanoparticles at endocytosis inhibiting conditions. This dye can traverse the cell membrane either through endocytosis or pores, hence, lack of calcein fluorescence in the cell indicated that nanoparticles did not perturb the cell membrane during internalization.

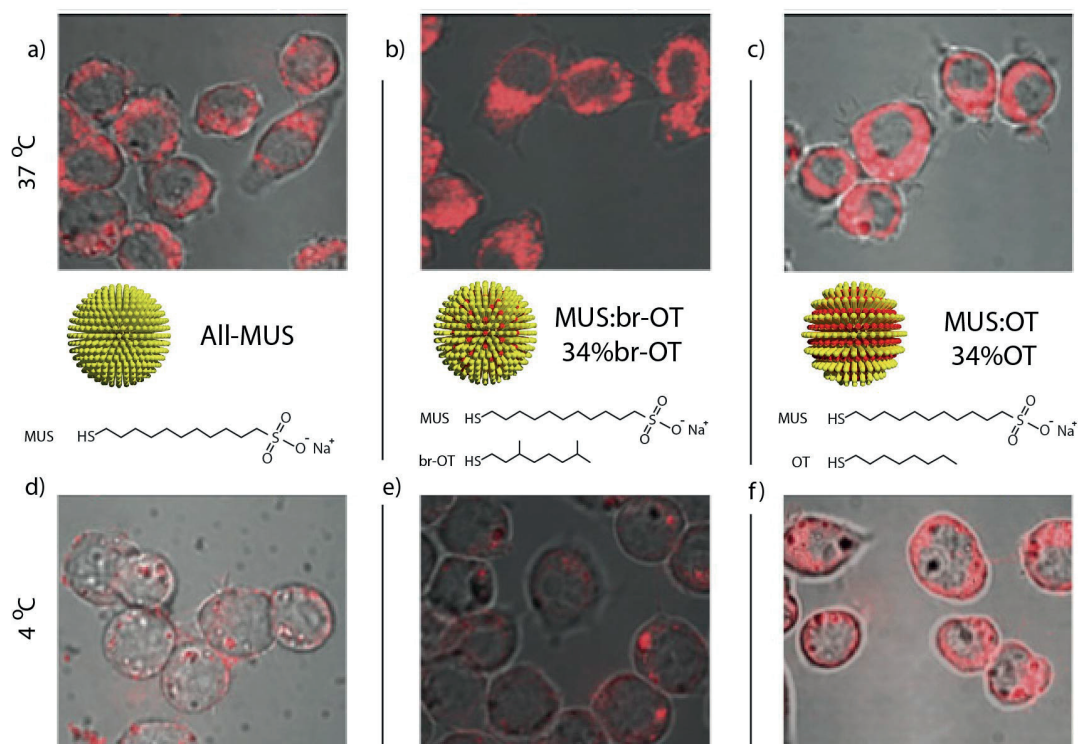


Figure 2-7 Cell uptake of amphiphilic nanoparticles. Cell were incubated with nanoparticles for 3 hours a, b, c) at 37 °C, d, e, f) at 4 °C. This figure is adapted from ⁶ and modified further with an inspiration from ⁶⁹ with permission.

Furthermore, MUS:OT nanoparticles were incubated with three distinct cell lines; dendritic mouse clonal cells (DC2.4), mouse fibroblast (3T3), cervical cancer cells (HeLa)¹⁶⁴. This study included MUS:OT 66%OT nanoparticles, allowing the comparison of the effect of ligand ratio on the surface of nanoparticles in cellular uptake. Consistent with the previous study, MUS:OT 34%OT showed the highest amount of internalization regardless of cell type, incubation time, and temperature. It should be noted that no significant difference between structured MUS:OT 34%OT and non-structured MUS:br-OT 34%br-OT was found in this case. The uptake of all types of nanoparticles was observed in less than 1 min, indicating rapid process kinetics¹⁶⁴.

Based on the surface plasmon resonance of nanoparticles, photothermal heterodyne imaging was also used to study the internalization behavior of nanoparticles. Similarly, MUS:OT 34%OT nanoparticles showed higher internalization than All-MUS particles even at very low concentrations (10 nM)²¹³.

Having proven the spontaneous, energy independent internalization of MUS:OT nanoparticles, erythrocytes were used to investigate the internalization behavior further, as these cells do not facilitate endocytic uptake¹⁶³. The intake of MUS:OT (34%OT) particles increased two-fold when sialic acid, normally present on the erythrocyte membrane surface was stripped, suggesting that existence of anionic membrane groups inhibited the interaction of particles with the membrane¹⁶³.

Considering the cell penetrating behavior of MUS:OT particles, they were used to deliver oligonucleotides into cancer (B16-F0 melanoma) cells. Cargo loaded MUS:OT nanoparticles traversed the cell membrane through diffusion, but accumulated in the cytosol⁹, in agreement with previous studies^{6,164}.

2.3.3 Toxicity of nanoparticles

Toxicity studies of any nanoparticle types internalized by cells are paramount for biological or medicinal applications. The mechanism of nanoparticle-related cell toxicity has been thoroughly studied, and was found to stem from factors such as material, size, shape, surface charge, and hydrophobicity of particles²⁰³. For instance positively charged gold and silica nanoparticles are more cytotoxic than their similar sized negatively charged counterparts^{214,215}. Toxicity can result in a multitude of phenomena, including inflammation, indirect DNA damage, and cellular damage^{216–218}.

Cellular uptake of nanoparticles plays a key role in their toxicity. Especially for the inherently toxic metal nanoparticles, their endocytic uptake indirectly affects their toxicity²¹⁹. Since, lysosomes maintain an acidic pH and host the degrading enzyme protease, metal nanoparticles corrode and release toxic metal ions (*e.g.* Ag⁺, Cd²⁺, Fe^{2+/3+}, Au^{1+/3+}) into the cytoplasm. This indirect toxicity of nanoparticles is called 'lysosome-enhanced Trojan horse effect'²²⁰.

Understanding the cause-and-effect relation between nanoparticles and cells allows the modification of nanoparticle design, thus eliminating any harmful effects. Nanoparticles can be designed in order to favor passive uptake, minimized brute force cell damage, or they can

be modified to escape from lysosomal escape. Also, the lysosome-enhanced Trojan horse effect can be avoided by synthesizing nanoparticles resistant to acidic pH etching by further surface modification, or biocompatible materials can be used as the nanoparticle core.

2.4 Nanoparticles and Lipid Bilayers

Combining nanoparticles and liposomes creates a versatile platform for the detailed study of cell-nanoparticle interaction. These hybrid systems employ physical properties of both nanoparticles and liposomes for vast amount of biological applications including drug or gene delivery, theranostics, diagnostics, etc.²²¹. In these systems various types of nanoparticles have been used, including quantum dots^{189,222–224}, nanodiamonds²²⁵, superparamagnetic iron nanoparticles (SPION)^{226–228}, gold nanoparticles^{229–232}, silica nanoparticles^{125,198}, to name a few. Nanoparticle-liposome hybrid systems have been formed following various strategies; loading hydrophobic particles into the bilayer, encapsulating hydrophilic nanoparticles in the liposomes, chemically binding the nanoparticles to the liposomes or through absorption of nanoparticles on the surface (Figure 2-8).

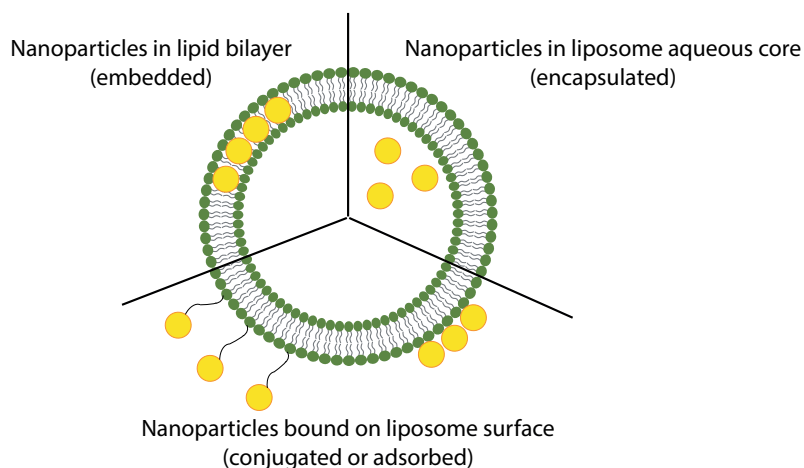


Figure 2-8 Schematic illustration of various approaches for design of nanoparticle liposome hybrid systems. Figure is adapted from reference ²²¹ with permission and modified further.

Based on the structure of the hybrid systems, liposomes can serve as a delivery vehicle for hydrophobic nanoparticles so that these nanoparticles can be used in biological applications. Also, liposomes concentrate the nanoparticles and protect them from the immune system. On the other side, nanoparticles grant a better stability to liposomes. Moreover,

nanoparticles can be conjugated on the surface of liposomes and dictate the delivery of liposomes to the target area. The most important contribution of nanoparticles to these hybrid platforms, however, is to enable stimuli triggered delivery or therapeutic functions. Liposomes-SPION systems, for instance, have been used to kill cancer cells through magnetic field induced hyperthermia²³³, and as a drug delivery method, in which the SPIONs were embedded in the liposomal bilayer²³⁴. Similar systems in which SPIONs are located in the bilayer or inside the liposome have been suggested as contrast agents, imaging probes^{226,228}. Similarly, liposome-gold nanoparticle systems enable drug delivery upon a photo- or acoustic trigger that targets the core of the nanoparticles²³⁰. Additionally, some studies have demonstrated gold nanoparticle mediated drug delivery from liposomes in which the surface properties of gold nanoparticles changed triggered by pH stimuli^{231,232}.

On the other hand, liposome-nanoparticle composite systems have been used for more fundamental research focusing on nanotoxicology²³⁵, effects of nanoparticles on the bilayer, etc. in which liposomes serve as a model membrane²²⁵. For instance, citrate coated gold nanoparticles happen to induce gelification (phase change of lipids from fluid to gel phase) on the bilayer from the interaction sites locally²³⁶ and subsequently increase the phase transition temperature of the lipids²³⁷. Moreover, other gold nanoparticles have been shown to interact differently with bilayers, depending on the phase of the bilayer^{238,239}. Furthermore, the role of amphiphilicity of the nanoparticle surface during lipid bilayer interaction has been studied. Cationic amphiphilic nanoparticles were shown to prevent the growth of tubular structures by blocking the edges of the bilayers²⁴⁰, whereas anionic amphiphilic Janus nanoparticles disrupted the bilayers²⁴¹. Upon penetration of a bilayer by anionic amphiphilic Janus nanoparticles, the nanoparticle surface coating rearranged itself to have hydrophobicity and hydrophilicity match between ligands and lipid molecules²⁴². Furthermore, there have been studies to investigate the interaction parameters in terms of size and self-assembly of the nanoparticles in the liposomes^{229,243,244}.

2.4.1 MUS:OT nanoparticles and lipid bilayers

MUS:OT nanoparticles can traverse the cell membrane through energy independent pathways without any pore formation observed. This phenomenon, reminiscent of cell

penetrating particles, has gained attention and thus the mechanism behind it has been the subject of many studies. To do that reductionist model systems based on giant unilamellar vesicles (GUVs), and lipid bilayers were used experimentally. Additionally, complex molecular dynamics simulations were carried out to shed light on the principles of membrane insertion of these nanoparticles.

2.4.1.1 *Experimental studies*

Despite the complexity of cell membranes, MUS:OT nanoparticles can penetrate into the cytosol through a spontaneous, non-disruptive path. Various characterization techniques such as confocal laser scanning microscopy (CLSM), electron microscopy (EM), atomic force microscopy (AFM), electrochemistry, etc. have been used to study this phenomenon. In cases where cell use was not optimal, reductionist systems such as GUVs, SUVs, and standing bilayers were used.

Prabhani *et al.*²⁴⁵, have studied the MUS:OT nanoparticle – cell membrane interaction working with GUVs using CLSM. Since the nanoparticles were below the resolution limit of the light microscope, nanoparticles were fluorescently labeled with thiolated BODIPY similar to previously described cellular uptake experiments in Chapter 2.3.2. GUVs themselves were also labeled with 1,2-dioleoyl-sn-glycero-3-phosphoethanolamine-N-(7-nitro-2-1,3-benzoxadiazol-4-yl) (NBD-PE), which enabled the monitoring of both membranes and nanoparticles from two different channels. In each experiment, the NBD channel (Figure 2-9, green channel) showed the formation of many multilamellar vesicles with every lipid composition and buffer used. Amphiphilic nanoparticles interacted with zwitterionic DOPC vesicles in water as shown in the red channel. Once the vesicles became anionic due to the mixture of DOPG/DOPC lipids in the bilayer, nanoparticles were no longer adsorbed on the bilayer. Mechanistically speaking, the electrostatic repulsion between nanoparticles and the bilayers inhibited their interaction. Nanoparticles, however, did interact with the same DOPC/DOPG vesicles when the vesicles were formed in phosphate buffered saline (PBS), which consists of physiological electrolytes that screened the like charges.

Furthermore, to investigate the effect of lipid phases on the nanoparticle-liposome interaction, liposomes made of both a 1,2-dipalmitoyl-sn-glycero-3-phosphatidylcholine (DPPC)/DOPC mixture and only DPPC were used. DPPC only vesicles, which contain only gel phase lipids, did not show any adsorption of nanoparticles²⁴⁵. This result dictates the necessity of fluid phase based lipid flexibility in the bilayer for nanoparticles to interact.

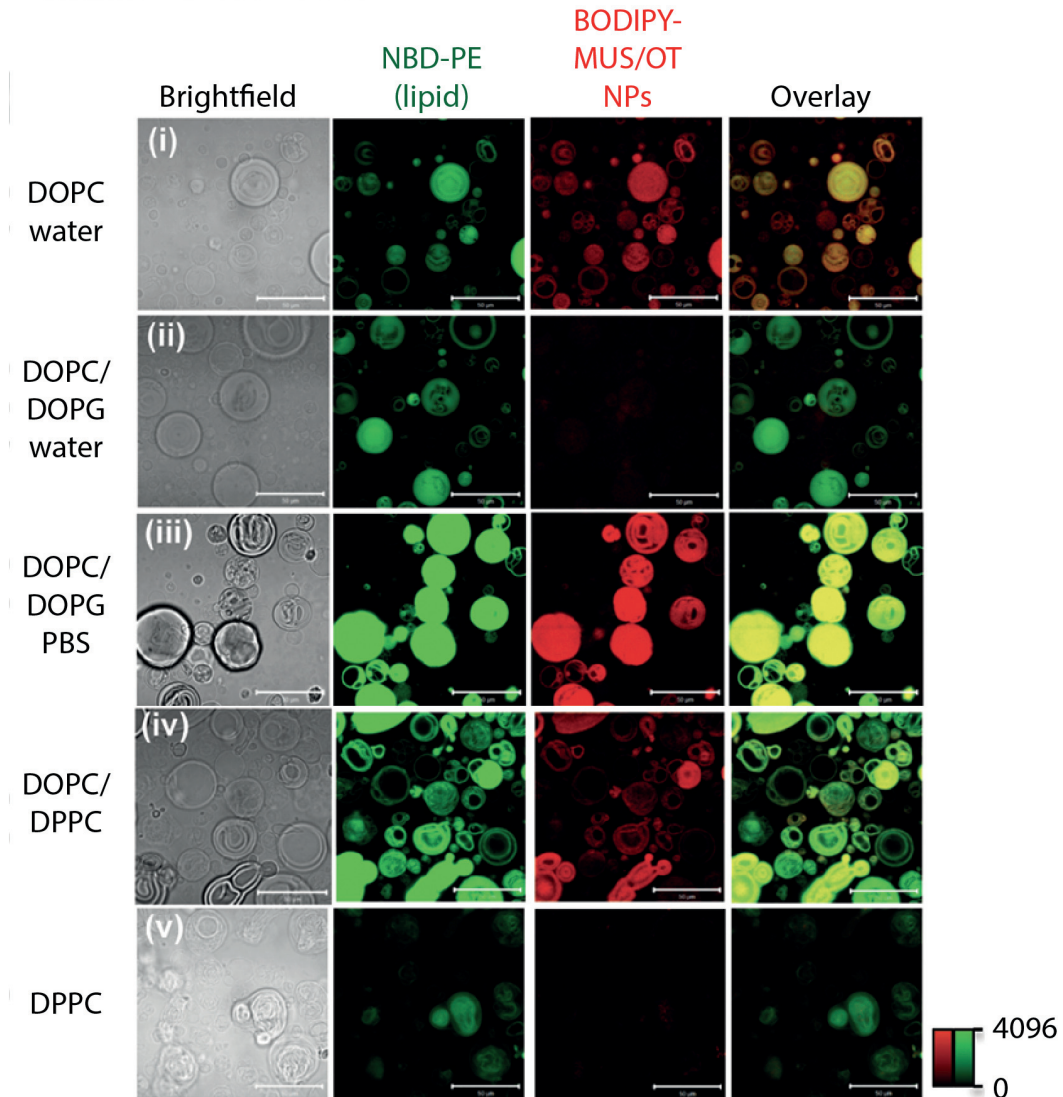


Figure 2-9 CLSM images of MUS:OT nanoparticles incubated with GUVs made of various lipids. i) Nanoparticles incubated with all zwitterionic DOPC liposomes in water, ii) Nanoparticles incubated with anionic lipids made of DOPC/DOPG in water, iii) Nanoparticles incubated with anionic lipids made of DOPC/DOPG in PBS, iv) Nanoparticles incubated with liposomes made of DOPC/DOPC which consists of fluid and gel phase together, v) Nanoparticles incubated with gel phase liposomes made DPPC. The image is reproduced from ²⁴⁶ with permission.

The aforementioned method of BODIPY labeling of nanoparticles was used to determine the membrane insertion of MUS:OT nanoparticles. *In silico*, BODIPY was shown to bend towards hydrophobic pockets of nanoparticles in aqueous solutions, and subsequently, be quenched²⁴⁶. Once the nanoparticles penetrated into the membrane completely, BODIPY was observed towards the hydrophobic lipid tails in the bilayer. The quenching effect of the nanoparticle, hence, was not effective^{245,247}. These results however were not conclusive, since the simulations for the behavior of BODIPY considered the state only of nanoparticles embedded in the membrane²⁴⁵. In other words, any partial insertions of nanoparticles were disregarded, which could have displayed similar fluorescence; the BODIPY ligand can leave from quenching territory of nanoparticles and reach the hydrophobic core of bilayers from this proximity. Despite any controversy though, fluorescent based studies have offered invaluable information on the interaction between liposome and nanoparticle.

AFM was further used to characterize the membrane insertion behavior of nanoparticles. MUS:OT 34%OT particles were found to penetrate DOPC bilayers, with the edges acting as an initial insertion gateway (Figure 2-10). The yellow-like regions around the perimeter of bilayers were interpreted, based on height, as the nanoparticles. Their presence towards the center of the bilayer further underlined the ability of nanoparticles to diffuse in the bilayer laterally⁷.

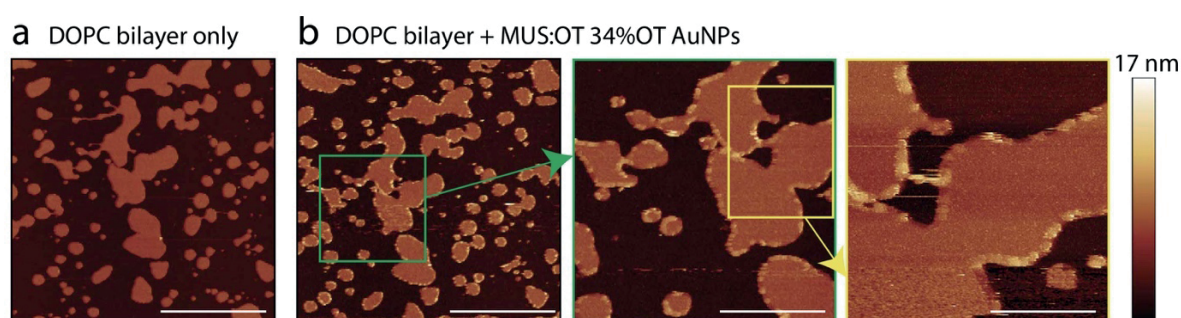


Figure 2-10 AFM topography images of DOPC supported bilayers incubated with MUS:OT 34%OT nanoparticles in PBS. a) DOPC bilayer only (lighter brown features), b) DOPC with nanoparticles, the images were subsequently zoomed in. The yellow-like boundaries correspond to nanoparticles around the perimeter of the bilayers. The image is reproduced with permission from reference ⁷.

Nanoparticles insertion in the bilayer was also proven through a non-microscopic method. This method was based on the capacitance measurements of a bilayer lipid membrane upon

interaction with nanoparticles (Figure 2-11). MUS:OT 34%OT nanoparticles of various sizes below 10 nm showed an increase in the capacitance, indicating nanoparticle embedment into the lipid bilayer. On the contrary, All-MUS particles of same sizes did not show any change in the capacitance, which was interpreted as no interaction with the bilayers.

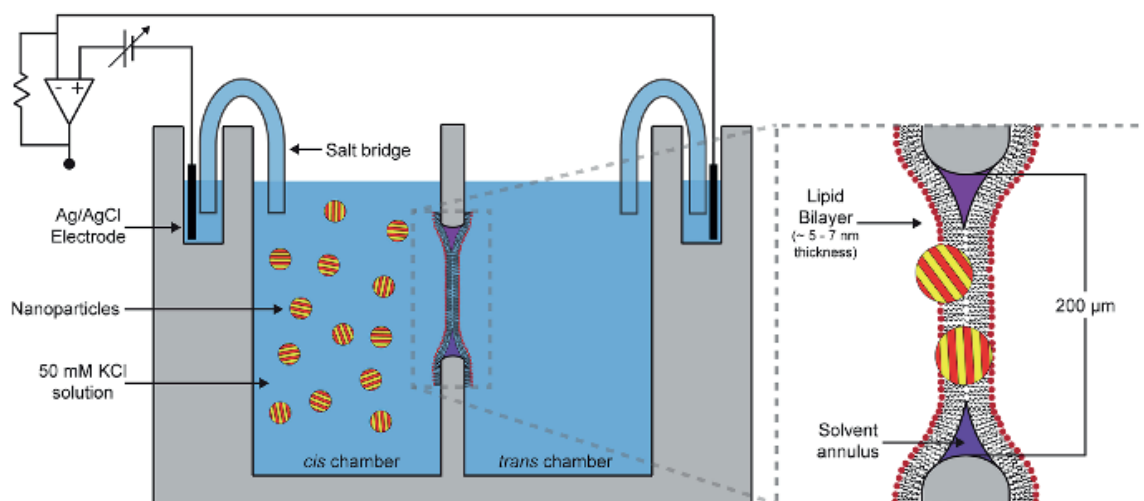


Figure 2-11 Schematic illustration of capacitance measuring set-up based on nanoparticle adsorption. The image is reproduced with permission from reference ²⁴⁸.

The importance of the previously discussed studies was underlined via a study of Yang *et al.*¹⁶⁵. Based on previous observations, a system of interbilayer crosslinked multilamellar lipid vesicles accommodating MUS:OT 50%OT nanoparticles on the bilayers was designed and applied in cancer radiotherapy, where nanoparticles were used as radiosensitizers. The nanoparticles were transferred to and internalized in the cancer cells by vesicles. Following irradiation, gold nanoparticles were separated from liposomes, dispersed into the target tumor cells and enhanced the effect of radiotherapy through radiation damage and concentrated X-ray energy due to their high atomic number.

2.4.1.2 Computational studies

It has been experimentally established that MUS:OT nanoparticles spontaneously and non-disruptively penetrate into the cell. To gain a physical understanding of the process computational studies (employing different models, *e.g.* MARTINI model, coarse grained, dissipative particle dynamics method, atomistic molecular dynamics) were carried out by

several research groups, using lipid bilayers as a cell model. Here, however, studies from Katz lab will be reviewed in detail and compared with other models, as those are considered the most relevant to the experimental work presented in this thesis.

These studies use MUS:OT 50%OT gold nanoparticles with a diameter of 2 nm and all-DOPC zwitterionic lipid bilayers. Despite the high water solubility of these nanoparticles, the flexibility of the ligands on the surface and the free volume accessible to them creates an interface between water and the hydrophobic alkane backbone of the ligands. Initially, ligands on the surface of nanoparticles cluster to minimize the solvent accessible hydrophobic area¹⁶⁷. Despite this, the hydrophobic force resulting from the unfavorable interface between water and the solvent accessible surface area on the nanoparticles is the driving force of the particle insertion into the bilayer¹⁶⁰. Following the insertion, in order to remain fused into the bilayer, the flexible ligands deform and transport their charged head group out of the hydrophobic bilayer core. Figure 2-12 represents the charged ligand transport through the bilayer core, termed the ‘snorkeling’ behavior of the ligands. Studies by Simonelli *et al.*¹⁶⁹ was in agreement with this model, as the same 3 step insertion path was proposed, the sole difference being the longer time found necessary for the first hydrophobic contact and flipping of the lipids to span the membrane.

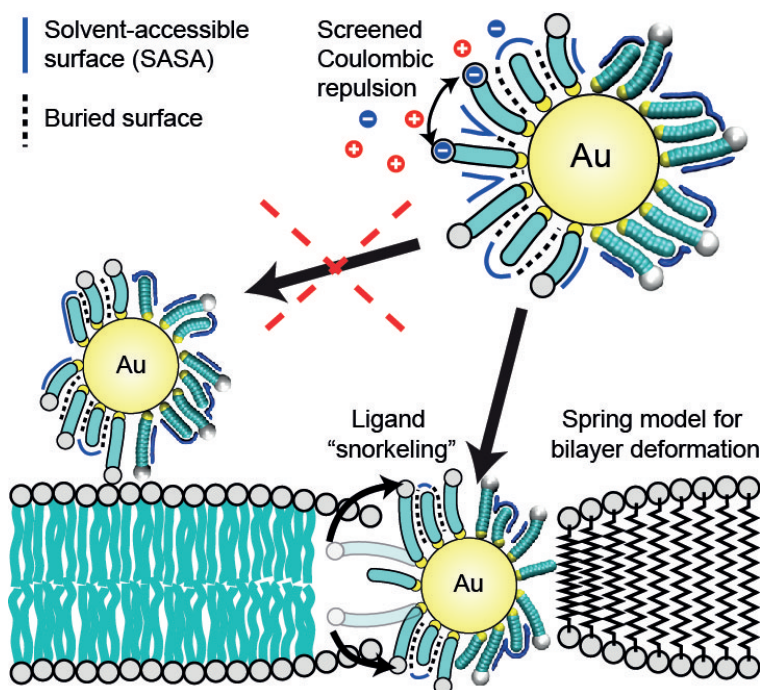


Figure 2-12 Schematic representation of the interaction between MUS:OT nanoparticles and lipid bilayer. The hydrophobic driving force enables particles to penetrate into the bilayer instead of being adsorbed to surface

due to electrostatic interactions. The amount of the hydrophobic force is sufficient to overcome several energy penalties including electrostatic interaction, thickness change of bilayer, conformational restriction of the ligands at insertion stage, and finally the insertion of the charged ligand towards the hydrophobic core of the bilayer, referred as snorkeling. The image is reproduced with permission from reference ¹⁶⁰.

Ligand snorkeling is one big energy penalty in the insertion process that nanoparticles need to overcome, but not the only one. Chronologically, first, the electrostatic interaction has to be eliminated, as to not have nanoparticles adsorbed on the surface of lipids. Moreover, the mechanical deformation in the vicinity of the inserted nanoparticles has to be compensated for. Finally, conformational restrictions of the ligands due to the decrease in flexibility after insertion need to be balanced. Considering all the energy inputs and penalties, the formulation presented in equation 2.1 determines the total change of the free energy of the nanoparticles during insertion and consequently the behavior of nanoparticles.

$$\Delta G_{\text{tot}} = \Delta G_{\text{phob}} + \Delta G_{\text{philic}} + \Delta E_{\text{elec}} + \Delta E_{\text{thick}} - T\Delta S_{\text{conf}} \quad (2.1)$$

Where ΔG_{tot} is the total free energy change in the system, ΔG_{phob} is the energy of the hydrophobic effect, ΔG_{philic} is the energy penalty of insertion of the charged head groups in hydrophobic part of the bilayer, ΔE_{elec} is the change of electrostatic energy between charged groups, ΔE_{thick} is the energy cost of changes in the bilayer thickness in the vicinity of nanoparticles, and ΔS_{conf} is the conformational change of the ligands upon embedding. Each of the energy elements in this formulation changes with the core size of nanoparticles, ligand type, and ligand ratio on the coating of the nanoparticles. For instance, nanoparticles with smaller size have higher free volume, which increases the flexibility of the ligands and the consequent snorkeling behavior. A higher amount of hydrophobic content on the surface also favors snorkeling¹⁶⁷. Similarly, the hydrophilic penalty, ΔG_{philic} , decreases with fewer charged ligands existing on the surface of nanoparticles. Moreover, the conformational entropy of the ligands diminishes as the mismatch between bilayer thickness and nanoparticle size increases, due to the constrained flexibility of hydrophilic ligands. This is slightly alleviated by increased flexibility of hydrophobic ligands within the hydrophobic part of the bilayer. Introduction of branches on the hydrophobic ligands further inhibits the penetration, an effect directly correlated to the flexibility of ligands¹⁶⁷. On the contrary, increasing the length

of hydrophobic ligands increases ligand flexibility and consequently the solvent accessible hydrophobic area, which in turn promotes insertion¹⁷⁰. The formulation used for nanoparticles is similar to calculations of free energy elements for transmembrane proteins inserted in the bilayer^{249,250}.

MUS:OT nanoparticles with different core size, ligand ratio, and surface structure are simulated through the same formulation, in order to determine the specific size for nanoparticles with different ligand ratios to be fused into the lipid bilayer, if at all possible. In Figure 2-12 the minimum core size of MUS:OT nanoparticles that allows membrane insertion, as a function of different ligand ratios, is presented. Insertion of All-MUS nanoparticles was found to be favored by core size between 1 to 3.5 nm, in which the free volume is higher. The high free volume eased the snorkeling behavior, despite having only bulky sulfonate groups, which limit the ligand bending. MUS:OT 50%OT nanoparticles, which have a higher hydrophobic content, tend to require higher diameters for insertion. This enables a higher hydrophobic driving force due to the larger exposed hydrophobic surface area. Taking all possible factors into account, MUS:OT 50%OT particles fuse into bilayer predominantly, compared to MUS:OT 34%OT and All MUS particles regardless of surface morphology, unless there is a Janus type configuration in which two different types of ligands segregate from each other^{160,167}. Different from this simulation, Gao *et al.*²⁵¹ demonstrated that striped amphiphilic nanoparticles dictate the lowest free energy barrier to traverse the membrane based on the anisotropic ligand structure and subsequent obstacles on the rotational degree of freedom.

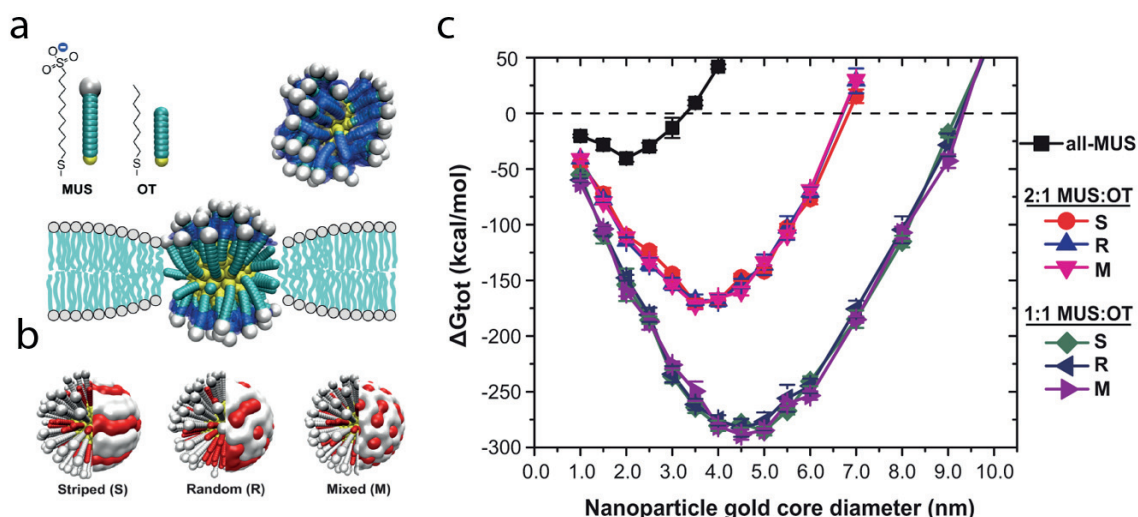


Figure 2-13 a) Representation of the ligands on the gold nanoparticles in simulations. b) Suggested surface morphology on the nanoparticles. c) Free energy diagram of nanoparticles as a function of size, ligand ratio, and surface morphology. Ligand ratio on the surface of the nanoparticles determines the favorable sizes to be embedded in the bilayer. This figure is reproduced with permission from reference ¹⁶⁰.

Given that membrane insertion of nanoparticles is thermodynamically favorable, next, the kinetics of the process were studied. In the atomistic model simulations that contain a ribbon bilayer and MUS:OT 50%OT nanoparticles of 2 nm core diameter, nanoparticles tend to penetrate into bilayers from highly curved edges but not through their planar face⁷. Nanoparticles' insertion has two big activation energies to overcome: i) the first contact in which the nanoparticles initiate the insertion, and ii) the final configuration of the nanoparticle in the bilayer (Figure 2-13).

The first barrier was overcome by the protrusion of aliphatic lipid molecules, a process in which lipids flipped over in order to make a hydrophobic contact with the aliphatic surface molecules of the nanoparticles. This contact accelerated the penetration of nanoparticles into the bilayer and remained intact during this transition process. Lipid molecules could protrude in two different ways in which the hydrophobic part close to the lipid head (elbow), or the atoms near the end of a lipid tail (splay) made a contact with the solvent. Unlike the planar bilayers, which accommodated an elbow type protrusion, vesicles and micelles had splay type protrusions. For lipid tails to protrude, being stated on the highly curved part increased the probability as it increased the lipid fluctuations and dictated lipids maximally being exposed

to water and being close enough to contact the nanoparticles. The saturation level of lipids affected their protrusion, unlike the lipids' length¹⁷³. Moreover, the protrusion is a stochastic movement by which the lipids can relax through either going back into the lipid core or making a hydrophobic contact with the nanoparticle surface.

The second barrier was the rearrangement of the ligands in the bilayer, in which an iterative process of the rearrangement of the ligands in the vicinity of the nanoparticles is proposed. In parallel to the rearrangement of the ligands, nanoparticles diffuse into the bulk of the bilayer. Simulations that do not consider the flexibility of the hydrophobic alkane backbone of the ligands or their functional groups result in an overestimation of the second energy barrier¹⁷¹.

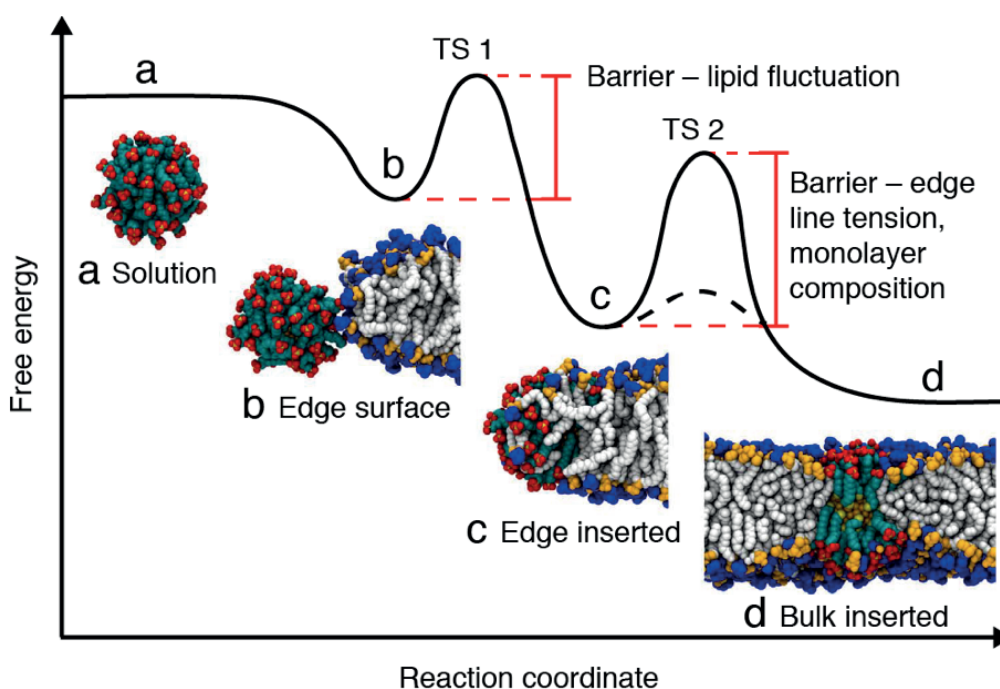


Figure 2-14 Representation of the AII-MUS particles through the transition states of membrane embedding. a) Nanoparticle is in the solution. b) Nanoparticles approaches to edge of the bilayer through electrostatic interaction, then lipid tails fluctuate and initiate the first transition state (TS1) leading the nanoparticle being inserted in the bilayer in a metastable phase. c) By the insertion of the nanoparticle, the hydrophobic solvent exposed area decreases. Ligands start to rearrange themselves in the bilayer which is defined as the second transition state (TS2). d) Nanoparticle propagated to the bulk and they are stable in the bilayer in which the ligands of the nanoparticles completely rearranged resulting in the lowest free energy state. The image is adapted from reference ⁷ with permission.

Although the size and ligand ratio of the nanoparticles' surface monolayer can affect the transition states, no further investigation has been carried out except the comparison between MUS:OT 50%OT and All MUS particles. In multiple simulation attempts, All MUS particles lead to lower amount of successful insertions than MUS:OT 50%OT particles, which can be attributed to a lower amount of hydrophobic content on the surface available for contact by lipid molecules. In this regard, the energy difference between state **a** and state **b**, as presented in Figure 2-14, should depend on the size of the nanoparticles, as well as the ligand ratio. Having the first barrier of the bilayer insertion as the hydrophobic contact between the lipid and ligand molecules, the simulations support the hypothesis of bilayer penetration driven by a hydrophobic force.

Nanoparticles have not exhibited penetration into defect-free flat membranes. However, the introduction of even a low-curvature on the bilayer facilitates the insertion of nanoparticles. The process commences with a tail protrusion based hydrophobic contact, followed by hydrophobic ligands blending within the lipid tails. When the nanoparticle slightly penetrates into the lipid monolayer, it induces a curvature and facilitates the ending of the overall insertion with the relaxation of the curvature¹⁷⁰ (Figure 2-15).

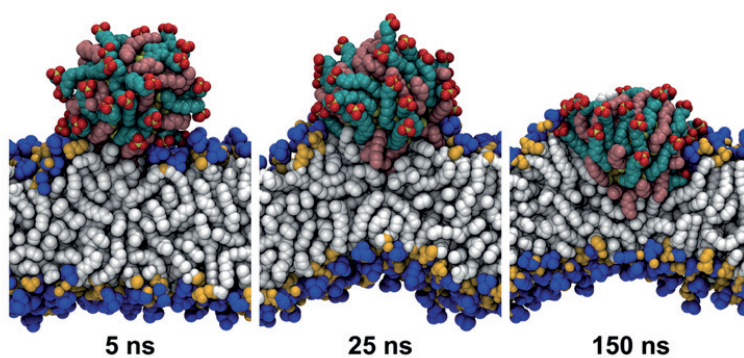


Figure 2-15 Simulation snapshots representing the behavior of MUS:OT 50:50 particles in the bilayer. At 5 ns the lipid tail protrudes and makes the first hydrophobic contact with the ligands on the nanoparticles. Up to 25 ns, nanoparticle diffuse into the membrane and introduce a curvature to the bilayer. Later, nanoparticles reaches the midplane of the bilayer and reduced solvent accessible hydrophobic area significantly following the flattening of the curvature. The image is adapted from reference ¹⁷⁰ with permission.

Following the insertion of MUS:OT nanoparticles into the membrane, in the vicinity of nanoparticle a local perturbation in the lipid packing is observed, resulting in a decrease in the bilayer thickness^{160,175}. In a more complex system containing a lipid bilayer formed of 30%

cholesterol and DPPC, MUS:OT nanoparticles still penetrate the membrane. However, they concentrate at the interface of cholesterol and DPPC and reduce the surrounding cholesterol amount¹⁷⁴. Since cholesterol rigidifies and introduces order to the membrane, a reduced amount of cholesterol in the surrounding of MUS:OT nanoparticles area indicates that they induce disorder in their vicinity. When the system includes multiple MUS:OT particles, they interact with each other and consequently align as dimers, trimers, or tetramers along the interface¹⁷⁵. Interestingly, this behavior has been explained through an orderphobic driving force in which the nanoparticles self-assemble to reduce high surface tension due to the deformation and decrease of the thickness of the membrane (Figure 2-16).

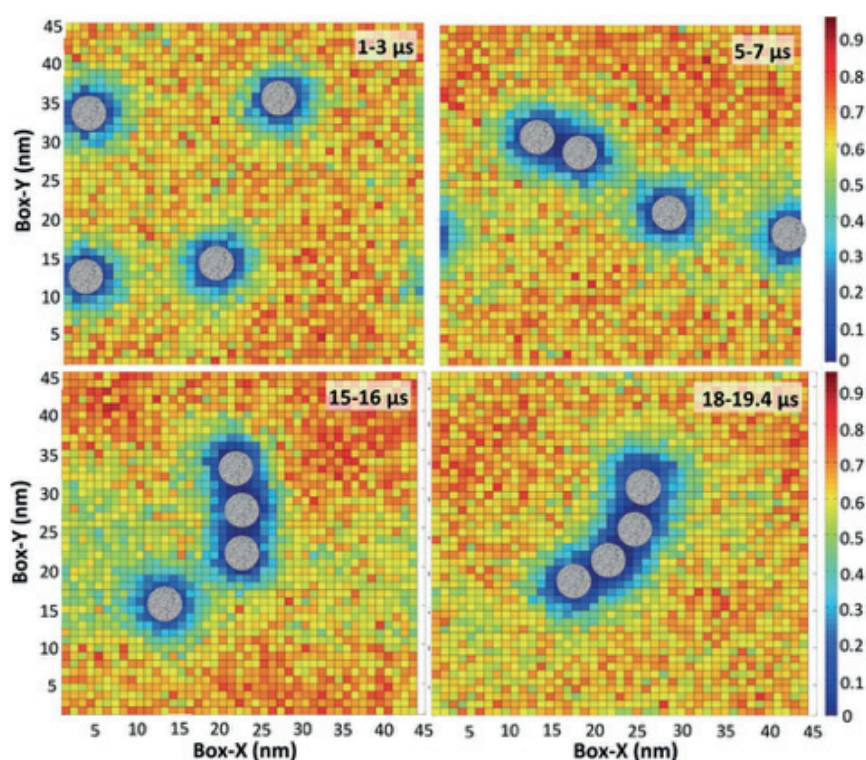


Figure 2-16 Snapshots of simulations showing the process of nanoparticles forming chain like structures and how cholesterol is depleted from the vicinity of nanoparticles. The figure is reproduced with permission from reference ¹⁷⁵.

In fact, the overall process described above is reminiscent to membrane proteins acting upon the cell membrane. Particularly the way the hydrophobic parts match with the lipid bilayer and charged parts of nanoparticles are exposed to water mirrors how transmembrane proteins display themselves in the membrane. Moreover, some peptides are sensitive to membrane curvature and lipid packing defects, through which they initiate the first

contact²⁵². In another example, arginine in certain membrane proteins bends towards the lipid-water interfaces, employing a behavior similar to snorkeling of ligands on the nanoparticles^{253,254}. Furthermore, certain peripheral proteins generate bilayer curvature, by expanding on the bilayer top after being inserted slightly on the bilayer²⁵⁵. Another example is Gramicidin A protein which also forms chain-like structures on the membrane²⁵⁶. Unlike membrane proteins though, MUS:OT nanoparticles penetrate into the membrane spontaneously without using a translocon apparatus²⁵⁷, which makes the nanoparticles advantageous in their use as protein analogs.

2.5 Synthesis and Characterization of MUS:OT Particles

To synthesize MUS:OT nanoparticles a modified Brust method (hereafter called as one-phase method) and Stucky method are employed^{258,259}. These two methods differ based on the size distribution of the synthesized nanoparticles. The one-phase method results in more polydisperse and small particles - ~2 nm, whereas the Stucky method leads to more monodisperse and bigger nanoparticles - ~5 nm. Polydisperse particles, later, can be fractionated through a sucrose gradient of 20-50% sucrose and cleaned extensively to eliminate all remaining sucrose from the nanoparticles. By doing that, it is possible to acquire monodispersed nanoparticle populations of ~2 nm and ~3 nm. Moreover, a new technique produces more monodisperse particles in which the as-synthesized OT nanoparticles are subject to ligand exchange by MUS. The amount of MUS and the reaction time are adjusted in order to acquire the aimed ligand ratio on the surface and the desired diameter of the nanoparticles²⁶⁰.

Practically, obtaining MUS:OT protected Au nanoparticles poses some challenges. First, the charged ligand (MUS) and the hydrophobic ligand (OT) are immiscible. Therefore, the solubility of the nanoparticles and ligands always needs to be taken into account both in any synthesis and characterization process. Moreover, the purity of the MUS ligand molecules utilized, *e.g.* the content of inorganic salts, has been shown to largely affect the quality, reproducibility, as well as colloidal stability of the nanoparticles²⁶¹.

In appendix A, we outline the detailed synthesis and characterization of one of the most widely used amphiphilic nanoparticles, *i.e.* 11-mercaptoundecane-1-sulfonic acid (MUS) and 1-octanethiol (OT) protected gold nanoparticles. A protocol for the synthesis of the negatively charged MUS ligand is reported to ensure the purity and thus the reproducibility of the nanoparticle synthesis. Then, the procedure to generate these nanoparticles based on common one-phase and Stucky synthesis followed by thorough purification work-ups is reported in detail. Various necessary characterization techniques²⁶², *i.e.* transmission electron microscopy (TEM), ultra violet-visible spectroscopy (UV-vis), thermogravimetric analysis (TGA), and nuclear magnetic resonance (NMR) have been combined to obtain a robust and complete characterization of all the parameters necessary to define nanoparticles.

3 Design Parameters on Nanoparticle-Liposome Interactions

This chapter covers the interaction between nanoparticles and liposomes as a function of nanoparticle core size, ligand types and their relative ratios and the liposome size. The nanoparticle-liposomes systems were imaged using cryo-EM and some of the systems were investigated through tomograms.

3.1 Introduction

Amphiphilic MUS:OT gold nanoparticles have been shown to traverse the cell membranes through an energy-independent path, similarly to cell penetrating peptides. This behavior was attributed to structure of the ligands adopt on the surface of the particle, forming linear stripe-like domains that alternate hydrophilic and hydrophobic domains at the molecular scale. Although it is known that the surface ligands and the size of nanoparticles affected cellular uptake of the nanoparticles, there was paucity of information to elucidate the mechanism of entry. Therefore, liposomes have been used as a model system computationally, and experimentally to investigate the insertion mechanism of nanoparticles. For the liposomes, zwitterionic DOPC lipids which are the main constituents of the cell membrane were used.

The computer simulations showed that the driving force for membrane insertion was the hydrophobic force, based on solvent accessible surface area of the ligand coating. Different size and surface coating of nanoparticles contributed to this energy to overcome energy penalties on the way to insertion. In other words, there were favored sizes respective to specific ligand ratios for membrane insertion. Experimentally, however, nanoparticles were labelled with BODIPY dyes and any fluorescence signal on the membrane of giant vesicles under CLSM was considered as membrane insertion. Furthermore, cryo-EM was used to acquire images of liposomes. Cryo-EM is a good characterization technique for liposomes because it allows imaging the liposomes in their solvated state, using a low electron dose that does not damage them. To demonstrate that nanoparticles are in the liposome bilayer, a

single image does not suffice: tilting the sample or tomograms are necessary to ensure a nanoparticle is in the bilayer and not simply overlaying within its confines in a 2D image.

This chapter of the thesis establishes a deep understanding on nanoparticle-membrane interaction as a function of nanoparticle and liposome properties. Therefore, we formed a matrix of conditions in which nanoparticles of different sizes and surface coatings were incubated with different liposomes of different dimensions. To characterize these systems, we used a better establishment of cryo-EM by acquiring stereopair images and tomograms of subject liposome systems (a more detailed description of the cryo-EM technique is provided in Appendix C). We observed 5 different nanoparticle-liposome systems to be further used in biological functions in which nanoparticles exhibited membrane protein-mimetic features.

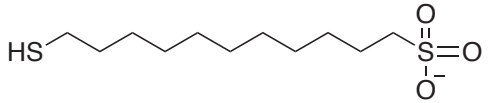
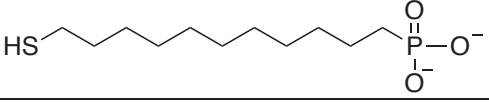
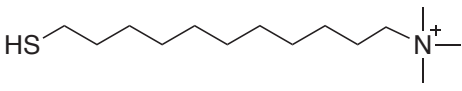
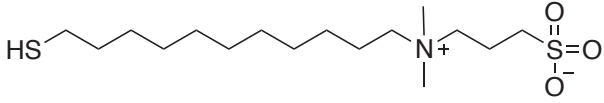
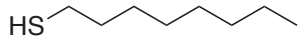
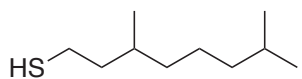
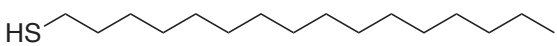
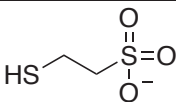
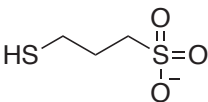
3.2 Materials and Methods

Nanoparticles

Prior to any experiments with liposomes, the gold nanoparticles with various surface chemistries (Table 3-1) were synthesized and characterized to determine the size of the nanoparticles and the ligand ratio on their surfaces. MUS:OT gold nanoparticles were synthesized following two methods: one-phase and modification on the Stucky^{258,259} method. The synthesis of MUS:OT gold nanoparticles and characterization in detail can be found in Appendix A. To achieve specific average core size and narrow polydispersity for the gold nanoparticles with different ligand ratios, nanoparticle batches were fractionated. Approximately 30 mg of nanoparticle formed 10 mg/ml solution in MilliQ® water (Millipore, MA) which was fractionated using a sucrose gradient between 20-50%. Fractionated nanoparticles were used after removing the sucrose by centrifuging the sample several times (~11 times) with MilliQ® water using Amicon filters, 30 KDa. (VWR, PA).

PEG nanoparticles were synthesized also following the 1-phase method in which the PEG₄ (Iris biotech) is used to coat the surface of the gold particles. TMA, MUP, and ZW ionic nanoparticles were synthesized by Paulo Jacob Silva²⁶¹. Nanoparticles were kept as stocks of 4 mg/ml solutions in MilliQ® water at room temperature, unless otherwise stated.

Table 3-1 Chemical structures of thiolated ligands coating the surfaces of the nanoparticles.

Ligand Names	Ligand Structures
11-mercaptoundecane-1-sulfonic acid (MUS)	
11-mercaptoundecane-1-phosphonic acid (MUP)	
N,N,N-trimethyl-10-undecenylammonium chloride (TMA)	
3-[(11-mercapto-undecyl)-N,N-dimethyl-amino]-propane-1-sulfonate (ZW)	
1-Octanethiol (OT)	
3,7 dimethyloctane 1-thiol (br-OT)	
1-Hexadecanethiol (HDT)	
2-mercaptoethanesulfonic acid (MES)	
3-mercapto-1-propanesulfonic acid (MPSA)	

Liposomes

The most abundant lipid in the cell membrane, 1,2-dioleoyl-*sn*-glycero-3-phosphocholine (DOPC, Avanti Lipids) was used as a model membrane in our studies. Prior to liposome formation, 80 μ l of lipid chloroform solution was dried in glass vials inside a desiccator overnight. 200 μ l of MilliQ® water was added to hydrate the lipid and the solution was vortexed and sonicated in a bath sonicator until no visible lipid films remained. Small liposomes (diameter 60 nm by DLS) were formed using a probe sonicator which was operated at 40% and 60% amplitudes for 30 s intervals for a total of 3 min. To obtain larger liposomes (> 100 nm) took place via extrusion of the hydrated lipid solution with 200 nm carbon filters (Whatman, UK) in mini extruder (Avanti lipids, AL) 21 times. At the end of two methods, liposomes had the concentration of 4 mg/ml (5 mM). Liposomes were kept in a 4 °C fridge and used one week after preparation. For cryo imaging ~2.5 mM of vesicles were incubated

with a final concentration of 0.28 mg/ml or 1.4 mg/ml nanoparticles presented in Table 3-2 at a final volume of 30 μ l at room temperature overnight, without any agitation.

Cryo-EM microscopy

Grids for cryo-EM and tomograms were prepared in a commercial vitrification system (Vitrobot Mark IV, FEI, Netherlands) with 100% humidity at 22 °C. 4 μ l of sample was pipetted on the lacey carbon grid (300 mesh, Electron Microscopy Science, Hatfield, PA) which was glow discharged for 3 seconds beforehand. Prior to plunge freezing excess sample was blotted under a blotting force of -15 for 2 seconds. After plunge freezing the grids were transferred at -178 °C into a Gatan 626 cryo-holder (Gatan inc. Warrendale, PA) and imaged in a FEI Tecnai F20 microscope (FEI) operated at 200kV. The total electron dose for one image was ~ 30 e/ \AA^2 and it was acquired using magnification of 50000X or 62000X (pixel size 0.2 nm and 0.16 nm respectively) with defocus values of -0.8 to -2.4 μ m. For stereopair images, tilting angles of $\pm 10^\circ$, $\pm 15^\circ$, $\pm 20^\circ$, or $\pm 30^\circ$ were used. Images were recorded by Eagle (2048 x 2048 pixels, FEI) and BM-Ceta camera (4096 x 4096 pixels, FEI).

Tomogram was aligned and reconstructed from a tilt series which were mostly acquired between $\pm 60^\circ$ with 2 degree increments. Total electron dose for the tomogram ranged from 30 to 100 e/ \AA^2 and they were acquired using magnification 2900X (0.32 nm) and 50000X (pixel size 0.2 nm) with the defocus value ranging between -3 to -5 μ m. Images for tomograms were recorded using a FalconIII camera (4096 x 4096 pixels, FEI), unless otherwise specified. Alignments of the images and reconstructions of the tomograms were done using 3DInspect (FEI).

3.3 Results

Various nanoparticles were synthesized and characterized to be incubated with liposomes. To have a systematic approach, MUS:OT nanoparticles were chosen carefully to form a matrix with similar average core diameter and ligand ratios. By doing so, we were able to compare the effect of size, ligand ratio on the surface, ligand length, surface structure, surface charge,

and sulfonate groups on the interaction with liposomes. The nanoparticles used in this thesis are presented in Table 3-2.

Table 3-2 List of nanoparticles that were used in the experiments and their representative core diameters in nm. a) Interacting nanoparticles, nanoparticles have surface coverage with sulfonate terminated ligands, b) non-interacting nanoparticles.

a	All MUS	10% OT	20% OT	30% OT	50% OT	MPSA	MES	30% br-OT	20% HDT
1	2.3 ± 0.7	1.7 ± 0.5	2 ± 0.9	2.1 ± 1		1.8 ± 0.5	1.8 ± 0.6		
2				2.4 ± 1.9					2.6 ± 1.3
3		3.1 ± 0.5	3.3 ± 1.1	2.7 ± 1.3	2.9 ± 1.2				
4	5.7 ± 0.9	5.1 ± 1.5		5 ± 0.8				4.6 ± 1	

b	TMA	PEG	ZW	MUP
1				
2			2.9 ± 0.9	
3	3.9 ± 1.6			3.7 ± 1.3
4		4.2 ± 1.7		

Interaction between liposomes and nanoparticles were evaluated through cryo-EM images. Since cryo-EM images provide a 2D projection of the samples, more detail was obtained by acquiring images at angles different from 0°. These image pairs were called stereopair images, and made it possible to track locations of features specific to the sample, *e.g.* areas with different contrast, shape. To better visualize the samples, tomograms were acquired under many different angles (mostly more than 60 different angles). The construction of a tomogram provided a better visualization of the system thanks to the overlaying of these images that generated a 3D reconstruction of the samples.

Although it was shown that MUS:OT nanoparticles directly interacted with the membrane in less than one minute, the samples were incubated overnight to be able to compare more stable systems. First, we observed the necessity of sulfonate groups on the nanoparticle surface for a patterned interaction. Figure 3-1 depicts the liposomes incubated with different kinds of nanoparticles. All-MUS nanoparticles enabled the formation of liposome aggregates, whereas cationic TMA particles disrupted the liposomes. Meanwhile, the zwitterionic ZW particles and neutral PEG particles did not show any attraction towards liposomes.

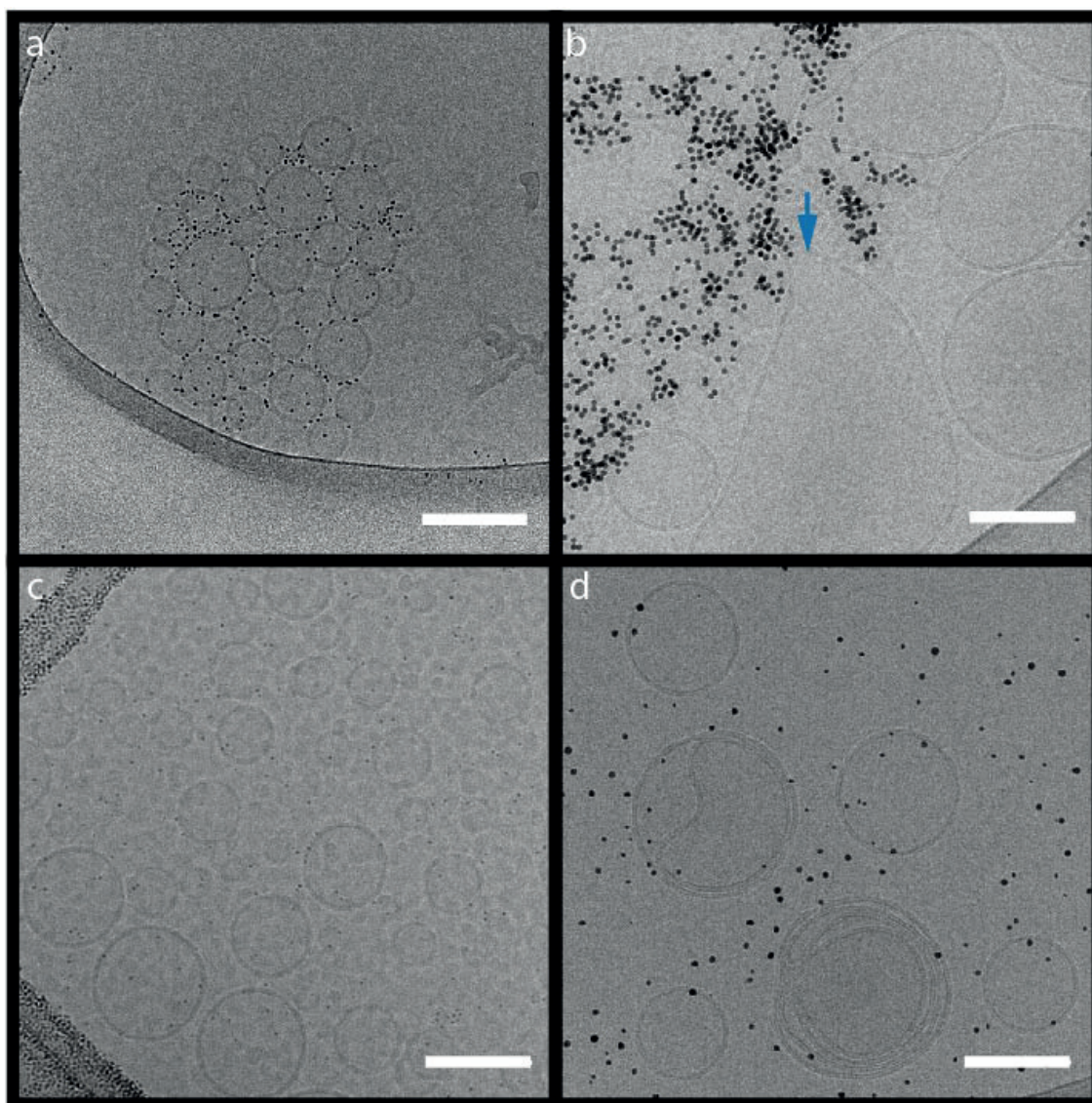


Figure 3-1 DOPC liposomes incubated with nanoparticles coated with different ligand molecules. a) All MUS particles aggregate the liposomes, b) TMA nanoparticles distort the liposomes: in the middle of the image an elongated and open vesicle can be observed (indicated with blue arrow), c) ZW nanoparticles do not interact with liposomes, they are attached on the grid and dispersed throughout the ice, d) PEG particles also depict no interactions. Scale bars are 100 nm.

Moreover, All-MUS nanoparticles were compared with another anionic nanoparticle to determine if these systems were surface charge or chemistry driven. To this end, MUP particles were chosen for comparison and stereopair images were acquired. Figure 3-2 depicts that MUP particles did not show any distinctive pattern, even though some particles could be seen adsorbed onto the liposomes.

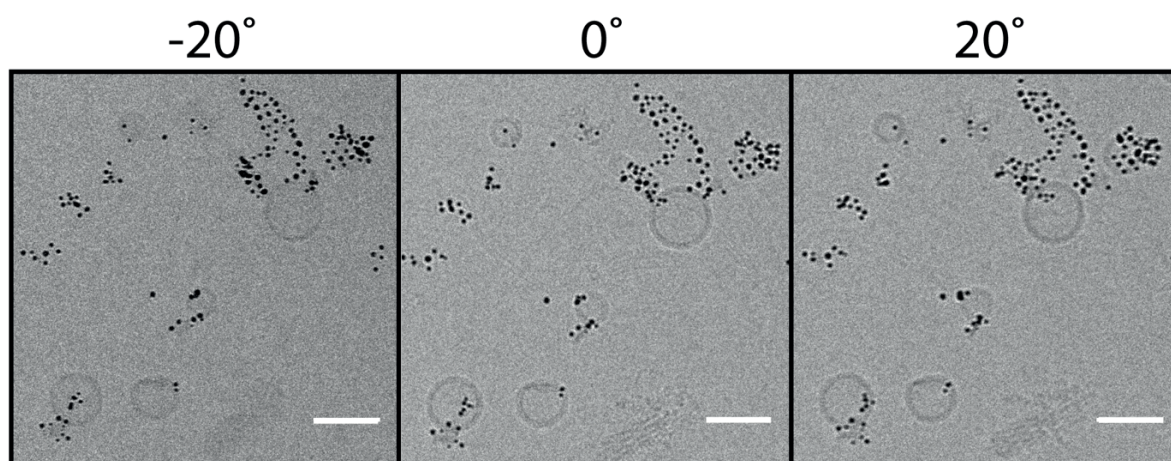


Figure 3-2 Stereopair images of MUP particles incubated with DOPC liposomes. Scale bars are 50 nm.

Furthermore, we systematically increased the hydrophobic content of MUS:OT nanoparticles with different average core sizes and we observed different hybrid liposome-nanoparticle systems. This research expanded the scope of previously reported studies on the MUS:OT nanoparticles with liposomes^{160,245} and provided a more established explanation. We categorized the nanoparticle-liposome interactions into 5 different systems: individual attachment, vesicle aggregation, close packed arrangements, bilayer insertion, and ring formation. Some of these systems were observed within every group of sulfonate-terminated nanoparticles; some of the interactions were specific to or had tendencies to be observed with a certain class of nanoparticles at the nanoparticle concentration of 0.28 mg/ml.

3.3.1 Individual attachment

Liposomes that had nanoparticles adsorbed on the surface without attracting another liposome were classified as ‘individual attachment’. This system consisted of one or many nanoparticles and one liposome in which the nanoparticles interacted solely with this liposome (Figure 3-3). Regardless of the size or surface properties of the interacting nanoparticles (sulfonate terminated nanoparticles), individual attachments of nanoparticles were observed in every liposome interacting nanoparticle combinations at the nanoparticles concentration of 0.28 mg/ml. Therefore, this system was not specific to any nanoparticle or liposome type.

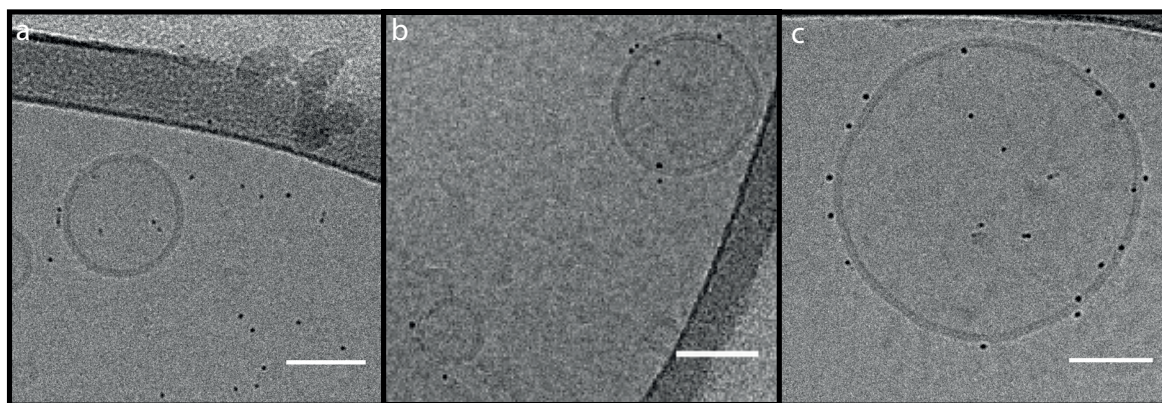


Figure 3-3 Individual attachments of nanoparticles on the liposomes. a) MUS:OT 20%OT (2 ± 0.9 nm) nanoparticles, b, c) All-MUS (2.3 ± 1.3 nm) nanoparticles. Scale bars are 50 nm.

Having single images of liposomes was not sufficient to evaluate the whole system, thus a tomogram was acquired. Figure 3-4 depicts the interaction of MUS:OT 10%OT nanoparticles with DOPC liposomes and the blue arrows point to nanoparticle-induced curvature on the membrane.

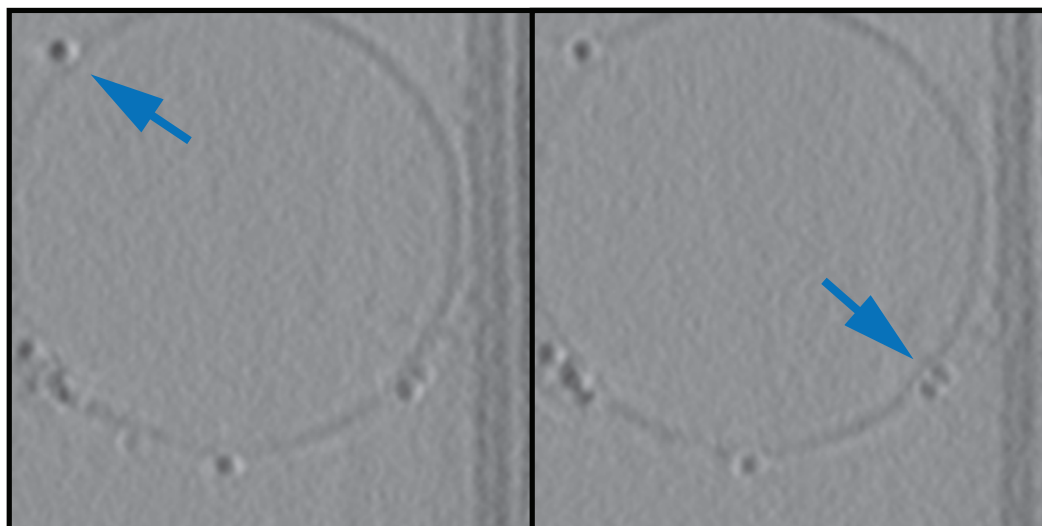


Figure 3-4 Frames from constructed tomograms liposomes with MUS:OT 20%OT (2.8 ± 1.4 nm) particles showing individual attachments of nanoparticles on the bilayer. Blue arrows indicate the membrane curving towards liposome interior as a result of nanoparticle adsorption. The size of the big liposome is approximately 150 nm.

3.3.2 Vesicle aggregation

Another liposome-nanoparticle system was ‘vesicle aggregates’ in which nanoparticles were observed to bridge the liposomes and form a multi-liposomal system (Figure 3-5). Stereopair images provided the relative locations of liposomes and nanoparticles. For instance, yellow circles mark the nanoparticles that were individually attached to the surface, whereas blue arrows point to the nanoparticles in between adjacent liposomes. Due to tilting, these two nanoparticles overlapped in the image of -20° then, appeared as two separate particles at 0° and 20° .

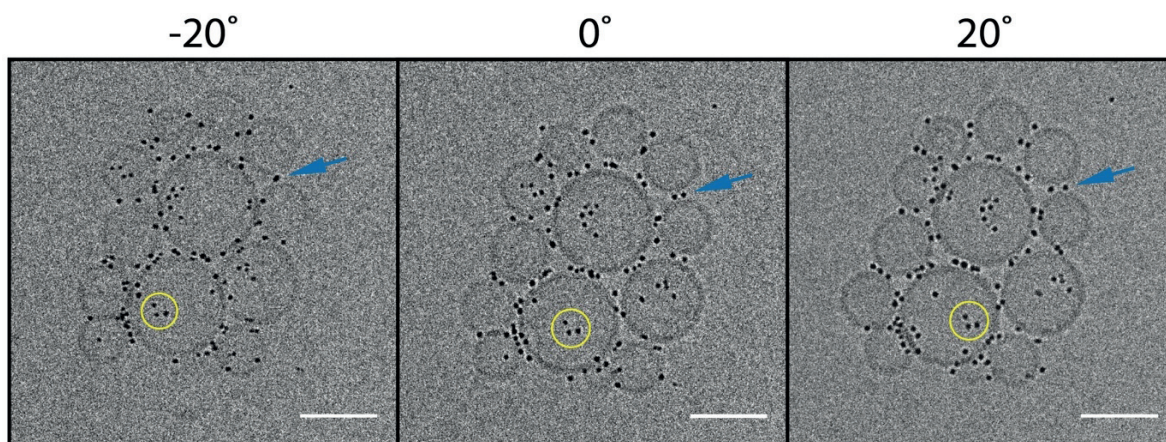


Figure 3-5 All MUS (2.7 ± 1.3 nm) particles forming vesicle aggregates with multiple vesicles. Scale bars are 50 nm.

Similar to individual attachment systems, vesicle aggregates were observed within every interacting sulfonate terminated nanoparticle-liposome systems at the nanoparticle concentration of 0.28 mg/ml. The size of these aggregates differed depending on how many liposomes connected through the nanoparticles. Still, there were no correlations between the size of aggregates and the type of nanoparticle. Mostly, aggregate systems consisting of more than 5 liposomes were observed, even though some cases included only two liposomes bridged by nanoparticles. For instance, Figure 3-6 depicts a two-liposome system in which multiple nanoparticles stayed between two vesicles, just like during hemifusion.

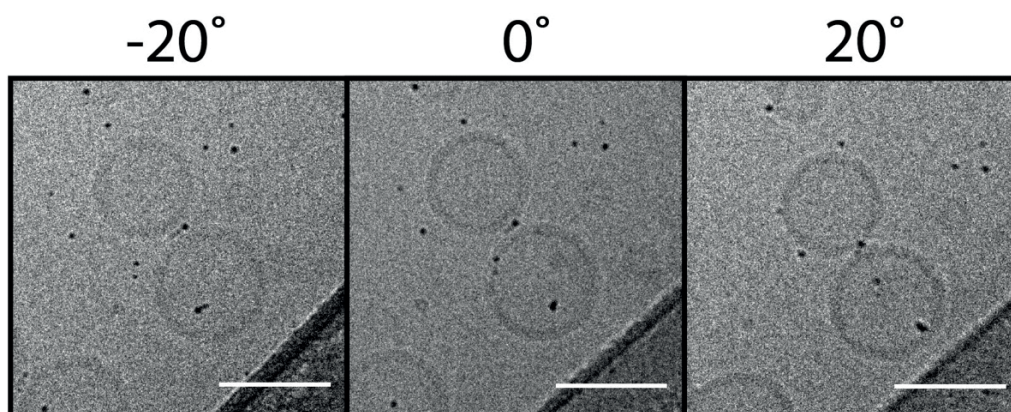


Figure 3-6 MUS:OT 20%OT, (2 ± 0.9 nm) nanoparticles bridging two vesicles. Scale bars are 50 nm.

To determine if the vesicle aggregates actually represented hemifusion, focused images of liposomes were required, because hemifusion necessitates that the outer leaflets of two adjacent liposomes merge. In Figure 3-7, the zero tilt image is a good representation of in focus image in which the hydrophobic and hydrophilic parts of the bilayer were distinguishable. In Figure 3-7, however, every bilayer occupied with nanoparticles did not show any mixing of lipid bilayers or subsequent distortion on the membrane.

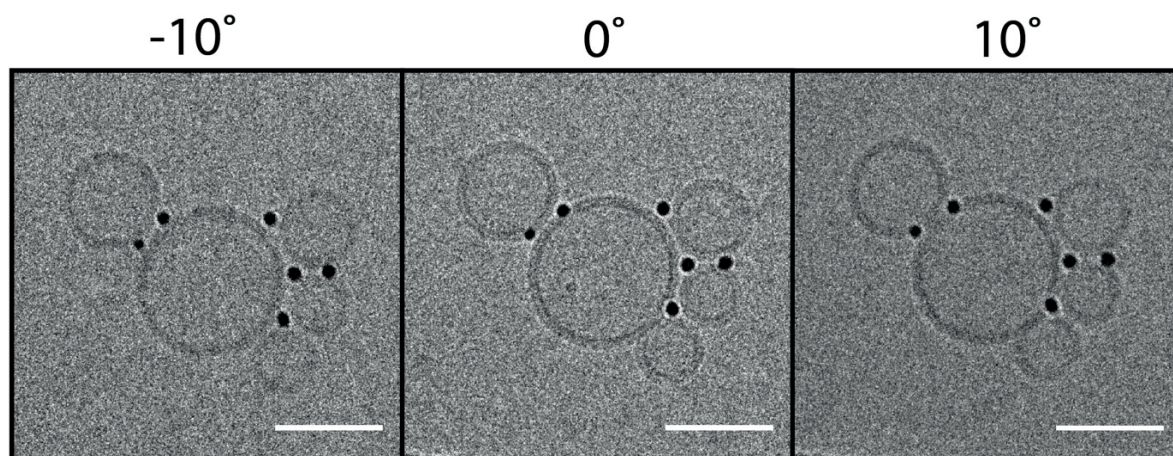


Figure 3-7 MUS:OT 10%OT (5.1 ± 1.5 nm) nanoparticles forming vesicle aggregates. Scale bars are 50 nm.

3.3.3 Close packed arrangements

Sulfonate terminated nanoparticles exhibited an ordered arrangement in between or on the vesicles, predominantly when they were incubated with larger vesicles (> 100 nm). These formations were classified as 'close packed arrangements'. Figure 3-8 shows the comparison

of effect of liposome sizes incubated with the same nanoparticles on nanoparticle-liposome hybrid systems. MUS:OT 10%OT nanoparticles formed vesicle aggregates with small liposomes, whereas larger liposomes lead to close packed arrangements. Still, since the close packed arrangements also bridged the liposomes, they could also be considered as a subcategory of vesicle aggregates: the close packed arrangements were studied separately. These close packed arrangements dictated modifications on the shape of liposomes. As shown in Figure 3-12a, the assembly of nanoparticles could flatten the liposome surface and even induced a convex shape on the liposomes.

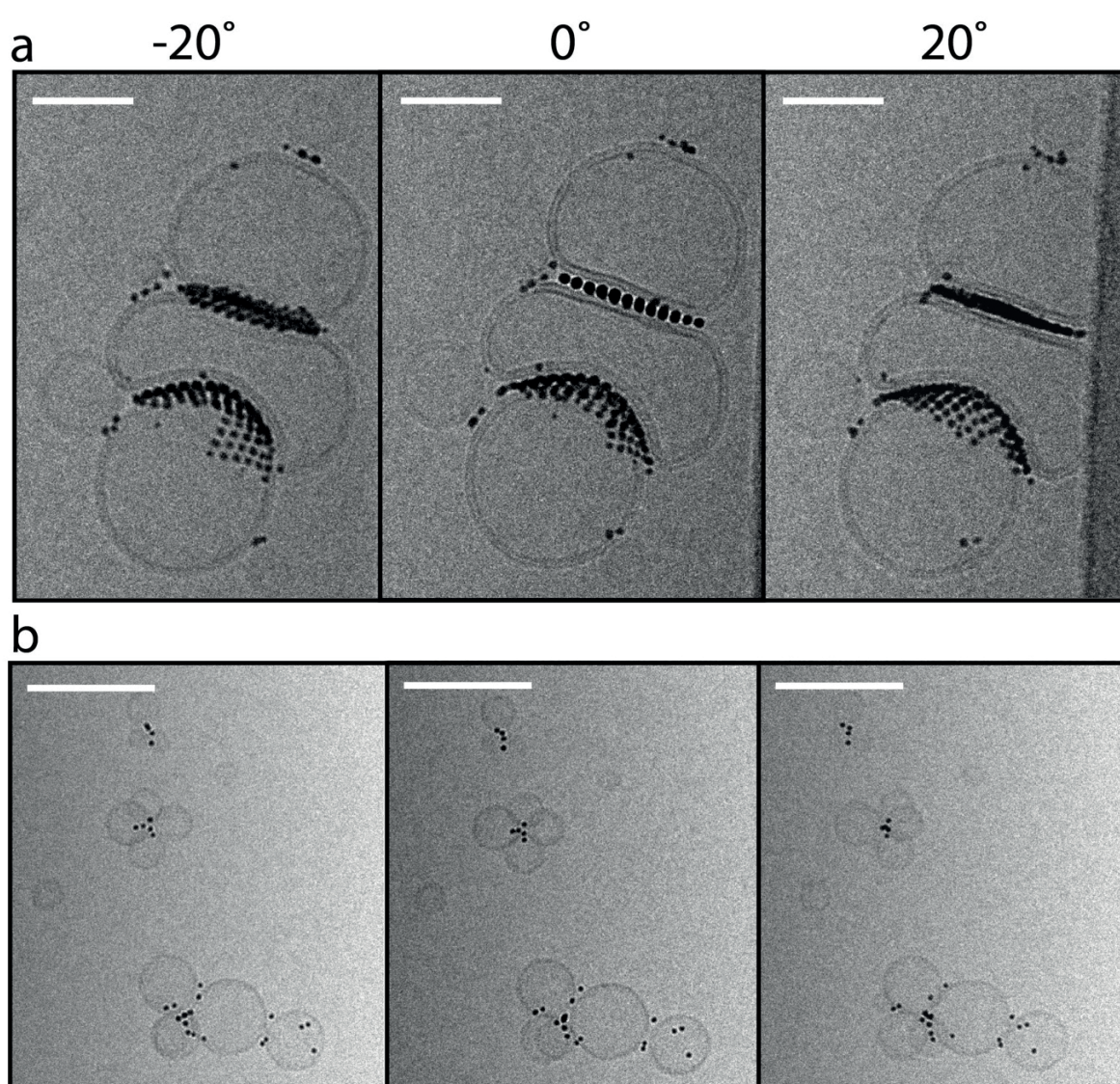


Figure 3-8 a) Fractionated MUS:OT 10%OT (3.1 ± 0.5 nm) nanoparticles incubated with large liposomes (> 100 nm), b) small liposomes (~60 nm). Scale bars are 100 nm.

We also checked the effect of nanoparticle size on the formation of this ordered arrangement. Figure 3-9 depicts large liposomes incubated with MUS:OT 10%OT (1.7 ± 0.5 nm) nanoparticles and close packed arrangements were still observed. Some particles, however, seemed to attach randomly on the surface. Even in these cases the distortions on the shape of the liposomes also were observed.

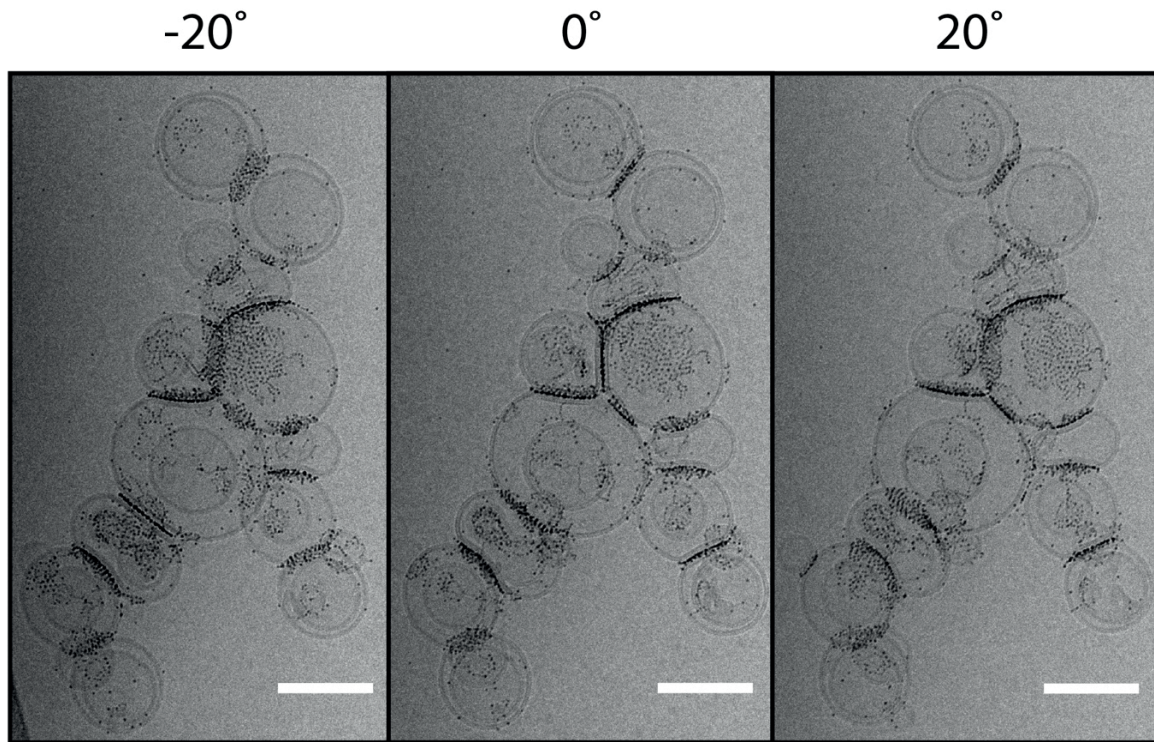


Figure 3-9 Fractionated MUS:OT 10%OT (1.7 ± 0.5 nm) nanoparticles incubated with liposomes > 100 nm. Scale bars are 100 nm.

We also verified if this behavior was driven by monodispersity, because, so far the MUS:OT 10%OT nanoparticles we used were fractionated and quite monodisperse with a standard deviation of 0.5 nm. To this end we incubated the large liposomes with the non-fractionated mother batch of MUS:OT 10%OT nanoparticles and we still observed close packed arrangements of nanoparticles (Figure 3-10).

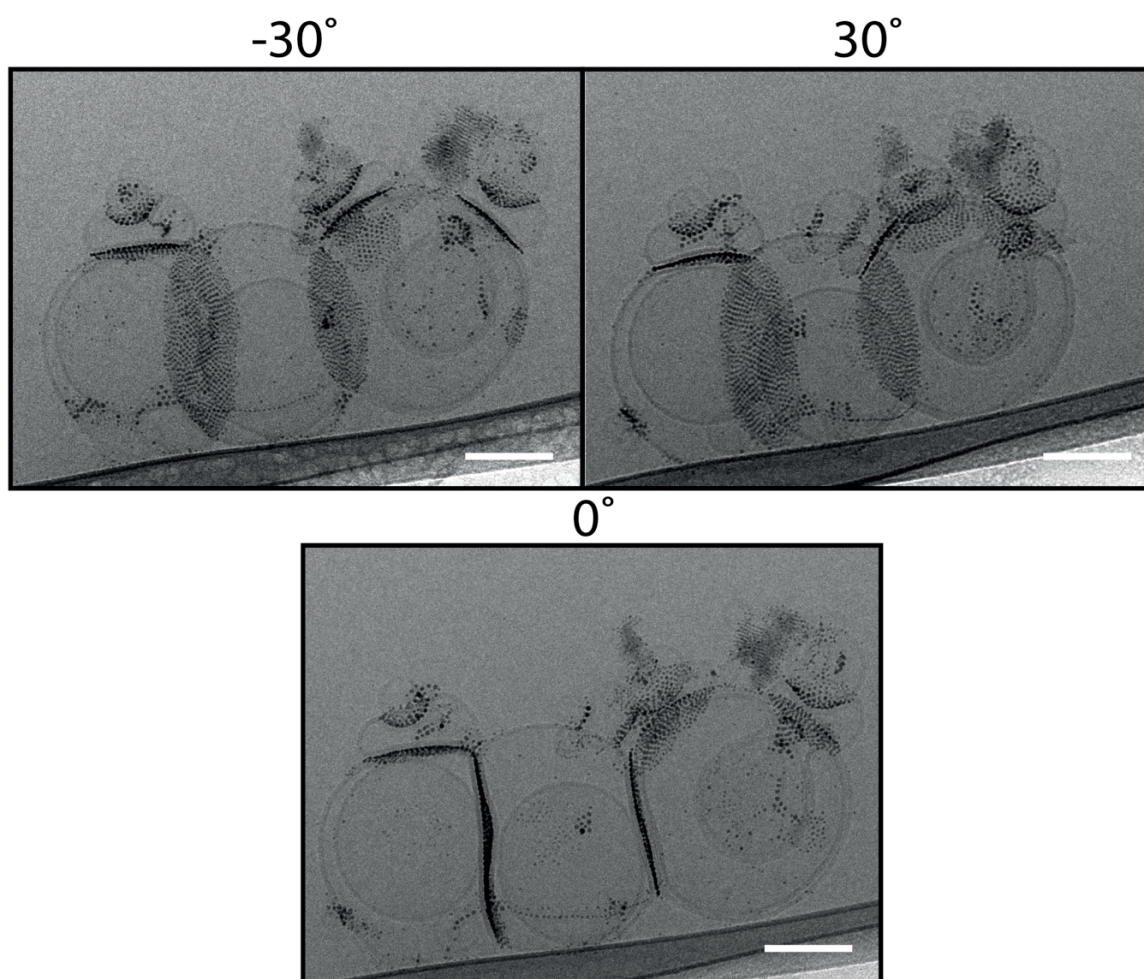


Figure 3-10 Non fractionated MUS:OT 10%OT (2.8 ± 1.4 nm) nanoparticles incubated with large liposomes larger than 100 nm. Scale bars are 100 nm.

To rule out the effect of surface chemistry on the aggregate formation, All-MUS particles were incubated with large liposomes (Figure 3-11). Although All-MUS particles induced change in the shape of vesicles, the nanoparticles, did not arrange themselves in close packed order. This phenomenon revealed that the shape change in the liposomes did not depend on the ordered arrangements of nanoparticles, but on high local concentrations of nanoparticles.

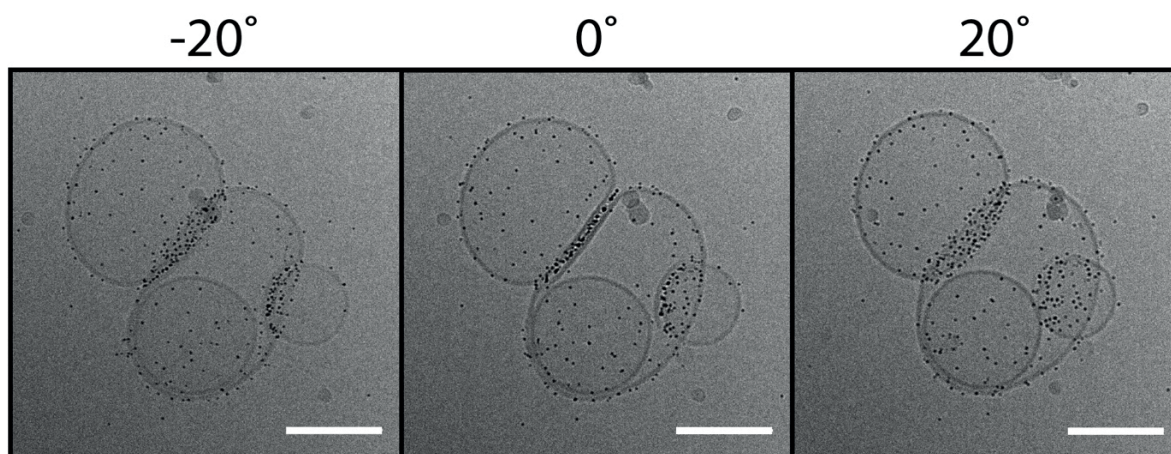


Figure 3-11 All-MUS (2.3 ± 0.7 nm) nanoparticles incubated with large liposomes > 100 nm. Scale bars are 100 nm.

In contrast to All-MUS particles, nanoparticles with shorter sulfonated ligands lead to the formation of close packed arrangement (Figure 3-12a,b). When we compared the interparticle distances of nanoparticles with similar sizes in the close packed arrangements, MPSA particles showed a slightly higher value (3.76 ± 0.2 nm) than MES particles (3.53 ± 0.3 nm), whereas MUS:OT (6.12 ± 0.5 nm) showed a value two-fold higher. Given these values and considering the theory for hydrophobic ligands and bilayer, we speculate that sulfonated ligands existed on the lateral plane instead of completely attaching to the bilayer surface.

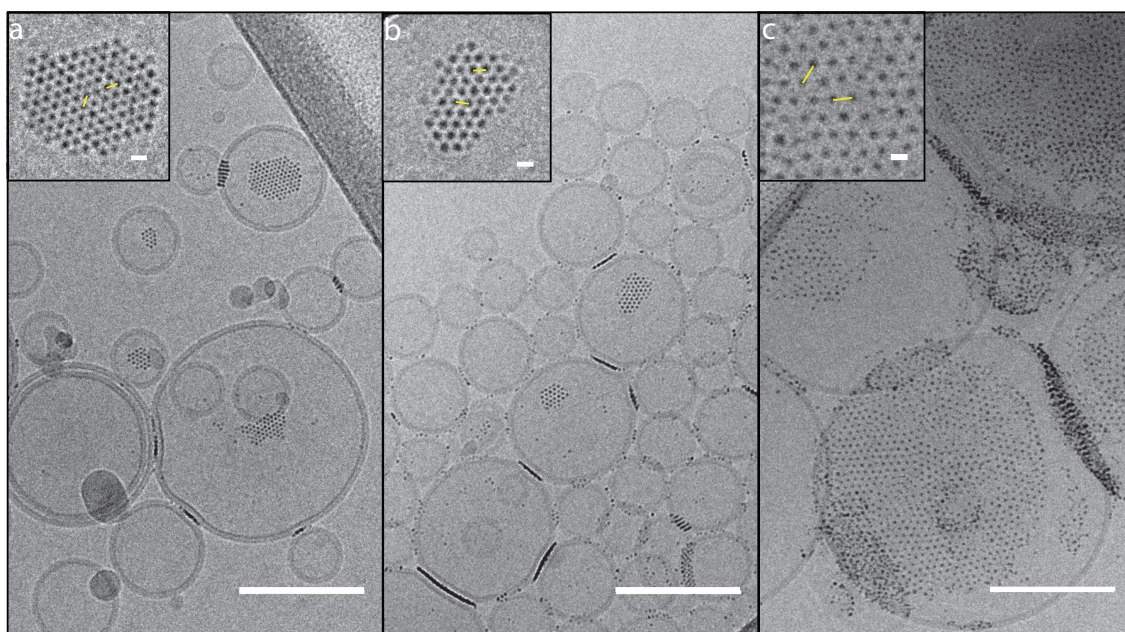


Figure 3-12 a) MES (1.8 ± 0.6 nm) particles, b) MPSA (1.8 ± 0.5 nm) particles, c) MUS:OT 10%OT (1.7 ± 0.5 nm) particles with DOPC liposomes. All of the particles exhibited close packed arrangements. Scale bars are 100 nm.

3.3.4 Bilayer insertion

As computationally and experimentally shown before by multiple groups, MUS:OT nanoparticles were able to penetrate into the bilayers. The systems in which we observed nanoparticles penetrated in the bilayer and span the bilayer were called 'bilayer insertion'. Neither a single image, nor stereopairs would exhibit the bilayer insertion directly, which is why we acquired tomograms to investigate 'bilayer insertion' in detail.

Since the membrane insertion of nanoparticles were shown to be driven by hydrophobicity, water soluble nanoparticles with the highest hydrophobic content were chosen to investigate this phenomenon. Nanoparticles with less hydrophobicity were also favored for membrane insertion depending on the core diameter, but still with a lower probability of providing a good sample for a tomogram. Figure 3-13 depicts a frame from a tomogram reconstruction of DOPC liposomes with MUS:OT 30%OT nanoparticles. The red arrow indicates the nanoparticle in a bilayer that changed its packing in the vicinity of the nanoparticle to adapt.

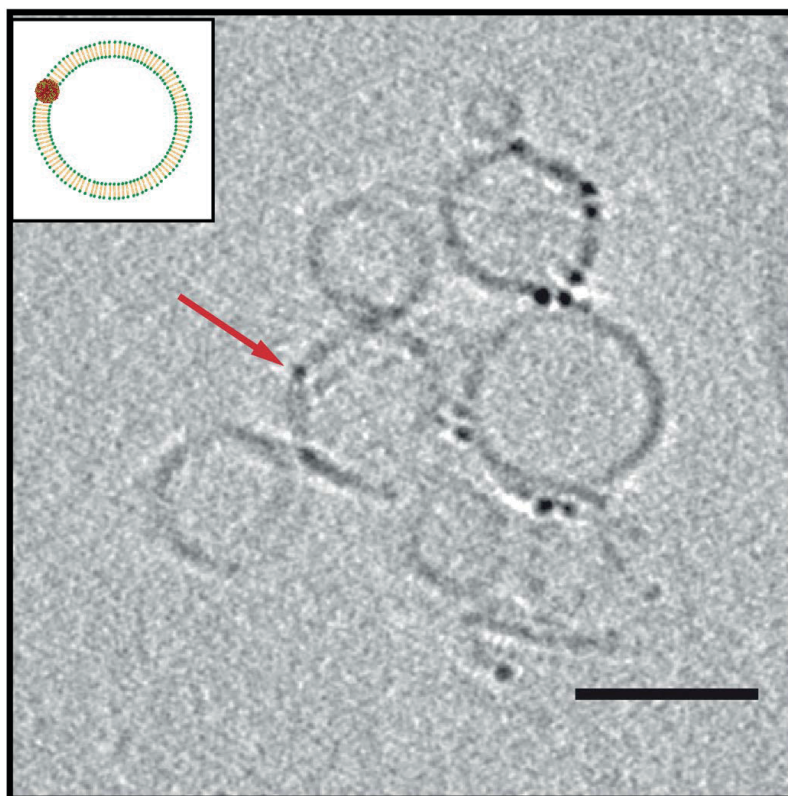


Figure 3-13 A frame from constructed tomogram showing nanoparticle, MUS:OT 30%OT (2.4 ± 1.9 nm), in the bilayer. Scale bar is 100 nm.

Van Lehn *et al.*¹⁶⁰ calculated the diameter of MUS:OT 34%OT nanoparticles that could penetrate into the bilayer spontaneously to $\sim 6,5$ nm. Therefore, we could observe the membrane insertion of bigger MUS:OT 30%OT particles in which multiple nanoparticles align in the bilayer together (Figure 3-14). This sample contains nanoparticles at the concentration of 1,4 mg/ml.

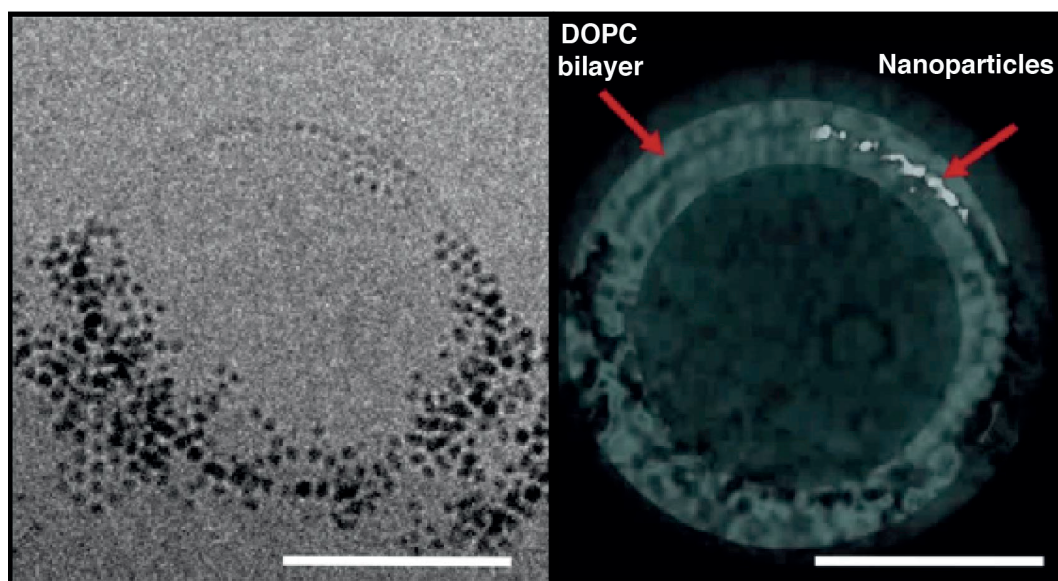


Figure 3-14 A frame from aligned file of tomogram acquisition and the 3D construction of the tomogram with Chimera. The 3D reconstruction was done by Dr. Davide Demurtas. They both show the nanoparticles, MUS:OT 30%OT (5 ± 0.8 nm) embedded in the membrane of a large liposome. Scale bars are 100 nm.

3.3.5 Ring formation

Another liposome-nanoparticle hybrid system was called 'ring formation' in which the nanoparticles aligned in the form of rings on the liposomes. This system is further elucidated in Chapter 5.

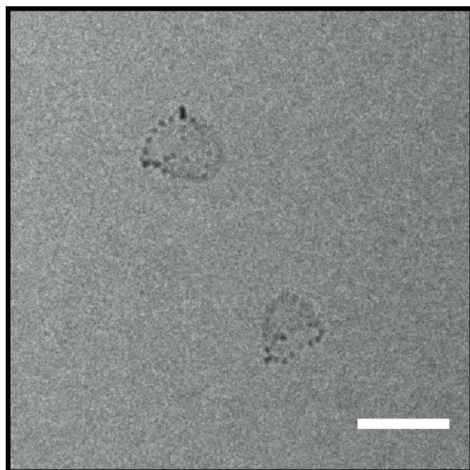


Figure 3-15 MUS:OT 30%OT (2.1 ± 1 nm) particles forming ring patterns with small liposomes. Scale bar is 50 nm.

3.4 Discussion

As shown in the theoretical studies, the nanoparticles first approached the membrane through electrostatic attraction. Then, the bilayer insertion behavior of nanoparticles was driven by hydrophobic forces based on the hydrophobic solvent accessible surface area. Thus, if this hydrophobic driving force of the nanoparticles was not high enough to overcome energy penalties, we believe that nanoparticles might attach to the surface but not penetrate in the bilayer completely.

Moreover, the bilayer insertion mechanism had two energy barriers: lipid protrusion and flipping of sulfonated ligand to other side of the bilayer. Given that, the latter was defined as having low probability by Salassi *et al.*²⁶³, we believe that individually attached nanoparticles could be frozen in this stage of bilayer insertion and remain partially inserted, just like Figure 3-3 and 3-4. Energetically, the interplay between adhesive energy of nanoparticle and the bending energy of DOPC membrane can result in the formation of local curvatures on the

membrane. This curvature strikingly resembles the bending of the bilayer during the non-specific endocytic uptake of nanoparticles, which is mentioned in Chapter 2.

Based on the simulations, one can say that the electrostatic interaction between nanoparticle and bilayers made the formation of vesicle aggregates possible. It is, however, probable for ligands to segregate on the surface after partially inserting into one liposomes through hydrophobic contact and attach electrostatically to another liposome. Nanoparticles, also can make hydrophobic contacts with two adjacent bilayers and expose the charged ligands in the aqueous phase in between. Regardless of the interaction mechanism, DOPC liposomes exhibit a slight negative charge overall, even though the DOPC lipids are zwitterionic. Thus, to obtain a stable system made of multiple liposomes bearing negative overall charge should be challenging due to electrostatic repulsion. Therefore, we think that the adsorption of nanoparticles on the membrane should be energetically higher than electrostatic repulsion. Given all, we hypothesize that this behavior of nanoparticles strikingly resembles that of adhesion proteins on the cellular membrane, such as tight junctions.

Once a nanoparticle interacted with bilayer (through insertion or individual attachments), it was shown to induce disengagement to the vicinity on the bilayer. Therefore, multiple nanoparticles (*e.g.* tens of nanoparticles) could align in close packed patterns. Given the simulations demonstrated that the bilayer inserted nanoparticles did not favor the formation of 2D alignments in the bilayer, we believe that close packed arrangement of nanoparticles did not take place within the bilayer. Consequently, cryo-EM images indicated the bilayer without any nanoparticles embedded in it (Figure 3-8a).

Moreover it is possible that the elasticity of the liposomes could be correlated to the fluid-phase of lipid molecules with two double bonds. The interplay between the adhesion force of nanoparticles and membrane elasticity could allow these liposomes to be stabilized into these shapes without bursting. This bending behavior of nanoparticles showed striking resemblance to the curvature inducing membrane proteins. For instance, nanoparticles aligned on the surface of the liposomes and formed a scaffold that bends the liposomes, just like BAR domain proteins.

During bilayer insertion of nanoparticles, simulations counted the bilayer mismatch in the vicinity of particles as an energy penalty. Based on the frame from tomogram of nanoparticles insertion in Figure 3-13, we claim that MUS:OT 30%OT nanoparticles induced packing constraints similar to cell membrane proteins on the cellular membrane. Additionally, combination of bilayer insertion and having the vesicle aggregated could be considered similar to a pre-fusion state in which the liposomes were brought in close proximity by nanoparticles just like fusion proteins.

Once we increased the concentration of MUS:OT 30%OT nanoparticles 5-fold, we observed multiple nanoparticles inserted into the bilayer together (Figure 3-14). The simulations showed nanoparticles accumulated together in the bilayer to reduce the overall energy of the system due to the defects induced by nanoparticle insertion. In fact, cell membrane proteins, which have a thickness mismatch with the membrane, also aggregate in the bilayer to reduce the packing constraints of the system. In this case, one should also consider the high concentrations of nanoparticles relative to the liposomes which could ease the bilayer insertion.

Table 3-3 lists the summary of small liposome-nanoparticle interactions based on the evaluation of approximately 27 cryo-EM images per sample. In the table 'not checked' stands for the nanoparticle-liposome combinations which were not imaged, 'no' and 'yes' indicate the interactions that were not observed, or vice versa. In terms of nanoparticles, individual attachment of nanoparticles and vesicle aggregations were observed with every type of interacting sulfonate terminated nanoparticles. Bilayer insertion, however, were observed for nanoparticles with high hydrophobic content, whereas ring formation occurred only with small nanoparticles having high hydrophobic content. Close packed arrangements of nanoparticles, however, were almost always observed with larger liposomes (> 100 nm).

Statistically, more than 50% of the systems imaged were vesicle aggregations. Considering each vesicle aggregate consisted of more than 5 liposomes in average, more than 80% of interacting liposomes in the system formed vesicle aggregates. For bilayer insertion, a total of 37 tomograms were acquired with 5 different nanoparticles and two of them showed the bilayer insertions. Unlike biological samples, nanoparticle-liposome systems demonstrated

various types of formations. Since tomograms gave the best results with crowded and homogeneous samples, this feature of the nanoparticle-liposome hybrid system was not the most convenient for tomogram acquisition. Therefore, we can still claim that other MUS:OT 30%OT particles penetrate into the bilayer regardless of lack of tomographic proof. Statistics of ring formations will be discussed further in Chapter 5.

Table 3-3 The summary of different liposome-nanoparticle hybrid systems observed with various sulfonated interacting nanoparticle types with small liposomes.

Nanoparticles	Size (nm)	Individual attachment	Vesicle aggregation	Bilayer insertion	Ring formation	Close packed arrangement	Bare liposomes
All-MUS	2.3 ± 0.7	#13	#36	Not checked	No	No	#44
	5.7 ± 0.9	#14	#67	Not checked	No	Not checked	#43
MUS:OT 10%OT	1.7 ± 0.5	#54	#103	No	No	Yes	#12
	3.1 ± 0.5	#46	#61			Yes	#82
	5.1 ± 1.5	#20	#38			Yes	#41
MUS:OT 20%OT	2 ± 0.9	#93	#23	Not checked	No	Not checked	#181
	3.3 ± 1.1	#36	#116				#199
MUS:OT 30%OT	2.1 ± 1	#64	#5	Not checked	#181	No	#165
	2.4 ± 1.9	#10	#63	#1	#19	Not Checked	#0
	5 ± 0.8	#14	#48	No	No	Yes	#108
MUS:HDT 20%HDT	2.6 ± 1.3	#37	#21	Not checked	#18	Not checked	#338

Table 3-4 depicts the statistics of close packed arrangements, separately. Nanoparticle-large liposome systems demonstrated the formation of close packed arrangements, but it was still possible to see individual attachments of nanoparticles within these samples. Close packed arrangements and curvature inducing behavior of nanoparticles were counted separately, because these formations could also be observed independently. Vesicle aggregates similar to small liposomes were counted as 'other'. Similar to small liposomes, approximately 80% of the interacting large liposomes participated in vesicle aggregations. Formations of close packed arrangements or curvature inducing behavior were observed in the range from 28% (All-MUS) to 95% (MUS:OT 10%OT).

Table 3-4 The summary of different liposome-nanoparticle hybrid systems observed with various sulfonated interacting nanoparticle types with large liposomes.

Nanoparticles	Size (nm)	Individual attachment	Vesicle aggregation			Bilayer insertion	Ring formations	Bare Liposomes	
			Close packed arrangements	Curvature inducing behavior	Other				
All-MUS	2.3 ± 0.7	#10	#14			Not checked	No	#5	
			No	#4	#10				
MUS:OT 10%OT	1.7 ± 0.5	#9	#69			No	No	No	
			#48	#49	#3				
	3.1 ± 0.5	#10	#76				No	No	#1
			#46	#47	#5				
MUS:OT 30%OT	2.1 ± 1	#4	#4			Not checked	#18	#68	
			No	#10	No				
	2.7 ± 1.3	#36	#18			Not checked	#7	#2	
			#5	#10	#3				
	5 ± 0.8	#2	#13			#1	No	#2	
			#12	#11	#1				
MUS:br-OT	4.6 ± 1	#8	#18			Not checked	No	No	
			#4	#9	#7				
MES	1.8 ± 0.5	#48	#85			Not checked	No	#250	
			#73	#62	#12				
MPSA	1.8 ± 0.6	#58	#63			Not checked	No	#64	
			#32	#32	#18				

3.5 Conclusions

To conclude, we hypothesize that various nanoparticle-liposome systems can form depending on the size and surface coating of nanoparticles and liposome size. Our findings showed that cationic nanoparticles disrupted the liposomes, whereas zwitterionic and neutral nanoparticles did not show any particular interaction. Negatively charged nanoparticles interacted with liposomes in which MUP particles formed individual attachments, while MUS particles lead to formation of more complex nanoparticle-liposome hybrids. To increase the amphiphilicity of the MUS nanoparticles, hydrophobic ligands were introduced and the effect of ligand ratio on the liposome interaction was checked.

The sulfonate terminated amphiphilic nanoparticles regardless of size and ligand ratio on the surface formed individual attachments and vesicle aggregations with small liposomes. Nanoparticles forming vesicle aggregations behaved similar to cell adhesion proteins, such as tight junctions. With larger liposomes, however, same nanoparticles formed close packed

arrangements and acted as curvature inducing membrane proteins, such as BAR domains. On the other hand, nanoparticles with the highest hydrophobic content (*i.e.* the upper limit for the water solubility) induced formation of other systems, as well. For instance, regardless of size, MUS:OT 30%OT particles inserted in the bilayer, similar to the transmembrane proteins and cell penetrating peptides. Additionally, the smallest particles with highest hydrophobic contents (*e.g.* OT and HDT) aligned themselves in a ring pattern in the bilayer of the liposomes which could be irrelevant to the membrane proteins. Lastly, MUS:OT 30%OT (~3 nm) nanoparticles combined both bilayer insertion and vesicle aggregations. This collective behavior resembles to fusion proteins (*e.g.* SNARE) which brings the vesicles in close proximity prior to fusion event.

This resemblance between nanoparticles and membrane proteins is a consequence of the amphiphilic nature of these nanoparticles, as well as the sulfonate terminated groups on the surface. This resemblance lead further use of these nanoparticles as synthetic analogues of membrane proteins in certain applications like fusion which is investigated in Chapter 4. Further images of the nanoparticle liposome systems are shown in the Appendix B.

4 Nanoparticle Mediated Vesicle Fusion

In this chapter, based on the systematic study on nanoparticle-liposome systems presented in Chapter 3, fusogenic behavior of amphiphilic nanoparticles (*e.g.* MUS:OT 30%OT, ~3 nm) is being presented. A fast fusion process similar to synaptic cleft fusion upon Ca^{2+} addition was mediated by nanoparticles. A content mixing assay was used to quantitatively characterize the fusion process and this assay showed that MUS:OT 30%OT particles facilitated the fusion process. Based on the content mixing assay, effects of different types of nanoparticles, *e.g.* ZW, All-MUS particles, different concentrations of Ca^{2+} on fusion event were compared. Then, cryo-EM was used to quantitatively analyze the sizes of the liposomes in each step of the fusion process. Highest average of liposome sizes was observed with liposomes incubated with nanoparticles upon Ca^{2+} addition. Tomograms of the liposomes with nanoparticles after Ca^{2+} were acquired and showed the nanoparticles embedded in the bilayer. This study has been recently submitted to a peer reviewed journal.

4.1 Introduction

Vesicle fusion plays a key role in fundamental cellular functions including reproduction, cargo transport, and hormone secretion⁴¹. Fusion process consists of multiple intermediate states and energy barriers to be overcome^{264,265}. First of all, It is necessary for membranes to be in close proximity which is not energetically favored due to repulsive forces between lipid head groups²⁶⁶. Then, the outer leaflets of the membranes have to initiate a contact and form a stalk-like formation between two membranes^{267,268}. This contact either evolves in a hemifusion state, in which the inner leaflets still stay unmixed, or leads directly to fusion following the expansion of the stalk formation^{264,269}.

In biological systems, a specific class of proteins, called fusion proteins, mediate and facilitate fusion events through different pathways²⁸. Synaptic cleft fusions take place between two neurons in which neurotransmitters are released from fused vesicles for signaling purposes. This type of fusion happens rapidly, and therefore, it is mediated by certain fusion proteins

called SNAREs and an action potential - Ca^{2+} trigger²⁷⁰. SNARE proteins are placed in opposing areas of the cell membrane and the neurotransmitter vesicle. Each SNARE proteins has 2 helical bundles. These helical bundles interlock complementarily between opposite proteins, in order to keep the membranes to be fused in a close proximity. Then, within the membranes connected via the SNARE complex, perturbation of the lipids leading to a stalk formation starts. When calcium ions are introduced to this complex, the stalk rapidly expands and turns into a fusion pore through which the neurotransmitters are released²⁷¹. Although the outline of this synaptic fusion process is understood well, no consensus has been made to explain how SNAREs behave in each step and how Ca^{2+} ions trigger the formation of the fusion pore on a molecular basis. Despite any such uncertainties however, it is accepted that SNARE proteins mediate fusion events even when integrated into synthetic liposomes²⁷¹.

To be able to assess the fusogenic behavior of proteins and other fusogens, various fluorescence assays can be carried out: (i) labeling the lipids with FRET (Förster energy transfer) couples^{272,273}, (ii) trapping hydrophobic self-quenching dyes between lipids⁴⁴, and (iii) content mixing assays. In lipid mixing assays including (i) and (ii), the lipid mixing occurs starting from the first hydrophobic contact between membranes, leading to a fluorescence change of the system^{271,274,275}. However, despite, and because of their simplicity, these assays are not sufficient to distinguish between inner and outer layer lipid mixing, hemifusion and fusion. It is nevertheless possible to refine them further, for example via introduction of a quencher on outer leaflets. In this way any fluorescence change can be attributed solely to a fusion event⁵².

Content mixing assays have been also commonly used to monitor the fusion process. In this assay type, liposomes are loaded with particular chemicals and upon fusion the contents of the liposomes mix, leading a product with a different fluorescence response than the initial contents²⁷⁶. The most widespread content mixing assay is based on terbium (Tb)-dipicolinic acid (DPA) coupling in which the Tb-DPA complex results in a fluorescence that is 100 fold higher than Tb itself^{277,278}. In this assay Tb and DPA are separately encapsulated into the liposomes through a process rather cumbersome, because of the low efficiency of passive loading, long time necessary and complicated cleaning of the loaded liposomes from free molecules. It is, however, possible to improve the efficiency of such an assay by using only

one type of loaded liposomes, combined with empty ones. These assays employ self-quenching fluorophores loaded in the liposomes at high concentration. Upon fusion with empty liposomes, the fluorophores are diluted and fluoresce anew²⁷⁹. Content mixing assays with self-quenching dyes are more convenient in terms of load efficiency and practicality.

The role of MUS:OT nanoparticles in mediation of fusion events has been demonstrated before. Previous computational and experimental studies have shown that MUS:OT nanoparticles penetrate into the bilayer and settle there, just like a membrane protein^{7,172}. Moreover, presented within this thesis, sulfonate terminated amphiphilic nanoparticles formed various nanoparticle-liposome hybrid systems in which they behave similar to certain membrane proteins. Independently from the core size and surface coating, all of the sulfonate terminated amphiphilic nanoparticles formed vesicle aggregations with small liposomes. Nanoparticles acted similar to cell adhesion proteins (*i.e.* tight junctions) in vesicle aggregates. With larger liposomes they formed close packed arrangements in which they showed similarities to curvature inducing proteins. Particles having the highest hydrophobic content that is required to maintain the water solubility, however lead to different system formations, such as bilayer insertion. Combining bilayer insertion behavior of nanoparticles with their ability to bring other liposomes in close proximity just like SNARE proteins, we wanted to investigate the fusogenic properties of MUS:OT 30%OT (~3 nm) particles, and their subsequent utility as synthetic fusogens.

4.2 Materials and Methods

Nanoparticles

Nanoparticles were synthesized similar to Chapter 3. For the experimental work this chapter nanoparticles of MUS:OT 30% fra (2.4 ± 1.9 nm), MUS:OT 30% frb (2.6 ± 1.1 nm), All-MUS (2.3 ± 0.7 nm), ZW (2.9 ± 0.9 nm) were used.

Liposomes

80 μ l of 10mg/ml of 1,2-dioleoyl-*sn*-glycero-3-phosphocholine (DOPC) solution in chloroform was dried in desiccator All DOPC vesicles were prepared by extrusion of 5 mM lipid solution in MilliQ® with 200 nm, 100 nm, 50 nm, and 30 nm filters, successively. For cryo imaging 2.5

mM of vesicles were incubated with a final concentration of 0.1 mg/ml nanoparticles of MUS:OT 30%OT, (2.6 ± 1.1 nm) at final volume of 30 μ l at room temperature for 1 hour without any agitation. To initiate fusion, CaCl_2 solution were added from a concentrated 100 mM solution to final 2 mM concentration. Cryo samples of systems containing CaCl_2 were prepared directly after (less than 1 min) addition of CaCl_2 .

Cryo-EM imaging

Samples for cryo-EM were prepared and cryo-EM imaging conducted similar to Chapter 3.

Content mixing assay

For content mixing assay 200 μ l of 50 mM Sulphorhodamine B (SRB) (Sigma Aldrich) in 2.5 mM Tris was added to dried lipid film and sonicated at 50 °C for 2 hours. Then the lipid mixture passed through extrusion (Avanti lipids) with 200 nm filters (Whatman) 31 times. Following the extrusion free ligands were cleaned by size exclusion chromatography using 3 preppacked columns (Zeba spin filter, 7kD). Prior to using the columns, the columns were washed with 2.5 mM Tris and 50 mM NaCl buffer 3 times. Liposomes without free ligands were kept in the 4 °C fridge. To conduct content mixing assay SRB loaded and empty liposomes were mixed with 1:1 ratio and nanoparticles were incubated following cryo conditions for 1 hour. Calcium was introduced to the samples slowly having the final concentration of 2 mM and 1 mM. The fluorescent measurements were done on the samples 40 times diluted to avoid saturation. The spectrofluorometer (Jasco FP-6500) was operated at 300 V with excitation wavelength of 562 nm and emission of 578 to 700 nm. The bandwidths for both were 3 nm.

GUV fluorescence imaging

The fluorescence experiments between GUVs and SRB loaded SUVs were conducted by Berta Tinao in Universidad Computense Madrid under supervision of Dr. Laura Rodriguez Arriaga.

Simulations

Coarse-grained molecular dynamics simulations of nanoparticle mediated fusion process were conducted by Mukarram A. Tahir in Massachusetts Institute of Technology under supervision of Prof. Alfredo Alexander-Katz. In the simulations MUS:OT 50% OT nanoparticles

(Figure 4-1) of 2 nm core diameter and all DOPC planar bilayers and liposomes with a 20 nm diameter were used.

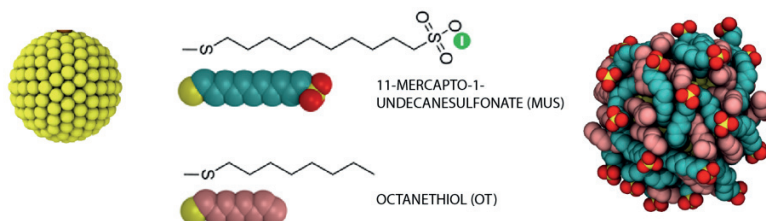


Figure 4-1 The representation of the nanoparticles in the coarse-grained molecular dynamics.

4.3 Results and Discussion

4.3.1 Simulations

Simulations of nanoparticle mediated fusion were performed based on two main systems; planar bilayers and vesicles. It was in general observed that without any stimuli, such as the addition of nanoparticles, the liposomes stayed tethered within the scope of the simulation's time scale, which was up to a few microseconds. On the contrary, the addition of amphiphilic MUS:OT nanoparticles led to rapid stalk formation between the bilayers, and eventual observation of fusion. Stalk formation was attributed to a lowering of the energy barrier by the nanoparticles, through electrostatic attraction between the nanoparticle ligands and the charged lipid headgroups, as well as increase of solvent accessible surface area mediated by the nanoparticles' amphiphilic nature.

Planar bilayers were initially chosen as a model system, in order to eliminate any curvature effects. The simulations were performed on two planar bilayers with a distance of 1 nm. No interaction between the intact bilayers was observed. One MUS:OT 50%OT nanoparticle was then embedded in one of the simulated bilayers (Figure 4-2a). As shown previously, this distance was sufficient for protein free liposomes to start a stalk formation²⁸⁰. Despite the lack of curvature, the MUS:OT 50%OT nanoparticle was still able to promote a formation of a lipid protrusion from the adjacent membrane (Figure 4-2b), and consequently a lipid exchange between the outer leaflets of the membranes started. At the end of the simulation, the formation of a stalk between the two membranes was observed, in which the nanoparticle displaced the neighboring charged head groups of the lipid molecules from the

hydrophobic parts of the bilayer, replacing them with its own hydrophobic ligands (OT molecules) (Figure 4-2c). The high speed of stalk formation (~ 450 ns) demonstrated the possible fusogenic behavior of MUS:OT nanoparticles.

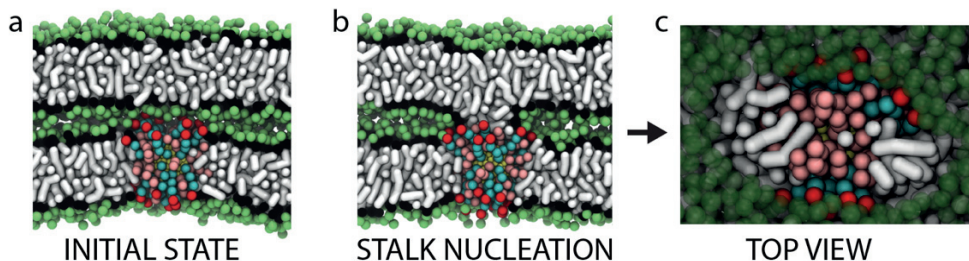


Figure 4-2 Snapshots from the simulations of planar bilayers. a) Initial state of the bilayers in which one MUS:OT 50%OT nanoparticle was embedded into one bilayer, b) Stalk nucleation upon the lipid extraction from adjacent bilayer towards the nanoparticle, c) Top view of the stalk formation.

A more biologically relevant system was further simulated, consisting of two 20 nm DOPC liposomes spaced 2 nm apart. The system was simulated with and without the presence of MUS:OT nanoparticles. Without the nanoparticles, no attraction between liposomes was observed, as in the previous case. Once an MUS:OT 50% OT nanoparticle was embedded in the bilayer, after approximately 500 ns, nanoparticle-mediated fusion stalk formation commenced, and was completed after approximately 800 ns (Figure 4-3). The formation of the fusion stalk was mediated by the electrostatic attraction between the exposed charged groups of the nanoparticle (MUS, sulfonate group) and the lipid head groups of opposing liposomes, as well as the amphiphilic character of the nanoparticle (and resulting solvent accessible surface area). During the first step of stalk formation, electrostatic interactions between the nanoparticle and the lipids allowed the liposomes to retain their initial closeness, lowering the relevant energy barrier which was also associated with the repulsive hydration forces. Furthermore, during the second step, the amphiphilic nature of the nanoparticle further decreased the energy barrier for a lipid molecule extraction from an adjacent bilayer. This molecule would participate in the first hydrophobic contact, eventually leading to stalk formation.

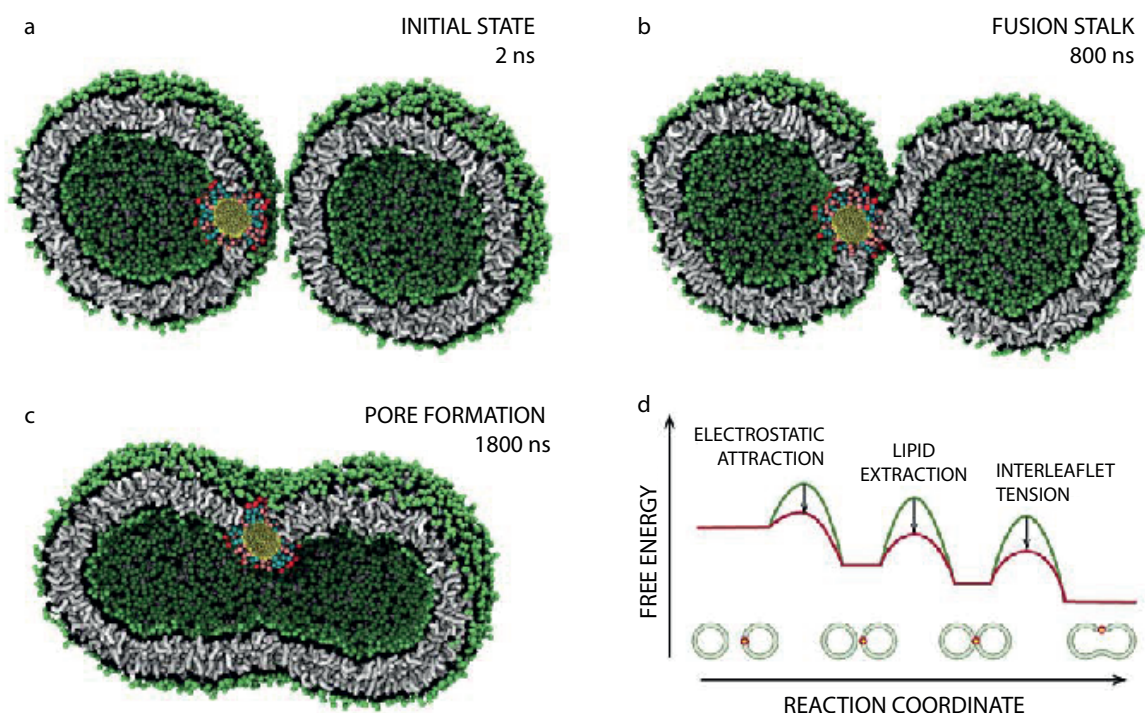


Figure 4-3 Snapshots from the simulations of the fusion process that was mediated by MUS:OT 50%OT nanoparticles. a) The initial state in which the nanoparticle was embedded into the membrane of one of the liposome, b) The opposing liposome came together and by lipid protrusion nanoparticles facilitated the stalk formation in which two liposomes exchange lipids and stay destabilized, c) Upon addition of Ca^{2+} (in simulations, Ca^{2+} was induced by a membrane asymmetry due removal of lipids from the outer leaflets) pore formation occurred, d) The reaction coordinate of overall fusion process, indicating the intermediate states and associated energy barriers of the process.

As demonstrated in the literature⁴⁵, the final stage of nanoparticle-mediated liposome fusion is described by pore formation (Figure 1-7). For the further development of the stalk into a pore, a contact of the inner leaflets was needed²⁸¹. However, contrary to SNARE proteins⁴⁹, configurational restrictions of the nanoparticles in the bilayer prevented any contact between the inner leaflets. In this case, expansion of the fusion stalk prior to pore formation required an external stimulus.

To overcome this hurdle, the effect of ions to the system was studied. Calcium ions were introduced to the surrounding medium, leading to condensation of the outer leaflet's area-per-lipid, resulting in a membrane asymmetry. This asymmetry applied a tension on the inner leaflet, allowing contact formation between the inner leaflets, which ultimately led to expansion of the stalk into a fusion pore (Figure 4-4).

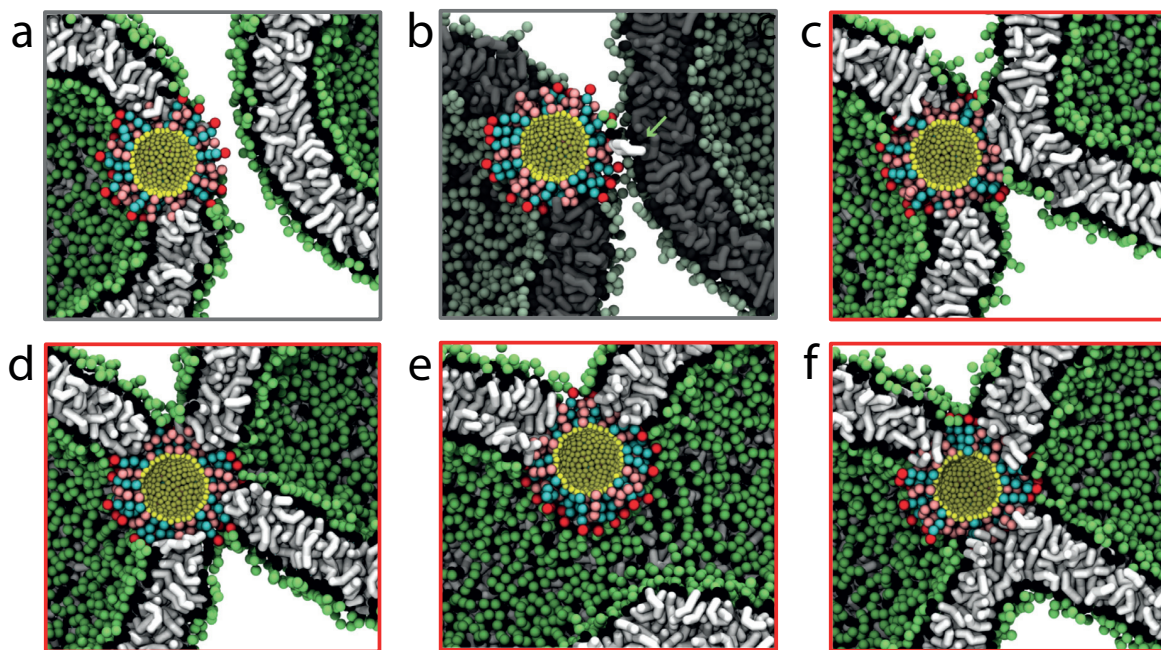


Figure 4-4 Snapshots from simulations pointing the transition states during stalk and pore formation. a, b) Stalk formations have an energy barrier due to lipid extraction from the adjacent membrane. Here, after the lipid extraction (pointed with green arrow) formation of the stalk was initiated. c, d, e, f) For the pore formation the energy barrier was associated with the inner leaflet contact. Upon inducing Ca^{2+} based membrane asymmetry to the system stalk expands and the pore forms.

Moreover, two additional simulations with different initial stages were performed, to evaluate the effect of the initial stage of the system to the fusion process. First, a system consisting of two separate liposomes and a non-embedded MUS:OT 50% OT nanoparticle was considered (Figure 4-5a). In this case, the nanoparticle first penetrated into the bilayer (Figure 4-5b) and then the system proceeded to the formation of a stalk between the liposomes. Secondly, a system of a MUS:OT 50%OT nanoparticle already bridging two liposomes was simulated (Figure 4-5c). As this system had already overcome the first energy barrier, liposome fusion was completed upon Ca^{2+} triggering.

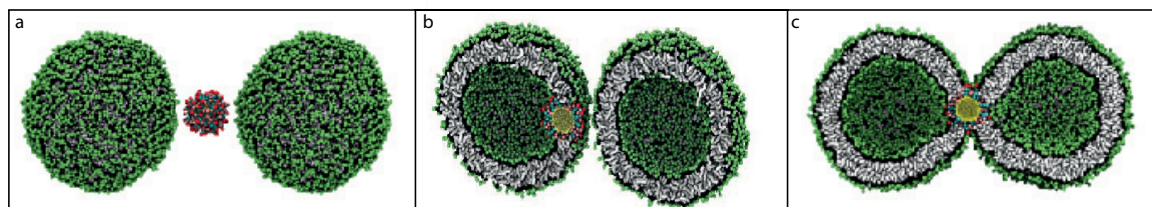


Figure 4-5 Snapshots from the simulations illustrating different initial states of fusion process. a) Two liposomes with a nanoparticle free in the solution, b) The nanoparticles is embedded within one of the liposome's membrane, c) The nanoparticle is fused within the membranes of both liposomes.

4.3.2 Cryo-EM studies

So far, the computational studies have explained the role of nanoparticles in the mechanism of nanoparticle-mediated fusion process, but have left the effect of liposome size unexplored. Cryo-electron microscopy has previously been used to determine the size distribution of liposomes²⁸². It was, therefore, selected as a suitable technique for the investigation of the fusion process as a function of liposome size, through liposome size histograms construction. In order to form reliable histograms, extremely monodisperse liposomes were produced via extrusion, in which 4 different filters (with 200, 100, 50, and 30 nm pore sizes) were used to downscale the size of liposomes. Liposomes without nanoparticle addition, and liposomes incubated with MUS:OT 30%OT nanoparticles, before and after Ca^{2+} addition were imaged. Upon addition of the Ca^{2+} , the samples for cryo-EM were prepared in less than 1 min. In general the amount of the liposomes on the grid with Ca^{2+} was strikingly higher than the liposomes without Ca^{2+} . This could be explained by the fact that glow discharging of the grids made the carbon surface negatively charged and electrostatically attractive to systems with Ca^{2+} .

Before Ca^{2+} addition liposomes were only found far apart from each other, despite the high concentration of lipids in the samples (2.5 mM) (Figure 4-6a). Incubation of the liposomes with nanoparticles was found to lead to liposome complexation, where the nanoparticles were bridging the liposomes (Figure 4-6c). These complexes mostly consisted of more than two liposomes, with nanoparticles bridging two liposomes at a time. Addition of Ca^{2+} to these complexes led to an immense increase in the size of the liposomes. Supporting the argument of nanoparticle mediated liposome fusion, at least one nanoparticle was always present at contact points between the big liposomes (Figure 4-6d).

Based on the constructed histogram of the liposomes, the highest amount of large liposome population corresponded to nanoparticle incubated liposomes, after Ca^{2+} addition (Figure 4-6). Due to cryo-EM's limitation on ice thickness that was sufficient to provide a visibility on the liposomes, liposomes with a diameter higher than 500 nm were excluded from the histograms. This boundary was set in order to avoid imaging artefacts, since the larger liposomes were squeezed within the vitrified ice, leading to a false diameter. Formation of

large liposomes was observed after Ca^{2+} addition to bare liposomes as well, the amount was not significant when compared to the case of nanoparticle-mediated liposome fusion.

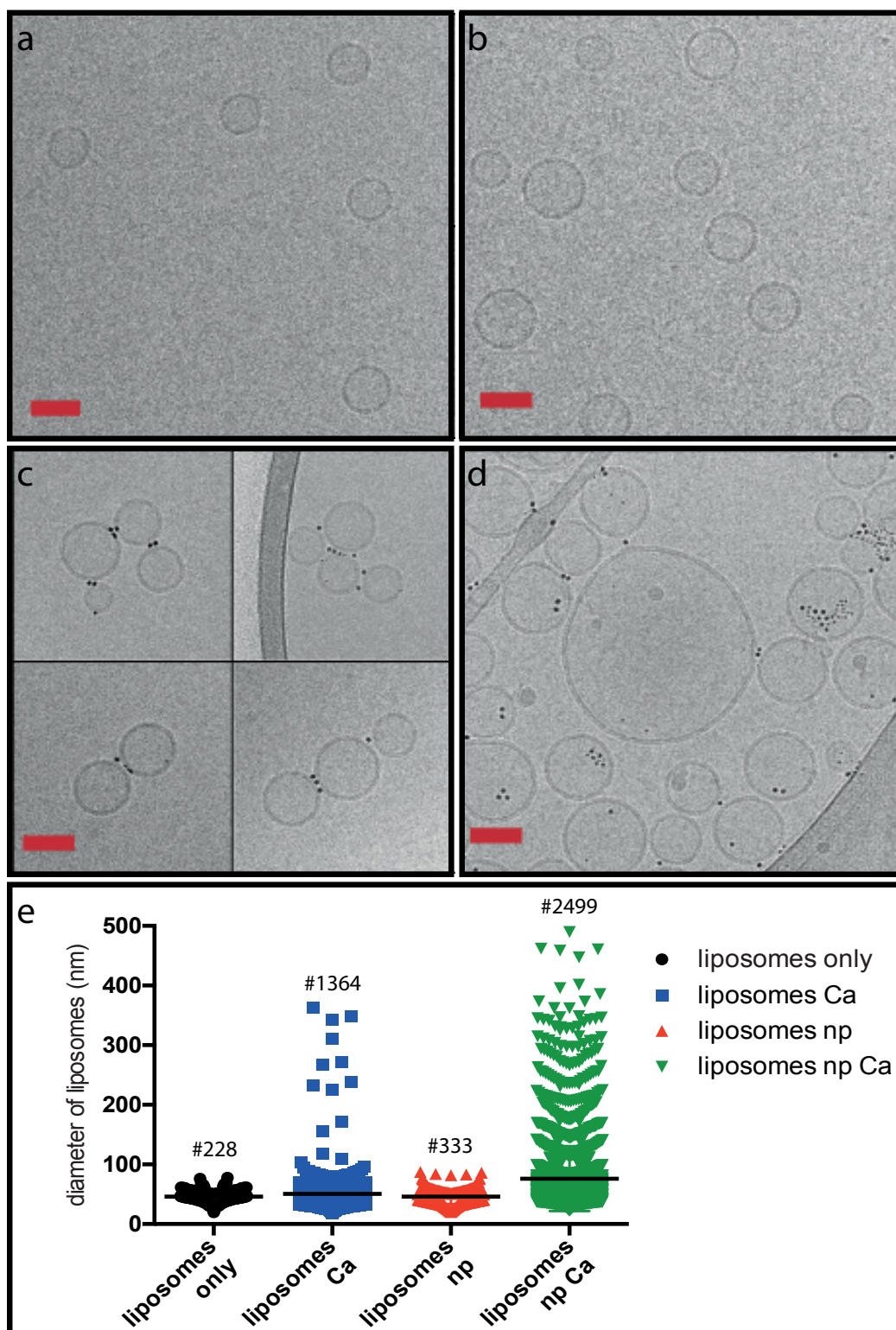


Figure 4-6 Cryo-EM images representing different stages of nanoparticles mediated fusion process. a) Liposomes only, b) Liposomes after Ca^{2+} addition, c) Liposomes and nanoparticles, after 1 hour incubation, d)

After Ca^{2+} addition to already incubated liposome and nanoparticles. Scale bars are 50 nm. e) Histograms of the liposomes size in each case. Black lines indicates the average size of each population and numbers above each column of the histogram represent the amount of liposomes that were counted. Each dot on the histogram represents one liposome.

The performed simulations had shown that different initial stages of liposomes and nanoparticles also let fusion occur. This was interpreted as a consistent presence of nanoparticles in the lipid bilayer throughout the entire fusion process, regardless of the initial state of the system. To be able to experimentally confirm this argument, we acquired cryo-EM tomograms. In the frames acquired from reconstructed tomograms the nanoparticles were consistently seen embedded in the bilayers (Figure 4-7).

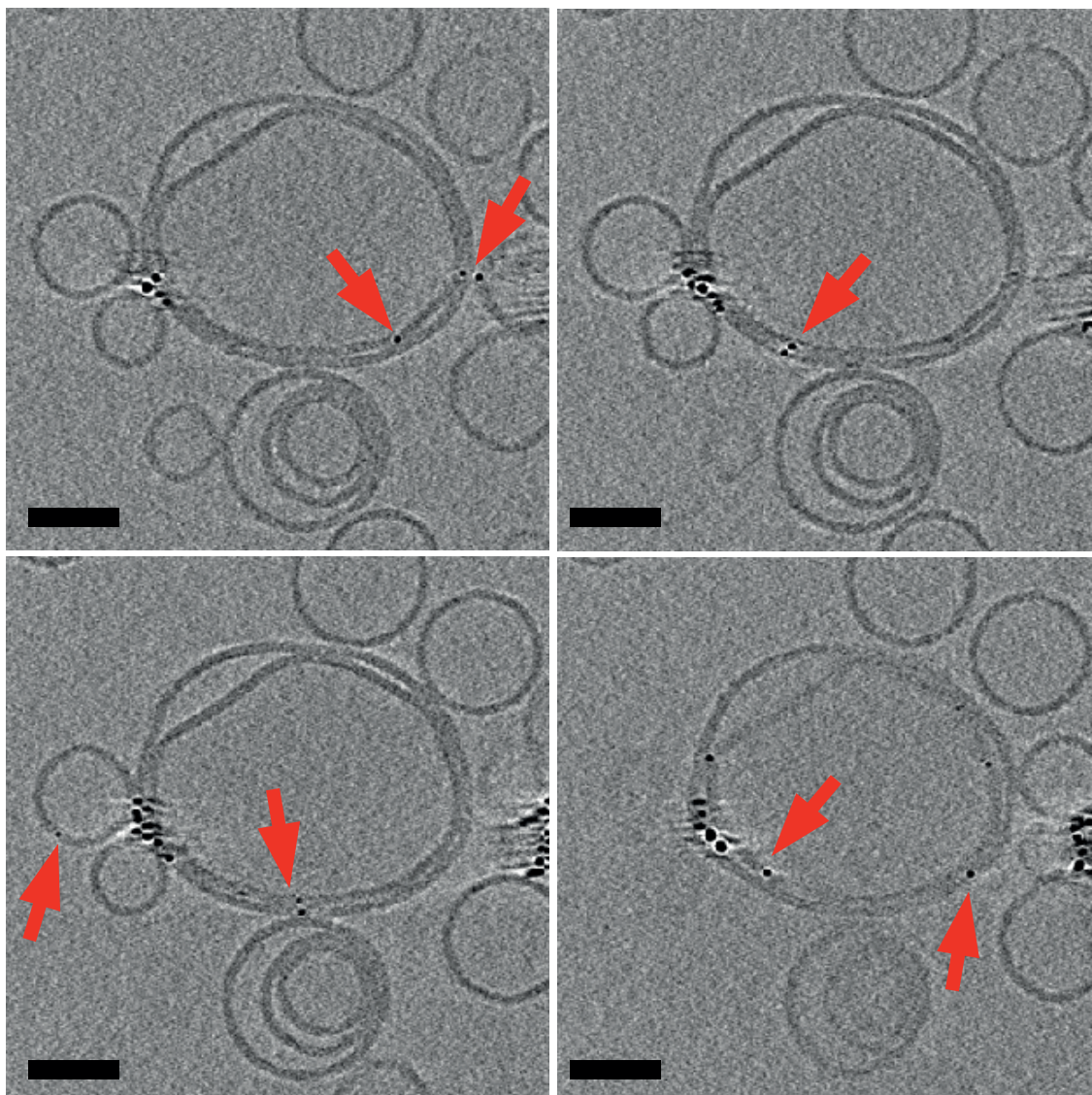


Figure 4-7 The frames from the tomograms of liposomes incubated with MUS:OT 30%OT nanoparticles upon addition of Ca^{2+} . Red arrows points the nanoparticles embedded in the membranes. The scale bars are 50 nm.

Another characteristic observed during our experiments was the multilamellarity of liposomes. To avoid multilamellarity in the initially produced liposomes, they are typically extruded with filters smaller than 100 nm. In our case, we extruded the liposomes with 50 nm and 30 nm filters more than 50 times. Multilamellar liposomes were not observed prior to fusion, but were present in the samples imaged following the fusion. This phenomenon could be explained as the effect of an osmotic shock, in which the liposomes fused but the higher Ca^{2+} concentration outside of the liposomes led to water molecules' flow through the bilayer and towards the exterior. A second parameter contributing to multilamellar liposome formation was the rapid cryo-EM sample preparation, which did not allow sufficient time for water molecules to cross the all bilayers., leading to reshaping of the fused liposomes in a multilamellar form.

4.3.3 Content mixing assay

To be able to quantify and investigate the fusion event further, a fluorescent content mixing assay was carried out. In this assay a self-quenching dye, Sulphorhodamine B (SRB), was used. SRB was encapsulated into the liposomes at a self-quenching concentration. Thus, once the loaded liposomes were fused with empty liposomes, SRB was diluted, and an increase in the overall fluorescence of the system was induced. The mechanism of the assay is illustrated in Figure 4-8.

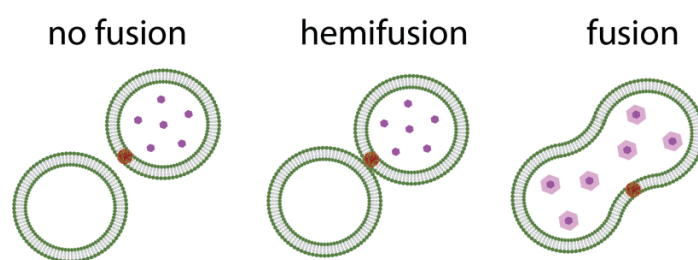


Figure 4-8 Schematic illustration of how content mixing assay measures the fusion event. One liposome was loaded with the dye at self-quenching concentration. Loaded liposomes were incubated with empty liposomes and subject nanoparticles. Upon addition of Ca^{2+} the fusion occurred and the dye got diluted. Depending on the dilution, the dye started to show high fluorescence.

In this assay we chose zwitterionic nanoparticles (ZW) as the negative control, since they did not show any affection towards DOPC liposomes, as discussed in Chapter 3. Moreover, liposomes without nanoparticles were considered as another negative control.

Content mixing assay conditions deviated from the conditions used for cryo-EM imaging, as for cryo-EM imaging a high concentration of subject populations was required, whereas for fluorescence measurement the same high concentration caused saturation on the detector of the spectrofluorometer. Therefore, the samples were diluted 40 times to reach a reliable fluorescence signal in the content mixing assay. The effect of different factors in liposome fusion was studied through this method: time scale, nanoparticle ligand ratio, nanoparticle core size and Ca^{2+} concentration.

The content mixing assay showed the highest fluorescence (*highest amount of fusion events*) from MUS:OT 30%OT (2.6 ± 1.1 nm) incubated liposomes 5 min after the addition of 2mM Ca^{2+} , as shown in Figure 4-9. This increase in intensity corresponded to 22%, when compared to the fluorescent emission of the system before Ca^{2+} addition. Fluorescence in only liposomes (SUVs) and liposomes with ZW systems also increased a little upon slow addition of 2 mM Ca^{2+} . This event was theoretically predicted, as it is known that some initial events of fusion can statistically occur also in an unperturbed systems²⁷⁴. Compared however to MUS:OT 30%OT nanoparticle-mediated fusion, this increase in fluorescence was not significant (Figure 4-9).

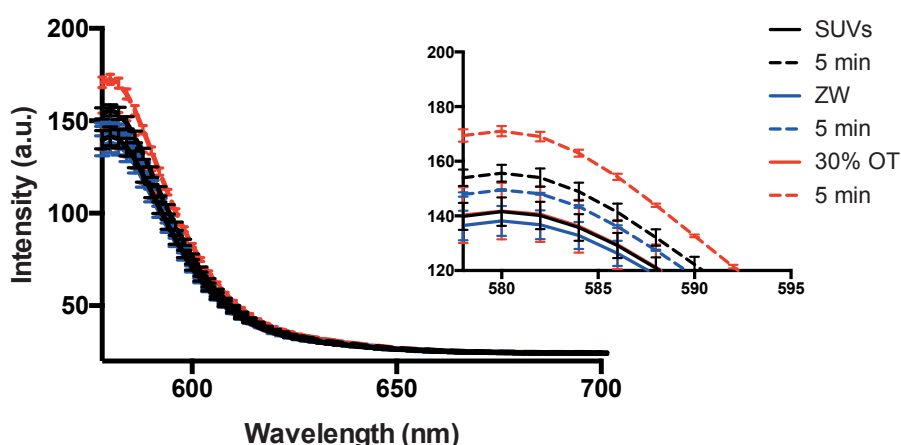


Figure 4-9 Fluorescence measurement during the fusion process. Effect of 2 mM Ca^{2+} on liposomes alone (SUVs) and liposomes incubated with ZW, and MUS:OT 30%OT nanoparticles were compared.

This fusogenic behavior of MUS:OT 30%OT particles could be observed even after 1 min following Ca^{2+} addition, with an increase in fluorescence by 20%, pointing to a fast fusion behavior, similar to synaptic cleft fusion. However, to compare the fusogenic ability of

amphiphilic nanoparticles at sufficient conditions, all fluorescence values compared correspond to values recorded after 5 min of Ca^{2+} addition.

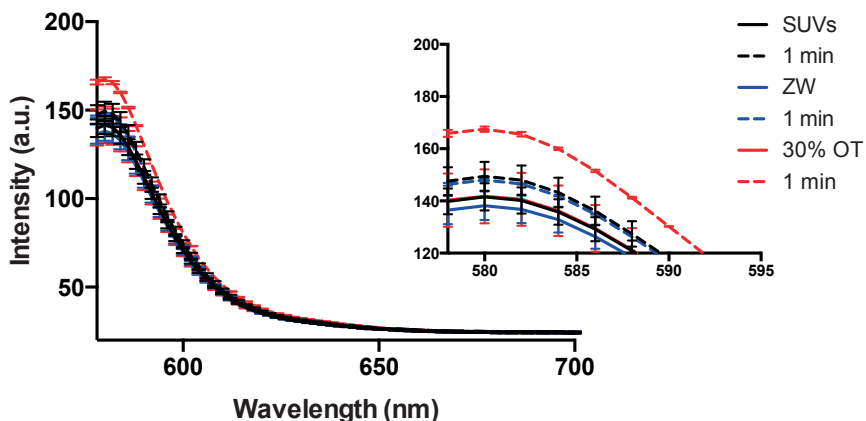


Figure 4-10 Fluorescence measurement of fusion process. Effect of 2 mM Ca^{2+} on liposomes alone (SUVs) and liposomes incubated with ZW, and MUS:OT 30%OT nanoparticles were compared.

The fusogenic behavior of All-MUS particles and MUS:OT 30%OT particles with the same NMR ratio but similar core diameters was also compared (Figure 4-11). No significant differences between different fractions of MUS:OT 30%OT particles were detected. All-MUS particles, however were found to lead to non-significant fusion events.

Between All-MUS and MUS:OT 30%OT fraction A and B particles with similar core size, a less fusogenic behavior from All-MUS particles was expected. This is because more hydrophobic particles tend to be able to be spontaneously inserted into a lipid membrane over a larger diameter range, *in silico*.¹⁶⁰ Therefore, we believe within the same nanoparticle size range fewer All-MUS than MUS:OT 30%OT particles were inserted in a membrane, thus decelerating lipid extraction from the opposing bilayer, and ultimately liposomes' fusion.

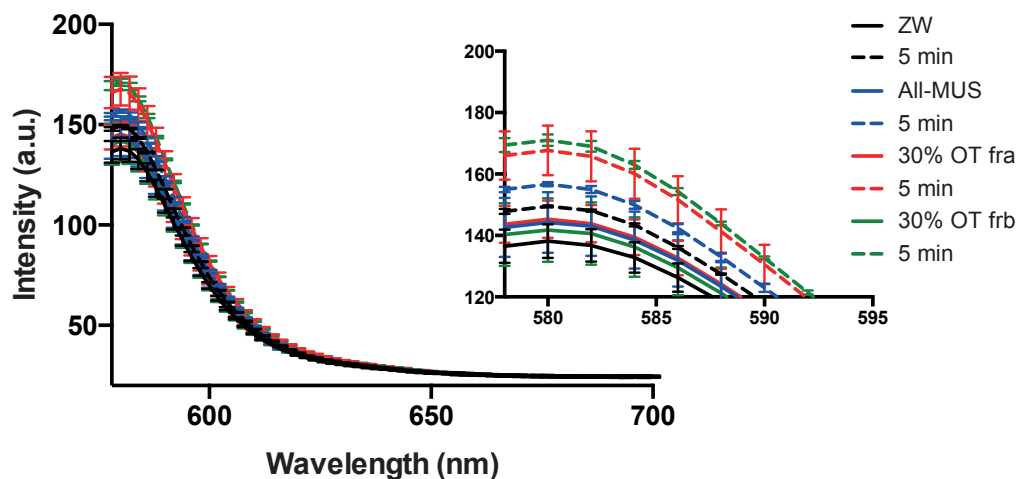


Figure 4-11 Fluorescence measurements of nanoparticle mediated fusion process with different types of nanoparticles. All-MUS nanoparticles showed less, almost none fusogenic behavior compared to MUS:OT 30%OT particles.

Moreover, the effect of Ca^{2+} concentration on the nanoparticle mediated fusion event was examined, by comparing 1 mM Ca^{2+} to 2 mM Ca^{2+} . Upon addition of 1 mM Ca^{2+} , the intensity of fluorescent emission increased 10% in 1 min and elevated up to 12% after 5 min (Figure 4-12). Upon addition of 2 mM Ca^{2+} a significant increase (17%) in fluorescence was observed, as soon as 1 min after Ca^{2+} addition.

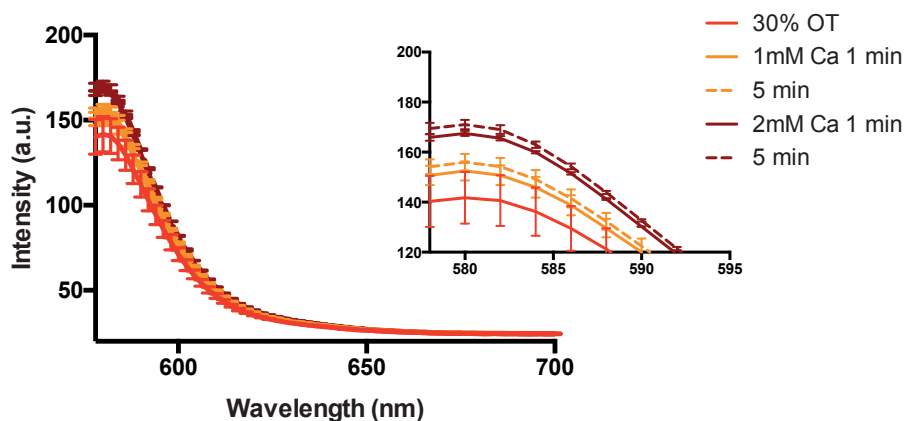


Figure 4-12 Fluorescence measurements of fusion events with MUS:OT 30%OT nanoparticles. Effect of 1 mM and 2 mM Ca^{2+} was compared after 1 min and 5 min.

Two way-ANOVA test was conducted to determine the statistical significance on all of the fluorescence experiments. This test allowed for the comparison of each systems (*i.e.* different nanoparticles, before, or after Ca^{2+}) with each other. No statistical significance was observed

between all the samples before addition of Ca^{2+} (e.g. $p > 0.5$). Control groups such as only liposomes (SUVs), liposomes incubated with ZW particles and also All-MUS particles, did not show any statistically significant increase upon addition of Ca^{2+} ($p > 0.5$). On the other hand, 30%OT fra and frb particles showed statistical significance with a $p \leq 0.01$ upon addition of 2 mM Ca^{2+} compared to their initial states (i.e. before Ca^{2+} addition). After Ca^{2+} , however, 30%OT fra and frb did not show statistical significance compared to controls (SUVs, ZW after Ca^{2+}) even though the standard deviations of the curves did not overlap. Therefore, statistical significance of the system will be improved (e.g. lower p values) by modifying experimental conditions such as, nanoparticle concentration, imaging voltage, etc.

Since the content mixing assay was established with 2 mM Ca^{2+} , another system including giant unilamellar vesicles (GUVs) was designed in which the fusion events between empty GUVs and loaded SUVs were examined. This system was selected due to its closer resemblance to the synaptic cleft in which small vesicles fuse into the synaptic cleft. Furthermore, curvature effects were minimized due to the large diameter of the GUVs (50 μm). Even in this system, however, fusion events upon addition of Ca^{2+} were induced only when the system of vesicles had already been incubated with MUS:OT 30%OT nanoparticles. Upon fusion, the self-quenched SRB in the SUVs was released into the GUVs, leading to a visible increase in the fluorescence.

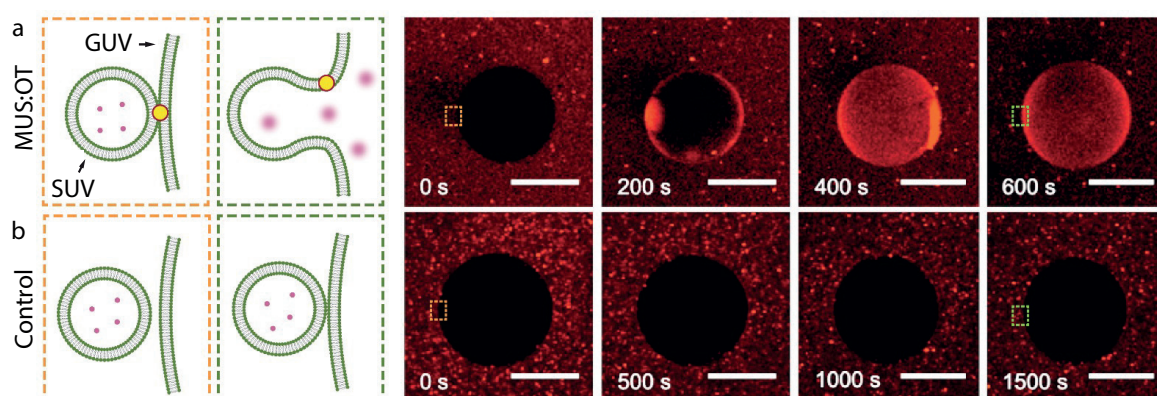


Figure 4-13 Demonstration of nanoparticle mediated fusion at the microscale. This experiment included empty giant unilamellar vesicles (GUVs) and sulphorhodamine B loaded small unilamellar vesicles (SUVs). a) Schematic representation of the operational principle of the fusion assay and the fusion process occurred between nanoparticle-incubated SUVs and GUVs upon addition of Ca^{2+} . b) Schematic representation and experimental timeline of no fusion that was observed without Ca^{2+} .

4.4 Conclusions

To conclude, our results clearly demonstrated that amphiphilic nanoparticles mediate the fusion of bilayers. The phenomenon was studied computationally, via molecular dynamics simulations, and experimentally, via cryo-EM and a content mixing assay.

Computational studies offered a detailed description of the mechanism through which nanoparticles mediated liposome fusion. Amphiphilic nanoparticles played a key role in reducing the energy barriers correlated to the steps of liposome fusion (increasing proximity of vesicles, stalk formation). Amphiphilic nanoparticles embedded within the bilayer, exposing their charged sulfonate groups to the exterior, allowed an increase in electrostatic attractive forces between two bilayers and, conversely, reduction of repulsive hydration forces. Doing so, the energy barrier for liposomes to stay at close proximity decreased. Moreover, the presence of the amphiphilic nanoparticles in the bilayer increased the probability of lipid extraction from counter bilayers, initiating the hydrophobic contact and then a spontaneous stalk formation. After stalk formation, the system was energetically stable. The energy barrier for the fusion pore formation remained high, and an external stimulus was required. This stimulus or stimuli would apply a tension to the membrane from the outer leaflet, and thus the inner leaflets would make a contact and commence the pore formation. A divalent cation, Ca^{2+} was used as the required stimulus, allowing the transition of the system from the local energy minimum of stalk formation to the global energy minimum of pore formation.

Experimentally, cryo-EM and a content mixing assay were used to quantify the fusion process. Cryo-EM images showed that nanoparticles brought the liposomes in close proximity. Furthermore, reconstructed tomograms showed that nanoparticles were embedded in the bilayer upon fusion. From analysis of cryo-EM images a histogram for the size of liposomes was constructed. This histogram showed that the highest amount of large liposomes was obtained upon addition of Ca^{2+} to the liposomes incubated with nanoparticles.

The content mixing assay supported the results of the cryo-EM study. MUS:OT 30%OT particles mediated the fusion event by increasing the fluorescence by 20% in 1 min and 22%

in 5 min. Moreover, MUS:OT 30%OT particles were compared to All-MUS particles and were found to induce fusion more than All-MUS.

In conclusion, our study offers a clear indication that amphiphilic MUS:OT 30%OT (~3 nm) particles are the first synthetic fusogenic system able to mimic the synaptic vesicle fusion encountered in biological systems, while the mode in which the nanoparticles operate as a fusogenic system was studied in detailed.

5 Ring Formations

This chapter describes the formation of ring patterns on the liposomes. The ring patterns were first discovered using cryo-electron microscopy, and then, characterized by a fluorescence assay to determine the structure of the system.

5.1 Introduction

Presented within this thesis, sulfonate terminated amphiphilic nanoparticles formed various nanoparticle-liposome hybrid systems in which they mimic certain membrane proteins. Independently from the core size and surface coating, all of the sulfonate terminated amphiphilic nanoparticles formed vesicle aggregations with small liposomes and formed close packed arrangements with larger liposomes. In these systems, they displayed resemblance to cell adhesion and curvature inducing proteins, respectively. Particles having the highest hydrophobic content (*i.e.* upper limit to maintain the water solubility), however, lead to different system formations, such as bilayer insertion regardless of the core diameter. Among the particles having highest amount of hydrophobic ligand, small particles specifically, self-assembled as ring patterns in the bilayer of liposomes, non-dependent on the hydrophobic ligand type. This behavior was not similar to any proteins known, but still could be used for added complexity in the artificial liposome systems. Therefore, these patterns were investigated from a self-assembly perspective.

The physical properties of nanoparticles depend on their individual characteristics that include size, shape, material, how the ligands self-assemble on the surfaces, to name a few, as well as on their collective behavior such as their size distribution, concentration, self-assembly, etc.²⁸³. Nanoparticles can self-assemble spontaneously depending on the interplay between the inter-nanoparticle and external forces²⁸⁴.

Recently, many studies have shown self-organization of nanoparticles in the bilayers of liposomes for possible biological and medical applications. For example, Rasch *et al.*²⁴³ and

Sakaguchi *et al.*²⁸⁵ separately demonstrated the formation of stable nanoparticle-liposome systems, in which the membranes were densely loaded with 2 nm dodecanethiol coated nanoparticles, either completely or in a Janus pattern. Park *et al.*²⁸⁶ loaded stearylamine coated gold nanoparticles in the membrane of the liposomes, which was found to affect the fluidity of the bilayer. Loading the liposomes in these cases was achieved based on the hydrophobic nature of the nanoparticles and their subsequent interactions with the bilayers in which the nanoparticles were introduced during the liposome formation.

In silico, Sharma *et al.*²⁸⁷ introduced hydrophobically coated gold nanoparticles with a diameter of 1 nm to lipid nanodiscs. The nanodisc served as a template for a ring-like pattern formation of nanoparticles surrounding its edges. Since the lipid disc was in its crystalline phase, the nanoparticles could not propagate towards the center. However, upon increasing the temperature above the phase transition temperature of the lipids, the nanoparticles formed a close packed ring pattern and transformed the nanodisc into a liposome with a ring-shaped opening. The tendency of nanoparticles to form close packed arrangements, combined with the fluidity of the lipid disc above the phase transition temperature made the shape transformation of the lipid disc possible.

The assembly of MUS:OT nanoparticles in liposomes was also studied by Gkeka *et al.*¹⁷⁵. In this work, the MUS:OT 50%OT nanoparticles penetrated into the bilayer and formed chain like structures, *e.g.* dimer, trimers. During the formation of chains, nanoparticles favored penetration into the bilayer, towards defects in the vicinity of already inserted nanoparticles. However, they did not form 2D clusters, a phenomenon explained as an effect of contact between nanoparticles from various sides, which in turn, mitigated the probability of ligand flip, required for membrane insertion.

As described in Chapter 3, we observed different nanoparticle-liposome hybrid systems and, therefore, in this chapter the ring formation behavior of nanoparticles is further discussed. To investigate the phenomenon, first we analyzed cryo-EM images to assess the structure of ring patterns. Furthermore, a fluorescence leakage assay was conducted to further evaluate the structure of this hybrid form. The formation of ring patterns was observed after as little

as 1 hour of nanoparticle-liposome incubation, as well as when particles other than MUS:OT nanoparticles (*e.g.* MUS:HDT) were used.

5.2 Materials and Methods

Nanoparticles

Nanoparticles were synthesized similarly to Chapter 3 as outlined in Appendix A in detail. In this chapter MUS:OT 30%OT-1 (2.1 ± 1 nm), MUS:OT 30%-2 (2.4 ± 1.9 nm), MUS:HDT 20%HDT (2.6 ± 1.3 nm), and All-MUS (2.3 ± 0.7 nm) nanoparticles were used. As a control system, cationic (TMA, 5.9 ± 3.5 nm) and zwitterionic (ZW 2.9 ± 0.9 nm) nanoparticles were synthesized by Paulo Henrique Jacob Silva²⁶¹ and used. Nanoparticles were kept as stock solutions of 4 mg/ml in MilliQ® water, unless otherwise stated.

Liposomes

Probe sonicated liposomes were prepared similarly the method described in Chapter 3. For cryo imaging ~2.5 mM of vesicles were incubated with a final 0.28 mg/ml concentration of MUS:OT 30%OT or MUS:HDT 20%HDT nanoparticles at a final volume of 30 μ l at room temperature, either for 1 hour or overnight, without any agitation.

Cryo-EM microscopy

Sample preparation for cryo-EM and fluorescence imaging were conducted in the same way as outlined in Chapter 3.

Fluorescence leakage assay

Sulphorhodamine B (SRB) loaded liposomes were prepared similarly to the method used in Chapter 4 for fusion assay. To conduct a leakage assay, however, SRB loaded liposomes were mixed with nanoparticles at a final concentration of 0.28 mg/ml. The fluorescent measurements were done on samples diluted 40 times, in order to avoid saturation. The spectrofluorometer (Jasco FP-6500) was operated at 275 V with excitation wavelength of 562 nm and emission of 578 to 700 nm. The bandwidths for both were 3 nm.

5.3 Results and Discussion

5.3.1 Cryo-EM

To investigate the ring patterns, we acquired stereopair images similar to other nanoparticle-liposome hybrids presented in Chapter 3. Acquiring images from different angles add a third dimension to them, which made the recognition of ring formations easier and allowed for better determination of the overall liposome shape. Figure 5-1 depicts the formation of ring patterns with MUS:OT 30%OT nanoparticles after overnight incubation with liposomes. Three separate liposomes hosted the ring patterns of nanoparticles and stereopair images indicated they were not spherical. The liposomes were found elongated and flattened at the side of the ring patterns.

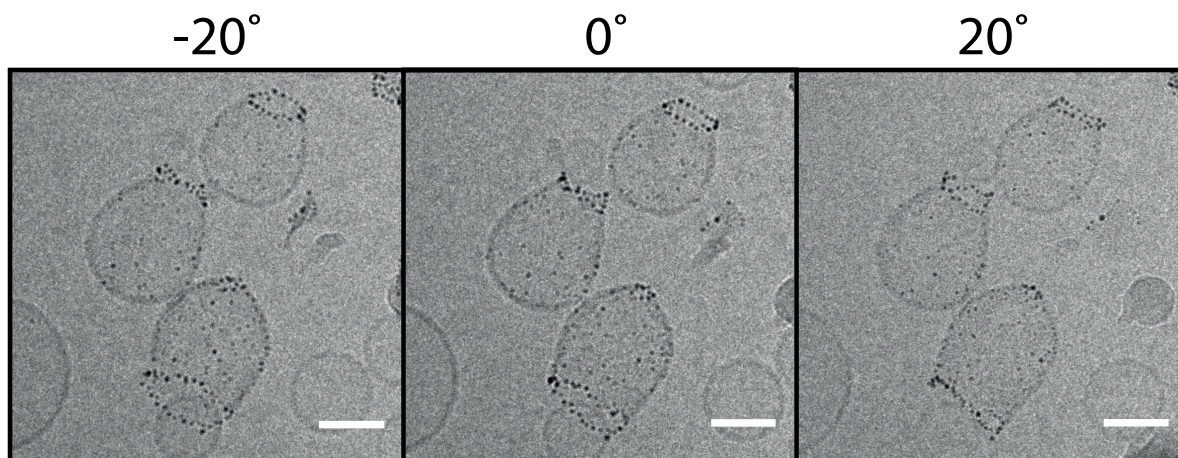


Figure 5-1 Stereopair images of MUS:OT 30%OT-1 (2.1 ± 1 nm) ring formations on liposomes, recorded by cryo-EM. Scale bars are 50 nm.

Nanoparticles formed ring patterns even after as little as 1 hour of incubation. Figure 5-2a shows the ring formations after 1 hour incubation, whereas Figure 5-2b presents examples from overnight incubations.

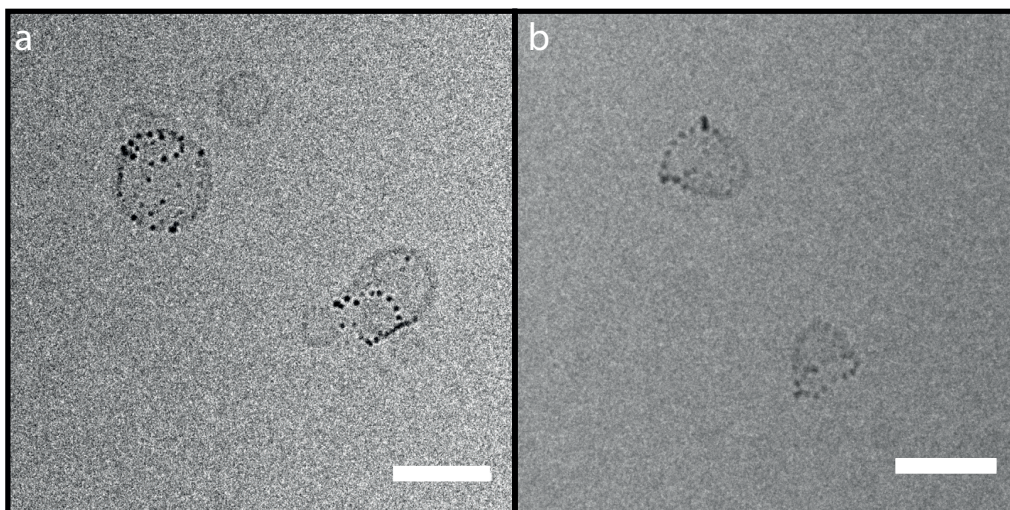


Figure 5-2 Stereopair images of MUS:OT 30%OT-1 (2.1 ± 1 nm) ring formations on liposomes, recorded by cryo-EM, a) after 1 hour incubation, b) after overnight incubation. Scale bars are 50 nm.

We also think that concentrations of liposomes and nanoparticles played a key role on the formation of rings. In an attempt to increase frequency of ring patterns in cryo-EM sample, the concentration of both nanoparticles and liposomes were increased while keeping their relative ratios constant. Figure 5-3 depicts the vesicle aggregations that occurred in highly concentrated liposomes with ring forming particles. Even though blue arrows point to the possible ring formations, a stereopair image or tomograms is required to verify their 3D structure.

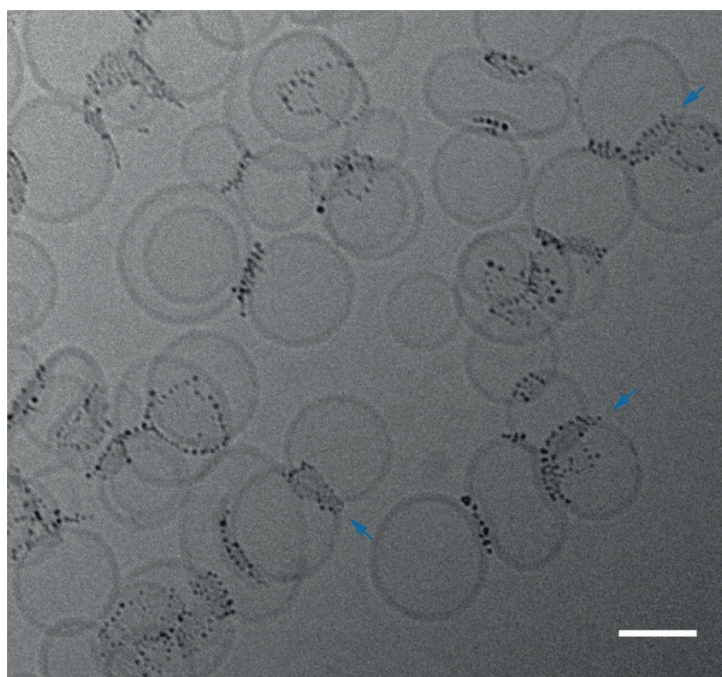


Figure 5-3 Overnight incubation of MUS:OT 30%OT-1 (2.1 ± 1 nm) particles with DOPC liposomes with higher nanoparticle and liposome concentration. Blue arrows point the possible ring formations. Scale bar is 100 nm.

Similar to MUS:OT 30%OT nanoparticles, which had the highest hydrophobic ligand content for water solubility, the use of MUS:HDT 20%HDT under the same incubation conditions also resulted in ring formation on the DOPC liposomes. HDT has 16 carbons on the alkane chain, and thus, for water solubility the surface of nanoparticles could tolerate less HDT than OT ligands. It was also noted that these systems had smaller vesicles aggregating with liposomes.

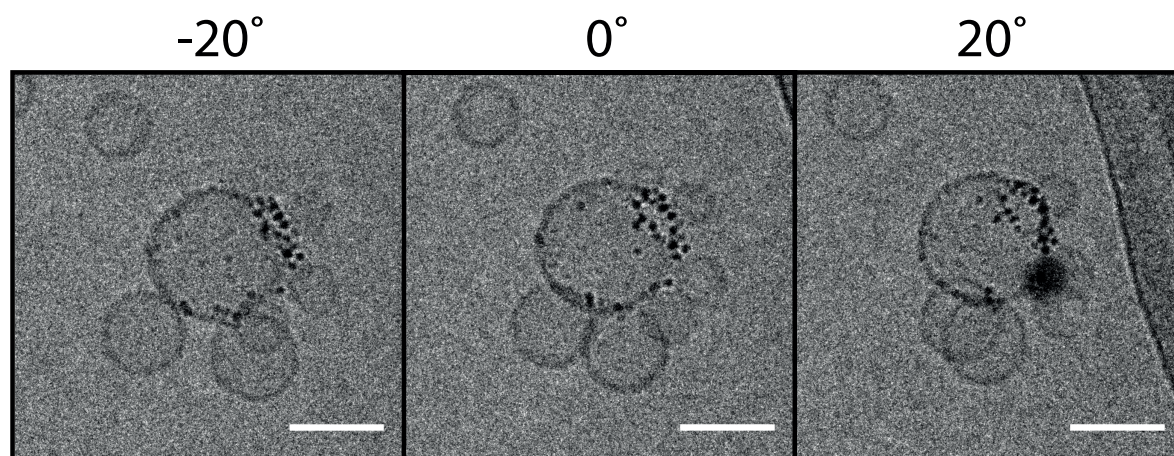


Figure 5-4 Stereopair images of MUS:HDT 20%HDT (2.6 ± 1.3 nm) ring formations on liposomes, recorded by cryo-EM. Scale bars are 50 nm.

A different batch of MUS:OT 30% OT nanoparticles with similar size also mediated the formation of the ring patterns. This batch, however, did not form ring patterns in individual liposomes but assembled the ring formations within the vesicle aggregates.

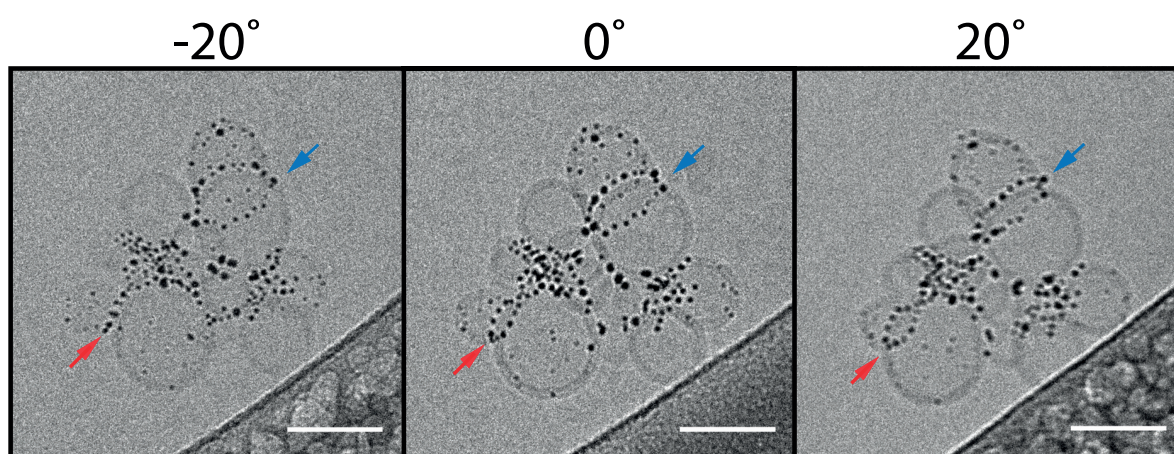


Figure 5-5 Stereopair images of MUS:OT 30%OT-2 (2.4 ± 1.9 nm) (batch B) ring formations on liposomes, recorded by cryo-EM. Scale bars are 50 nm.

Table 5-1 presents the amount of ring patterns observed in the cryo-EM images. MUS:OT 30%OT-2 particles formed aggregates of more than 10 liposomes, thus each aggregate was counted individually. Among counted nanoparticle-liposome hybrids, ring formations were

observed within the range of 30 to 60%. This low percentage compared to vesicle aggregations observed in Chapter 3 can be explained observing that more particles were required to form ring patterns than vesicle aggregates.

Table 5-1 Amount of liposomes (all sizes) and aggregates imaged by cryo-EM and ring patterns observed. Liposomes were counted as the ones with ring patterns, other types of interactions (e.g. individual attachments, vesicle aggregations) and bare liposomes with no nanoparticles.

	Total amount of liposomes or aggregates	Liposomes or aggregates		
		Ring pattern	Other interactions	Bare liposomes
MUS:OT 30%OT-1 (2.1 ± 1 nm) overnight	1640 liposomes	181	102	1357
MUS:OT 30%OT-2 (2.4 ± 1.9 nm) overnight	63 aggregates	19	44	0
MUS:OT 30%OT-1 (2.1 ± 1 nm) 1 h	87 liposomes	18	31	38
MUS:HDT 20%HDT (2.6 ± 1.3 nm) overnight	425 liposomes and aggregates	18	19	388

In contrast to MUS:OT 30%OT-2 and MUS:HDT 20%HDT, MUS:OT 30%OT-1 particles did not show any formation of vesicle aggregates while forming the ring patterns. For MUS:OT 30%OT-1 particles, the percentage of ring patterns after 1 hour incubation (~48%) increased slightly to ~63% for overnight incubation indicating the formation of ring pattern was rapid but still slightly dependent on the incubation time.

Given that ring formations were only observed when MUS:OT 30% OT and MUS:HDT 20% HDT nanoparticles were used, we hypothesize that the ring formations occurred because of the high degree of hydrophobic ligands present on the surface of these nanoparticles. Additionally, the ring patterns were observed only with nanoparticles of 2.5 nm size. As shown in Chapter 3, MUS:OT 30%OT nanoparticles with an average core diameter of 5 nm did not show any ring formations. Therefore we hypothesize that small nanoparticle diameters were necessary for bilayer insertion and subsequent ring formations. To further analyze the system, we conducted a fluorescent leakage assay. This assay would show us if there was a continuous bilayer between the rings, or if the rings disrupted the liposomes.

5.3.2 Leakage assay

For the leakage assay, a self-quenching dye sulphorhodamine B (SRB) was used similar to the fusion assay mentioned in Chapter 4. Liposomes loaded with self-quenching concentration of SRB were incubated with different types of nanoparticles overnight. Their fluorescence was then measured, and the results are presented in Figure 3.5. The nanoparticles used were chosen based on the results previously recorded via cryo-EM images: 30%OT-1 (ring forming nanoparticles, 2.1 ± 1.1 nm), All-MUS (no-ring formation, but interaction with liposomes), and ZW (no ring-formation, no interaction). The fluorescence resulting from liposomes loaded with nanoparticles was lower than SRB-only loaded liposomes due to nanoparticle absorbance (*i.e.* quenching due to absorbance).

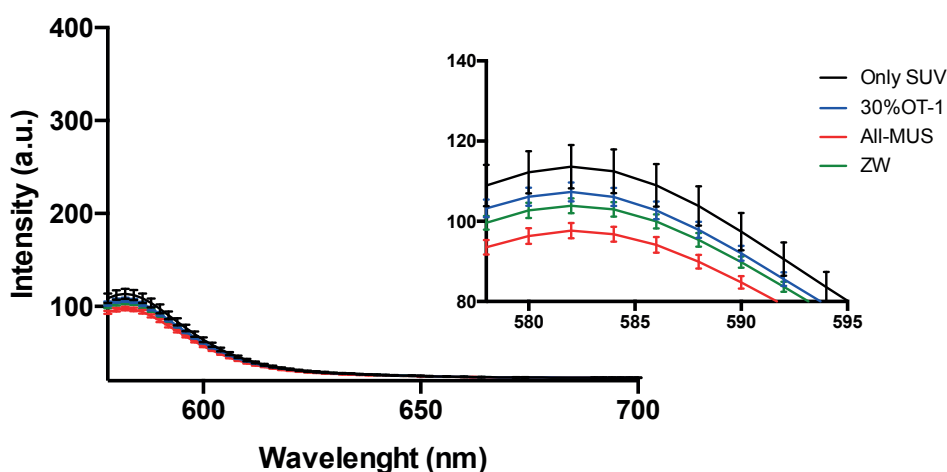


Figure 5-6 Fluorescence spectra of SRB-loaded liposomes (SUV) after overnight incubation with nanoparticles, 30%OT-1 (ring formation on individual liposomes), ZW (non-interacting nanoparticle), All-MUS (interacting, but not ring forming nanoparticles). It is observed that incubation of nanoparticles reduced the fluorescence intensity of the system.

To isolate the interaction of SRB with nanoparticles, the fluorescence of 5 μ M SRB with and without nanoparticles in solution was recorded. Figure 3-6 represents the decrease in the fluorescence of SRB upon introduction of the nanoparticles to the system. Normalizing the results presented in Figure 3-5 based on the nanoparticle quenching of the fluorophore (Figure 3-6), similar fluorescence intensities for only liposomes (112.2 a.u.) and 30%OT-1 ring forming particles (111.013 a.u.) were calculated. These similar values, contrary to our expectations, did not indicate a significant leakage trend that would result from ring formations with an opening inside.

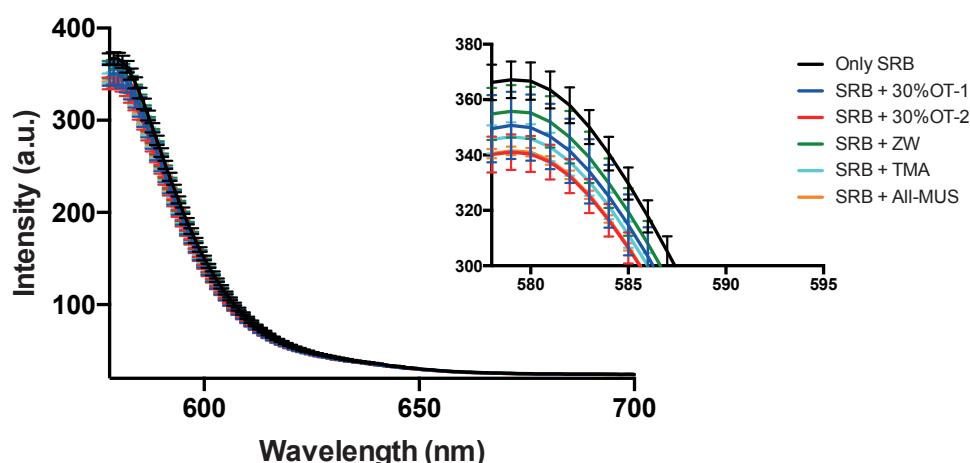


Figure 5-7 Fluorescence spectra of 5 μ M SRB ligand only incubated with nanoparticles, demonstrating the quenching effect of the nanoparticles. The nanoparticle concentration used was the same as in the liposome co-incubation experiments.

Next, we measured the leakage of liposomes after 1 h incubation with nanoparticles. This time we included 30%OT-2 (2.4 ± 1.9 nm) and TMA particles which were respectively ring forming particles within vesicle aggregates, and cationic particles that disrupt the integrity of the vesicles. Figure 3-7 depicts the high fluorescence that resulted from TMA particles upon vesicle disruption. No significant difference was recorded in the fluorescence values of the liposome systems incubated with other nanoparticle types, indicating no disruption of the liposome integrity. In all fluorescence assays, one way-Anova statistical test was conducted and showed that there was no statistical significance between fluorescence values between nanoparticles and only liposome ($p > 0.5$), except TMA particles which had a p value of $p \leq 0.001$ compared to rest.

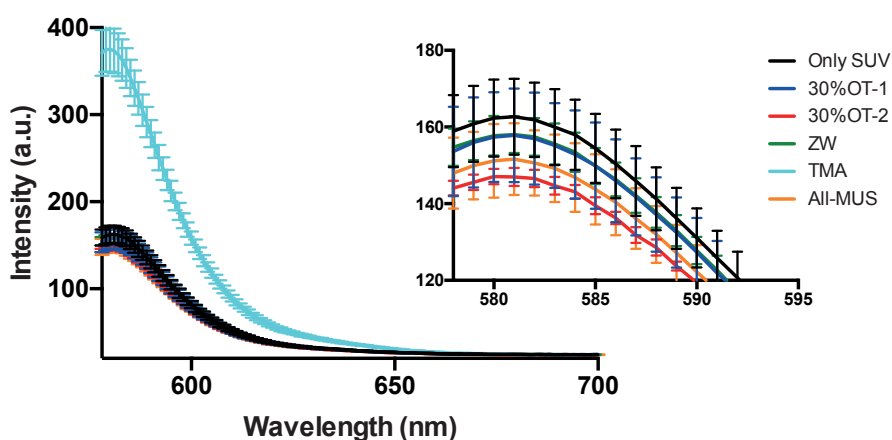


Figure 5-8 Fluorescence spectra of SRB loaded liposomes after 1 hour incubation with nanoparticles in an external solution with 50mM NaCl. In addition to SRB loaded liposomes only (only SUV), 30%OT-1 (ring

formation on individual liposomes), 30%OT-2 (ring formation within vesicle aggregates), ZW (non-interacting nanoparticle), TMA (cationic vesicle disrupting nanoparticles), and All-MUS (interacting but not ring forming nanoparticles) nanoparticles were used. The results indicate that liposomes incubated with nanoparticles did not facilitate an increase the fluorescence.

Guided by the results of the fluorescence assay and the cryo-EM images, some conclusions on the effect of ring formation on the liposomes can be drawn. Since the fluorescence did not increase during the incubation of ring-forming MUS:OT nanoparticles with liposomes, it is clear that the ring patterns did not form a hole on the liposomes. Furthermore, because the cryo-EM images depicted non-spherical shapes of liposomes with an almost flat bilayer sheet between the rings, we hypothesize that the nanoparticles altered the aligning of lipid molecules in that flat bilayer area, possibly resulting in crystalline disks, as observed *in silico* by Sharma *et al.*²⁸⁷ and previously discussed.

In the literature, there have been examples of certain shape modifications on the liposomes due to different lipid tail alignments in the bilayer. For instance, Neuhaus, *et al.*²⁸⁸ demonstrated that interdigitated or tightly packed membranes, due to the chemical modifications on the structure of lipid molecules, led to vesicle structures consisting of flat surfaces, *e.g.* vesicle cubes. In these structures, the edges were discontinuous in terms of packing and in fact presented membrane defects. It has also been demonstrated that MUS:OT nanoparticles embedded in a bilayer can induce some defects in their vicinity and multiple nanoparticles favor the formation of chains in the bilayer¹⁷⁵.

Taken together, we hypothesize that ring forming particles penetrated into the bilayer, formed chain-like structures which subsequently evolved to a hoop around the liposome. Following this ring formation, we think that the lateral pressure that the nanoparticles applied on the bilayer mediated the flattening of the bilayer sheet in between the rings.

The flattening of the liposome between the ring formations could be also the reason that we could not see the bilayer in cryo-EM images clearly. Defocusing on the images made it possible to observe the bilayer, nanoparticles, however, appeared surrounded by Fresnel fringes.

Thus, the combination of the high contrast of gold nanoparticles and the Fresnel fringes dominated the signal recorded in an image, diminishing the contrast of the bilayer.

5.4 Conclusion

To summarize, we observed a particular behavior of nanoparticles on the liposomes, during which they formed rings. The ring formations were limited to small (~2.5 nm) nanoparticles having the highest hydrophobic content they could bear for water solubility, *e.g.* MUS:OT 30%OT and MUS:HDT 20%HDT. These nanoparticles formed rings either on individual liposomes or within vesicle aggregations. Particularly in individual liposomes, a shape distortion of the liposomes was also observed.

To better understand the structure of these nanoparticle-liposome hybrids, a fluorescent leakage assay was conducted. The results obtained did not indicate any significant fluorescent signal arising from liposome incubation with ring-forming nanoparticles, pointing to a close, intact liposome system regardless of ring formations. Therefore, we assumed a mechanism of bilayer insertion of these nanoparticles, followed by the formation of chain-like ring structures. Between these structures the bilayer sheet was hypostasized to be flattened due to a lateral force of nanoparticles. This chapter provides the first experimental description of flat, disc-shaped membrane sheet in between nanoparticle rings.

6 Conclusions and Outlook

6.1 Conclusions

Protein analogues are important for granting protein-like characteristics to artificial biomimetic systems, mostly made of liposomes. Additionally, these materials are suitable model platforms to study the principles of protein functions in various environments. Metal nanoparticles are good candidates as protein analogues, serving efficiently both of these purposes of protein-mimic materials. Furthermore, they can be tailored based on specific applications, as several of their characteristic parameters, such as core material, size, shape, and surface chemistry, can be adjusted. Their nano-scale size also adds more interesting physical characteristics (*e.g.* surface plasmon resonance) that can be used to further functionalize the system.

Recently, Verma *et al.*⁶ showed that amphiphilic gold nanoparticles (MUS:OT particles) were able to penetrate the cell membrane through a non-disruptive, energetically independent path similar to cell penetrating peptides. Many similar studies conducted with MUS:OT particles followed, highlighting the importance and potential of this system for biological applications. However, the exact nature of the protein-mimetic behavior of amphiphilic gold nanoparticles remained unknown. This is the question that this thesis addressed: a rigorous investigation of the key parameters of the interaction between MUS:OT nanoparticles and liposomes, and identification of the parameters and mechanisms that allow the nanoparticles to perform protein-like functions.

To do so, we systematically examined the nanoparticle-liposome hybrid systems as a function of nanoparticle diameter, surface properties, and liposome size by cryo-EM. As a technique, cryo-EM allowed us to monitor the liposome-nanoparticle hybrid systems as “snapshots” of a real-time *in vitro* system, thus reaching conclusions pertaining to their state under physiological conditions. Acquisitions of multiple images from the same sample with different rotations (stereopair images and tomograms) provided more structural information, where needed. Based on these studies, we demonstrated the necessity of sulfonic acid groups on

the terminal part of nanoparticle surface ligands to dictate a patterned interaction. This conclusion was supported by the observation that cationic nanoparticles disrupted the liposomes, whereas zwitterionic and neutral nanoparticles did not show any attraction towards them. Furthermore, anionic phosphonated nanoparticles, showed a much weaker interaction compared to sulfonated nanoparticles towards the liposomes in which they individually stick on the membrane. These results are discussed in detail in Chapter 3.

To be able to verify the effect of size and ligand ratio on the protein-mimic behavior of MUS:OT nanoparticles, nanoparticles with ligand ratios ranging from All-MUS to MUS:OT 30%OT were synthesized. Core diameter of the nanoparticles varied between 1.7-6 nm. The matrix of combinations for nanoparticle-liposome systems underlined the formations of 5 discernible nanoparticle-liposome systems and additional fusogenic properties in which nanoparticles acted as certain protein analogs. These systems were individual attachments of nanoparticles, vesicle aggregates, close packed arrangements of nanoparticles, bilayer insertion, ring formation, and fusogenic behavior of nanoparticles. These results are discussed in detail in Chapter 3.

All of the sulfonated amphiphilic nanoparticles, regardless of size and ligand ratio on the surface, showed individual attachment and vesicle aggregations when they were incubated with small liposomes. In the vesicle aggregation systems, nanoparticles acted just like cell adhesion proteins, *e.g.* tight junctions. The same particles interacted with larger liposomes and formed close packed arrangements, in which they functioned in a manner similar to curvature inducing proteins, *e.g.* BAR domains, by introducing high curvatures locally on the liposomes. In addition to this behavior, sulfonated nanoparticles with the highest hydrophobic content (*i.e.* upper limit of hydrophobicity on the surface that preserves the water solubility of the nanoparticles), displayed further interactions. MUS:OT nanoparticles with 30%OT, regardless of core size, penetrated into the bilayers of both sizes of liposomes, spontaneously, just like cell penetrating peptides. The bilayer inserted nanoparticles also kept the liposomes in proximity, just like SNARE-like fusion proteins. Ring formations, however, were only observed with small particles (~2 nm) having surface coatings of MUS:OT 30%OT or MUS:HDT 20%HDT. These patterns were not analogous to the behavior of any proteins.

Figure 6-1 presents a summary of nanoparticle-liposome interactions as a function of nanoparticle size and hydrophobic content.

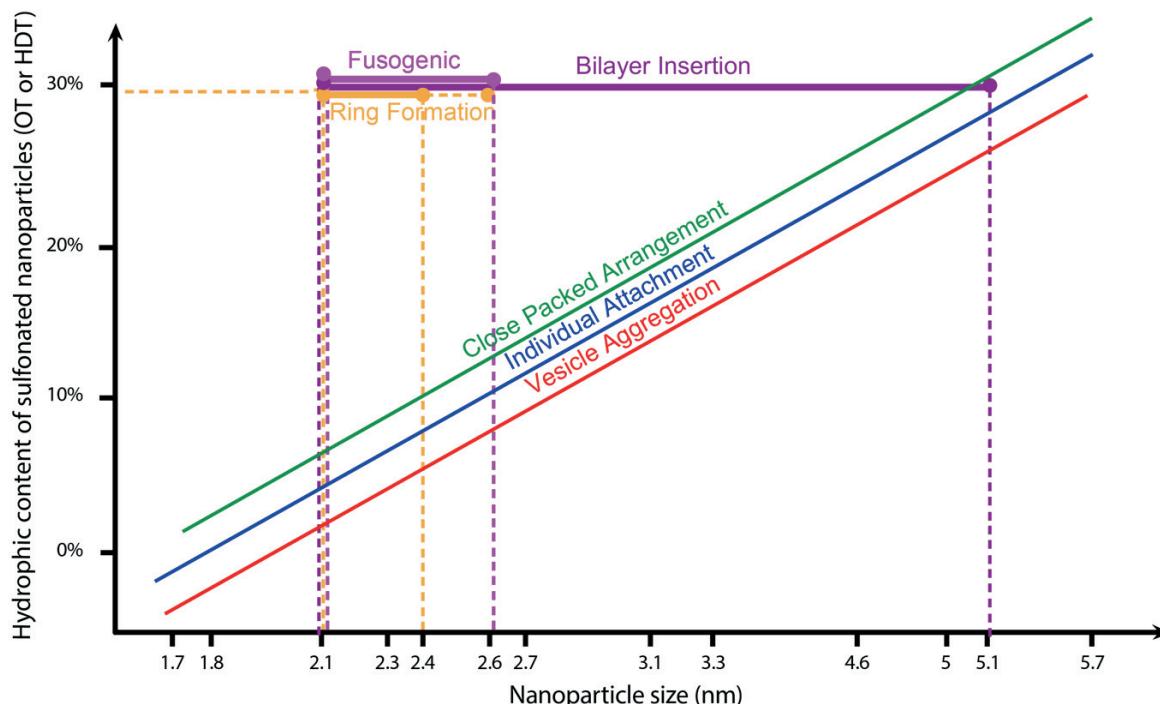


Figure 6-1 Graphical summary of nanoparticle-liposome systems and fusogenic behaviors as a function of size and hydrophobic content. Vesicle aggregations, individual attachments, and close packed arrangements were observed with every nanoparticles regardless of ligand type, core size, and hydrophobic content on the surface. Particles hosting highest amount of hydrophobic content on the surface demonstrated additional behaviors; 2.1 to 5 nm showed bilayer insertion, 2.1 to 2.7 nm demonstrated fusogenic behaviors, and 2.1 to 2.4 nm with 30%OT, 2.6 nm with 20%HDT self-assembled into rings patterns in the bilayer of the liposomes.

The fusogenic behavior of MUS:OT 30%OT (~3 nm) particles was further investigated, experimentally and computationally. Insertion of these particles into the bilayer enabled liposomes to stay in close proximity, which was considered as the first intermediate state upon fusion. Furthermore, *in silico* nanoparticles inserted in the bilayer were shown to drag vesicles close by in order to initiate a stimuli triggered fusion event. To be able to study the fusogenic behavior both cryo-EM and a content mixing fluorescence assay were used. Cryo-EM provided the images of liposomes which were used as the basis to form a histogram of the liposome sizes. According to this histogram, nanoparticles led to vesicle fusion upon Ca^{2+} addition in less than one minute. Similarly, content mixing assays allowed to study and establish the fusogenic properties of MUS:OT 30%OT nanoparticles compared to control particles, like ZW. Thus, within this thesis we provided the first synthetic nanoparticle

fusogens in the field, or, in other words, the first protein-mimetic nanoparticles for fusion. These results are discussed in detail in Chapter 4.

Apart from protein-mimetic behaviors of nanoparticles, certain nanoparticles formed ring patterns in the bilayers of liposomes. These ring patterns mostly changed the shape of the liposomes by flattening the bilayer sheet surrounded by them. To be able to characterize this system, in terms of whether the ring patterns led to an open or closed system due to vesicle disruption, we used a leakage assay. Cationic TMA particles, demonstrated to disrupt the liposomes, were used as the positive control in this assay and where the only ring-forming particles found to show leakage. Therefore, we concluded that MUS:OT nanoparticles form ring patterns, through which they locally apply pressure and flatten the lipid bilayer sheet, while maintaining a closed system. These results are discussed in detail in Chapter 5.

6.2 Outlook

This project can further propagate in two paths; (i) Further characterization of other protein-mimetic features of MUS:OT nanoparticles, such as close packed arrangements of nanoparticles for curvature inducing, (ii) Adaptation of these nanoparticle-liposome hybrid systems into artificial cells for further complexity for cell-like vesicles.

6.2.1 Characterization of other protein-mimetic features

The work presented here demonstrated the formations of several nanoparticle-liposome hybrid systems in which nanoparticles acted like protein-mimetics. For future studies, a comprehensive characterization should be carried on nanoparticles' adhesion and curvature inducing behaviors. Wang *et al.*²³⁷ showed that surface adsorbed citrate coated nanoparticles could shift the phase transition temperature of the liposomes. Based on this phenomenon, such ordered alignment that we observed on the liposomes would be expected to effect the mechanical features of the bilayer, *e.g.* fluidity of lipids. Fluidity in membranes enables the lateral movements (*e.g.* translation, rotation) of proteins in the membrane, and thus plays a key role in the maintaining the functions of cell membrane proteins²⁸⁹. Figure 6-1 depicts that

the nanoparticles both act as an adhesive in between of adjacent liposomes and induce a shape change on the liposomes, mostly flattening of the bilayer compared the unoccupied liposomes.

Flattening of the liposome bilayer makes it possible to characterize the system with a Langmuir monolayer model through rheology²⁹⁰. If the adsorbed nanoparticles change and decrease the fluidity of bilayers, thus these nanoparticles can be used as a blockage to inhibit protein movements for specific functions.

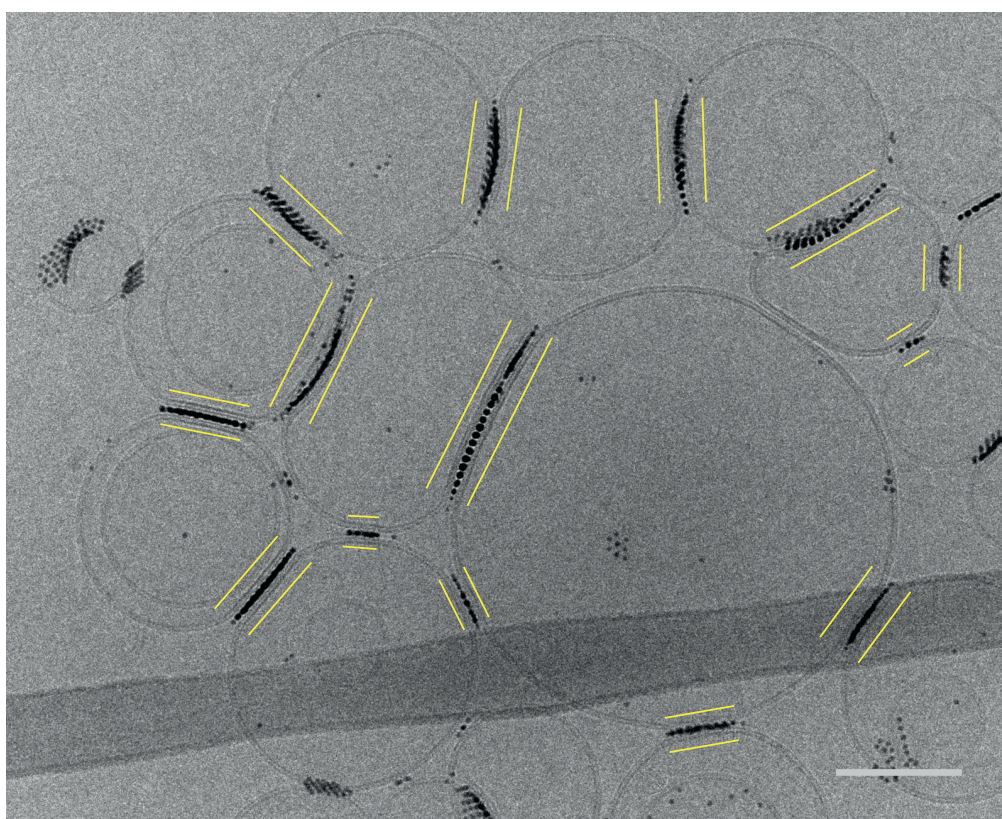


Figure 6-2 MUS:OT 10%OT particles incubated with larger liposomes. Nanoparticle mediated adhesion of liposomes and shape changes, mostly flattening of the bilayer, were emphasized with yellow parallel lines. Scale bar is 100 nm.

6.2.2 Artificial cells

Many recent studies have focused on fabricating artificial cells to provide insights on properties of biological cells or to be used in biotechnology for advanced applications such as

non-nature based enzymatic reactions²⁹¹. Mostly, a bottom up approach has been chosen to constitute the artificial cells in which non-living components are assembled to form the cell.

Several functions similar to living cells have been separately achieved in artificial cells²⁹². Self-replication, catalysis in the aqueous phase, passing of genetic information to daughter cells and compartmentalization in the aqueous phase are among many of them²⁹³. Still, it is challenging to achieve many functions together. Compartmentalization in the artificial cells is essential to govern multiple incompatible reactions separately. These compartments can be formed through double emulsion, phase separation in aqueous media, polymer capsules, and liposomes²⁹⁴.

The introduction of nanoparticles to artificial cells widens the research areas – ranging from therapeutics to medical imaging – employing nanoparticles' broad range of composition, functionality, and stability. A nanoparticle's ability to induce a strong response to externally-applied fields such as ionizing radiation, etc. supposedly contributes to advantages of artificial cells in the fields of therapeutics and diagnostics.

In particular, the overall protein-mimetic features of MUS:OT nanoparticles presented within this thesis can add more complexity to the artificial cells systems. For instance, adhesion proteins like properties of MUS:OT nanoparticles can mediate the formation of compartmental systems in the cells and facilitate communication of different compartments (Figure 6-2). Fusogenic properties of nanoparticles can also contribute to the formation of artificial cells through a signaling path in which the nanoparticles can mediate some reactions in the compartments.

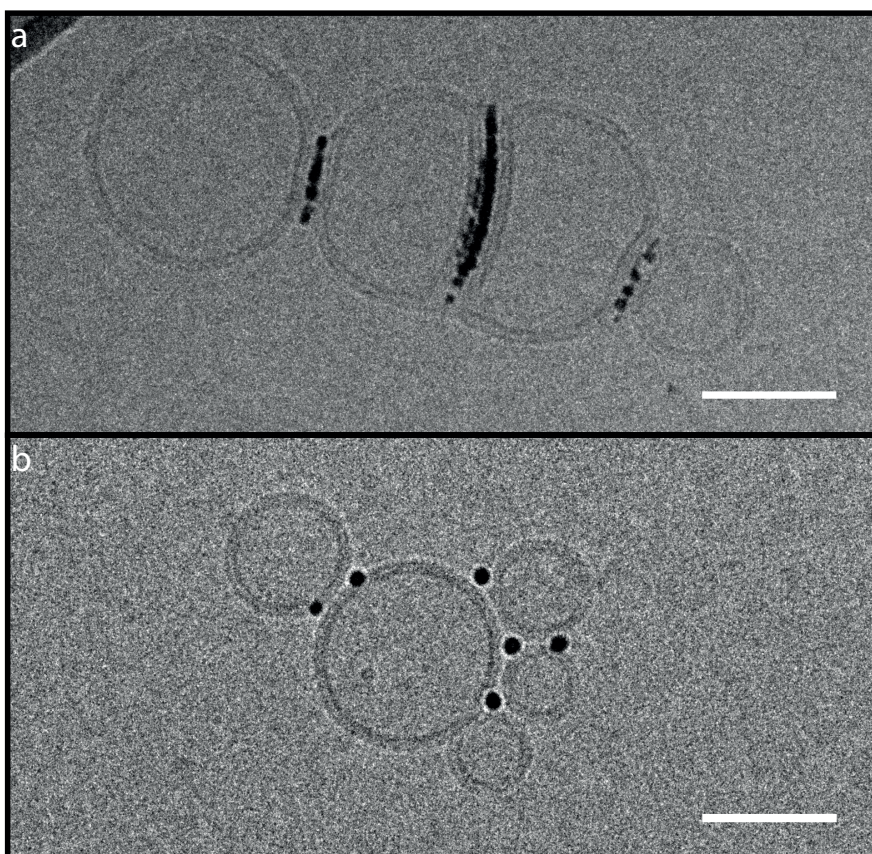


Figure 6-3 Examples to compartmentalization with nanoparticles and liposomes. a) MUS:OT 10%OT (3.1 ± 0.5 nm) with large liposomes, b) MUS:OT 10%OT (5.1 ± 1.5 nm) with small liposomes. Scale bars are 50 nm.

Appendix A

Protocol for the synthesis and characterization of MUS:OT gold nanoparticles

1 Synthesis of 11-mercaptoundecane-1-sulfonic acid (MUS)

1.1 Sodium undec-10-eneulfonate:

- 1.1.1 Add 11-bromo-1-undecene (25 mL, 111.975 mmol), sodium sulfite (28.75 g, 227.92 mmol), and benzyltriethyl-ammonium bromide (10 mg) to a mixture of 200 mL methanol and 450 mL DI-water (4:9 v/v MeOH:H₂O ratio) in a 1 L round bottom flask.
- 1.1.2 Reflux the reaction mixture at 102 °C for 48h. Cap the system with a pressure relief mechanism: for example, a balloon with a needle. The solution becomes transparent after the reaction.
- 1.1.3 Connect the reaction mixture to a rotary evaporator (Rotavap) to evaporate MeOH and reduce the volume to approximately 300mL.
- 1.1.4 Extract the remaining aqueous solution with diethyl ether 5 times with separatory funnel of 1 L. Unreacted 11-bromo-1-undecene stays in diethyl ether and the sulfonated product stays in H₂O.
Note: CAUTION: Release any pressure buildup frequently during extraction.
- 1.1.5 The aqueous phase is evaporated in a rotary evaporator. Since the product is a surfactant, foaming will occur during the evaporation. To avoid this problem;
 - 1.1.5.1 Add ethanol to mixture to accelerate the evaporation of H₂O. When bubbles start forming, remove the flask from the rotavap, add more ethanol and re-connect to rotavap. Repeat this process until the solution mixture decreases significantly and do not form bubbles.
 - 1.1.5.2 Put a bit of grease (or Teflon ring strips or any other sealant) between the flask and the trap and decrease the vacuum slowly.
- 1.1.6 Dry the white powder directly by connecting the flask to high vacuum. The drier the powder, the less inorganic salts will creep into the following steps.
- 1.1.7 Suspend the white powder in 400 mL of methanol. Sonication helps dissolve the maximum amount of product.
- 1.1.8 To increase the solubility, methanol can be gently heated close to its boiling point (~64 °C).
- 1.1.9 Filter the solution to get rid of excess salt. Use a filtering flask connected to vacuum pump and filtering funnel with filter paper. Both the product and the inorganic salts are white powders when dry: the product is soluble in methanol while the salts are not.
- 1.1.10 Evaporate the methanolic solution in a rotary evaporator at 45 °C, redissolve the white powder in methanol and filter the solution. (Protocol steps 1.1.7, 1.1.8, 1.1.9). Repeat this process twice, to decrease the amount of inorganic salts.
- 1.1.11 Collect the white, methanol soluble powder of approximately 30 g at this scale.
- 1.1.12 Perform ¹H-NMR of the product in D₂O. ¹H-NMR (D₂O): 5.97 (m, 1H), 5.09 (m, 2H), 2.95 (t, 2H), 2.10 (m, 2H), 1.77 (q, 2H), 1.44 (br s, 12H).

1.2 Sodium 11-acetylthio-undecanesulfonate:

- 1.2.1 Dissolve the amount of sodium undec-10-enesulfonate (reaction product of 1.1) in 500 ml of methanol. Add 2.6 times excess of thioacetic acid to the solution and stir in front of a UV lamp (250 Watt) overnight.
- 1.2.2 Monitor the reaction by taking a small amount of solution from the reaction and evaporating to check by $^1\text{H-NMR}$. Once the peaks corresponding to double bond disappear, the reaction can be stopped.
- 1.2.3 Evaporate all of MeOH in a rotary evaporator until the solid residue turns to orange-red. Work mindfully because of the strong odors from the thioacetic acid.
- 1.2.4 Wash the product with diethyl ether using a filtering flask to remove excess thioacetic acid, until no more colored (orange-yellow) substances appear in the diethyl ether supernatant.
- 1.2.5 Dry the solid under high vacuum, and then dissolve in methanol yielding a yellow solution.
- 1.2.6 Add 3 g of carbon black to the solution, mix vigorously, and filter the mixture through Celite in a fluted filter paper. The porous structure of carbon black captures the colored side product material. The filtered solution should be clear.
- 1.2.7 Evaporate the solvent completely in rotary evaporator and collect approximately 35 g of white solid.
- 1.2.8 Perform $^1\text{H-NMR}$ of the product in D_2O . $^1\text{H-NMR}$ (D_2O): 2.93 (t, 4H), 2.40 (s, 3H), 1.77 (m, 2H), 1.62 (m, 2H), 1.45 (br s, 14H).

1.3 11-mercaptoundecane-1-sulfonic acid (MUS):

- 1.3.1 Reflux sodium 11-acetylthio-undecanesulfonate at 102 °C in 400 mL of 1M HCl for 12 h to cleave the thioacetate group and obtain a thiol.
- 1.3.2 Add 200mL of 1M NaOH the final solution and add 400 mL of DI-water to have a 1 L volume. This aims to keep the solution slightly acidic and prevent the crystallization of inorganic salts with the product.
- 1.3.3 Keep the clear solution at 4 °C and it will crystallize overnight. We believe that this step is crucial to remove excess salt. To accelerate the crystallization, add some already synthesized MUS to the solution.
- 1.3.4 Centrifuge down the viscous white product in 50 mL centrifuge tubes, and dry under high vacuum. (Filtering is not advised because of the surfactant nature of the product: excessive foaming will occur and product will be lost)
- 1.3.5 Collect approximately 12 g (about 30% yield) of methanol soluble MUS from this purification step. More material can be extracted from the supernatant of the centrifugation step, by reducing volume and keeping it at 4°C.
- 1.3.6 Perform NMR of the final product in D_2O . $^1\text{H-NMR}$ (D_2O): 2.93 (t, 4H), 2.59 (t, 3H), 1.78 (m, 2H), 1.65 (m, 2H), 1.44 (br s, 14H). Calculated molar mass (including the sodium counterion) of the product is 290.42 g/mol.

2 1-Phase Synthesis Method

2.1 Preparation of reagents

- 2.1.1 Clean all glassware (one 250 ml and one 500 ml one-neck round bottom flasks, a 125 ml separation funnel, and a small funnel) with fresh Aqua Regia (hydrochloric acid and nitric acid with 3 to 1 ratio, respectively). Rinse the glassware with excess amount of water and ethanol and dry them in the oven.
- 2.1.2 Weigh 152.9 mg (0.45 mmol) Gold(III) chloride trihydrate ($\text{HAuCl}_4 \cdot 3\text{H}_2\text{O}$) in a small glass vial.
- 2.1.3 Weigh 87 mg (0.3 mmol) 11-mercaptoundecane-1-sulfonic acid (MUS) in a glass vial of 20 ml.
- 2.1.4 Add 10 ml of methanol to dissolve the MUS, sonicate to ensure complete dissolution.
- 2.1.5 Add 26 μl (0.15 mmol) of 1-octanethiol (OT) to the methanol solution and shake to mix the ligands.
- 2.1.6 Weigh approximately 13 mmol (500 mg) of sodium borohydride (NaBH_4) and mix with 100 ml of ethanol in the 250 ml round bottom flask under vigorous stirring.

2.2 Synthesis of gold nanoparticles

- 2.2.1 Dissolve gold salt to in 100 ml ethanol in the 500 ml round bottom flask and start stirring at 800 rpm with a magnetic bar on a stirring plate. Make sure the gold salt dissolves completely.
- 2.2.2 Place a 100 ml separatory funnel above the round bottom flask. Put a funnel on the top of the separatory funnel with a paper filter inside. When the NaBH_4 is dissolved in ethanol, start filtering the solution into the separation funnel through the filter paper in the funnel.
- 2.2.3 Add the ligand solution into the reaction mixture. Wait 15 min for the formation of gold-thiolate complex. The color change of the reaction mixture from translucent yellow to turbid yellow indicates the formation of gold-thiolate complex.
- 2.2.4 Start adding the filtered NaBH_4 solution from the separatory funnel dropwise. Adjust the interval time of the drops so that the addition of NaBH_4 should take one hour.
- 2.2.5 After complete addition of NaBH_4 (~1 hour), remove the funnel. Keep stirring the reaction for one more hour. At the end of reaction, remove the magnetic stirring bar.
- 2.2.6 Use a septum to close the flask and pierce a needle into the septum to release the H_2 gas.
- 2.2.7 Keep the reaction mixture in the fridge (4 °C) to precipitate the nanoparticles overnight.

2.3 Work up of synthesis

- 2.3.1 Decant the supernatant ethanol to reduce the volume.
- 2.3.2 Transfer the remaining precipitates into 50 ml centrifuge tubes and centrifuge for 3 min at 4000 x g.

- 2.3.3 Decant supernatant, disperse the nanoparticles again with ethanol by vortexing and centrifuge it again. Repeat this washing process 4 more times.
- 2.3.4 Dry the nanoparticles under vacuum to get rid of residual ethanol.
- 2.3.5 To clean the nanoparticles from free hydrophilic ligands/molecules, dissolve the precipitates in 15 ml of DI-water and transfer into the centrifuge tubes with a filtration membrane 30KDa cutoff molecular weight. (Dialysis is also amenable for this procedure)
- 2.3.6 Centrifuge the centrifuge tubes for 5 min at 4000 x g to concentrate the np solution.
- 2.3.7 Add 15 ml more DI-water to this solution and centrifuge to concentrate again. Repeat this cleaning process for at least 10 times.
- 2.3.8 After the end of the centrifugation transfer the concentrated nanoparticles into a 15 ml falcon tube. To turn the nanoparticle into a manageable powder, either precipitate them by a solvent such as acetone, or freeze-dry the remaining aqueous solution.

3 Sticky Method

3.1 Preparation of Reagents

- 3.1.1 Prepare 120 ml of 1:9 (v/v) H₂O:dimethylformamide (DMF) mixture.
- 3.1.2 Weigh 247.8 mg (0.5 mmol) Chloro(triphenylphosphine)gold(I) ([C₆H₅)₃P]AuCl) in 40 ml glass scintillation vial.
- 3.1.3 Weigh 261 mg (0.9 mmol) 11-mercaptoundecane-1-sulfonic acid (MUS) in a glass vial of 40 ml and dissolve in 20 ml of reaction solution.
- 3.1.4 Add 78.09 µl (0.6 mmol) of 1-octanethiol (OT) to the reaction solution with MUS already and shake to mix the ligands.
- 3.1.5 Weigh approximately 1.5 mmol (140 mg) of borane tert-butylamine ((CH₃)₃CNH₂.BH₃) and mix with 20 ml of reaction mixture in 40 ml glass scintillation vial.

3.2 Synthesis of Nanoparticles

- 3.2.1 Put 60 ml of H₂O:DMF mixture into a 250 ml round bottom flask.
- 3.2.2 Put this round bottom flask in silicon oil bath and heat it to 120 °C with a condenser attached for reflux.
- 3.2.3 Add first gold precursor, then the ligands and wait for 15 min for the formation of gold-thiol complex
- 3.2.4 After 15 min, add all of the reducing agent through a funnel. The color of the reaction mixture should change directly at this step.
- 3.2.5 Reaction took place for 1,5 hours at 120 °C.
- 3.2.6 Then, the flask removed from the oil bath still attached to the condenser and stirred 1 more hour.
- 3.2.7 After 1 hour, the flask is put in the fridge overnight.

3.3 Work-up of the synthesis

- 3.3.1 Decant the supernatant and start washing particles with ethanol.
- 3.3.2 Transfer the remaining precipitates into 50 ml centrifuge tubes and centrifuge for 3 min at 4000 x g.
- 3.3.3 Decant supernatant, disperse the nanoparticles again with ethanol by vortexing and centrifuge it again. Repeat this washing process 4 more times.
- 3.3.4 Dry the nanoparticles under vacuum to get rid of residual ethanol.
- 3.3.5 To clean the nanoparticles from free hydrophilic ligands/molecules, dissolve the precipitates in 15 ml of DI-water and transfer into the centrifuge tubes with a filtration membrane 30KDa cutoff molecular weight. (Dialysis is also amenable for this procedure)
- 3.3.6 Centrifuge the centrifuge tubes for 5 min at 4000 x g to concentrate the np solution.
- 3.3.7 Add 15 ml more DI-water to this solution and centrifuge to concentrate again. Repeat this cleaning process for at least 10 times.
- 3.3.8 After the end of the centrifugation transfer the concentrated nanoparticles into a 15 ml falcon tube. To turn the nanoparticle into a manageable powder, either precipitate them by a solvent such as acetone, or freeze-dry the remaining aqueous solution.

4 Characterization of nanoparticles

4.1 Cleanliness

- 4.1.1 To check whether the nanoparticle is free from unbounded ligands, dissolve 5 mg of dry nanoparticles in 600 μ l D₂O.
- 4.1.2 Perform ¹H-NMR measurement of the particles.
- 4.1.3 If there are no sharp peaks of ligands, it means the nanoparticles are free from small molecules.

4.2 Ligand ratio

- 4.2.1 Prepare a 150 mg/ml methanol-d₄ solution of iodine.
- 4.2.2 Add 600 μ l of this solution to the ~5 mg of nanoparticles in a glass vial, to etch the nanoparticles.
- 4.2.3 Wrap the cap of the vial with parafilm and sonicate.
- 4.2.4 Acquire the ¹H-NMR spectrum.

4.3 Ligand density

- 4.3.1 Transfer 2 to 8 mg of nanoparticles to a TGA crucible.
- 4.3.2 Choose the temperature range from 30 °C to 900 °C and a speed of 5 °C per minute under N₂ gas.

4.4 Size distribution

- 4.4.1 TEM
 - 4.4.1.1 Prepare 0.1 mg/ml nanoparticle solution in DI-water.

4.4.1.2 Drop 5 μl of the prepared solution onto the 400 mesh carbon supported copper grid

4.4.1.3 Wait until it dries

4.4.2 UV-visible spectra

4.4.2.1 Prepare 0.2 mg/ml nanoparticle solution in DI-water.

4.4.2.2 Put the required amount of this solution in the quartz cuvette and scan from 200 nm to 700 nm.

Representative Results For the Protocol

The reaction steps to synthesize MUS are shown in Figure A-1. The ^1H -NMRs of the product of each steps are represented in Figure A-2. The synthesis workflow of the binary MUS:OT amphiphilic gold nanoparticles is described in Figure A-3. The work up of nanoparticles included washing with ethanol and DI-water several times. Prior to any characterization of nanoparticles, cleanliness of the nanoparticles from unbound free ligands was monitored by ^1H -NMR in D_2O , Figure A-4. The ratio of the two ligands was determined by etching the gold core using iodine and measuring ^1H NMR. Figure A-5 shows the representative spectra as well as the procedure of NMR peak assignments and ligand ratio calculation. Stoichiometric ratio vs NMR ratio of OT resulting from various synthesis is compared in Figure A-6. The size distribution of the nanoparticles was characterized by TEM (Figure A-7a, b). Localized surface plasmonic resonance absorption was measured with UV-Vis spectra (Figure A-7c). Finally, surface coverage of the nanoparticles is examined by TGA as shown in Figure A-8.

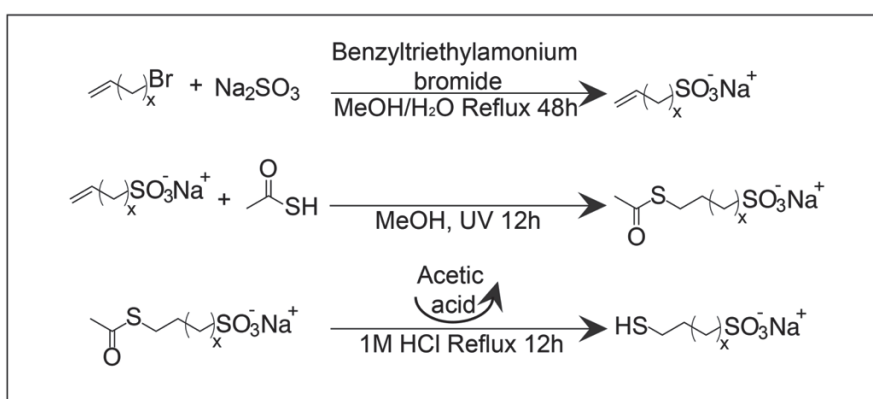


Figure A- 1 Schematic of synthesis of MUS. MUS synthesis is the key point of the reproducibility of amphiphilic nanoparticle synthesis. If MUS includes high amount of salt, the stoichiometric ratio of the ligands may deviate. $X=9$.

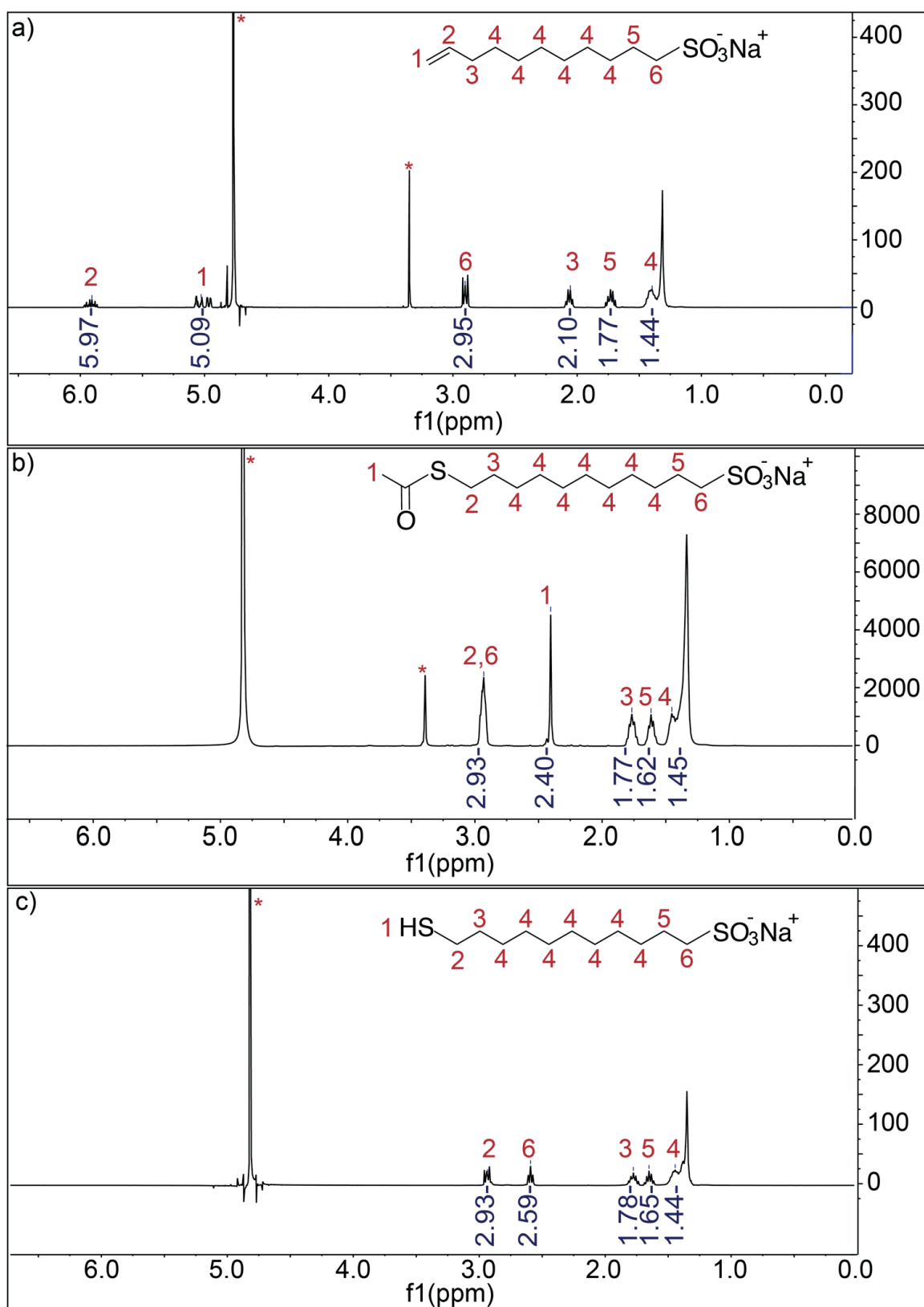


Figure A- 2 NMR spectra of the molecules after each step in MUS synthesis. a) ¹H-NMR spectrum of Sodium undec-10-eneulfonate in D₂O. b) ¹H-NMR spectrum of Sodium 11-acetylthio-undecanesulfonate in D₂O. c) ¹H-NMR spectrum of 11-mercaptoundecane-1-sulfonic acid in D₂O. In all spectra * indicates the solvent peaks.

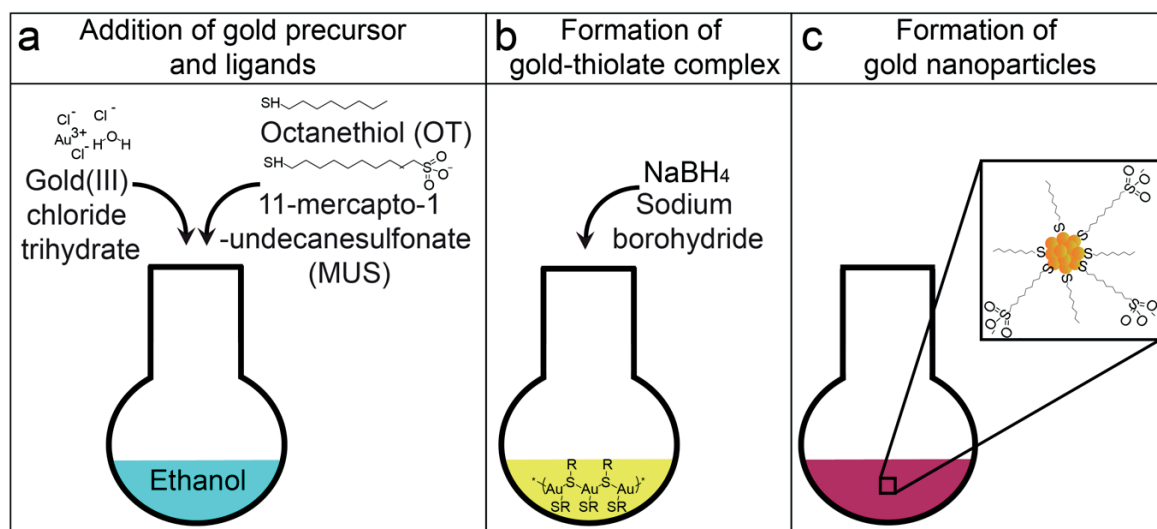


Figure A- 3 Schematic of amphiphilic nanoparticle synthesis with 1-phase method. a) Preparation of the one phase chemical reduction reaction using ethanol the solvent. b) Gold-thiolate complex is allowed to form before the addition of reducing agent. At this stage the solution of gold salt became turbid. c) During the addition of reducing agent dropwise, gold nanoparticles are formed.

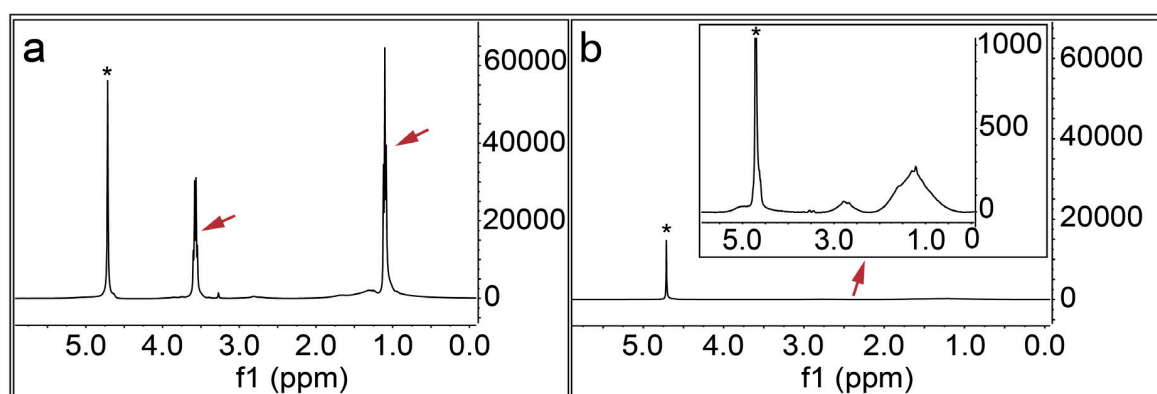


Figure A- 4 Cleanliness of the nanoparticles from unreacted free ligands. a) ^1H -NMR of the nanoparticles right after the synthesis and vacuum dried. D_2O is used as the solvent for ^1H -NMR analysis. Sharp peaks shown by red arrows indicate the existence of free unbound ligands. b) ^1H -NMR of the nanoparticles after thorough purification, *i.e.* washes and centrifugation with ethanol and DI-water. Red arrow points the magnified part of the spectrum, in which the peaks are broad, not sharp as before indicating the absence of free ligands. In both spectra * indicates the solvent peaks.

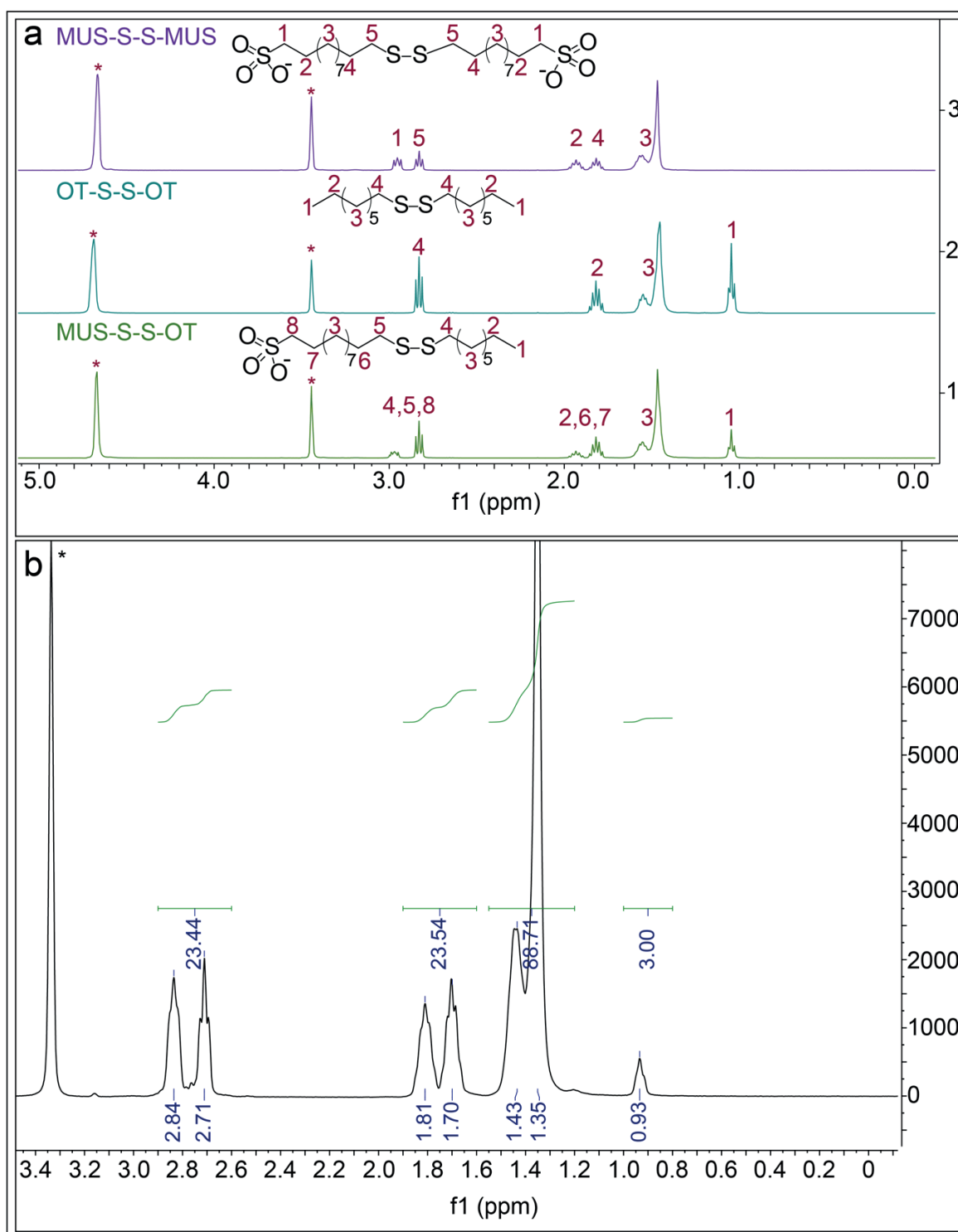


Figure A- 5 Ligand ratio calculation. a) Representative NMRs of combinations of disulfides (as references for ligands after core etching) and peak assignments for different protons in MeOD-d4. **b)** ¹H-NMR of etched nanoparticles in MeOD-d4. To find the ligand ratio between MUS and OT, we calculated the integrals of the peaks between 0.8-1 (I₁), 1.12-1.55 (I₂), 1.6-1.9 (I₃), and 2.6-3 (I₄) ppm. I₁ has 3 H from OT and I₂ has a combination of 14:10 H from the ligands MUS:OT, while this is 4:2 for I₃ and I₄. Then to find the OT ratio we normalized the I₁ to 3 and use formulations of $OT\% = \frac{1}{\left(\frac{12-10}{14}\right)} + 1$ for I₂ and $OT\% = \frac{1}{\left(\frac{13,4-2}{4}\right)} + 1$ for I₃ and I₄. These

formulations indicate the ratio of OT to MUS assuming there is 1 arbitrary unit of OT in the system. Three integrals gave similar values for OT percentage, *i.e.* 15.3, 15.9, and 15.9 from I_2 , I_3 , and I_4 , respectively. In all spectra * indicates the solvent peaks.

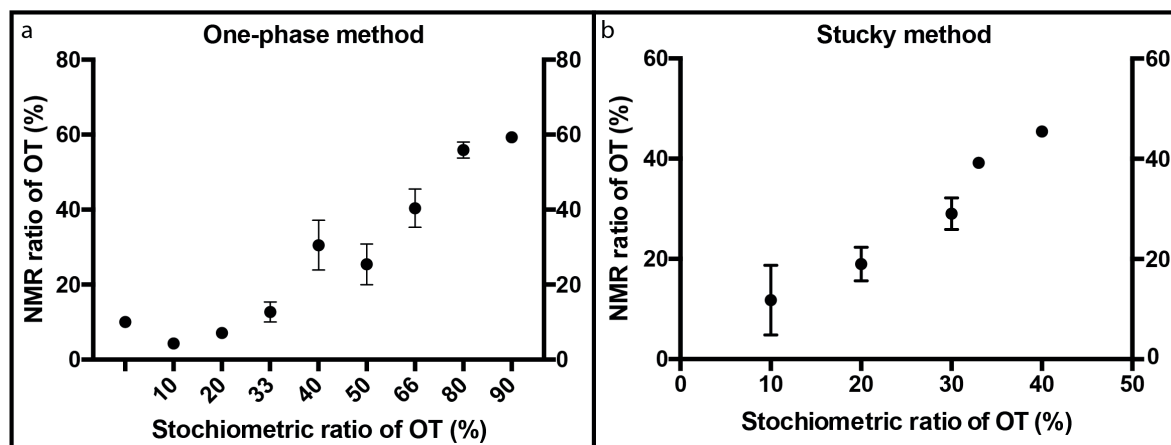


Figure A- 6 Comparison of stoichiometric and NMR ratios of OT on the particles. a) one phase method, b) Stucky method. It is possible to tune the amphiphilicity of the nanoparticles by changing the starting stoichiometric ratio of OT in the reaction. Error bars show the upper and lower limit of OT content acquired from the referred stoichiometric ratios. Stoichiometric ratios of 10%, 20%, and 90%OT were synthesized to observe the limits of OT content on the nanoparticle surfaces.

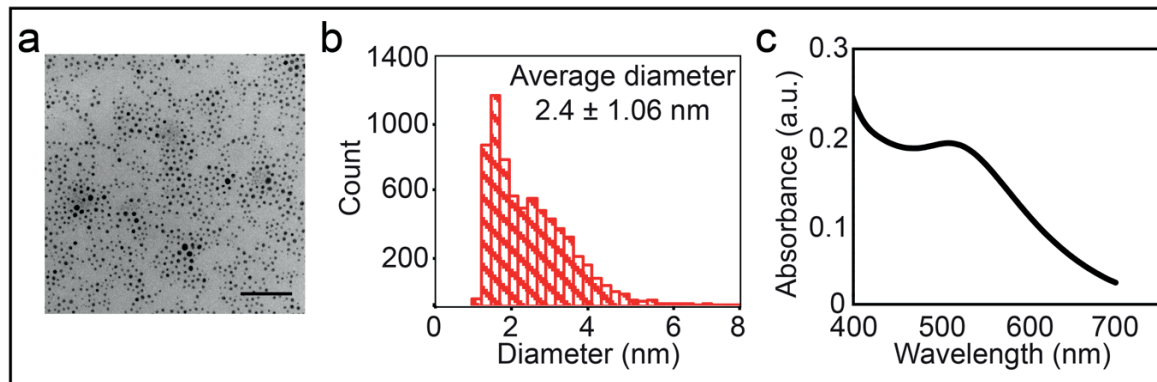


Figure A- 7 Size distribution of nanoparticles. a) Representative TEM image of MUS:OT nanoparticles. The scale bar is 20 nm. b) Histogram of core size of nanoparticles based on several TEM images. c) UV-vis spectra of the nanoparticles showed the characteristic surface plasmonic resonance peak of the nanoparticles at around 520 nm.

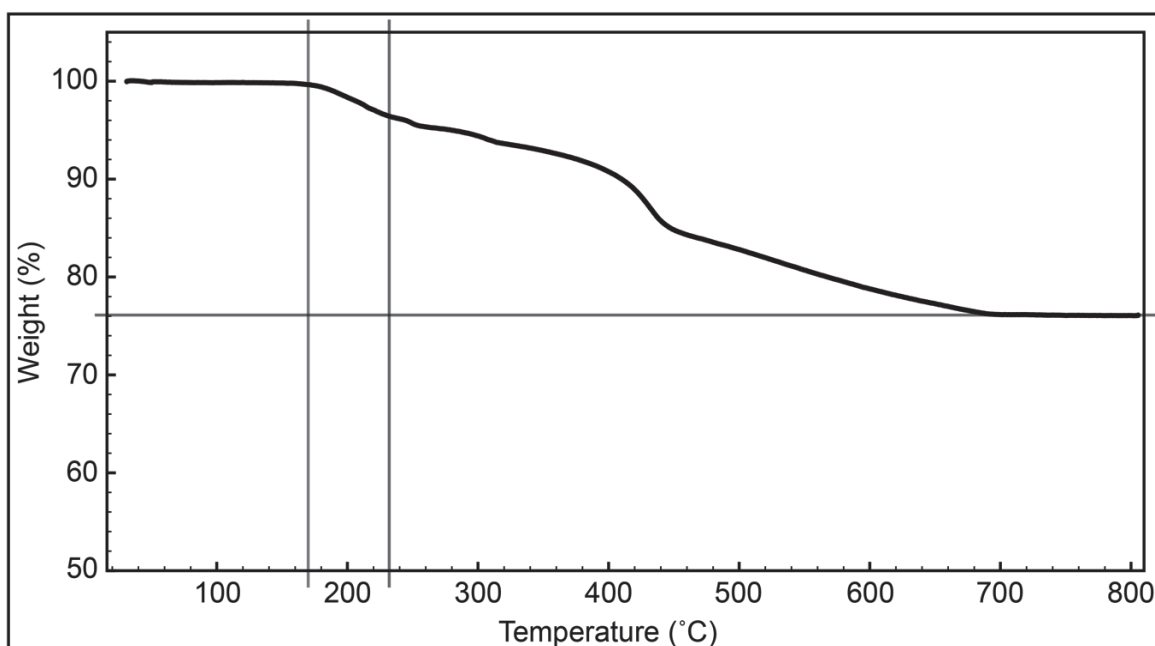


Figure A- 8 Ligand density analysis. TGA measurement of nanoparticles was done to determine ratio and density of organic material (ligands). The graph of the measurement is plotted weight percentage vs temperature. OT desorbs first between 176°C to 233°C. MUS degrades to smaller molecules and is totally burned at around 800°C. The remaining weight percentage corresponds the gold core of the nanoparticles. TGA, NMR, and TEM data (Figure 3) is combined to calculate the ligand density which is the ratio of total amount of ligand to gold surface in the sample. TEM data shows that the average diameter of the nanoparticles is 2.4 nm pointing approximately 18.08 nm² ($A_{par}=4\pi r^2$) of surface area, A_{par} and 7.23 nm³ ($V_{par}=4/3\pi r^3$) of volume, V_{par} per particle. Density of gold is 19.9 g/cm³ and the mass of one particle is $1.3969 \cdot 10^{-16}$ mg ($Mass_{particle} = V_{par} \times \text{density of gold} = 7.23 \text{ nm}^3 \times 19.9 \text{ g/cm}^3 \times 10^{-18} \text{ mm}^3/\text{nm}^3$). The remaining mass around 800°C corresponds to gold core only and there are $3.7 \cdot 10^{16}$ particle, N_{par} in the sample ($N_{par} = (Mass_{gold} / Mass_{particle}) = 5.17 \text{ mg} / 1.3969 \cdot 10^{-16} \text{ mg}$). Total surface area of the particles is $6.69 \cdot 10^{17} \text{ nm}^2$, A_{tot} ($A_{tot} = N_{par} \times A_{par} = 3.69 \cdot 10^{16} \times 18.08 \text{ nm}^2$). NMR of iodine etched nanoparticles showed MUS:OT ratio is 85:15 and the amount of organic content in TGA is 0.00146 g. Therefore, there is $3.26 \cdot 10^{18}$ amount of ligand, N_{ligand} , following the formula of $N_{ligand} = (Mass_{organic} / ((R_{OT} \times M_w(OT)) + (R_{MUS} \times M_w(MUS)))) / (R_{MUS} + R_{OT}) \times N_{Avogadro}$ ($3.26 \cdot 10^{18} = (0.00146 \text{ g} / ((15 \times 146 \text{ g/mol}) + (85 \times 291 \text{ g/mol}))) / (85 + 15) \times 6.02 \cdot 10^{23}$). Finally, the ligand density is 4.8 ligand/nm² calculated by dividing the N_{ligand} to A_{tot} ($4.8 = 3.26 \cdot 10^{18} / 6.69 \cdot 10^{17} \text{ nm}^2$).

Discussion of the Figures

This protocol describes first the synthesis of MUS ligand, then the synthesis and characterization of amphiphilic MUS:OT gold nanoparticles. By making MUS with low salt content enables the stoichiometric ratio of the nanoparticle synthesis more reliable which is the key for reproducible synthesis of MUS:OT nanoparticles of the aimed hydrophobic

content (Figure A-6). According to our finding, the use of methanol as a common solvent for MUS and OT and synthesis the particles in ethanol makes MUS:OT gold nanoparticles form in a robust way. The methods of characterization presented here make up a minimal list of experiments one needs to perform in order to acquire sufficient details of the nanoparticles and verify the success of their synthesis.

There are four critical steps in this protocol, (i) Synthesis of MUS with low salt content depending on the discarding colored impurities in each step and crystallization of MUS, (ii) Deciding on the stoichiometric ratio of OT, (iii) Work up of the nanoparticles, (iiii) Characterization of nanoparticles.

During the formation of nanoparticles MUS preferentially binds to the nanoparticle surfaces, which might be related to the solubility of the resulted nanoparticles. For example, 2 to 1 reaction ratio gives 15% OT on the surface provided by NMR calculation of etched gold nanoparticles. Therefore, a higher than aimed OT ratio should be used during the synthesis of the particles (Figure A-6). In order to be able to assess the relative ratios of the ligands on the surface, it is necessary to make sure there are no unbound ligands in the solution. The existence of unbounded ligands affects the determination of ligand ratio and density as well as the future tests that may lead to wrong interpretations. Repetitive cleaning cycles with different solvents (*i.e.* ethanol and DI-water) are required to eliminate all the unbound ligands. ^1H -NMR is of particular importance to confirm the purity of the nanoparticles. The line broadening effect of ligands owing to the complex chemical environment on the nanoparticles result in only broad peaks of the ligands. Any sharp peaks could come from the existence of unbounded ligands²⁹⁵. Furthermore, due to restricted mobility, the NMR peaks corresponding to the methylene adjacent to the thiol functional groups could not be detected, which is another signature of the nanoparticle NMR.

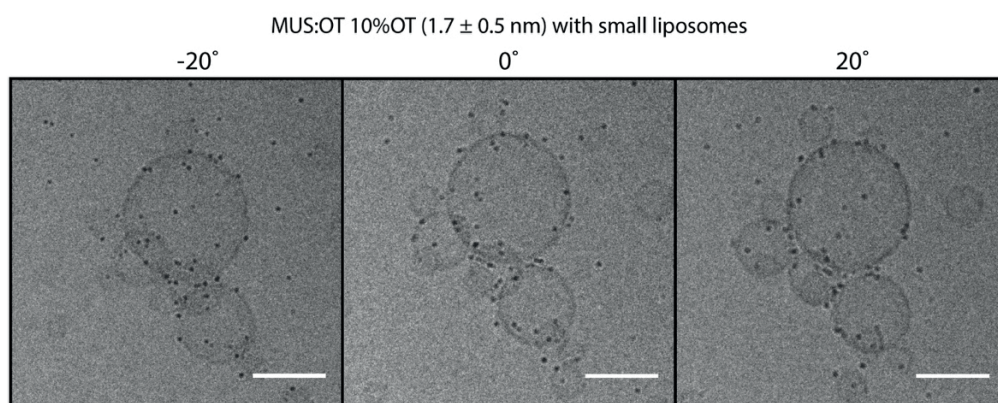
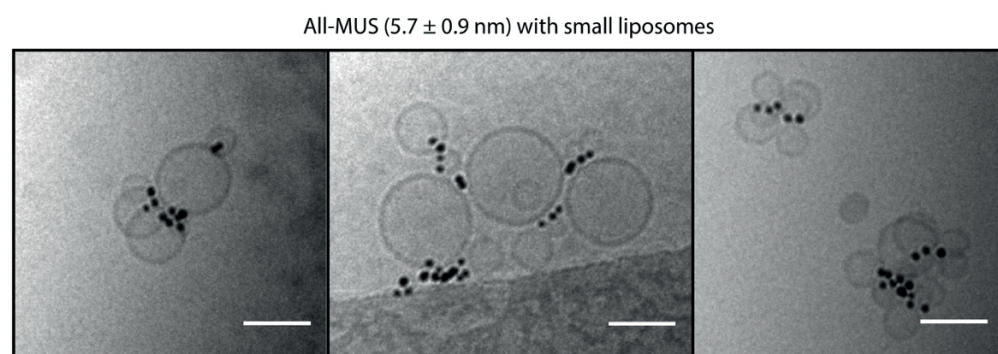
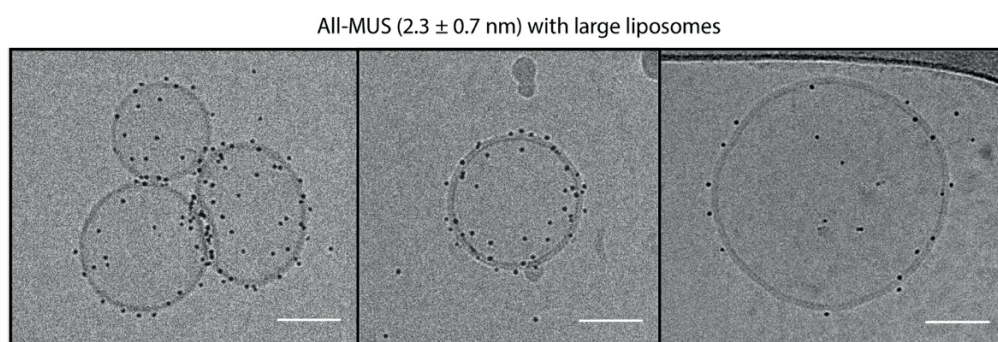
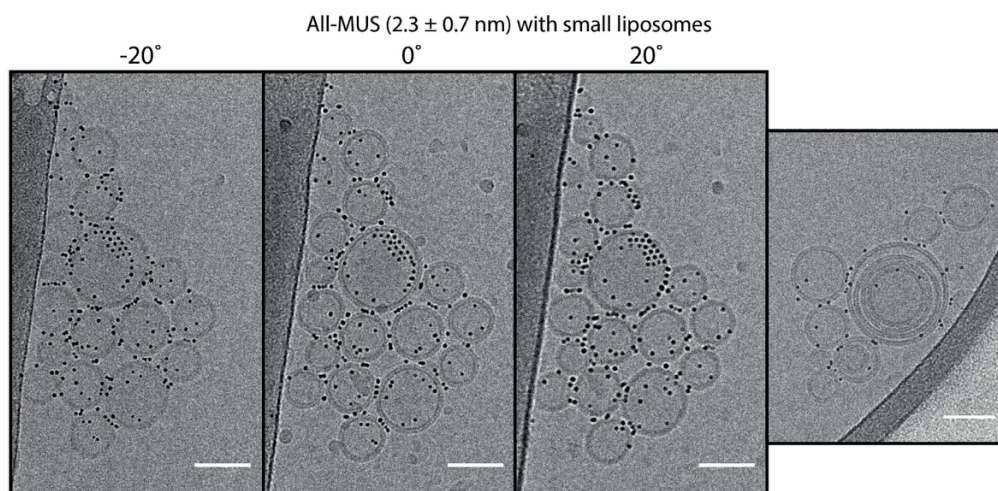
TGA is a straightforward method to calculate the percentage of the organic content of the nanoparticles. The evaluation of the surface ligand density of the ligands is based on the fact that all the thiolated ligands bind to surface gold atoms and all free ligands are washed before. To determine the ligand density, several assumptions such as the surface area as well as the packing density of the gold core should be made. TEM provides a size distribution of the gold

cores of nanoparticles that could be used to calculate approximate surface area of one nanoparticle. It should be noted that the nanoparticle synthesis described here produce a polydisperse population of particles with an average diameter of 2-3 nm and the size deviation up to 30% is normal. Also the average radius, which is used to calculate the average volume of one particle, combining with density of gold allows us to calculate the mass of one nanoparticle. Then, the mass measured by TGA over 800 °C enables us to calculate the amount of particle we had at the beginning. By using this value and the average core size, we can assume the total surface area of the gold nanoparticles. We can use the ligand ratio coming from NMR spectroscopy, and approximate about the moles of the ligands we have on the surface. The ratio of mole of ligands over surface area of gold nanoparticles provides the ligand density (Figure A-8). Clean nanoparticles should have approximately 4 ligands per nm². TGA data can also be used to estimate the ligand ratio, if the temperature interval is known for each ligand at which they desorb from the gold surface.

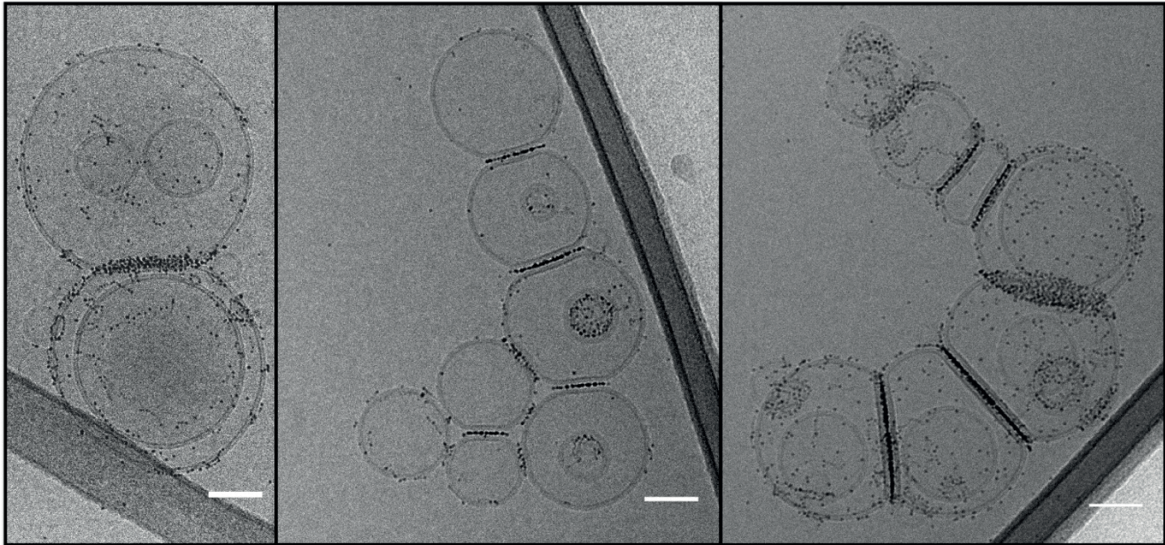
In summary, the protocol presented here provides a facile way to produce MUS ligand with low salt content and subsequently MUS:OT amphiphilic nanoparticles. One of the key factors on the reproducibility of these nanoparticles is to use MUS ligands with low inorganic salt content. These nanoparticles are very stable both as powder and in the solution (*e.g.* H₂O and physiological conditions), which should be emphasized as a requisition for many applications. Solid characterization of size and the surface properties of amphiphilic nanoparticles is essential for future applications in which the degree of amphiphilicity may play a key role.

Appendix B

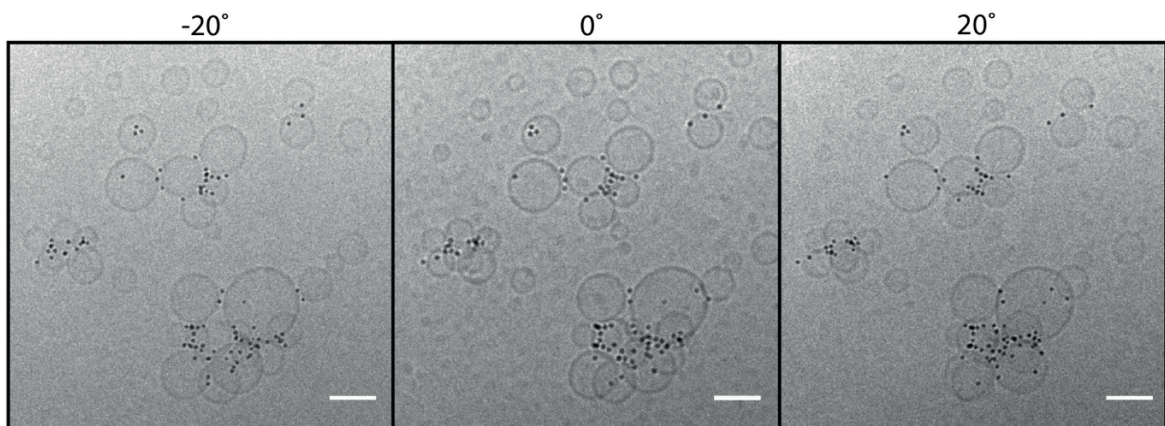
Additional images of nanoparticle-liposome systems. All the scale bars are 50 nm.



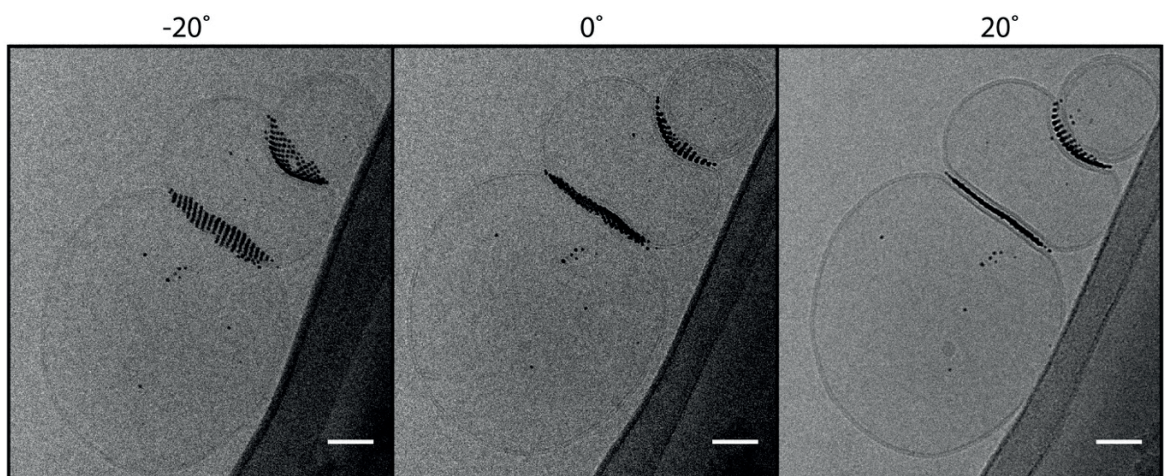
MUS:OT 10%OT (1.7 ± 0.5 nm) with large liposomes



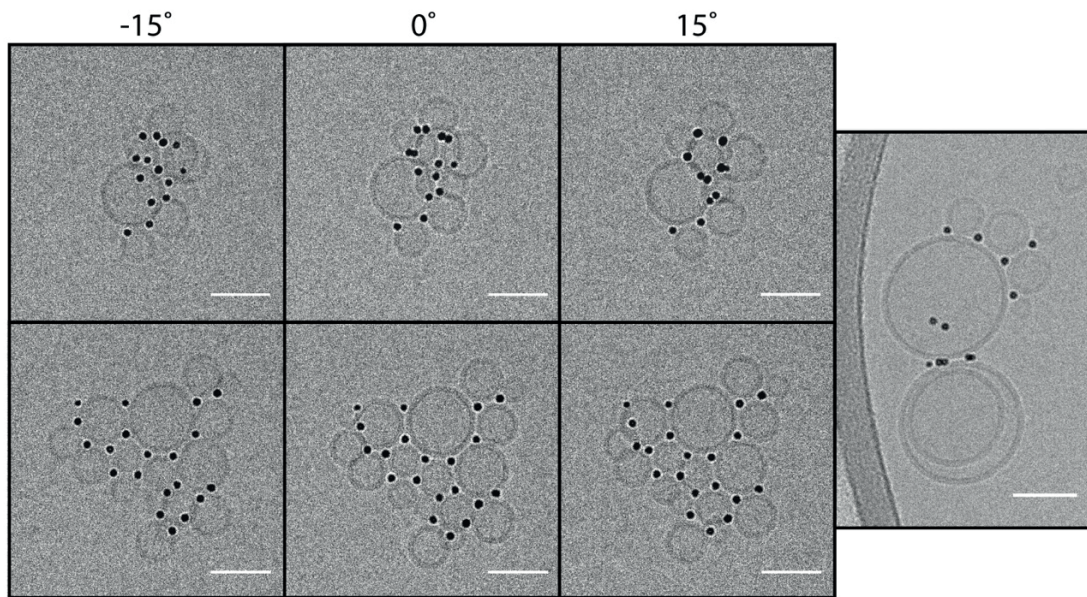
MUS:OT 10%OT (3.1 ± 0.5 nm) with small liposomes



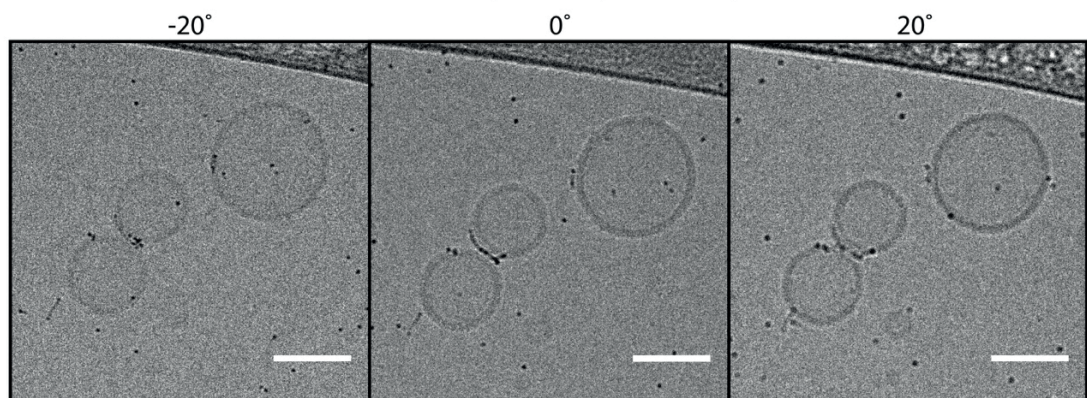
MUS:OT 10%OT (1.7 ± 0.5 nm) with large liposomes



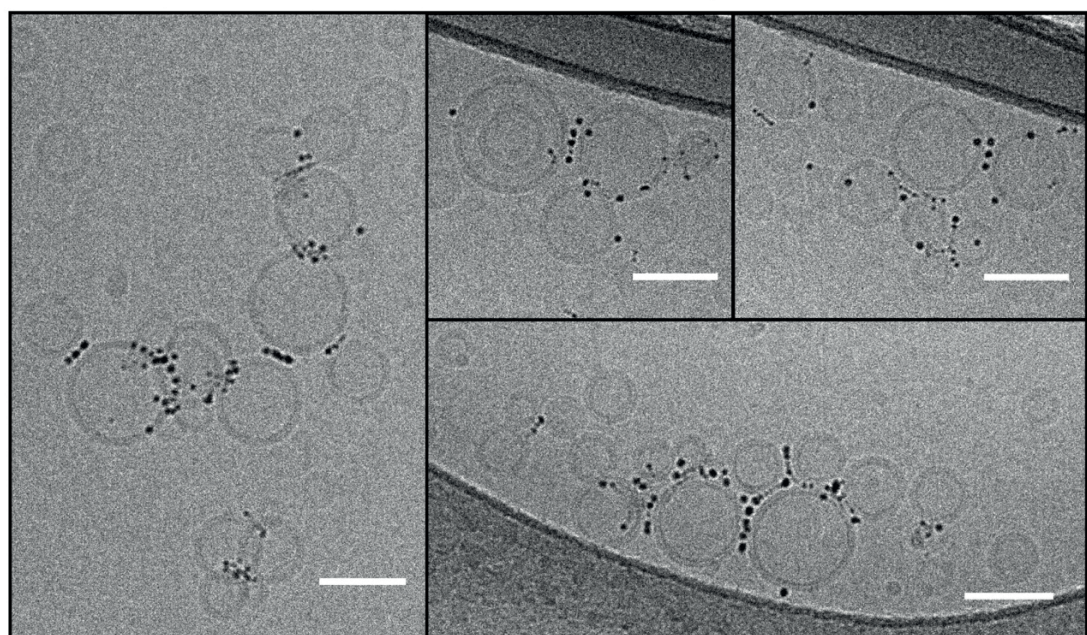
MUS:OT 10%OT (5.1 ± 1.5 nm) with small liposomes



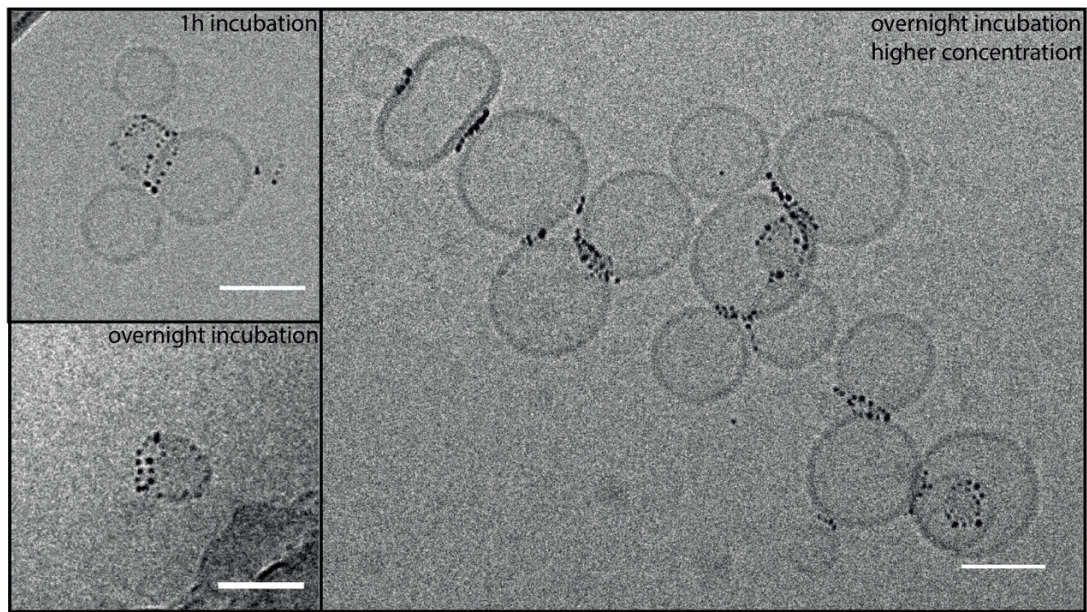
MUS:OT 20%OT (2 ± 0.9 nm) with small liposomes



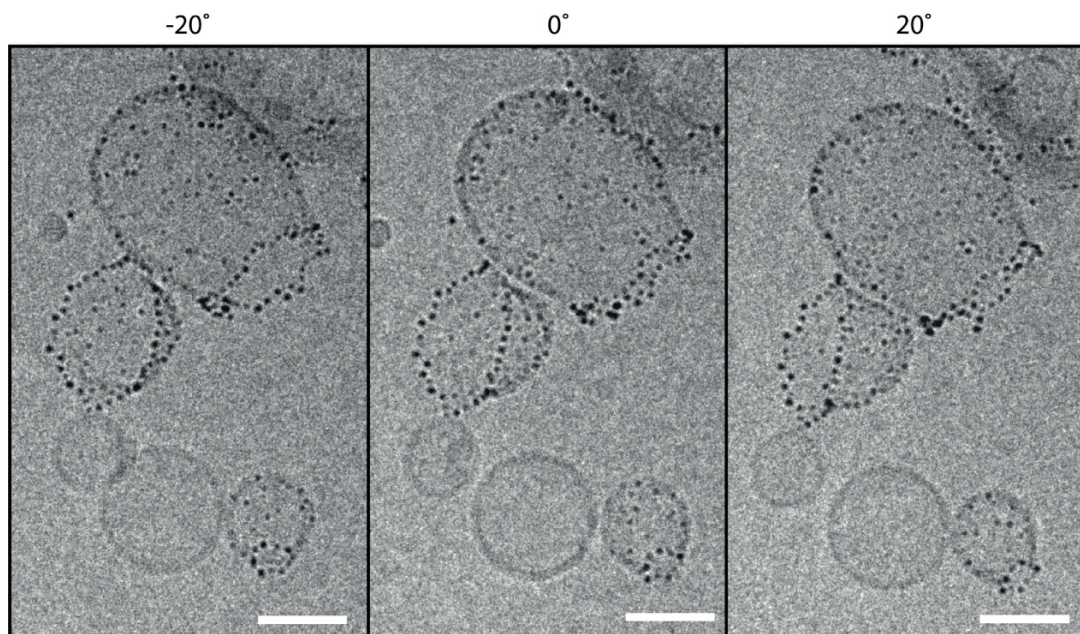
MUS:OT 20%OT (3.3 ± 1.1 nm) with small liposomes



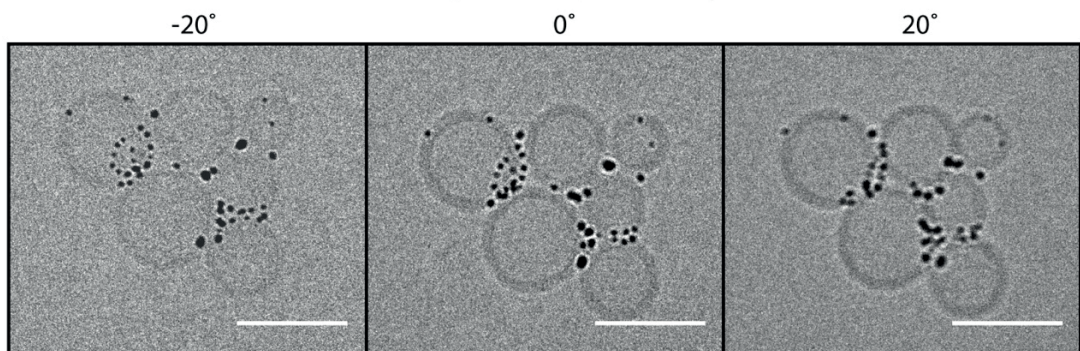
MUS:OT 30%OT (2.1 ± 1 nm) with small liposomes



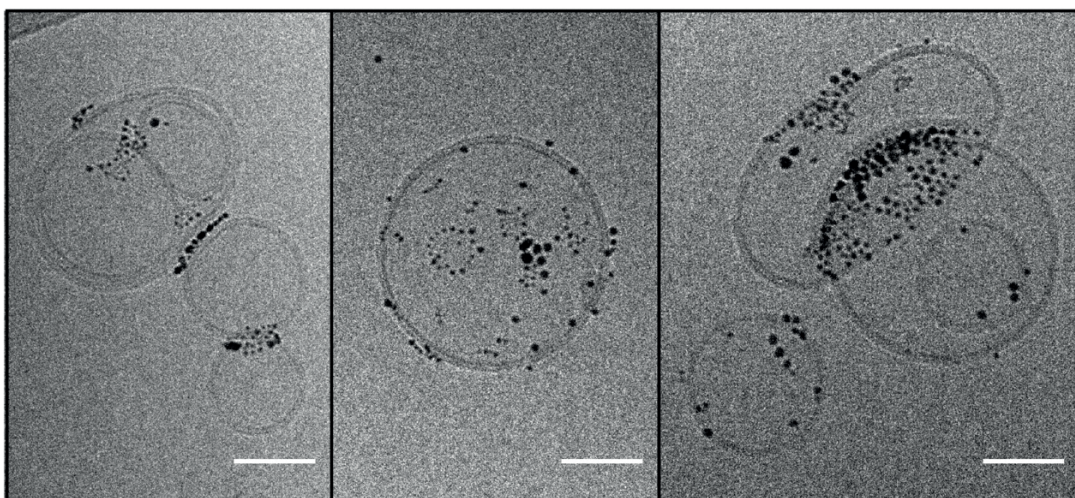
MUS:OT 30%OT (2.1 ± 1 nm) with large liposomes



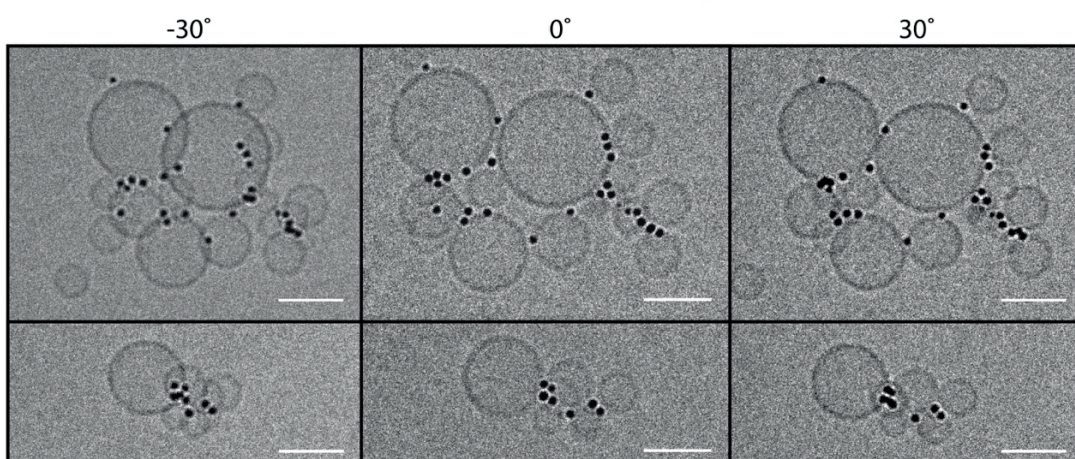
MUS:OT 30%OT (2.4 ± 1.9 nm) with small liposomes



MUS:OT 30%OT (2.7 ± 1.3 nm) with large liposomes



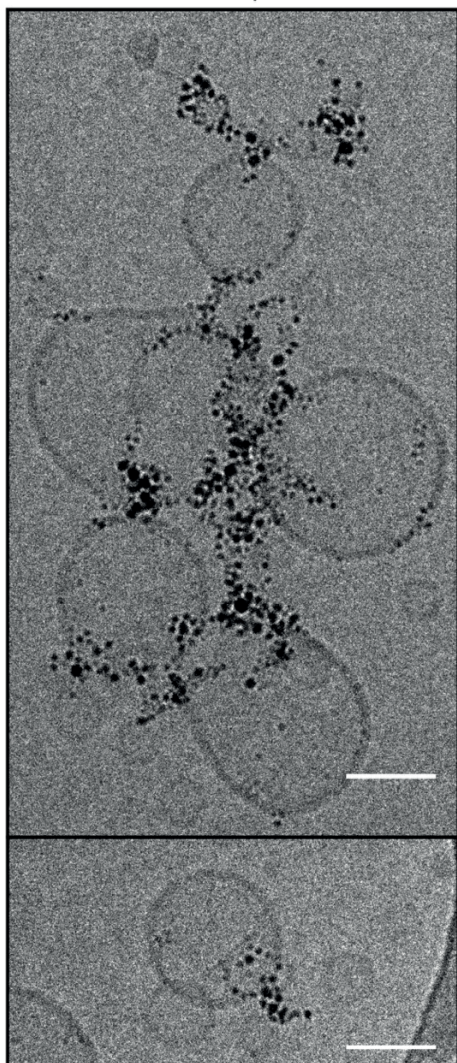
MUS:OT 30%OT (5 ± 0.9 nm) with small liposomes



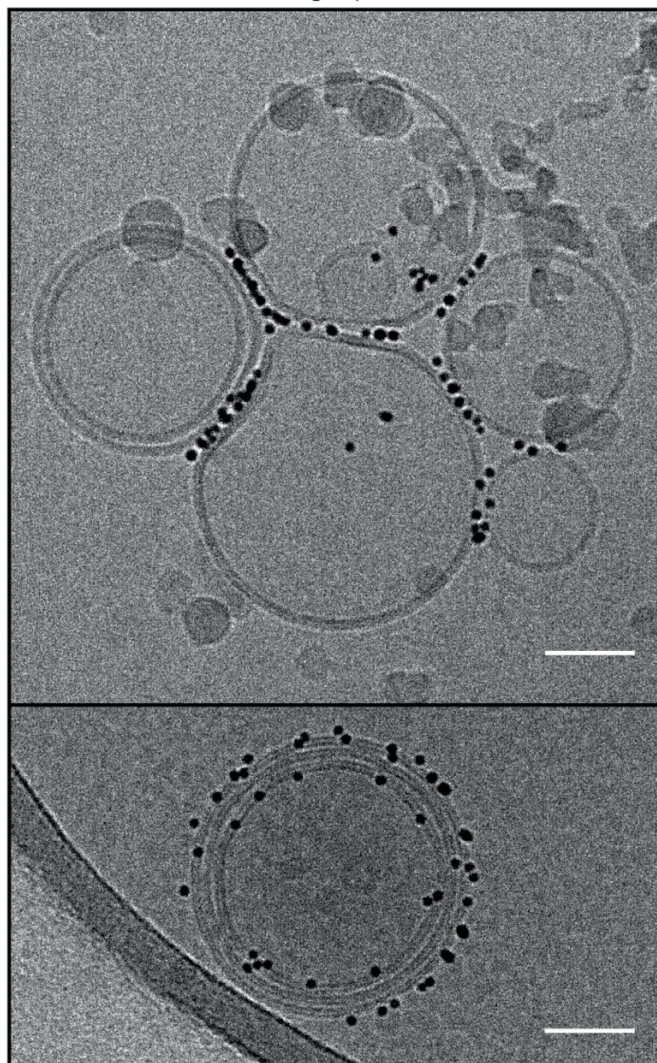
MUS:OT 30%OT (5 ± 0.9 nm) with large liposomes



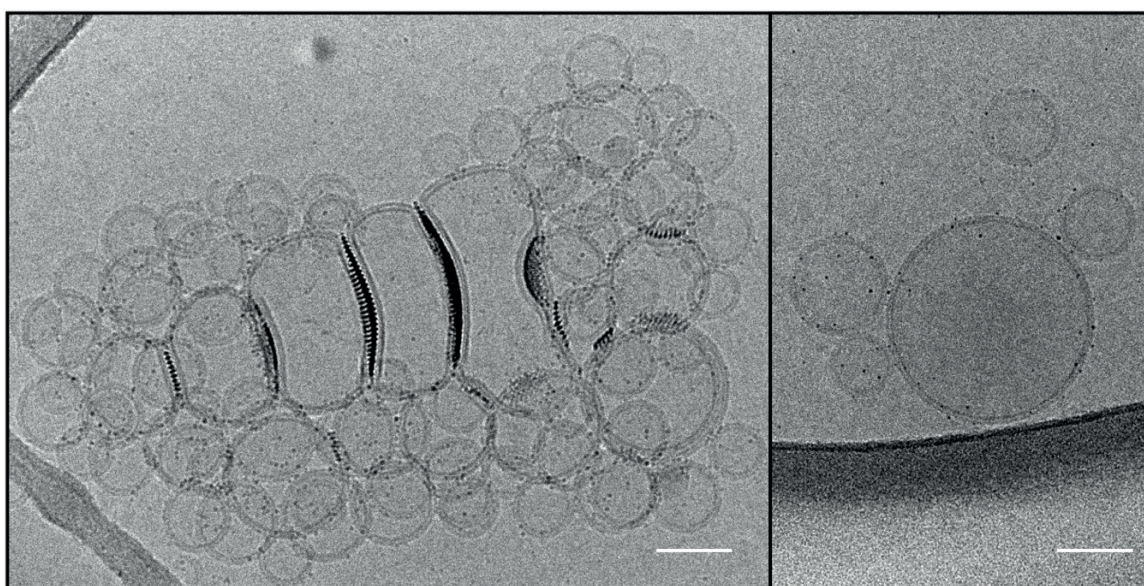
MUS:HDT 20%OT (2.6 ± 1.3 nm)
with small liposomes



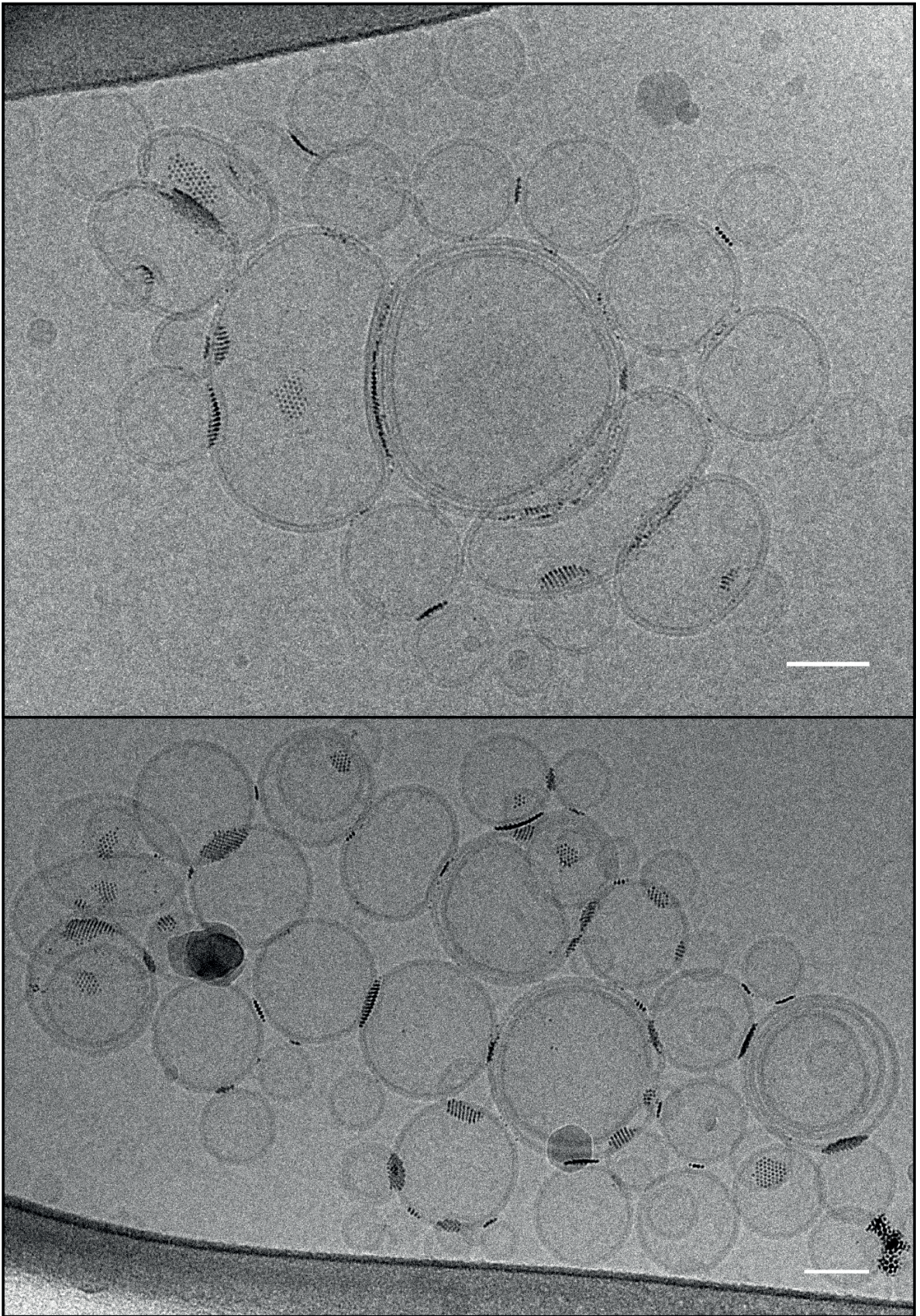
MUS:br-OT 30%br-OT (4.6 ± 1 nm)
with large liposomes



All-MPSA (1.8 ± 0.5 nm) with large liposomes



All-MES (1.8 ± 0.6 nm) with large liposomes



Appendix C

Cryo electron microscopy

Microscopy is an important characterization technique for the structure of biological components. Even though electron microscopy offers a higher resolution than light microscopy, imaging of biological samples was limited by the instrumental constraints. The necessity of a high vacuum in the microscope is inherently incompatible with the biological specimens' native hydrated state. Cryo-transmission electron microscopy has enabled the imaging of delicate biological samples by freezing them in vitrified ice (*i.e.* amorphous ice without any crystal formations) in which they can maintain their hydrated native form²⁹⁶. Related to this thesis, cryo-EM has been used to characterize many liposomal systems^{228,297–300}.

A general workflow for cryo-EM session starts with sample optimization (*i.e.* increasing homogeneity and concentration), sample preparation, imaging and image processing. For example, if a tomogram is acquired during imaging, then the workflow after imaging includes image alignments, 3D reconstruction, and further post processing. Finally, the data becomes ready to be interpreted³⁰¹.

The sample preparation for cryo-EM varies depending on the size of the samples. For instance, samples over 10 μm are prepared by high pressure freezing, whereas samples below 10 μm are prepared by plunge freezing. Figure A-1 depicts the plunge freezing method in which the sample is deposited on a grid, the excess sample is blotted and the grid is plunge-frozen in a cryogen such as liquid ethane around 100 K faster than the formation of crystalline ice³⁰². Furthermore, if the thickness of the sample is above 500 nm, it can be thinned by various methods such as vitreous sectioning, and focused ion beam milling. The upper limit of sample thickness is 500 nm for electrons to traverse the sample for image formation. Still, it is crucial to prepare thin samples not to lose electrons with multiple scattering. Once the sample is ready it is important to keep the temperature during sample transfer, and storage below -135°C to avoid the formation of cubic ice.

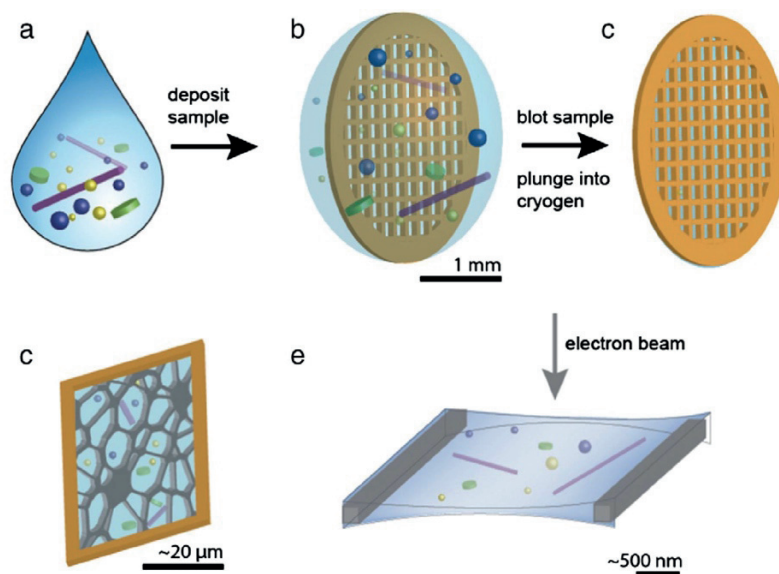


Figure C- 1 Schematic illustration of cryo-EM samples prepared by plunge freezing. The figure is adapted from reference³⁰³ with permission.

Although trapped in vitreous ice the imaging of sensitive biological samples remains challenging. Therefore, cryo-EM uses a low electron dose imaging strategy to avoid beam damage of the sample. A region of interest (ROI) is localized at low magnification, focusing is performed in the vicinity of the ROI, and the image of ROI is acquired with high magnification and electron dose (*i.e.* $100 \text{ e}/\text{\AA}^2$) during a defined exposure time. A shutter in the column mediates the discrete exposure of electron beam to the samples³⁰⁴.

Biological samples predominantly consist of light atoms like carbon, oxygen, nitrogen or hydrogen, that only provide low contrast in EM. To increase the contrast of the images without additional staining techniques the most common strategy is to underfocus the sample (defocusing). Defocusing is introduced by focusing the electron beam below the image plane which shifts the contrast transfer function (CTF) to lower spatial frequencies. This change on the CTF makes the sample visible, while losing the information at high spatial frequencies which gives the high resolution information after post processing³⁰⁵. Recently, phase plates have been used to induce phase contrast without defocusing and subsequent compromise from high resolution information.

To be able to acquire further structural information from the sample, a single image may not be sufficient. Tomography provides more detailed data in which the images of different

orientations of the same sample are acquired by rotating the sample around an axis³⁰⁶. These images are, then back-projected to form a 3D volume of the sample. Figure C-2 depicts the methodology of the tomogram acquisition.

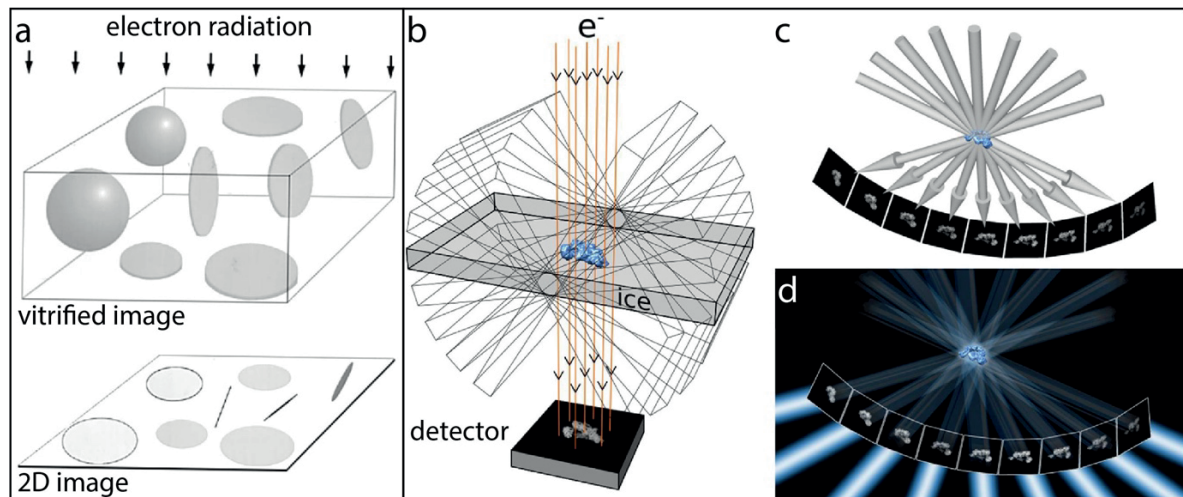


Figure C- 2 Schematic illustrations of methodology of tomogram acquisition a) 2D projection of lipid vesicles and disks in electron microscope, b) 2D projections acquired with different angles, c) a tilt-series formed through compilation of each image, d) tilt-series formed the 3D tomogram. This figure is adapted from references^{297,307} with permission.

There are three possible acquisition schemes for tomograms: single-axis, dual-axis tilt or conical tilt. The most common approach is the single-axis acquisition in which the sample is rotated around one fixed tilt axis. The key strategy of tomogram acquisition is the distribution of the total electron dose to each single tilted image, even though low electron dose increases the noise level of the images. But, still this will ensure the stability of the sample without inducing beam damage^{301,308}. Noise level can be decreased through introduction of energy filters to the column in which the electrons are separated depending on their wavelength.

Generally, a tilting series between -60° to $+60^\circ$ with an increments of 2° yielding 61 images provides sufficient data. This can exceed up to 280 images by decreasing the increments, increasing boundary angles and employing dual-axis tilt. With an increase in the tilting angle, the thickness of the sample subject to electron beam increases³⁰⁷. This phenomenon results in multiple scattering of electron beam and a subsequent contrast and data loss. Boundaries on the extremes of tilting angles and the sample thickness change cause information loss along the z axis, which is called 'missing wedge'. That is why the alignment of the 2D

projections of tilting angles is important for an accurate tomogram. To ameliorate the conditions fiducial markers can be used to act as reference points for the alignment of the images.

3D reconstruction of a tomogram is done through the back-projection of each tilted image, construction of 3D Fourier volume and then transformation of it into real space yielding the 3D tomographic volume. During this process, the images are also processed to decrease the noise. Following the tomogram reconstruction, the data is mostly ready to be interpreted. However, additional post processing schemes like sub-tomogram averaging can be followed for better resolution and subsequently further details³⁰⁹.

References

- (1) Luo, D.; Carter, K. A.; Razi, A.; Geng, J.; Shao, S.; Giraldo, D.; Sunar, U.; Ortega, J.; Lovell, J. F. Biomaterials Doxorubicin Encapsulated in Stealth Liposomes Conferred with Light-Triggered Drug Release. *Biomaterials* **2016**, *75*, 193–202.
- (2) Samad, A.; Sultana, Y.; Aqil, M. Liposomal Drug Delivery Systems: An Update Review. *Curr. Drug Deliv.* **2007**, *4*, 297–305.
- (3) El Maghraby, G. M.; Barry, B. W.; Williams, a. C. Liposomes and Skin: From Drug Delivery to Model Membranes. *Eur. J. Pharm. Sci.* **2008**, *34*, 203–222.
- (4) Giljohann, D. A.; Seferos, D. S.; Daniel, W. L.; Massich, M. D.; Patel, P. C.; Mirkin, C. A. Gold Nanoparticles for Biology and Medicine. *Angew. Chemie - Int. Ed.* **2010**, *49*, 3280–3294.
- (5) Michel, R.; Gradzielski, M. Experimental Aspects of Colloidal Interactions in Mixed Systems of Liposome and Inorganic Nanoparticle and Their Applications. *Int. J. Mol. Sci.* **2012**, *13*, 11610–11642.
- (6) Verma, A.; Uzun, O.; Hu, Y.; Hu, Y.; Han, H.-S.; Watson, N.; Chen, S.; Irvine, D. J.; Stellacci, F. Surface-Structure-Regulated Cell-Membrane Penetration by Monolayer-Protected Nanoparticles. *Nat. Mater.* **2008**, *7*, 588–595.
- (7) Van Lehn, R. C.; Ricci, M.; Silva, P. H. J.; Andreozzi, P.; Reguera, J.; Voïtchovsky, K.; Stellacci, F.; Alexander-Katz, A. Lipid Tail Protrusions Mediate the Insertion of Nanoparticles into Model Cell Membranes. *Nat. Commun.* **2014**, *5*, 4482–4493.
- (8) Van Lehn, R. C.; Alexander-Katz, A. Free Energy Change for Insertion of Charged , Monolayer-Protected Nanoparticles into Lipid Bilayers. *Soft Matter* **2014**, *10*, 648–658.
- (9) Jewell, C. M.; Jung, J. M.; Atukorale, P. U.; Carney, R. P.; Stellacci, F.; Irvine, D. J. Oligonucleotide Delivery by Cell-Penetrating “Striped” Nanoparticles. *Angew. Chemie - Int. Ed.* **2011**, *50*, 12312–12315.
- (10) Singer, S. J.; Nicolson, G. L. The Fluid Mosaic Model of the Structure of Cell Membranes. *Science* **1972**, *175*, 720–731.
- (11) Sezgin, E.; Levental, I.; Mayor, S.; Eggeling, C. The Mystery of Membrane Organization: Composition, Regulation and Roles of Lipid Rafts. *Nat. Rev. Mol. Cell Biol.* **2017**, *18*,

- 361–374.
- (12) Van Meer, G.; Voelker, D. R.; Feigenson, G. W. Membrane Lipids: Where They Are and How They Behave. *Nat. Rev. Mol. Cell Biol.* **2008**, *9*, 112–124.
 - (13) Israelachvili, J. N.; Ninham, B. W. Theory of Self-Assembly of Lipid Bilayers and Vesicles. *Biochim. Biophys. Acta* **1977**, *470*, 185–201.
 - (14) Edidin, M. Lipids on the Frontier: A Century of Cell-Membrane Bilayers. *Nat. Rev. Mol. Cell Biol.* **2003**, *4*, 414–418.
 - (15) Harayama, T.; Riezman, H. Understanding the Diversity of Membrane Lipid Composition. *Nat. Rev. Mol. Cell Biol.* **2018**, *19*, 281–296.
 - (16) Pabst, G.; Kučerka, N.; Nieh, M.-P.; Katsaras, J. *Liposomes, Lipid Bilayers and Model Membranes: From Basic Research to Application*; 2014.
 - (17) Pike, L. J. Lipid Rafts. *J. Lipid Res.* **2003**, *44*, 655–667.
 - (18) Gable, K.; Gupta, S. D.; Han, G.; Niranjanakumari, S.; Harmon, J. M.; Dunn, T. M. A Disease-Causing Mutation in the Active Site of Serine Palmitoyltransferase Causes Catalytic Promiscuity. *J. Biol. Chem.* **2010**, *285*, 22846–22852.
 - (19) Gulbins, E.; Palmada, M.; Reichel, M.; Lüth, A.; Böhmer, C.; Amato, D.; Müller, C. P.; Tischbirek, C. H.; Groemer, T. W.; Tabatabai, G.; *et al.* Acid Sphingomyelinase-Ceramide System Mediates Effects of Antidepressant Drugs. *Nat. Med.* **2013**, *19*, 934–938.
 - (20) Iizuka-Hishikawa, Y.; Hishikawa, D.; Sasaki, J.; Takubo, K.; Goto, M.; Nagata, K.; Nakanishi, H.; Shindou, H.; Okamura, T.; Ito, C.; *et al.* Lysophosphatidic Acid Acyltransferase 3 Tunes the Membrane Status of Germ Cells by Incorporating Docosahexaenoic Acid during Spermatogenesis. *J. Biol. Chem.* **2017**, *292*, 12065–12076.
 - (21) Wigger, L.; Cruciani-Guglielmacci, C.; Nicolas, A.; Denom, J.; Fernandez, N.; Fumeron, F.; Marques-Vidal, P.; Ktorza, A.; Kramer, W.; Schulte, A.; *et al.* Plasma Dihydroceramides Are Diabetes Susceptibility Biomarker Candidates in Mice and Humans. *Cell Rep.* **2017**, *18*, 2269–2279.
 - (22) Perrotti, F.; Rosa, C.; Cicalini, I.; Sacchetta, P.; Del Boccio, P.; Genovesi, D.; Pieragostino, D. Advances in Lipidomics for Cancer Biomarkers Discovery. *Int. J. Mol. Sci.* **2016**, *17*, 1992–2018.
 - (23) Schaefer, E. J.; Bongard, V.; Beiser, A. S.; Lamon-Fava, S.; Robins, S. J.; Au, R.; Tucker, K. L.; Kyle, D. J.; Wilson, P.; Wolf, P. Plasma Phosphatidylcholine Docosahexaenoic Acid

- Content and Risk of Dementia and Alzheimer Disease: The Framingham Heart Study. *Arch. Neurol.* **2006**, *63*, 1545–1550.
- (24) Yeagle, P. L. *The Membranes of Cells The Membranes of Cells Third Edition*; 2016.
- (25) Zimmerberg, J.; Kozlov, M. M. How Proteins Produce Cellular Membrane Curvature. *Nat. Rev. Mol. Cell Biol.* **2006**, *7*, 9–19.
- (26) Farsad, K.; De Camilli, P. Mechanisms of Membrane Deformation. *Curr. Opin. Cell Biol.* **2003**, *15*, 372–381.
- (27) Peter, B. J.; Kent, H. M.; Mills, I. G.; Vallis, Y.; Butler, P. J. G.; Evans, P. R.; McMahon, H. T. BAR Domains as Sensors of Membrane Curvature: The Amphiphysin BAR Structure. *Science* **2004**, *303*, 495–499.
- (28) Chernomordik, L. V.; Kozlov, M. M. Protein-Lipid Interplay in Fusion and Fission of Biological Membranes. *Annu. Rev. Biochem.* **2003**, *72*, 175–207.
- (29) Zimmerberg, J.; McLaughlin, S. Membrane Curvature: How BAR Domains Bend Bilayers. *Curr. Biol.* **2004**, *14*, 250–252.
- (30) Stahelin, R. V.; Long, F.; Peter, B. J.; Murray, D.; De Camilli, P.; McMahon, H. T.; Cho, W. Contrasting Membrane Interaction Mechanisms of AP180 N-Terminal Homology (ANTH) and Epsin N-Terminal Homology (ENTH) Domains. *J. Biol. Chem.* **2003**, *278*, 28993–28999.
- (31) Lee, M. C. S.; Orci, L.; Hamamoto, S.; Futai, E.; Ravazzola, M.; Schekman, R. Sar1p N-Terminal Helix Initiates Membrane Curvature and Completes the Fission of a COPII Vesicle. *Cell* **2005**, *122*, 605–617.
- (32) Royle, S. J. The Cellular Functions of Clathrin. *Cell Mol. life Sci.* **2006**, *63*, 1823–1832.
- (33) Takei, K.; Haucke, V.; Slepnev, V.; Farsad, K.; Salazar, M.; Chen, H.; De Camilli, P. Generation of Coated Intermediates of Clathrin-Mediated Endocytosis on Protein-Free Liposomes. *Cell* **1998**, *94*, 131–141.
- (34) Gumbiner, B. M. Cell Adhesion: The Molecular Basis of Tissue Architecture and Morphogenesis. *Cell* **1996**, *84*, 345–357.
- (35) Braga, V. M. M. Cell – Cell Adhesion and Signalling. *Curr. Opin. Cell Biol.* **2002**, *14*, 546–556.
- (36) Furuse, M.; Itoh, M.; Hirase, T.; Nagafuchi, A.; Yonemura, S.; Tsukita, S.; Tsukita, S. Direct Association of Occludin with ZO-1 and Its Possible Involvement in the Localization of Occludin at Tight Junctions. *J. Cell Biol.* **1994**, *127*, 1617–1626.

- (37) Takeichi, M. The Cadherins: Cell-Cell Adhesion Molecules Controlling Animal Morphogenesis. *Development* **1988**, *102*, 639–655.
- (38) Kumar, N. M.; Gilula, N. B. The Gap Junction Review Communication Channel. *Cell* **1996**, *84*, 381–388.
- (39) Garrod, D. R. Desmosomes and Hemidesmosomes. *Curr. Opin. Cell Biol.* **1993**, *5*, 40–40.
- (40) Green, K. J.; Gaudry, C. A. Are Desmosomes More than Tethers for Intermediate Filaments? *Nat. Rev. Mol. Cell Biol.* **2000**, *1*, 208–216.
- (41) Jahn, R.; Lang, T.; Südhof, T. C. Membrane Fusion. *Cell* **2003**, *112*, 519–533.
- (42) Martens, S.; McMahon, H. T. Mechanisms of Membrane Fusion: Disparate Players and Common Principles. *Nat. Rev. Mol. Cell Biol.* **2008**, *9*, 543–556.
- (43) Mondal Roy, S.; Sarkar, M. Membrane Fusion Induced by Small Molecules and Ions. *J. Lipids* **2011**, *2011*, 1–14.
- (44) Diao, J.; Ishitsuka, Y.; Lee, H.; Joo, C.; Su, Z.; Syed, S.; Shin, Y. K.; Yoon, T. Y.; Ha, T. A Single Vesicle-Vesicle Fusion Assay for in Vitro Studies of Snares and Accessory Proteins. *Nat. Protoc.* **2012**, *7*, 921–934.
- (45) Chen, Y. A.; Scheller, R. H. SNARE-Mediated Membrane Fusion. *Nat. Rev. Mol. Cell Biol.* **2001**, *2*, 98–106.
- (46) Bennett, M. K.; Calakos, N.; Scheller, R. H. Syntaxin: A Synaptic Protein Implicated in Docking of Synaptic Vesicles at Presynaptic Active Zones. *Science* **1992**, *257*, 255–259.
- (47) Oyler, G. a; Higgins, G. a; Hart, R. a; Battenberg, E.; Bloom, F. E.; Wilson, M. C.; Oyler, A.; Higgins, A.; Hart, A.; Bloom, F. The Identification of a Novel Synaptosomal-Associated Protein, SNAP-25, Differentially Expressed by Neuronal Subpopulations. *J. Cell Biol.* **1989**, *109*, 3039–3052.
- (48) Baumert, M.; Maycox, P. R.; Navone, F.; Camilli, P. De; Jahn, R. Synaptobrevin: An Integral Membrane Protein of 18000 Daltons Present in Small Synaptic Vesicles of Rat Brain. *EMBO J.* **1989**, *8*, 379–384.
- (49) Jahn, R.; Scheller, R. H. SNAREs - Engines for Membrane Fusion. *Nat. Rev. Mol. Cell Biol.* **2006**, *7*, 631–643.
- (50) Chen, Y. A.; Scales, S. J.; Patel, S. M.; Doung, Y.-C.; Scheller, R. H. SNARE Complex Formation Is Triggered by Ca²⁺ and Drives Membrane Fusion. *Cell* **1999**, *97*, 165–174.
- (51) Chen, X.; Araç, D.; Wang, T. M.; Gilpin, C. J.; Zimmerberg, J.; Rizo, J. SNARE-Mediated

- Lipid Mixing Depends on the Physical State of the Vesicles. *Biophys. J.* **2006**, *90*, 2062–2074.
- (52) Shi, L.; Shen, Q.; Kiel, A.; Wang, J.; Wang, H.; Melia, T. J.; Rothman, J. E.; Pincet, F. SNARE Proteins : One to Fuse and Fusion Pore Open. *Science* **2012**, 1355–1359.
 - (53) Munson, M. Synaptic-Vesicle Fusion: A Need for Speed. *Nat. Struct. Mol. Biol.* **2015**, *22*, 509–511.
 - (54) Geppert, M.; Südhof, T. C. RAB3 and Synaptotagmin: The Yin and Yang of Synaptic Membrane Fusion. *Annu. Rev. Neurosci.* **1998**, *21*, 75–95.
 - (55) Tang, J.; Maximov, A.; Shin, O. H.; Dai, H.; Rizo, J.; Südhof, T. C. A Complexin/Synaptotagmin 1 Switch Controls Fast Synaptic Vesicle Exocytosis. *Cell* **2006**, *126*, 1175–1187.
 - (56) van den Bogaart, G.; Jahn, R. Inside Insight to Membrane Fusion. *Proc. Natl. Acad. Sci.* **2011**, *108*, 11729–11730.
 - (57) Pooga, M.; Langel, Ü. *Cell-Penetrating Peptides - Methods and Protocols*; 2015.
 - (58) Heitz, F.; Morris, M. C.; Divita, G. Twenty Years of Cell - Penetrating Peptides : From Molecular Mechanisms to Therapeutics. *Br. J. Pharmacol.* **2009**, *157*, 195–206.
 - (59) Kristensen, M.; Birch, D.; Nielsen, H. M. Applications and Challenges for Use of Cell-Penetrating Peptides as Delivery Vectors for Peptide and Protein Cargos. *Int. J. Mol. Sci.* **2016**, *17*, 185–202.
 - (60) Guidotti, G.; Brambilla, L.; Rossi, D. Cell-Penetrating Peptides: From Basic Research to Clinics. *Trends Pharmacol. Sci.* **2017**, *38*, 406–424.
 - (61) Ziegler, A. Thermodynamic Studies and Binding Mechanisms of Cell-Penetrating Peptides with Lipids and Glycosaminoglycans. *Adv. Drug Deliv. Rev.* **2008**, *60*, 580–597.
 - (62) Lis, L. J.; McAlister, M.; Fuller, N.; Rand, R. P.; Parsegian, V. A. Interactions between Neutral Phospholipid Bilayer Membranes. *Biophys. J.* **1982**, *37*, 657–665.
 - (63) Deshayes, S.; Plénat, T.; Aldrian-Herrada, G.; Divita, G.; Le Grimellec, C.; Heitz, F. Primary Amphipathic Cell-Penetrating Peptides: Structural Requirements and Interactions with Model Membranes. *Biochemistry* **2004**, *43*, 7698–7706.
 - (64) Magzoub, M.; Kilk, K.; Eriksson, L. E. G.; Langel, Ü.; Gräslund, A. Interaction and Structure Induction of Cell-Penetrating Peptides in the Presence of Phospholipid Vesicles. *Biochim. Biophys. Acta - Biomembr.* **2001**, *1512*, 77–89.
 - (65) Datrie, M.; Schumann, M.; Wieprecht, T.; Winkler, A.; Beyermann, M.; Krause, E.;

- Matsuzaki, K.; Murase, O.; Bienert, M. Peptide Helicity and Membrane Surface Charge Modulate the Balance of Electrostatic and Hydrophobic Interactions with Lipid Bilayers and Biological Membranes. *Biochemistry* **1996**, *35*, 12612–12622.
- (66) Oehlke, J.; Krause, E.; Wiesner, B.; Beyermann, M.; Bienert, M. Extensive Cellular Uptake into Endothelial Cells of an Amphipathic β -Sheet Forming Peptide. *FEBS Lett.* **1997**, *415*, 196–199.
- (67) Sigal, C. T.; Zhou, W.; Buser, C. A.; McLaughlin, S.; Resh, M. D. Amino-Terminal Basic Residues of Src Mediate Membrane Binding through Electrostatic Interaction with Acidic Phospholipids. *Proc. Natl. Acad. Sci.* **1994**, *91*, 12253–12257.
- (68) Futaki, S.; Ohashi, W.; Suzuki, T.; Niwa, M.; Tanaka, S.; Ueda, K.; Harashima, H.; Sugiura, Y. Stearylized Arginine-Rich Peptides: A New Class of Transfection Systems. *Bioconjug. Chem.* **2001**, *12*, 1005–1011.
- (69) Patrick, R. Cell-Penetrating Nanoparticles : Characterization and Function. **2013**, 5859.
- (70) Lundberg, M.; Wikström, S.; Johansson, M. Cell Surface Adherence and Endocytosis of Protein Transduction Domains. *Mol. Ther.* **2003**, *8*, 143–150.
- (71) Fretz, M. M.; Penning, N. A.; Al-Taei, S.; Futaki, S.; Takeuchi, T.; Nakase, I.; Storm, G.; Jones, A. T. Temperature-, Concentration- and Cholesterol-Dependent Translocation of L- and D-Octa-Arginine across the Plasma and Nuclear Membrane of CD34⁺ Leukaemia Cells. *Biochem. J.* **2007**, *403*, 335–342.
- (72) Pack, D. W.; Hoffman, A. S.; Pun, S.; Stayton, P. S. Design and Development of Polymers for Gene Delivery. *Nat. Rev. Drug Discov.* **2005**, *4*, 581–593.
- (73) Wang, H. Y.; Chen, J. X.; Sun, Y. X.; Deng, J. Z.; Li, C.; Zhang, X. Z.; Zhuo, R. X. Construction of Cell Penetrating Peptide Vectors with N-Terminal Stearylized Nuclear Localization Signal for Targeted Delivery of DNA into the Cell Nuclei. *J. Control. Release* **2011**, *155*, 26–33.
- (74) Mouritsen, O. G.; Bagatolli, L. A.; Mersini-houghton, L. *Life — As a Matter of Fat*; 2005.
- (75) Alberts, B.; Johnson, A.; Lewis, J.; Raff, M.; Roberts, K.; Walter, P. *Molecular Biology of the Cell*; 2013; Vol. 53.
- (76) Ramanathan, M.; Shrestha, L. K.; Mori, T.; Ji, Q.; Hill, J. P.; Ariga, K. Amphiphile Nanoarchitectonics: From Basic Physical Chemistry to Advanced Applications. *Phys. Chem, Chem, Phys.* **2013**, *15*, 10580–10611.
- (77) Parkar, N. S.; Akpa, B. S.; Nitsche, L. C.; Wedgewood, L. E.; Place, A. T.; Sverdlov, M. S.;

- Chaga, O.; Minshall, R. D. Vesicle Formation and Endocytosis: Function, Machinery, Mechanisms, and Modeling. *Antioxid. Redox Signal.* **2009**, *11*, 1301–1312.
- (78) Jesorka, A.; Orwar, O. Liposomes: Technologies and Analytical Applications. *Annu. Rev. Anal. Chem.* **2008**, *1*, 801–832.
- (79) Liu, Q.; Boyd, B. J. Liposomes in Biosensors. *Analyst* **2013**, *138*, 391–409.
- (80) Rawle, R. J.; Van Lengerich, B.; Chung, M.; Bendix, P. M.; Boxer, S. G. Vesicle Fusion Observed by Content Transfer across a Tethered Lipid Bilayer. *Biophys. J.* **2011**, *101*, L37–L39.
- (81) Meers, P.; Ali, S.; Erukulla, R.; Janoff, A. S. Novel Inner Monolayer Fusion Assays Reveal Differential Monolayer Mixing Associated with Cation-Dependent Membrane Fusion. *Biochim. Biophys. Acta - Biomembr.* **2000**, *1467*, 227–243.
- (82) Lei, G.; MacDonald, R. C. Lipid Bilayer Vesicle Fusion: Intermediates Captured by Highspeed Microfluorescence Spectroscopy. *Biophys. J.* **2003**, *85*, 1585–1599.
- (83) Marsden, H. R.; Tomatsu, I.; Kros, A. Model Systems for Membrane Fusion. *Chem. Soc. Rev.* **2011**, *40*, 1572–1585.
- (84) Bangham, A. D. A Correlation between Surface Charge and Coagulant Action of Phospholipids. *Nature* **1961**, *192*, 1197–1198.
- (85) Ganta, S.; Devalapally, H.; Shahiwala, A.; Amiji, M. A Review of Stimuli-Responsive Nanocarriers for Drug and Gene Delivery. *J. Control. Release* **2008**, *126*, 187–204.
- (86) Sapra, P.; Allen, T. M. Ligand-Targeted Liposomal Anticancer Drugs. *Prog. Lipid Res.* **2003**, *42*, 439–462.
- (87) Sessa, G.; Weissmann, G. Phospholipid Spherules (Liposomes) as a Model for Biological Membranes. *J. Lipid Res.* **1968**, *9*, 310–318.
- (88) Andes-Koback, M.; Keating, C. D. Complete Budding and Asymmetric Division of Primitive Model Cells to Produce Daughter Vesicles with Different Interior and Membrane Compositions. *J. Am. Chem. Soc.* **2011**, *133*, 9545–9555.
- (89) Nomura, S. I. M.; Tsumoto, K.; Hamada, T.; Akiyoshi, K.; Nakatani, Y.; Yoshikawa, K. Gene Expression within Cell-Sized Lipid Vesicles. *ChemBioChem* **2003**, *4*, 1172–1175.
- (90) Long, M. S.; Jones, C. D.; Helfrich, M. R.; Mangeney-Slavin, L. K.; Keating, C. D. Dynamic Microcompartmentation in Synthetic Cells. *Proc. Natl. Acad. Sci.* **2005**, *102*, 5920–5925.
- (91) Arriaga, L. R.; Datta, S. S.; Kim, S. H.; Amstad, E.; Kodger, T. E.; Monroy, F.; Weitz, D. A.

- Ultrathin Shell Double Emulsion Templated Giant Unilamellar Lipid Vesicles with Controlled Microdomain Formation. *Small* **2014**, *10*, 950–956.
- (92) Pereira de Souza, T.; Steiniger, F.; Stano, P.; Fahr, A.; Luisi, P. L. Spontaneous Crowding of Ribosomes and Proteins inside Vesicles: A Possible Mechanism for the Origin of Cell Metabolism. *ChemBioChem* **2011**, *12*, 2325–2330.
- (93) Bally, M.; Bailey, K.; Sugihara, K.; Grieshaber, D.; Vörös, J.; Stäler, B. Liposome and Lipid Bilayer Arrays towards Biosensing Applications. *Small* **2010**, *6*, 2481–2497.
- (94) Walde, P.; Ichikawa, S. Enzymes inside Lipid Vesicles: Preparation, Reactivity and Applications. *Biomol. Eng.* **2001**, *18*, 143–177.
- (95) Von Hoff, D. D.; Layard, Ma. W.; Basa, P.; Davis, H. L.; Von Hoff, A. L.; Rozenzweig, M.; Muggia, F. Risk Factors for Doxorubicin-Induced Congestive Heart Failure. *Ann. Intern. Med.* **1979**, *91*, 710–717.
- (96) Barenholz, Y. Doxil® - The First FDA-Approved Nano-Drug: Lessons Learned. *J. Control. Release* **2012**, *160*, 117–134.
- (97) Maherani, B.; Arab-Tehrany, E.; R. Mozafari, M.; Gaiani, C.; Linder, M. Liposomes: A Review of Manufacturing Techniques and Targeting Strategies. *Curr. Nanosci.* **2011**, *7*, 436–452.
- (98) Okamoto, Y.; Kojima, R.; Schwizer, F.; Bartolami, E.; Heinisch, T.; Matile, S.; Fussenegger, M.; Ward, T. R. A Cell-Penetrating Artificial Metalloenzyme Regulates a Gene Switch in a Designer Mammalian Cell. *Nat. Commun.* **2018**, *9*, 1–7.
- (99) Xu, C.; Hu, S.; Chen, X. Artificial Cells: From Basic Science to Applications. *Mater. Today* **2016**, *19*, 516–532.
- (100) Köhler, V.; Wilson, Y. M.; Dürrenberger, M.; Ghislieri, D.; Churakova, E.; Quinto, T.; Knörr, L.; Häussinger, D.; Hollmann, F.; Turner, N. J.; *et al.* Synthetic Cascades Are Enabled by Combining Biocatalysts with Artificial Metalloenzymes. *Nat. Chem.* **2013**, *5*, 93–99.
- (101) Sennuga, A.; Van Marwijk, J.; Boshoff, A.; Whiteley, C. G. Enhanced Activity of Chaperonin GroEL in the Presence of Platinum Nanoparticles. *J. Nanoparticle Res.* **2012**, *14*, 824–835.
- (102) Tonga, G. Y.; Jeong, Y.; Duncan, B.; Mizuhara, T.; Mout, R.; Das, R.; Kim, S. T.; Yeh, Y.-C.; Yan, B.; Hou, S.; *et al.* Supramolecular Regulation of Bioorthogonal Catalysis in Cells Using Nanoparticle-Embedded Transition Metal Catalysts. *Nat. Chem.* **2015**, *7*, 597–

603.

- (103) Kuna, J. J.; Voïtchovsky, K.; Singh, C.; Jiang, H.; Mwenifumbo, S.; Ghorai, P. K.; Stevens, M. M.; Glotzer, S. C.; Stellacci, F. The Effect of Nanometre-Scale Structure on Interfacial Energy. *Nat. Mater.* **2009**, *8*, 837–842.
- (104) Pelaz, B.; Jaber, S.; De Aberasturi, D. J.; Wulf, V.; Aida, T.; De La Fuente, J. M.; Feldmann, J.; Gaub, H. E.; Josephson, L.; Kagan, C. R.; *et al.* The State of Nanoparticle-Based Nanoscience and Biotechnology: Progress, Promises, and Challenges. *ACS Nano* **2012**, *6*, 8468–8483.
- (105) Kirchner, C.; Liedl, T.; Kudera, S.; Pellegrino, T.; Javier, A. M.; Gaub, H. E.; St?lzle, S.; Fertig, N.; Parak, W. J. Cytotoxicity of Colloidal CdSe and CdSe/ZnS Nanoparticles. *Nano Lett.* **2005**, *5*, 331–338.
- (106) Ishii, D.; Kinbara, K.; Ishida, Y.; Ishii, N.; Okochi, M.; Yohda, M.; Aida, T. Chaperonin-Mediated Stabilization and ATP-Triggered Release of Semiconductor Nanoparticles. *Nature* **2003**, *423*, 628–632.
- (107) Lin, Y.; Ren, J.; Qu, X. Nano-Gold as Artificial Enzymes: Hidden Talents. *Adv. Mater.* **2014**, *26*, 4200–4217.
- (108) Lin, Y.; Ren, J.; Qu, X. Catalytically Active Nanomaterials: A Promising Candidate for Artificial Enzymes. *Acc. Chem. Res.* **2014**, *47*, 1097–1105.
- (109) Wei, H.; Wang, E. Nanomaterials with Enzyme-like Characteristics (Nanozymes): Next-Generation Artificial Enzymes. *Chem. Soc. Rev.* **2013**, *42*, 6060–6093.
- (110) Comotti, M.; Della Pina, C.; Matarrese, R.; Rossi, M. The Catalytic Activity of “Naked” Gold Particles. *Angew. Chemie - Int. Ed.* **2004**, *43*, 5812–5815.
- (111) Jv, Y.; Li, B.; Cao, R. Positively-Charged Gold Nanoparticles as Peroxidase Mimic and Their Application in Hydrogen Peroxide and Glucose Detection. *Chem. Commun.* **2010**, *46*, 8017–8019.
- (112) He, W.; Zhou, Y. T.; Wamer, W. G.; Hu, X.; Wu, X.; Zheng, Z.; Boudreau, M. D.; Yin, J. J. Intrinsic Catalytic Activity of Au Nanoparticles with Respect to Hydrogen Peroxide Decomposition and Superoxide Scavenging. *Biomaterials* **2013**, *34*, 765–773.
- (113) Manea, F.; Houillon, F. B.; Pasquato, L.; Scrimin, P. Nanozymes: Gold-Nanoparticle-Based Transphosphorylation Catalysts. *Angew. Chemie - Int. Ed.* **2004**, *43*, 6165–6169.
- (114) Pasquato, L.; Rancan, F.; Scrimin, P.; Mancin, F.; Frigeri, C. N-Methylimidazole-Functionalized Gold Nanoparticles as Catalysts for Cleavage of a Carboxylic Acid Ester.

- Chem. Commun.* **2000**, *2*, 2253–2254.
- (115) Kisailus, D.; Najarian, M.; Weaver, J. C.; Morse, D. E. Functionalized Gold Nanoparticles Mimic Catalytic Activity of a Polysiloxane-Synthesizing Enzyme. *Adv. Mater.* **2005**, *17*, 1234–1239.
- (116) Foulkes, J. M.; Malone, K. J.; Coker, V. S.; Turner, N. J.; Lloyd, J. R. Engineering a Biometallic Whole Cell Catalyst for Enantioselective Deracemization Reactions. *ACS Catal.* **2011**, *1*, 1589–1594.
- (117) Bharali, D. J.; Klejbor, I.; Stachowiak, E. K.; Dutta, P.; Roy, I.; Kaur, N.; Bergey, E. J.; Prasad, P. N.; Stachowiak, M. K. Organically Modified Silica Nanoparticles: A Nonviral Vector for in Vivo Gene Delivery and Expression in the Brain. *Proc. Natl. Acad. Sci. U. S. A.* **2005**, *102*, 11539–11544.
- (118) Gurezka, R.; Laage, R.; Brosig, B.; Langosch, D. A Heptad Motif of Leucine Residues Found in Membrane Proteins Can Drive Self-Assembly of Artificial Transmembrane Segments. *J. Biol. Chem.* **1999**, *274*, 9265–9270.
- (119) Mihara, H.; Tomizaki, K.; Fujimoto, S.; Aoyagi, H.; Nishino, N. Artificial Membrane Protein Functionalized with Electron Transfer System. *Chem. Lett.* **1996**, *25*, 187–188.
- (120) Edlinger, C.; Einfalt, T.; Spulber, M.; Car, A.; Meier, W.; Palivan, C. G. Biomimetic Strategy to Reversibly Trigger Functionality of Catalytic Nanocompartments by the Insertion of PH-Responsive Biovalves. *Nano Lett.* **2017**, *17*, 5790–5798.
- (121) Kotov, N. A. Inorganic Nanoparticles as Protein Mimics. *Science*. **2010**, *330*, 188–189.
- (122) Daniel, M. C. M.; Astruc, D. Gold Nanoparticles: Assembly, Supramolecular Chemistry, Quantum-Size Related Properties and Applications toward Biology, Catalysis and Nanotechnology. *Chem. Rev.* **2004**, *104*, 293–346.
- (123) Kelly, K. L.; Coronado, E.; Zhao, L. L.; Schatz, G. C. The Optical Properties of Metal Nanoparticles: The Influence of Size, Shape, and Dielectric Environment. *J. Phys. Chem. B* **2003**, *107*, 668–677.
- (124) Jain, P. K.; Huang, X.; El-Sayed, I. H.; El-Sayed, M. A. ChemInform Abstract: Noble Metals on the Nanoscale: Optical and Photothermal Properties and Some Applications in Imaging, Sensing, Biology, and Medicine. *ChemInform* **2009**, *40*, 7–9.
- (125) Ruedas-Rama, M. J.; Walters, J. D.; Orte, A.; Hall, E. a H. Fluorescent Nanoparticles for Intracellular Sensing: A Review. *Anal. Chim. Acta* **2012**, *751*, 1–23.
- (126) Chen, S.; Yuan, R.; Chai, Y.; Hu, F. Electrochemical Sensing of Hydrogen Peroxide Using

- Metal Nanoparticles: A Review. *Microchim. Acta* **2013**, *180*, 15–32.
- (127) Schmid, G. *Nanoparticles: From Theory to Application*; 2004.
- (128) Tan, Y.; Li, Y.; Zhu, D. *Noble Metal Nanoparticles*; Vol. 8.
- (129) Link, S.; El-Sayed, M. A. Optical Properties and Ultrafast Dynamics of Metallic Nanocrystals. *Annu. Rev. Phys. Chem.* **2003**, *54*, 331–366.
- (130) Bakr, O. M.; Amendola, V.; Aikens, C. M.; Wenseleers, W.; Li, R.; Negro, L. D.; Schatz, G. C.; Stellacci, F. Silver Nanoparticles with Broad Multiband Linear Optical Absorption. *Angew. Chemie - Int. Ed.* **2009**, *121*, 6035–6040.
- (131) Su, K. H.; Wei, Q. H.; Zhang, X.; Mock, J. J.; Smith, D. R.; Schultz, S. Interparticle Coupling Effects on Plasmon Resonances of Nanogold Particles. *Nano Lett.* **2003**, *3*, 1087–1090.
- (132) Heinz, H.; Pramanik, C.; Heinz, O.; Ding, Y.; Mishra, R. K.; Marchon, D.; Flatt, R. J.; Estrela-Lopis, I.; Llop, J.; Moya, S.; *et al.* Nanoparticle Decoration with Surfactants: Molecular Interactions, Assembly, and Applications. *Surf. Sci. Rep.* **2017**, *72*, 1–58.
- (133) Altavilla, C.; Ciliberto, E.; Agarwal, A.; Bakshi, S. R.; Lahiri, D.; Altavilla, C.; Ciliberto, E.; Dong, L.; Nelson, B.; Choi, W.; *et al.* *Inorganic Nanoparticles Synthesis, Applications, and Perspectives*; 2011.
- (134) Feldheim, D. .; Foss, C. A. *Metal Nanoparticles: Synthesis, Characterization, and Applications*; 2002.
- (135) Faraday, M. The Bakerian Lecture: Experimental Relations of Gold (and Other Metals) to Light. *Philos. Trans. R. Soc. London* **1857**, *147*, 145–181.
- (136) Turkevich, J., Stevenson, P. C., Hillier, J. A Study of the Nucleation and Growth Processes I N the Synthesis of Colloidal Gold. **1951**, *11*, 55–75.
- (137) Lamer, V. K.; Dinegar, R. H. Theory, Production and Mechanism of Formation of Monodispersed Hydrosols. *J. Am. Chem. Soc.* **1950**, *72*, 4847–4854.
- (138) Polte, J. Fundamental Growth Principles of Colloidal Metal Nanoparticles - a New Perspective. *CrystEngComm* **2015**, *17*, 6809–6830.
- (139) Nagarajan, R.; Hatton, T. A. *Nanoparticles: Synthesis, Stabilization, Passivation, and Functionalization*; 2008; Vol. 996.
- (140) Ulman, A. Formation and Structure of Self-Assembled Monolayers. *Chem. Rev.* **1996**, *96*, 1533–1554.
- (141) Love, J. C.; Estroff, L. A.; Kriebel, J. K.; Nuzzo, R. G.; Whitesides, G. M. Self-Assembled Monolayers of Thiolates on Metals as a Form of Nanotechnology. *Chem. Rev.* **2005**,

105, 1103–1169.

- (142) Ionita, P.; Volkov, A.; Jeschke, G.; Chechik, V. Lateral Diffusion of Thiol Ligands on the Surface of Au Nanoparticles: An Electron Paramagnetic Resonance Study. *Anal. Chem.* **2008**, *80*, 95–106.
- (143) Centrone, A.; Penzo, E.; Sharma, M.; Myerson, J. M.; Jackson, A. M.; Marzari, N.; Stellacci, F. The Role of Nanostructure in the Wetting Behavior of Mixed-Monolayer-Protected Metal Nanoparticles. *Proc. Natl. Acad. Sci.* **2008**, *105*, 9886–9891.
- (144) Stranick, S. J.; Atre, S. V.; Parikh, a N.; Wood, M. C.; Allara, D. L.; Winograd, N.; Weiss, P. S. Nanometer-Scale Phase Separation in Mixed Composition Self-Assembled Monolayers. *Nanotechnology* **1999**, *7*, 438–442.
- (145) Carney, R. P.; DeVries, G. a.; Dubois, C.; Kim, H.; Jin, Y. K.; Singh, C.; Ghorai, P. K.; Tracy, J. B.; Stiles, R. L.; Murray, R. W.; *et al.* Size Limitations for the Formation of Ordered Striped Nanoparticles. *J. Am. Chem. Soc.* **2008**, *130*, 798–799.
- (146) Singh, C.; Ghorai, P. K.; Horsch, M. a.; Jackson, A. M.; Larson, R. G.; Stellacci, F.; Glotzer, S. C. Entropy-Mediated Patterning of Surfactant-Coated Nanoparticles and Surfaces. *Phys. Rev. Lett.* **2007**, *99*, 1–4.
- (147) Ghorai, P. K.; Glotzer, S. C. Molecular Dynamics Simulation Study of Self-Assembled Monolayers of Alkanethiol Surfactants on Spherical Gold Nanoparticles. *J. Phys. Chem. C* **2007**, *111*, 15857–15862.
- (148) Ghorai, P. K.; Glotzer, S. C. Atomistic Simulation Study of Striped Phase Separation in Mixed-Ligand Self-Assembled Monolayer Coated Nanoparticles. *J. Phys. Chem. C* **2010**, *114*, 19182–19187.
- (149) Luo, Z.; Marson, D.; Ong, Q. K.; Loiudice, A.; Kohlbrecher, J.; Radulescu, A.; Krause-Heuer, A.; Darwish, T.; Balog, S.; Buonsanti, R.; *et al.* Quantitative 3D Determination of Self-Assembled Structures on Nanoparticles Using Small Angle Neutron Scattering. *Nat. Commun.* **2018**, *9*, 1–10.
- (150) Ong, Q. K.; Reguera, J.; Silva, P. J.; Moglianetti, M.; Harkness, K.; Longobardi, M.; Mali, K. S.; Renner, C.; De Feyter, S.; Stellacci, F. High-Resolution Scanning Tunneling Microscopy Characterization of Mixed Monolayer Protected Gold Nanoparticles. *ACS Nano* **2013**, *7*, 8529–8539.
- (151) Luo, Z.; Hou, J.; Menin, L.; Ong, Q. K.; Stellacci, F. Evolution of the Ligand Shell Morphology during Ligand Exchange Reactions on Gold Nanoparticles. *Angew. Chemie*

- *Int. Ed.* **2017**, *56*, 13521–13525.

- (152) Jackson, A. M.; Myerson, J. W.; Stellacci, F. Spontaneous Assembly of Subnanometre-Ordered Domains in the Ligand Shell of Monolayer-Protected Nanoparticles. *Nat. Mater.* **2004**, *3*, 330–336.
- (153) Verma, A.; Stellacci, F. Effect of Surface Properties on Nanoparticle-Cell Interactions. *Small* **2010**, *6*, 12–21.
- (154) Yeh, Y.-C.; Creran, B.; Rotello, V. M. Gold Nanoparticles: Preparation, Properties, and Applications in Bionanotechnology. *Nanoscale* **2012**, *4*, 1871–1880.
- (155) Nel, A. E.; Mädler, L.; Velegol, D.; Xia, T.; Hoek, E. M. V.; Somasundaran, P.; Klaessig, F.; Castranova, V.; Thompson, M. Understanding Biophysicochemical Interactions at the Nano-Bio Interface. *Nat. Mater.* **2009**, *8*, 543–557.
- (156) Saha, K.; Rahimi, M.; Yazdani, M.; Kim, S. T.; Moyano, D. F.; Hou, S.; Das, R.; Mout, R.; Rezaee, F.; Mahmoudi, M.; *et al.* Regulation of Macrophage Recognition through the Interplay of Nanoparticle Surface Functionality and Protein Corona. *ACS Nano* **2016**, *10*, 4421–4430.
- (157) Walkey, C. D.; Olsen, J. B.; Song, F.; Liu, R.; Guo, H.; Olsen, D. W. H.; Cohen, Y.; Emili, A.; Chan, W. C. W. Protein Corona Fingerprinting Predicts the Cellular Interaction of Gold and Silver Nanoparticles. *ACS Nano* **2014**, *8*, 2439–2455.
- (158) Moyano, D. F.; Saha, K.; Prakash, G.; Yan, B.; Kong, H.; Yazdani, M.; Rotello, V. M. Fabrication of Corona-Free Nanoparticles with Tunable Hydrophobicity. *ACS Nano* **2014**, *8*, 6748–6755.
- (159) Pengo, P.; Şologan, M.; Pasquato, L.; Guida, F.; Pacor, S.; Tossi, A.; Stellacci, F.; Marson, D.; Boccardo, S.; Pricl, S.; *et al.* Gold Nanoparticles with Patterned Surface Monolayers for Nanomedicine: Current Perspectives. *Eur. Biophys. J.* **2017**, *46*, 749–771.
- (160) Van Lehn, R. C.; Atukorale, P. U.; Carney, R. P.; Yang, Y. S.; Stellacci, F.; Irvine, D. J.; Alexander-Katz, A. Effect of Particle Diameter and Surface Composition on the Spontaneous Fusion of Monolayer-Protected Gold Nanoparticles with Lipid Bilayers. *Nano Lett.* **2013**, *13*, 4060–4067.
- (161) Cagno, V.; Andreozzi, P.; D’Alicarnasso, M.; Silva, P. J.; Mueller, M.; Galloux, M.; Goffic, R. Le; Jones, S. T.; Vallino, M.; Hodek, J.; *et al.* Broad-Spectrum Non-Toxic Antiviral Nanoparticles with a Virucidal Inhibition Mechanism. *Nat. Mater.* **2018**, *17*, 195–203.
- (162) Uzun, O.; Hu, Y.; Verma, A.; Chen, S.; Centrone, A.; Stellacci, F. Water-Soluble

- Amphiphilic Gold Nanoparticles with Structured Ligand Shells. *Chem. Commun. (Camb)*. **2008**, 196–198.
- (163) Atukorale, P. U.; Yang, Y.-S.; Bekdemir, A.; Carney, R. P.; Silva, P. J.; Watson, N.; Stellacci, F.; Irvine, D. J. Influence of the Glycocalyx and Plasma Membrane Composition on Amphiphilic Gold Nanoparticle Association with Erythrocytes. *Nanoscale* **2015**, *7*, 11420–11432.
- (164) Carney, R. P.; Carney, T. M.; Mueller, M.; Stellacci, F. Dynamic Cellular Uptake of Mixed-Monolayer Protected Nanoparticles. *Biointerphases* **2012**, *7*, 3–11.
- (165) Yang, Y. S.; Carney, R. P.; Stellacci, F.; Irvine, D. J. Enhancing Radiotherapy by Lipid Nanocapsule-Mediated Delivery of Amphiphilic Gold Nanoparticles to Intracellular Membranes. *ACS Nano* **2014**, *8*, 8992–9002.
- (166) Huang, R.; Carney, R. P.; Ikuma, K.; Stellacci, F.; Lau, B. L. T. Effects of Surface Compositional and Structural Heterogeneity on Nanoparticle-Protein Interactions: Different Protein Configurations. *ACS Nano* **2014**, *8*, 5402–5412.
- (167) Van Lehn, R. C.; Alexander-Katz, A. Free Energy Change for Insertion of Charged, Monolayer-Protected Nanoparticles into Lipid Bilayers. *Soft Matter* **2014**, *10*, 648–658.
- (168) Rossi, G.; Monticelli, L. Gold Nanoparticles in Model Biological Membranes: A Computational Perspective. *Biochim. Biophys. Acta - Biomembr.* **2016**, *1858*, 2380–2389.
- (169) Simonelli, F.; Bochicchio, D.; Ferrando, R.; Rossi, G. Monolayer-Protected Anionic Au Nanoparticles Walk into Lipid Membranes Step by Step. *J. Phys. Chem. Lett.* **2015**, *6*, 3175–3179.
- (170) Van Lehn, R. C.; Alexander-Katz, A. Pathway for Insertion of Amphiphilic Nanoparticles into Defect-Free Lipid Bilayers from Atomistic Molecular Dynamics Simulations. *Soft Matter* **2015**, *11*, 3165–3175.
- (171) Van Lehn, R. C.; Alexander-Katz, A. Fusion of Ligand-Coated Nanoparticles with Lipid Bilayers: Effect of Ligand Flexibility. *J. Phys. Chem. A* **2014**, *118*, 5848–5856.
- (172) Lehn, R. C. Van; Alexander-katz, A. Membrane-Embedded Nanoparticles Induce Lipid Rearrangements Similar to Those Exhibited by Biological Membrane Proteins. *J. Phys. Chem. B* **2014**, *118*, 12586–12598.
- (173) Tahir, M. A.; Van Lehn, R. C.; Choi, S. H.; Alexander-Katz, A. Solvent-Exposed Lipid Tail Protrusions Depend on Lipid Membrane Composition and Curvature. *Biochim. Biophys.*

Acta - Biomembr. **2016**, *1858*, 1207–1215.

- (174) Gkeka, P.; Angelikopoulos, P.; Sarkisov, L.; Cournia, Z. Membrane Partitioning of Anionic, Ligand-Coated Nanoparticles Is Accompanied by Ligand Snorkeling, Local Disordering, and Cholesterol Depletion. *PLoS Comput. Biol.* **2014**, *10*.
- (175) Angelikopoulos, P.; Sarkisov, L.; Cournia, Z.; Gkeka, P. Self-Assembly of Anionic, Ligand-Coated Nanoparticles in Lipid Membranes. *Nanoscale* **2017**, *9*, 1040–1048.
- (176) Iida, R.; Kawamura, H.; Niikura, K.; Kimura, T.; Sekiguchi, S.; Joti, Y.; Bessho, Y.; Mitomo, H.; Nishino, Y.; Ijiri, K. Synthesis of Janus-like Gold Nanoparticles with Hydrophilic/Hydrophobic Faces by Surface Ligand Exchange and Their Self-Assemblies in Water. *Langmuir* **2015**, *31*, 4054–4062.
- (177) Xu, X.; Rosi, N. L.; Wang, Y.; Huo, F.; Mirkin, C. A. Asymmetric Functionalization of Gold Nanoparticles with Oligonucleotides. *J. Am. Chem. Soc.* **2006**, *128*, 9286–9287.
- (178) Rana, S.; Bajaj, A.; Mout, R.; Rotello, V. M. Monolayer Coated Gold Nanoparticles for Delivery Applications. *Adv. Drug Deliv. Rev.* **2012**, *64*, 200–216.
- (179) Agasti, S. S.; Chompoosor, A.; You, C.; Ghosh, P.; Kim, C. K.; Rotello, V. M. Photoregulated Release of Caged Anticancer Drugs from Gold Nanoparticles to Regulate Drug Release, Minimizing Side Effects and Improving. *J. Am. Chem. Soc.* **2009**, *131*, 5728–5729.
- (180) Simpson, C. A.; Agrawal, A. C.; Balinski, A.; Harkness, K. M.; Cliffel, D. E. Short-Chain PEG Mixed Monolayer Protected Gold Clusters Increase Clearance and Red Blood Cell Counts. *ACS Nano* **2011**, *5*, 3577–3584.
- (181) Benyettou, F.; Hardouin, J.; Lecouvey, M.; Jouni, H.; Motte, L. Pegylated versus Non-Pegylated $\gamma\text{Fe}_2\text{O}_3$ @ Alendronate Nanoparticles. *J. Bioanal. Biomed.* **2012**, *4*, 39–44.
- (182) Liu, Y.; Shipton, M. K.; Ryan, J.; Kaufman, E. D.; Franzen, S.; Feldheim, D. L. Synthesis, Stability, and Cellular Internalization of Gold Nanoparticles Containing Mixed Peptide-Poly(Ethylene Glycol) Monolayers. *Anal. Chem.* **2007**, *79*, 2221–2229.
- (183) Liu, X.; Li, H.; Chen, Y.; Jin, Q.; Ren, K.; Ji, J. Mixed-Charge Nanoparticles for Long Circulation, Low Reticuloendothelial System Clearance, and High Tumor Accumulation. *Adv. Healthc. Mater.* **2014**, *3*, 1439–1447.
- (184) Zheng, W.; Li, H.; Chen, W.; Ji, J.; Jiang, X. Recyclable Colorimetric Detection of Trivalent Cations in Aqueous Media Using Zwitterionic Gold Nanoparticles. *Anal. Chem.* **2016**, *88*, 4140–4146.

- (185) Ghosh, A.; Basak, S.; Wunsch, B. H.; Kumar, R.; Stellacci, F. Effect of Composition on the Catalytic Properties of Mixed-Ligand-Coated Gold Nanoparticles. *Angew. Chemie - Int. Ed.* **2011**, *50*, 7900–7905.
- (186) Wang, L.; Xu, L.; Kuang, H.; Xu, C.; Kotov, N. A. Dynamic Nanoparticle Assemblies. *Acc. Chem. Res.* **2012**, *45*, 1916–1926.
- (187) Mailander, V.; Landfester, K. Interaction of Gold Nanoparticles with Cells. *Biomacromolecules* **2009**, *10*, 2379–2400.
- (188) Shang, L.; Nienhaus, K.; Nienhaus, G. U. Engineered Nanoparticles Interacting with Cells: Size Matters. *J. Nanobiotechnology* **2014**, *12*, 1–11.
- (189) Zhao, F.; Zhao, Y.; Liu, Y.; Chang, X.; Chen, C.; Zhao, Y. Cellular Uptake, Intracellular Trafficking, and Cytotoxicity of Nanomaterials. *Small* **2011**, *7*, 1322–1337.
- (190) Chou, L. Y. T.; Ming, K.; Chan, W. C. W. Strategies for the Intracellular Delivery of Nanoparticles. *Chem. Soc. Rev.* **2011**, *40*, 233–245.
- (191) Pratten, M. K.; Lloyd, J. B. Pinocytosis and Phagocytosis: The Effect of Size of a Particulate Substrate on Its Mode of Capture by Rat Peritoneal Macrophages Cultured in Vitro. *BBA - Gen. Subj.* **1986**, *881*, 307–313.
- (192) Reifarh, M.; Hoepfner, S.; Schubert, U. S. Uptake and Intracellular Fate of Engineered Nanoparticles in Mammalian Cells: Capabilities and Limitations of Transmission Electron Microscopy—Polymer-Based Nanoparticles. *Adv. Mater.* **2018**, *30*, 1–28.
- (193) Bastiani, M.; Parton, R. G. Caveolae at a Glance. *J. Cell Sci.* **2010**, *123*, 3831–3836.
- (194) Nabi, I. R.; Le, P. U. Caveolae/Raft-Dependent Endocytosis. *J. Cell Biol.* **2003**, *161*, 673–677.
- (195) Zhang, S.; Gao, H.; Bao, G. Physical Principles of Nanoparticle Cellular Endocytosis. *ACS Nano* **2015**, *9*, 8655–8671.
- (196) Yi, X.; Shi, X.; Gao, H. Cellular Uptake of Elastic Nanoparticles. *Phys. Rev. Lett.* **2011**, *107*, 1–5.
- (197) Agudo-Canalejo, J.; Lipowsky, R. Uniform and Janus-like Nanoparticles in Contact with Vesicles: Energy Landscapes and Curvature-Induced Forces. *Soft Matter* **2017**, *13*, 2155–2173.
- (198) Michel, R.; Kesselman, E.; Plostica, T.; Danino, D.; Gradzielski, M. Internalization of Silica Nanoparticles into Fluid Liposomes : Formation of Interesting Hybrid Colloids. *Angew. Chemie* **2014**, *53*, 12441–12445.

- (199) Contini, C.; Schneemilch, M.; Gaisford, S.; Quirke, N. Nanoparticle–Membrane Interactions. *J. Exp. Nanosci.* **2018**, *13*, 62–81.
- (200) Huang, K.; Ma, H.; Liu, J.; Huo, S.; Kumar, A.; Wei, T.; Zhang, X.; Jin, S.; Gan, Y.; Wang, P. C.; *et al.* Size-Dependent Localization and Penetration of Ultrasmall Gold Nanoparticles in Cancer Cells, Multicellular Spheroids, and Tumors in Vivo. *ACS Nano* **2012**, *6*, 4483–4493.
- (201) Chithrani, B. D.; Chan, W. C. W. Elucidating the Mechanism of Cellular Uptake and Removal of Protein-Coated Gold Nanoparticles of Different Sizes and Shapes. *Nano Lett.* **2007**, *7*, 1542–1550.
- (202) Peiris, P. M.; Bauer, L.; Toy, R.; Tran, E.; Pansky, J.; Doolittle, E.; Schmidt, E.; Hayden, E.; Mayer, A.; Keri, R. A.; *et al.* Enhanced Delivery of Chemotherapy to Tumors Using a Multicomponent Nanochain with Radio-Frequency-Tunable Drug Release. *ACS Nano* **2012**, *6*, 4157–4168.
- (203) Fröhlich, E. The Role of Surface Charge in Cellular Uptake and Cytotoxicity of Medical Nanoparticles. *Int. J. Nanomedicine* **2012**, *7*, 5577–5591.
- (204) Kettler, K.; Veltman, K.; van de Meent, D.; van Wezel, A.; Hendriks, A. J. Cellular Uptake of Nanoparticles as Determined by Particle Properties, Experimental Conditions, and Cell Type. *Environ. Toxicol. Chem.* **2014**, *33*, 481–492.
- (205) Zahr, A. S.; Davis, C. A.; Pishko, M. V. Macrophage Uptake of Core-Shell Nanoparticles Surface Modified with Poly(Ethylene Glycol). *Langmuir* **2006**, *22*, 8178–8185.
- (206) Gao, J.; Zhang, O.; Ren, J.; Wu, C.; Zhao, Y. Aromaticity/Bulkiness of Surface Ligands to Promote the Interaction of Anionic Amphiphilic Gold Nanoparticles with Lipid Bilayers. *Langmuir* **2016**, *32*, 1601–1610.
- (207) Lund, T.; Callaghan, M. F.; Williams, P.; Turmaine, M.; Bachmann, C.; Rademacher, T.; Roitt, I. M.; Bayford, R. The Influence of Ligand Organization on the Rate of Uptake of Gold Nanoparticles by Colorectal Cancer Cells. *Biomaterials* **2011**, *32*, 9776–9784.
- (208) Xia, Q. S.; Ding, H. M.; Ma, Y. Q. Can Dual-Ligand Targeting Enhance Cellular Uptake of Nanoparticles? *Nanoscale* **2017**, *9*, 8982–8989.
- (209) Giljohann, D. A.; Seferos, D. S.; Patel, P. C.; Millstone, J. E.; Rosi, N. L.; Mirkin, C. A. Oligonucleotide Loading Determines Cellular Uptake of DNA-Modified Gold Nanoparticles. *Nano Lett.* **2007**, *7*, 3818–3821.
- (210) Tkachenko, A. G.; Xie, H.; Coleman, D.; Glomm, W.; Ryan, J.; Anderson, M. F.; Franzen,

- S.; Feldheim, D. L. Multifunctional Gold Nanoparticle-Peptide Complexes for Nuclear Targeting. *J. Am. Chem. Soc.* **2003**, *125*, 4700–4701.
- (211) Hu, Y.; Litwin, T.; Nagaraja, a R.; Kwong, B.; Katz, J.; Watson, N.; Irvine, D. J. Cytosolic Delivery of Membrane Impermeable Molecules in Dendritic Cells Using PH Responsive Core-Shell Nanoparticles. *Nano Lett.* **2007**, *7*, 3056–3064.
- (212) Andreozzi, P.; Martinelli, C.; Carney, R. P.; Carney, T. M.; Stellacci, F. Erythrocyte Incubation as a Method for Free-Dye Presence Determination in Fluorescently Labeled Nanoparticles. *Mol. Pharm.* **2013**, *10*, 875–882.
- (213) Leduc, C.; Jung, J. M.; Carney, R. R.; Stellacci, F.; Lounis, B. Direct Investigation of Intracellular Presence of Gold Nanoparticles via Photothermal Heterodyne Imaging. *ACS Nano* **2011**, *5*, 2587–2592.
- (214) Goodman, C. M.; McCusker, C. D.; Yilmaz, T.; Rotello, V. M. Toxicity of Gold Nanoparticles Functionalized with Cationic and Anionic Side Chains. *Bioconjug. Chem.* **2004**, *15*, 897–900.
- (215) Bhattacharjee, S.; de Haan, L. H. J.; Evers, N. M.; Jiang, X.; Marcelis, A. T. M.; Zuilhof, H.; Rietjens, I. M. C. M.; Alink, G. M. Role of Surface Charge and Oxidative Stress in Cytotoxicity of Organic Monolayer-Coated Silicon Nanoparticles towards Macrophage NR8383 Cells. *Part. Fibre Toxicol.* **2010**, *7*, 25.
- (216) Deng, Z. J.; Liang, M.; Monteiro, M.; Toth, I.; Minchin, R. F. Nanoparticle-Induced Unfolding of Fibrinogen Promotes Mac-1 Receptor Activation and Inflammation. *Nat. Nanotechnol.* **2011**, *6*, 39–44.
- (217) Bhabra, G.; Sood, A.; Fisher, B.; Cartwright, L.; Saunders, M.; Evans, W. H.; Surprenant, A.; Lopez-Castejon, G.; Mann, S.; Davis, S. A.; *et al.* Nanoparticles Can Cause DNA Damage across a Cellular Barrier. *Nat. Nanotechnol.* **2009**, *4*, 876–883.
- (218) Poland, C. A.; Duffin, R.; Kinloch, I.; Maynard, A.; Wallace, W. A. H.; Seaton, A.; Stone, V.; Brown, S.; MacNee, W.; Donaldson, K. Carbon Nanotubes Introduced into the Abdominal Cavity of Mice Show Asbestos-like Pathogenicity in a Pilot Study. *Nat. Nanotechnol.* **2008**, *3*, 423–428.
- (219) Connor, E. E.; Mwamuka, J.; Gole, A.; Murphy, C. J.; Wyatt, M. D. Gold Nanoparticles Are Taken up by Human Cells but Do Not Cause Acute Cytotoxicity. *Small* **2005**, *1*, 325–327.
- (220) Sabella, S.; Carney, R. P.; Brunetti, V.; Malvindi, M. A.; Al-Juffali, N.; Vecchio, G.; Janes,

- S. M.; Bakr, O. M.; Cingolani, R.; Stellacci, F.; *et al.* A General Mechanism for Intracellular Toxicity of Metal-Containing Nanoparticles. *Nanoscale* **2014**, *6*, 7052–7061.
- (221) Al-Jamal, W. T.; Kostarelos, K. Liposomes: From a Clinically Established Drug Delivery System to a Nanoparticle Platform for Theranostic Nanomedicine. *Acc. Chem. Res.* **2011**, *44*, 1094–1104.
- (222) Chen, C. S.; Yao, J.; Durst, R. A. Liposome Encapsulation of Fluorescent Nanoparticles: Quantum Dots and Silica Nanoparticles. *J. Nanoparticle Res.* **2006**, *8*, 1033–1038.
- (223) Gopalakrishnan, G.; Danelon, C.; Izewska, P.; Prummer, M.; Bolinger, P. Y.; Geissbühler, I.; Demurtas, D.; Dubochet, J.; Vogel, H. Multifunctional Lipid/Quantum Dot Hybrid Nanocontainers for Controlled Targeting of Live Cells. *Angew. Chemie - Int. Ed.* **2006**, *45*, 5478–5483.
- (224) Beloglazova, N. V.; Shmelin, P. S.; Speranskaya, E. S.; Lucas, B.; Helmbrecht, C.; Knopp, D.; Niessner, R.; De Saeger, S.; Goryacheva, I. Y. Quantum Dot Loaded Liposomes as Fluorescent Labels for Immunoassay. *Anal. Chem.* **2013**, *85*, 7197–7204.
- (225) Liu, J. Interfacing Zwitterionic Liposomes with Inorganic Nanomaterials: Surface Forces, Membrane Integrity, and Applications. *Langmuir* **2016**, *32*, 4393–4404.
- (226) Martínez-González, R.; Estelrich, J.; Busquets, M. A. Liposomes Loaded with Hydrophobic Iron Oxide Nanoparticles: Suitable T2 Contrast Agents for MRI. *Int. J. Mol. Sci.* **2016**, *17*, 1–14.
- (227) Salvatore, A.; Montis, C.; Berti, D.; Baglioni, P. Multifunctional Magnetoliposomes for Sequential Controlled Release. *ACS Nano* **2016**, *10*, 7749–7760.
- (228) Bonnaud, C.; Monnier, C. a.; Demurtas, D.; Jud, C.; Vanhecke, D.; Montet, X.; Hovius, R.; Lattuada, M.; Rothen-Rutishauser, B.; Petri-Fink, A. Insertion of Nanoparticle Clusters into Vesicle Bilayers. *ACS Nano* **2014**, *8*, 3451–3460.
- (229) Rasch, M. R.; Yu, Y.; Bosoy, C.; Goodfellow, B. W.; Korgel, B. A. Chloroform-Enhanced Incorporation of Hydrophobic Gold Nanocrystals into Dioleoylphosphatidylcholine (DOPC) Vesicle Membranes. *Langmuir* **2012**, *28*, 12971–12981.
- (230) Guo, H.; Kim, J. Physicochemical and Engineering Aspects Photothermally Induced Release from Liposome Suspended in Mixture Solution of Gold Nanoparticle and Thermo-Sensitive Polymer. *Colloids Surfaces A Physicochem. Eng. Asp.* **2015**, *469*, 73–82.

- (231) Thamphiwatana, S.; Fu, V.; Zhu, J.; Lu, D.; Gao, W.; Zhang, L. Nanoparticle-Stabilized Liposomes for Ph-Responsive Gastric Drug Delivery. *Langmuir* **2013**, *29*, 12228–12233.
- (232) Pornpattananankul, D.; Olson, S.; Aryal, S.; Sartor, M.; Huang, M.; Vecchio, K.; Zhang, L. Stimuli - Responsive Liposome Fusion Mediated by Gold Nanoparticles. *ACS Nano* **2011**, *4*, 1935–1942.
- (233) Zhang, Z. Q.; Song, S. C. Thermosensitive/Superparamagnetic Iron Oxide Nanoparticle-Loaded Nanocapsule Hydrogels for Multiple Cancer Hyperthermia. *Biomaterials* **2016**, *106*, 13–23.
- (234) Amstad, E.; Kohlbrecher, J.; Müller, E.; Schweizer, T.; Textor, M.; Reimhult, E. Triggered Release from Liposomes through Magnetic Actuation of Iron Oxide Nanoparticle Containing Membranes. *Nano Lett.* **2011**, *11*, 1664–1670.
- (235) Michel, R.; Plostica, T.; Abezgauz, L. L.; Danino, D.; Gradzielski, M. Control of the Stability and Structure of Liposomes by Means of Nanoparticles. *Soft Matter* **2013**, *9*, 4167–4177.
- (236) Wang, F.; Curry, D. E.; Liu, J. Driving Adsorbed Gold Nanoparticle Assembly by Merging Lipid Gel/Fluid Interfaces. *Langmuir* **2015**, *31*, 13271–13274.
- (237) Wang, F.; Liu, J. Self-Healable and Reversible Liposome Leakage by Citrate-Capped Gold Nanoparticles: Probing the Initial Adsorption/Desorption Induced Lipid Phase Transition. *Nanoscale* **2015**, *7*, 15599–15604.
- (238) Von White, G.; Chen, Y.; Roder-Hanna, J.; Bothun, G. D.; Kitchens, C. L. Structural and Thermal Analysis of Lipid Vesicles Encapsulating Hydrophobic Gold Nanoparticles. *ACS Nano* **2012**, *6*, 4678–4685.
- (239) Sugikawa, K.; Kadota, T.; Yasuhara, K.; Ikeda, A. Anisotropic Self-Assembly of Citrate-Coated Gold Nanoparticles on Fluidic Liposomes. *Angew. Chemie Int. Ed.* **2016**, *55*, 4059–4063.
- (240) Shin, S. H. R.; Lee, H. Y.; Bishop, K. J. M. Amphiphilic Nanoparticles Control the Growth and Stability of Lipid Bilayers with Open Edges. *Angew. Chemie - Int. Ed.* **2015**, *54*, 10816–10820.
- (241) Lee, K.; Zhang, L.; Yi, Y.; Wang, X.; Yu, Y. Rupture of Lipid Membranes Induced by Amphiphilic Janus Nanoparticles. *ACS Nano* **2018**, *12*, 3646–3657.
- (242) Lee, H. Y.; Shin, S. H. R.; Abezgauz, L. L.; Lewis, S. a.; Chirsan, A. M.; Danino, D. D.; Bishop, K. J. M. Integration of Gold Nanoparticles into Bilayer Structures via Adaptive

- Surface Chemistry. *J. Am. Chem. Soc.* **2013**, *135*, 5950–5953.
- (243) Rasch, M. R.; Rossinyol, E.; Hueso, J. L.; Goodfellow, B. W.; Arbiol, J.; Korgel, B. a. Hydrophobic Gold Nanoparticle Self-Assembly with Phosphatidylcholine Lipid: Membrane-Loaded and Janus Vesicles. *Nano Lett.* **2010**, *10*, 3733–3739.
- (244) Hou, W.-C.; Moghadam, B. Y.; Corredor, C.; Westerhoff, P.; Posner, J. D. Distribution of Functionalized Gold Nanoparticles between Water and Lipid Bilayers as Model Cell Membranes. *Environ. Sci. Technol.* **2012**, *46*, 1869–1876.
- (245) Atukorale, P. U.; Guven, Z. P.; Bekdemir, A.; Carney, R. P.; Van Lehn, R. C.; Yun, D. S.; Jacob Silva, P. H.; Demurtas, D.; Yang, Y.-S.; Alexander-Katz, A.; *et al.* Structure–Property Relationships of Amphiphilic Nanoparticles That Penetrate or Fuse Lipid Membranes. *Bioconjug. Chem.* **2018**, *29*, 1131–1140.
- (246) Atukorale, P. U.; Guven, Z. P.; Bekdemir, A.; Carney, R. P.; Van Lehn, R. C.; Yun, D. S.; Jacob Silva, P. H.; Demurtas, D.; Yang, Y.-S.; Alexander-Katz, A.; *et al.* Structure–Property Relationships of Amphiphilic Nanoparticles That Penetrate or Fuse Lipid Membranes. *Bioconjug. Chem.* **2018**, *acs.bioconjchem.7b00777*.
- (247) Atukorale, P. U. Amphiphilic Gold Nanoparticles : Mechanisms for Interaction with Membranes and Applications in Drug and Vaccine Delivery Members of Thesis Committee. **2014**.
- (248) Carney, R. P.; Astier, Y.; Carney, T. M.; Vo??tchovsky, K.; Jacob Silva, P. H.; Stellacci, F. Electrical Method to Quantify Nanoparticle Interaction with Lipid Bilayers. *ACS Nano* **2013**, *7*, 932–942.
- (249) Ben-Tal, N.; Ben-Shaul, A.; Nicholls, A.; Honig, B. Free-Energy Determinants of α -Helix Insertion into Lipid Bilayers. *Biophys. J.* **1996**, *70*, 1803–1812.
- (250) White, S. H.; Wimley, W. C. Membrane Protein Folding and Stability: Physical Principles. *Annu. Rev. Biophys. Biomol. Struct.* **1999**, *28*, 319–365.
- (251) Li, Y.; Li, X.; Li, Z.; Gao, H. Surface-Structure-Regulated Penetration of Nanoparticles across a Cell Membrane. *Nanoscale* **2012**, *4*, 3768–3775.
- (252) Vanni, S.; Vamparys, L.; Gautier, R.; Drin, G.; Etchebest, C.; Fuchs, P. F. J.; Antonny, B. Amphipathic Lipid Packing Sensor Motifs: Probing Bilayer Defects with Hydrophobic Residues. *Biophys. J.* **2013**, *104*, 575–584.
- (253) Dorairaj, S.; Allen, T. W. On the Thermodynamic Stability of a Charged Arginine Side Chain in a Transmembrane Helix. *Proc. Natl. Acad. Sci.* **2007**, *104*, 4943–4948.

- (254) Strandberg, E.; Killian, J. A. Snorkeling of Lysine Side Chains in Transmembrane Helices: How Easy Can It Get? *FEBS Lett.* **2003**, *544*, 69–73.
- (255) Campelo, F.; McMahon, H. T.; Kozlov, M. M. The Hydrophobic Insertion Mechanism of Membrane Curvature Generation by Proteins. *Biophys. J.* **2008**, *95*, 2325–2339.
- (256) Yoo, J.; Cui, Q. Membrane-Mediated Protein-Protein Interactions and Connection to Elastic Models: A Coarse-Grained Simulation Analysis of Gramicidin a Association. *Biophys. J.* **2013**, *104*, 128–138.
- (257) Hessa, T.; Kim, H.; Bihlamaier, K.; Lundin, C.; Boekel, J.; Andersson, H.; Nilsson, I.; White, S.; Von, G. Recognition of Transmembrane Helices by the Endoplasmic Reticulum Translocon. *Nature* **2005**, *433*, 377–381.
- (258) Brust, M.; Walker, M.; Bethell, D.; Schiffrin, D. J.; Whyman, R. Synthesis of Thiol-Derivatised Gold Nanoparticles In. **2000**, 801–802.
- (259) Zheng, N.; Fan, J.; Stucky, G. D. One-Step One-Phase Synthesis of Monodisperse Noble-Metallic Nanoparticles and Their Colloidal Crystals. *J. Am. Chem. Soc.* **2006**, *128*, 6550–6551.
- (260) Luo, Z.; Hou, J.; Menin, L.; Ong, Q. K.; Stellacci, F. Evolution of the Ligand-Shell Morphology during Ligand-Exchange Reaction on Gold Nanoparticles. *Angew. Chemie* **2017**, 13706–13710.
- (261) Henrique, P.; Silva, J. Discriminative Adsorption of Amphiphilic Monolayer Protected Gold Nanoparticles on Amyloid Fibers. **2016**, 7037.
- (262) Ong, Q.; Luo, Z.; Stellacci, F. Characterization of Ligand Shell for Mixed-Ligand Coated Gold Nanoparticles. *Acc. Chem. Res.* **2017**, *50*, 1911–1919.
- (263) Salassi, S.; Simonelli, F.; Bochicchio, D.; Ferrando, R.; Rossi, G. Au Nanoparticles in Lipid Bilayers: A Comparison between Atomistic and Coarse-Grained Models. *J. Phys. Chem. C* **2017**, *121*, 10927–10935.
- (264) Malinin, V. S.; Lentz, B. R. Energetics of Vesicle Fusion Intermediates: Comparison of Calculations with Observed Effects of Osmotic and Curvature Stresses. *Biophys. J.* **2004**, *86*, 2951–2964.
- (265) Grafmüller, A.; Shillcock, J.; Lipowsky, R. The Fusion of Membranes and Vesicles: Pathway and Energy Barriers from Dissipative Particle Dynamics. *Biophys. J.* **2009**, *96*, 2658–2675.
- (266) Schneck, E.; Sedlmeier, F.; Netz, R. R. Hydration Repulsion between Biomembranes

- Results from an Interplay of Dehydration and Depolarization. *Proc. Natl. Acad. Sci.* **2012**, *109*, 14405–14409.
- (267) Efrat, A.; Chernomordik, L. V.; Kozlov, M. M. Point-like Protrusion as a Prestalk Intermediate in Membrane Fusion Pathway. *Biophys. J.* **2007**, *92*, L61–L63.
- (268) Kozlovsky, Y.; Kozlov, M. M. Stalk Model of Membrane Fusion: Solution of Energy Crisis. *Biophys. J.* **2002**, *82*, 882–895.
- (269) Chakraborty, H.; Tarafdar, P. K.; Bruno, M. J.; Sengupta, T.; Lentz, B. R. Activation Thermodynamics of Poly(Ethylene Glycol)-Mediated Model Membrane Fusion Support Mechanistic Models of Stalk and Pore Formation. *Biophys. J.* **2012**, *102*, 2751–2760.
- (270) Rizo, J.; Rosenmund, C. Synaptic Vesicle Fusion. *Nat. Struct. Mol. Biol.* **2008**, *15*, 665–674.
- (271) Diao, J.; Grob, P.; Cipriano, D. J.; Kyoung, M.; Zhang, Y.; Shah, S.; Nguyen, A.; Padolina, M.; Srivastava, A.; Vrljic, M.; *et al.* Synaptic Proteins Promote Calcium-Triggered Fast Transition from Point Contact to Full Fusion. *Elife* **2012**, *1*, e00109–e00130.
- (272) Rørvig-Lund, A.; Bahadori, A.; Semsey, S.; Bendix, P. M.; Oddershede, L. B. Vesicle Fusion Triggered by Optically Heated Gold Nanoparticles. *Nano Lett.* **2015**, *15*, 4138–4188.
- (273) Chan, Y.-H. M.; Lenz, P.; Boxer, S. G. Kinetics of DNA-Mediated Docking Reactions between Vesicles Tethered to Supported Lipid Bilayers. *Proc. Natl. Acad. Sci.* **2007**, *104*, 18913–18918.
- (274) François-Martin, C.; Rothman, J. E.; Pincet, F. Low Energy Cost for Optimal Speed and Control of Membrane Fusion. *Proc. Natl. Acad. Sci.* **2017**, *114*, 1238–1241.
- (275) Düzgüneş, N.; Allen, T. M.; Fedor, J.; Papahadjopoulos, D.; Düzgüneş, N.; Allen, T. M.; Papahadjopoulos, D. Lipid Mixing during Membrane Aggregation and Fusion: Why Fusion Assays Disagree. *Biochemistry* **1987**, *26*, 8435–8442.
- (276) Kendall, D. A.; MacDonald, R. C. A Fluorescence Assay to Monitor Vesicle Fusion and Lysis. *J. Biol. Chem.* **1982**, *257*, 13892–13895.
- (277) Düzgüneş, N.; Wilschut, J. Fusion Assays Monitoring Intermixing of Aqueous Contents. *Methods Enzymol.* **1993**, *220*, 3–14.
- (278) Papahadjopoulos, D.; Nir, S.; Düzgüneş, N. Molecular Mechanisms of Calcium-Induced Membrane Fusion. *J. Bioenerg. Biomembr.* **1990**, *22*, 157–179.
- (279) Ries, O.; Löffler, P. M. G.; Rabe, A.; Malavan, J. J.; Vogel, S. Efficient Liposome Fusion

- Mediated by Lipid-Nucleic Acid Conjugates. *Org. Biomol. Chem.* **2017**, *15*, 8936–8945.
- (280) Aeffer, S.; Reusch, T.; Weinhausen, B.; Salditt, T. Energetics of Stalk Intermediates in Membrane Fusion Are Controlled by Lipid Composition. *Proc. Natl. Acad. Sci.* **2012**, *109*, E1609–E1618.
- (281) Risselada, H. J.; Bubnis, G.; Grubmüller, H. Expansion of the Fusion Stalk and Its Implication for Biological Membrane Fusion. *Proc. Natl. Acad. Sci.* **2014**, *111*, 11043–11048.
- (282) Coldren, B.; Van Zanten, R.; Mackel, M. J.; Zasadzinski, J. A.; Jung, H. T. From Vesicle Size Distributions to Bilayer Elasticity via Cryo-Transmission and Freeze-Fracture Electron Microscopy. *Langmuir* **2003**, *19*, 5632–5639.
- (283) Kotov, N. A.; Weiss, P. S. Self-Assembly of Nanoparticles: A Snapshot. *ACS Nano* **2014**, *8*, 3101–3103.
- (284) Min, Y.; Akbulut, M.; Kristiansen, K.; Golan, Y.; Israelachvili, J. N. The Role of Interparticle and External Forces in Nanoparticle Assembly. In *Nanoscience and Technology*; 2009; pp. 38–49.
- (285) Sakaguchi, N.; Kimura, Y.; Hirano-Iwata, A.; Ogino, T. Fabrication of Au-Nanoparticle-Embedded Lipid Bilayer Membranes Supported on Solid Substrates. *J. Phys. Chem. B* **2017**, *121*, 4474–4481.
- (286) Park, S.; Oh, S.; Mun, J.; Han, S. Loading of Gold Nanoparticles inside the DPPC Bilayers of Liposome and Their Effects on Membrane Fluidities. **2006**, *48*, 112–118.
- (287) Sharma, H.; Dormidontova, E. E. Lipid Nanodisc-Templated Self-Assembly of Gold Nanoparticles into Strings and Rings. *ACS Nano* **2017**, *11*, 3651–3661.
- (288) Neuhaus, F.; Mueller, D.; Tanasescu, R.; Balog, S.; Ishikawa, T.; Brezesinski, G.; Zumbühl, A. Vesicle Origami: Cuboid Phospholipid Vesicles Formed by Template-Free Self-Assembly. *Angew. Chemie - Int. Ed.* **2017**, *56*, 6515–6518.
- (289) Sprong, H.; van der Sluijs, P.; van Meer, G. How Proteins Move Lipids and Lipids Move Proteins. *Nat. Rev. Mol. Cell Biol.* **2001**, *2*, 504–513.
- (290) Espinosa, G.; Lopez-Montero, I.; Monroy, F.; Langevin, D. Shear Rheology of Lipid Monolayers and Insights on Membrane Fluidity. *Proc. Natl. Acad. Sci.* **2011**, *108*, 6008–6013.
- (291) Pohorille, A.; Deamer, D. Artificial Cells: Prospects for Biotechnology. *Trends Biotechnol.* **2002**, *20*, 123–128.

- (292) Buddingh', B. C.; Van Hest, J. C. M. Artificial Cells: Synthetic Compartments with Life-like Functionality and Adaptivity. *Acc. Chem. Res.* **2017**, *50*, 769–777.
- (293) Schoonen, L.; Van Hest, J. C. M. Compartmentalization Approaches in Soft Matter Science: From Nanoreactor Development to Organelle Mimics. *Adv. Mater.* **2016**, *28*, 1109–1128.
- (294) De Hoog, H. P. M.; Nallani, M.; Tomczak, N. Self-Assembled Architectures with Multiple Aqueous Compartments. *Soft Matter* **2012**, *8*, 4552–4561.
- (295) Marbella, L. E.; Millstone, J. E. NMR Techniques for Noble Metal Nanoparticles. *Chem. Mater.* **2015**, *27*, 2721–2739.
- (296) Dubochet, J.; Adrian, M.; Chang, J. J.; Homo, J. C.; Lepault, J.; McDowell, W.; Schultz, P. Cryo-Electron Microscopy of Vitrified Specimens. *Q. Rev. Biophys.* **1988**, *21*, 129–228.
- (297) Almgren, M.; Edwards, K.; Karlsson, G. Cryo Transmission Electron Microscopy of Liposomes and Related Structures. *Colloids Surfaces A Physicochem. Eng. Asp.* **2000**, *174*, 3–21.
- (298) Le Bihan, O.; Bonnafeux, P.; Marak, L.; Bickel, T.; Trépout, S.; Mornet, S.; De Haas, F.; Talbot, H.; Taveau, J. C.; Lambert, O. Cryo-Electron Tomography of Nanoparticle Transmigration into Liposome. *J. Struct. Biol.* **2009**, *168*, 419–425.
- (299) Huebner, S.; Battersby, B. J.; Grimm, R.; Cevc, G. Lipid-DNA Complex Formation: Reorganization and Fusion of Lipid Bilayers in the Presence of DNA as Observed by Cryo-Electron Microscopy. *Biophys. J.* **1999**, *76*, 3158–3166.
- (300) Helvig, S.; Azmi, I. D. M.; Moghimi, S. M.; Yaghmur, A. Recent Advances in Cryo-TEM Imaging of Soft Lipid Nanoparticles. **2015**, *2*, 116–130.
- (301) Vanhecke, D.; Asano, S.; Kochovski, Z. Cryo-Electron Tomography : Methodology , Developments. **2011**, *242*, 221–227.
- (302) Grassucci, R. A.; Taylor, D. J.; Frank, J. Preparation of Macromolecular Complexes for Cryo-Electron Microscopy. *Nat. Protoc.* **2007**, *2*, 3239–3246.
- (303) Newcomb, C. J.; Moyer, T. J.; Lee, S. S.; Stupp, S. I. Advances in Cryogenic Transmission Electron Microscopy for the Characterization of Dynamic Self-Assembling Nanostructures. *Curr. Opin. Colloid Interface Sci.* **2012**, *17*, 350–359.
- (304) Grassucci, R. A.; Taylor, D.; Frank, J. Visualization of Macromolecular Complexes Using Cryo-Electron Microscopy with FEI Tecnai Transmission Electron Microscopes. *Nat.*

Protoc. **2008**, *3*, 330–339.

- (305) Lučić, V.; Förster, F.; Baumeister, W. Structural Studies by Electron Tomography: From Cells to Molecules. *Annu. Rev. Biochem.* **2005**, *74*, 833–865.
- (306) Koning, R. I.; Koster, A. J. Cryo-Electron Tomography in Biology and Medicine. *Ann. Anat.* **2009**, *191*, 427–445.
- (307) Koning, R. I.; Koster, A. J.; Sharp, T. H. Advances in Cryo-Electron Tomography for Biology and Medicine. *Ann. Anat.* **2018**, *217*, 82–96.
- (308) McEwen, B. F.; Marko, M. The Emergence of Electron Tomography as an Important Tool for Investigating Cellular Ultrastructure. *J. Histochem. Cytochem.* **2001**, *49*, 553–563.
- (309) Lučić, V.; Rigort, A.; Baumeister, W. Cryo-Electron Tomography: The Challenge of Doing Structural Biology in Situ. *J. Cell Biol.* **2013**, *202*, 407–419.

Zekiye Pelin GUVEN
Materials Scientist and Engineer, PhD candidate
Chemin de Curtenaux 2, 1023 Crissier, Vaud
Phone: +41 78 816 53 84
zekiye.guven@epfl.ch or zpelin.guven@gmail.com

Education

École Polytechnique Fédérale de Lausanne, Lausanne, Switzerland (2014-2018)

PhD- Materials Science & Engineering

Sabancı University, Istanbul, Turkey, (2012–2014)

MSc-Materials Science & Engineering (GPA: 3.80/4.00)

Sabancı University, Istanbul, Turkey, (2007–2012)

BS-Materials Science & Engineering, Minor Honor Program in Chemistry (GPA: 3.74/4.00)

Uppsala University, Uppsala, Sweden, (Spring 2011)

Exchange Student

Work Experience

Graduate Research Assistant, Supramolecular Nanomaterials and Interfaces Laboratory, École Polytechnique Fédérale de Lausanne, *Fall 2014–Present*

Thesis subject: Nanoparticle and Liposome Interactions

Responsibilities included: Synthesis of ligands to modify gold nanoparticles, synthesis of gold nanoparticles, formation of vesicles, characterization of nanoparticle-vesicle hybrid systems with cryo-electron microscopy, confocal microscopy, and thorough fluorescence assays.

Submitted an abstract of results, “Signal transductions of vesicles”, to EDMX faculty presentations, Lausanne, (Sep 2015). Won a poster award.

Submitted an abstract of results, “Nanoparticle liposome interactions”, at “CIME Day”, Lausanne, Switzerland, (Apr 21–25, 2016). Won a poster award.

Submitted an abstract of results, “Nanoparticle for modification of vesicles”, at “Microscopy Conference”, Lausanne, Switzerland, (Aug 21–25, 2017). Won a poster award.

Submitted an abstract of results, “Nanoparticle vesicles interactions”, at “ICMSE”, Basel, Switzerland, (Aug 27–30, 2017).

‘Structure-Property Relationships of Amphiphilic Nanoparticles That Penetrate of Fuse Lipid Membranes’, DOI: 10.1021/acs.bioconjchem.7b00777

Supervisor. Prof. Francesco Stellacci.

Teaching Assistant for Thermodynamics for Materials Science course, École Polytechnique Fédérale de Lausanne, *2016–2017*

Responsibilities included: Leading recitation hours, preparing recitation and exam questions, and grading exam papers

Teaching Assistant for Mathematics, École Polytechnique Fédérale de Lausanne, *Spring 2018*

Responsibilities included: Leading recitation hours, grading exam papers

Graduate Research Assistant, Materials Science & Engineering, Sabancı University, 2012–2014

Thesis subject: Synthesis and characterization of mixed ligand chiral nanoparticles

Responsibilities included: Synthesis of gold/silver nanoparticles

Submitted an abstract of results, “Synthesis and characterization of mixed ligand chiral nanoparticles”, at European Material Research Society Meeting, Lille, France (May 26–30, 2014). Won a poster award.

“Synthesis and characterization of mixed ligand chiral nanoparticles”, DOI: 10.1039/C6DT00785F

Supervisor: Asst.Prof. Ozge Akbulut

Teaching Assistant for Introduction to Materials Science course, Sabancı University, 2012–2014

Responsibilities included: Leading recitation hours and laboratory sessions, preparing quizzes, grading exam papers, homework, and laboratory reports

Graduate Research Trainee, Supramolecular Nanomaterials and Interfaces Laboratory, École Polytechnique Fédérale de Lausanne, *Summer 2013*

Responsibilities included: Synthesis of silver, gold nanoparticles and characterization of nanomaterials

Submitted an abstract of results, “Curvature-dependent wetting of perfluorinated monolayers”, at American Chemical Society Meeting, Dallas, Texas (March 10–14, 2014).

“Curvature-dependent wetting of perfluorinated monolayers”, in preparation to be submitted as an article.

Supervisor: Prof. Francesco Stellacci

Undergraduate Research Assistant, Dept. of Materials Sci. & Metallurgy, University of Cambridge, *Summer 2011*

Project: Determining particle pick-up efficiency of fibers via harmonic analysis

Responsibilities included: Gravimetric measurements of linear density of fibers and determination of resonance frequencies of these fibers before and after exposure to particles

Supervisor: Prof. Alan H. Windle

Peer Tutor, Academic Support Program, Sabancı University, 2008–2012

Responsibilities included: Individual tutoring for the university freshman science course (introductory physics, chemistry and biology), moderating peer study session for Linear Algebra and Calculus.

Honors & Awards

- National Graduate Studies Scholarship in Abroad, The Scientific and Technological Research Council of Turkey (*TUBITAK*), 2012-2018, *withdrawn*
- National Graduate Studies Scholarship, *The Scientific and Technological Research Council of Turkey (TUBITAK)*, 2012–2014
- Tuition waiver for MSc, *Sabancı University*, 2012
- Award of Contribution to the University’s corporate structure and campus culture, *Sabancı University*, 2012

- Dean's High Honor list (6 semesters) and Honor list (two semesters), *Sabanci University*, 2007–2011
- Erasmus Summer Internship Mobility Student Scholarship, *European Union (EU)*, 2011
- Erasmus Exchange Student Scholarship, *European Union (EU)*, 2011
- Extra-Curricular Activities Award, *Sabanci University*, 2008, 2011
- Full Scholarship (awarded for success in the National University Entrance Exam, ranked 0.1% among 1.5 million participants), *Sabanci University*, 2007
- Government Scholarship for high achievement during elementary and high school studies, *Turkish Government*, 2000–2007

Skills

Lab Skills:	Cryo-Electron Microscopy (Cryo-EM), Transmission Electron Microscopy (TEM), Confocal Laser Scanning Microscopy (CLSM), Scanning Electron Microscopy (SEM), Thermal Gravimetric Analysis (TGA), Fourier Transform Infrared Spectroscopy (FT-IR), Dynamic Mechanical Analysis (DMA), Differential Scanning Calorimetry (DSC), Dynamic Light Scattering (DLS), UV-visible Spectroscopy (UV-Vis), Circular Dichroism Spectroscopy (CD), Flow Cytometry, Nuclear Magnetic Resonance (NMR), Spectra Fluorometer, Ultimate Testing Machine (UTM).
Computer Skills:	Image processing (Image J, iMod), Windows, MacOS, MS Office,
Language Skills:	Turkish (native), English (advanced), French (intermediate)